SECURITY CLASSIFICATION OF THIS PAGE

REPORT DOCUMENTATION PAGE

Form Approved OMB No. 0704-0188

1a. REPORT SECURITY CLASSIFICATION	1b. RESTRICTIVE MARKINGS
2a. SECURITY CLASSIFICATION AUTHORITY	3. DISTRIBUTION/AVAILABILITY OF REPORT Reproduction in whole or in part is permitted for any purpose of the United States Government
2b. DECLASSIFICATION/DOWNGRADING SCHEDULE	
4. PERFORMING ORGANIZATION REPORT NUMBER(S) N00014-89-J-1689	5. MONITORING ORGANIZATION REPORT NUMBER(S)
6a. NAME OF PERFORMING ORGANIZATION Materials Research Laboratory 6b. OFFICE SYMBOL (If applicable)	7a. NAME OF MONITORING ORGANIZATION
6c. ADDRESS (City, State, and ZIP Code) The Pennsylvania State University University Park, PA 16802	7b. ADDRESS (City, State, and ZIP Code)
8a. NAME OF FUNDING/SPONSORING ORGANIZATION 8b. OFFICE SYMBOL (If applicable)	9. PROCUREMENT INSTRUMENT IDENTIFICATION NUMBER
8c. ADDRESS (City, State, and ZIP Code)	10. SOURCE OF FUNDING NUMBERS PROGRAM ELEMENT NO. / PROJECT NO. / TASK NO. / WORK UNIT ACCESSION NO.

11. TITLE (Include Security Classification)
Electrostrictive Materials For Transducer Applications

12. PERSONAL AUTHOR(S)
L.E. Cross, R.E. Newnham, A.S. Bhalla, J.P. Dougherty, J.H. Adair, V.K. Varadan, V.V. Varadan

13a. TYPE OF REPORT	13b. TIME COVERED	14. DATE OF REPORT (Year, Month, Day)	15. PAGE COUNT
annual	FROM 2/89 TO 1/90		

16. SUPPLEMENTARY NOTATION

17. COSATI CODES			18. SUBJECT TERMS (Continue on reverse if necessary and identify by block number)
FIELD	GROUP	SUB-GROUP	

19. ABSTRACT (Continue on reverse if necessary and identify by block number)

This report documents work carried out in the Materials Research Laboratory of the Pennsylvania State University over the first year of a new three year Grant No. N00014-89-J-1689 on "Piezoelectric and Electrostrictive Materials for Transducer Applications". The program in MRL has been supplemented by an associated program in the Center for Engineering of Electronic and Acoustic Materials under V.V. and V.J. Varadan.

20. DISTRIBUTION/AVAILABILITY OF ABSTRACT	21. ABSTRACT SECURITY CLASSIFICATION
☐ UNCLASSIFIED/UNLIMITED ☐ SAME AS RPT. ☐ DTIC USERS	
22a. NAME OF RESPONSIBLE INDIVIDUAL	22b. TELEPHONE (Include Area Code) / 22c. OFFICE SYMBOL

DD Form 1473, JUN 86 Previous editions are obsolete. SECURITY CLASSIFICATION OF THIS PAGE

Abstract
Continued

Over the current year studies of the 3:0 type composite have evolved a new structure for a much more effective stress transforming composite. The device uses cavities in the electrode structure which are simple, inexpensive and robust. The sensitivity is higher than that of the end capped cylinder for equivalent PZT volume and we believe this will be a most important development for towed array hydrophones.

For agile transducer structures, the very high piezoelectric coefficients induced by DC bias in the lead magnesium niobate:lead titanate electrostrictors have been confirmed using both resonance and ultra-dilatometer methods. In parallel studies of aging in these systems a rather complete understanding of the aging process has been obtained and methods for fabricating PMN:PT systems with no aging developed, an essential need for the agile transducer.

The phenomenology of the PZT system has been completed and published and the equations are now being applied to studies of the properties of PZT compositions at the lead titanate end of the system. We expect that the phenomenology will be particularly valuable for the future evaluation of thin film PZTs where the breakdown field are such that $E_B.P_s$ is a large perturbation to the total energy.

In high strain actuators for surface modification and flow control antiferroelectric:ferroelectric systems have been explored which yield strains up to 0.85%. Effort is now being dedicated to understanding and eliminating fatigue effects in these charge switching systems.

In the associated program a detailed modeling of the 1:3 type PZT:polymer composite has now been completed.

TABLE OF CONTENTS

11. Q.M. Zhang, W.Y. Pan, S.J. Jang and L.E. Cross, "The Pressure Dependence of the Dielectric Response and Its Relation to Electrostriction," Ferroelectrics 88:147 (1989).
12. W.Y. Pan, W.Y. Gu, D.J. Taylor and L.E. Cross, "Large Piezoelectric Effect Induced by Direct Current Bias in PMN:PT Relaxor Ferroelectric Ceramics," Japanese J. Appl. Phys. 4:653 (1989).
13. D.J. Taylor, D. Damjanovic, A.S. Bhalla and L.E. Cross, "Complex Piezoelectric Elastic and Dielectric Coefficients of La doped $Pb(Mg_{1/3}Nb_{2/3})O_3$:0.07$PbTiO_3$ under DC Bias," Ferroelectric Letters.
14. W.Y. Gu, W.Y. Pan and L.E. Cross, "Effects of Thermal Treatment and DC Bias on Dielectric Aging in the PLZT 9.5:65:35 Relaxor Ferrolectric Ceramic," Ferroelectrics 89:47 (1989).
15. T.R. Shrout, W. Huebner, C.A. Randall and A.D. Hilton, "Aging Mechanisms in $Pb(Mg_{1/3}Nb_{2/3})O_3$-Based Relaxor Ferroelectrics," Ferroelectrics 93:361 (1989).
16. W.Y. Pan, T.R. Shrout and L.E. Cross, "Modelling the Aging Phenomenon in 0.9PMN:0.1PT Relaxor Ferroelectric Ceramic," J. Mat. Sci. 8:771 (1989).
17. Q.Y. Jiang, S.B. Krupanidhi and L.E. Cross, "Effects of the Lapped Surface Layer and Surface Stress on the Dielectric Properties of PLZT Ceramics," Proc. Symp. on Ceramic Dielectrics," Ed. H.C. Ling, Ceramic Soc. (1989).
18. S.W. Choi, T.R. Shrout, S.J. Jang and A.S. Bhalla, "Morphotropic Phase Boundary in $PbMg_{1/3}Nb_{2/3}O_3$-$PbTiO_3$ System," Materials Letters 8:253 (1989).
19. N. Kim, W. Huebner, S.J. Jang and T.R. Shrout, "Dielectric and Piezoelectric Properties of Lanthanum Modified Lead Magnesium Niobate-Lead Titanate Ceramics," Ferroelectrics 93:341 (1989).
20. M.T. Lanagan, N. Yang, D. Dube and S.J. Jang, "Dielectric Behaviour of the Relaxor $PbMg_{1/3}Nb_{2/3}O_3$-$PbTiO_3$ Solid Solution System in the Microwave Region," J. Am. Ceram. Soc. 72:481 (1989).
21. D.C. Dube, S.J. Jang and A. Bhalla, "Studying a Ferroelectric at Microwave Frequency," Ferroelectrics 87:303 (1988).
22. T.R. Shrout and J.P. Dougherty, "Lead Based $Pb(B_1B_2)O_3$ Relaxors vs. $BaTiO_3$ Dielectrics for Multilayer Capacitors," Proc. Symp. on Ceramic Dielectrics, Ed. H.C. Ling, Am. Ceram. Soc. (1989).

VOLUME II:

23. M.J. Haun, T.J. Harvin, M.T. Lanagan, Z.Q. Zhuang, S.J. Jang and L.E. Cross, "Thermodynamic Theory of $PbZrO_3$," J. Appl. Phys. 65:3173 (1989).
24. M.J. Haun, E. Furman, S.J. Jang and L.E. Cross, "Thermodynamic Theory of the Lead Zirconate-Titanate Solid Solution System, Part I. Phenomenology," Ferroelectrics 99:13 (1989).
25. M.J. Haun, E. Furman, H.A. McKinstry and L.E. Cross, "Thermodynamic Theory of the Lead Zirconate-Titanate Solid Solution System, Part II. Tricritical Behavior," Ferroelectrics 99:27 (1989).
26. M.J. Haun, Z.Q. Zhuang, E. Furman, S.J. Jang and L.E. Cross, "Thermodynamic Theory of the Lead Zirconate-Titanate Solid Solution System, Part III. Curie Constant and Sixth Order Polarization Interaction Dielectric Stiffness Coefficients," Ferroelectrics 99:45 (1989).
27. M.J. Haun, E. Furman, T.R. Halemane and L.E. Cross, "Thermodynamic Theory of the Lead Zirconate-Titanate Solid Solution System Part IV. Tilting of the Oxygen Octahedra," Ferroelectrics 99:55 (1989).
28. M.J. Haun, E. Furman, S.J. Jang and L.E. Cross, "Thermodynamic Theory of the Lead Zirconate-Titanate Solid Solution System Part V. Theoretical Calculations," Ferroelectrics 99:63 (1989).

29. M.J. Haun, Z.Q. Zhuang, E. Furman, S.J. Jang and L.E. Cross, "Electrostrictive Properties of the Lead Zirconate-Titanate Solid-Solution System," J. Am. Ceram. Soc. 72:1140 (1989).
30. M.J. Haun, E. Furman, S.J. Jang and L.E. Cross, "Modeling of the Electrostrictive, Dielectric and Piezoelectric Properties of Ceramic $PbTiO_3$," IEEE Trans. on Ultrasonics, Ferroelectrics and Frequency Control 36:393 (1989).
31. J.R. Oliver, R.R. Neurgaonkar and L.E. Cross, "Ferroelectric Properties of Tungsten Bronze Morphotropic Phase Boundary Systems," J. Am. Ceram. Soc. 72:202 (1989).
32. J.R. Oliver, R.R. Naugaonkar and L.E. Cross, "A Thermodynamic Phenomenology for Ferroelectric Tungsten Bronze $Sr_{0.6}Ba_{0.4}Nb_2O_6$ (SBN60)," J. Appl. Phys. 64:37 (1988).
33. Z.Q. Zhuang, M.J. Haun, S.J. Jang and L.E. Cross, "Composition and Temperature Dependence of the Dielectric, Piezoelectric and Elastic Properties of Pure PZT Ceramics," IEEE Transactions on Ultrasonics Ferroelectrics and Frequency Control 36:413 (1989).
34. J.N. Kim, M.J. Haun, S.J. Jang, L.E. Cross and X.R. Xue, "Temperature Behavior of Dielectric and Piezoelectric Properties of Samarium-Doped Lead Titanate Ceramics," IEEE Transactions on Ultrasonics Ferroelectrics and Frequency Control 36:389 (1989).
35. T.W. Dekleva, J.M. Hayes, L.E. Cross and G.L. Geoffroy, "Sol-Gel Processing of Lead Titanate in Two Methoxyethanol Investigation into the Nature of the Prehydrolized Solutions," Comm. to Am. Ceram. Soc. 71:C280 (1988).
36. W.Y. Pan, Q. Zhuang, A. Bhalla and L.E. Cross, "Field Forces Antiferroelectrics to Ferroelectric Switching in Modified Lead Zirconate Titanate Stannate Ceramics," J. Am. Ceram. Soc. 72:571 (1989).
37. W.Y. Pan, W.Y. Gu and L.E. Cross, "Transition Speed on Switching From a Field Induced Ferroelectric State to an Antiferroelectric Upon the Release of the Applied Field in $(PbLa)(ZrTiSn)O_3$ Antiferroelectric Ceramics," Ferroelectrics 99:185 (1989).

12. ASSOCIATED PROGRAM

APPENDICES

38. J.H. Jeng, V.V. Varadan and V.K. Varadan, "Design and Analysis of the Performance of PZT/Polymer Composite Transducers" (in press).

39. J.H. Jeng, X. Bao, V.V. Varadan and V.K. Varadan, "Finite Element-Eigenmode Analysis for the Design of 1-3 Composite Transducers Including the Effect of Fluid Loading" (in press).

ABSTRACT

This report documents work carried out in the Materials Research Laboratory of the Pennsylvania State University over the first year of a new three year Grant No. N00014-89-J-1689 on "Piezoelectric and Electrostrictive Materials for Transducer Applications". The program in MRL has been supplemented by an associated program in the Center for Engineering of Electronic and Acoustic Materials under V.V. and V.J. Varadan.

Over the current year studies of the 3:0 type composite have evolved a new structure for a much more effective stress transforming composite. The device uses cavities in the electrode structure which are simple, inexpensive and robust. The sensitivity is higher than that of the end capped cylinder for equivalent PZT volume and we believe this will be a most important development for towed array hydrophones.

For agile transducer structures, the very high piezoelectric coefficients induced by DC bias in the lead magnesium niobate:lead titanate electrostrictors have been confirmed using both resonance and ultra-dilatometer methods. In parallel studies of aging in these systems a rather complete understanding of the aging process has been obtained and methods for fabricating PMN:PT systems with no aging developed, an essential need for the agile transducer.

The phenomenology of the PZT system has been completed and published and the equations are now being applied to studies of the properties of PZT compositions at the lead titanate end of the system. We expect that the phenomenology will be particularly valuable for the future evaluation of thin film PZTs where the breakdown field are such that $E_B.P_s$ is a large perturbation to the total energy.

In high strain actuators for surface modification and flow control antiferroelectric:ferroelectric systems have been explored which yield strains up to 0.85%. Effort is now being dedicated to understanding and eliminating fatigue effects in these charge switching systems.

In the associated program a detailed modeling of the 1:3 type PZT:polymer composite has now been completed.

1. INTRODUCTION

This report documents work carried out in the Materials Research Laboratory of the Pennsylvania State University over the first year of a new three-year Grant No. N00014-89-J-1689 on "Piezoelectric and Electrostrictive Materials For Transducer Applications." The topics under study build on and expand the very extensive studies carried out under ONR support in earlier years.

For reporting purposes the activities are grouped under four major headings:

Piezoelectric Composites

Electrostrictive Materials

Phenomenological Studies

Conventional Piezoceramics.

To aid in all the low frequency studies, new instrumentation has been introduced and will be discussed in the composites section. The electrostrictive materials have been studied extensively for their aging behavior and now that aging is under control, agile transducers based on electrostrictors in which the piezoelectric effect can be switched on and off and controlled in both amplitude and phase are under study. Drawing upon the more conventional piezoelectrics work for both sensors and actuators the work on smart materials has been continued and expanded.

For the current year, the program in MRL has been reinforced by an associated funding to V.V. and V.J. Varadan in the Center for Engineering of Electronic and Acoustic Materials (CEEAM) in the College of Engineering. The topic of study has been a very detailed evaluation of the 1:3 type composites developed at an earlier time on the MRL program.

Following earlier precedent, the report will summarize briefly the highlights of activity over the year and will be backed up by an extensive set of appendices which are the papers published during the current year.

2. COMPOSITE TRANSDUCERS

2.1 Stress Re-distributing Systems.

One of the most exciting development on the program this last year has been the re-design of the crescent cavity transducers into a form which is exceedingly easy to construct, inexpensive and robust, but with exceedingly high sensitivity. We believe that this development could provide a "drop in" replacement for the end

capped cylinder hydrophone which could be much more robust, less expensive, and of higher sensitivity.

In earlier studies we had demonstrated the advantage of a narrow crescent shaped cavity in a ceramic PZT disc which acts to re-distribute stress and cancel out the disadvantageous T_1, T_2 components (fig. 1) under hydrostatic pressure.

Over the current year we have realized two major advantages.

(1) The narrow cavity has been transferred from the ceramic unit into a rigid electrode (fig. 2).

(2) The electrode is soldered to a fully silvered disk at high temperature so that thermal contraction puts the disc under strong biaxial compression (fig. 2).

Advantages for the present construction are:

* The shallow cavities (100 μ deep) are simple and inexpensive to machine in the metal electrode.

* Because of the built in compressive stress the finished transducer is exceedingly robust and will stand shock pressures which completely close the cavity.

* The sensitivity is higher than that of the end capped cylinder for an equivalent volume of PZT (i.e., the device exploits both d_{33} and d_{31}).

* The sensitivity is independent of pressure up to greater than 1,000 psi, with a wide flat frequency response and no spurious resonances.

* Self capacitance is very high so that the hydrophone can drive long cables.

* The construction is simple, inexpensive, robust, and likely to have very high reliability.

* The shape is compact and ideal for the segments in a towed array.

Typical sensitivity data are shown in fig. 3, which compares $d_h g_h$ to that of other proposed composites (note the break in scale). The stability against pressure change in both d_h and g_h coefficients is delineated in fig. 4 and the smooth approach to high frequency resonance without spurious lower frequency modes is demonstrated in fig. 5.

In summary, we believe the electrode cavity type 3:0 composite makes a step function advance in the state-of-the-art for a simple robust, inexpensive versatile hydrophone.

2.2 General Contributions.

Two invited papers by Newnham (Appendix 1) and Cross (Appendix 2) encapsulate much of the thinking behind the approaches being explored in these ONR studies. The clear conscious linking of structure and properties in these mostly

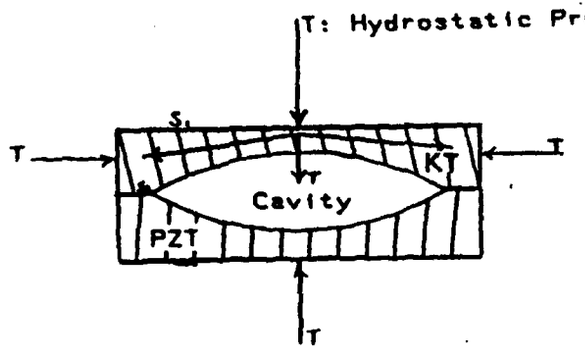

$T_x = T - KT = -(K-1)T$

T_x: Extensional Stress in X-Direction

K: Transformal Stress Amplifier Factor

$D_x = -d_{31} \cdot T_x = (K-1)Td_{31} = D_y$

$D_z = d_{33} \cdot T \equiv d_{33} \cdot T(S_1/S_2)$

$d_h = (B/S)/T = (D_x+D_y+D_z)/T \equiv 2(K-1)d_{31}+(S_1/S_2)d_{33}$

$g_h \equiv 46 \times 10^{-3}$ Vm/N

$d_h \equiv 231$ pC/N

$d_h \cdot g_h \sim 10{,}000 \times 10^{-15}$

Fig. 1. Original Ceramic Cavity Structure.

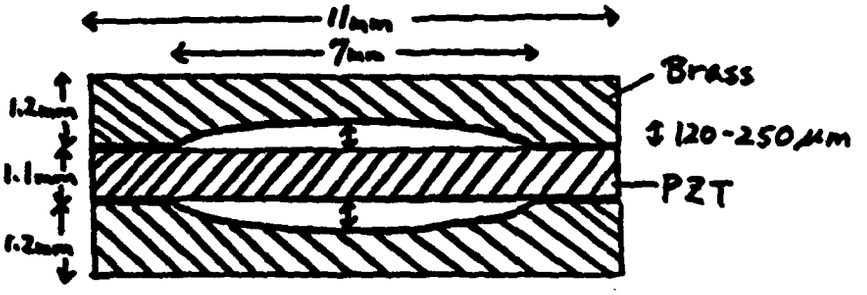

STRESS TRANSFORMING COMPOSITE

Fig. 2. New Electrode Cavity Structure.

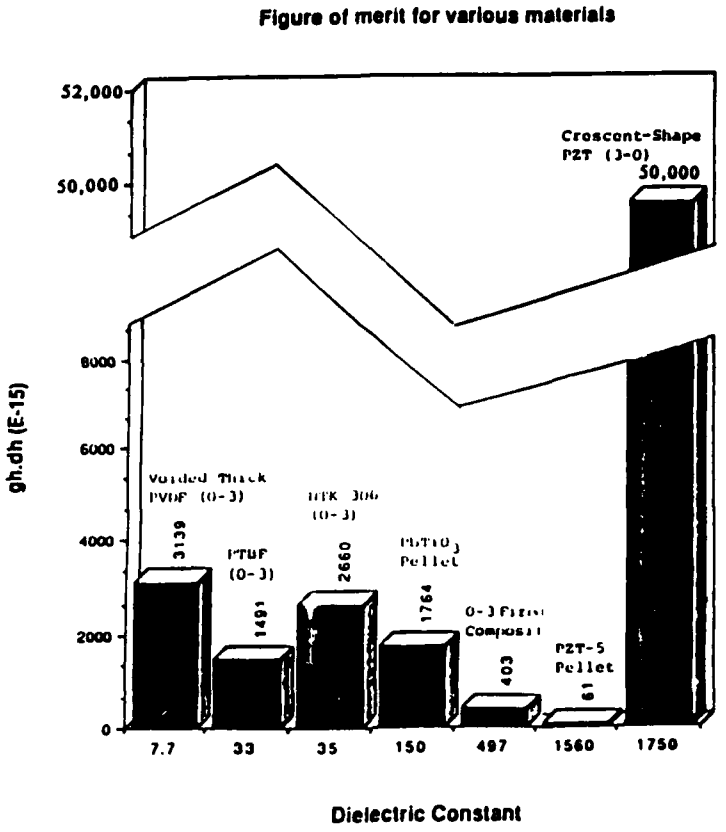

Fig. 3. Sensitivity d_{hgh} for electrode cavity structure.

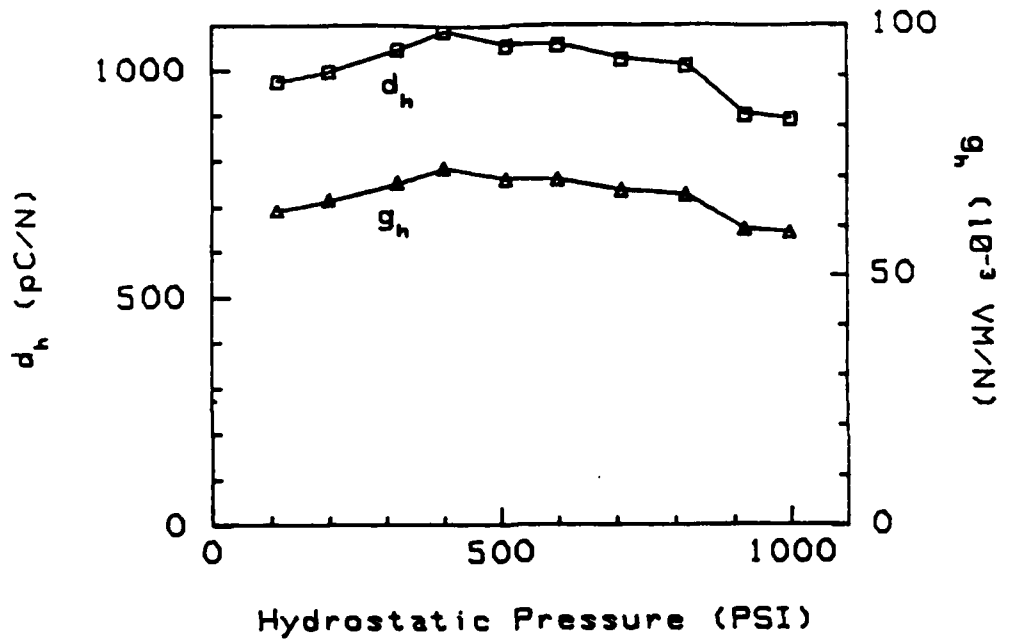

Fig. 4. Response d_h and g_h as a function of hydrostatic pressure.

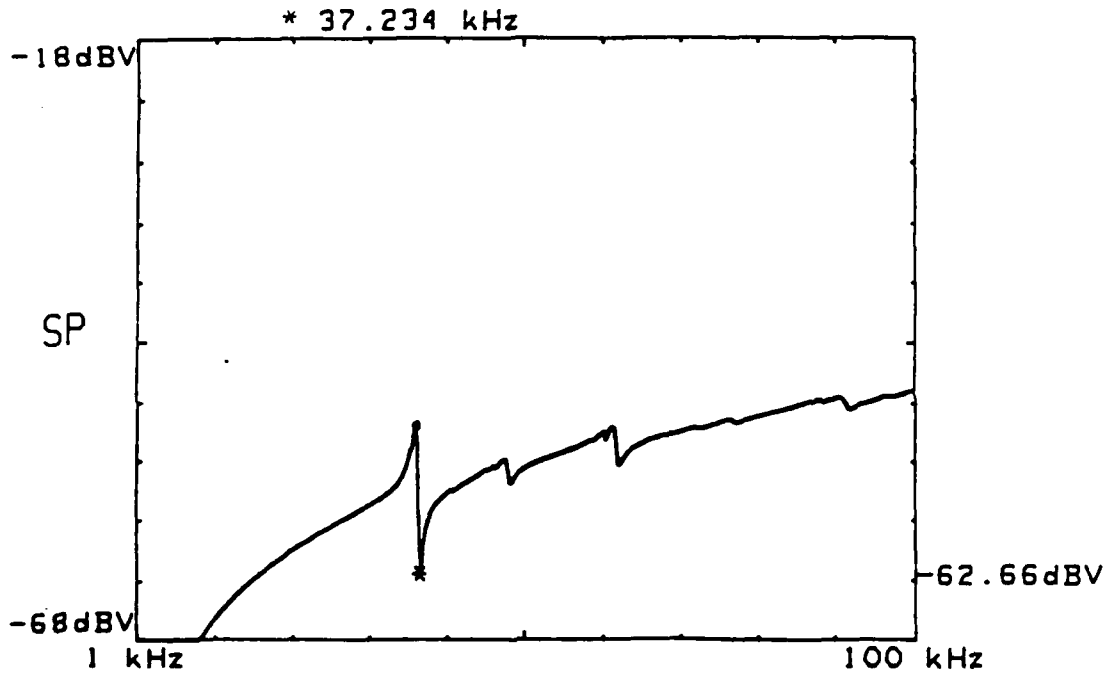

Fig. 5. Frequency response of the electrode cavity 3:0 structure.

perovskite systems, and the specific design of composite systems to improve material performance and to vanish the transducer into the material for large area sensor application. It is these modes of thinking which gave rise to the consideration of non-linear behavior in the electrostrictors to make agile transducers and the combination of sensor and responder with active electronics in a single composite to make smart ceramics (Appendix 3).

2.3 Instrumentation.

To explore the dispersive properties of the composites it has been necessary to evolve new AC ultradilatometry for piezoelectric deformation studies, and the single surface measuring system developed earlier, which was capable of resolving low frequency AC displacements of 10^{-3} A^{o}, has been of tremendous utility. This year the focus has been upon extending the ultradilatometer so as to be able to measure the separation between two surfaces. In this way we have been able to eliminate spurious flexure motion and all contributions from instrument resonances so as to measure high frequencies right through the sample resonance.

The development of the double beam two-surface measuring instrument is described in detail in Appendix 4, and demonstration of the sensitivity of 10^{-2} A is described. The use of this new instrument to measure high frequency strain response in PZT and PLZT ferroelectrics is described in Appendix 5. In a related family of experiments to prove out the capability in this instrument to resolve both amplitude and phase, the dilatometer has been used to map the real and imaginary parts of d_{31} for a PZT5 and to explore the phase delay with respect to the electric field at frequencies very close to resonance (Appendix 6).

For frequencies close to resonance in a piezoelectric, a new equivalent circuit has been derived which contains components associated with the piezoelectrically coupled energy loss and has been tested successfully for samples which show a significant piezoelectric phase angle (Appendix 7).

3. ELECTROSTRICTION.

3.1. Introduction.

Electrostriction in relaxor ferroelectric materials like lead magnesium niobate (PMN) and its solid solutions with lead titanate (PT) are now coming into increasing use in sensor and actuator systems and as high K dielectrics in capacitors. In all these areas it is important to have a broader basic understanding of the complex

origins of the useful elasto-dielectric properties and some effort has been dedicated to this end on this problem. Since the relaxors represent a very large class of most interesting self-assembling nanocomposites, the more detailed basic study is being carried out under DARPA/ONR contract N00014-86-K-0767 "Nanocomposites for Electronic Applications."

Basic topics studied on this program relate to the nature of the micropolar structure in lead magnesium niobate and its modification in PMN:PT solid solutions, particularly as these approach to the morphotropic compositions, to the build-up of the macropolar state under field and composition change, and to the coupling of the nanopolar regions to the dimensions of the sample, i.e, the elasto-dielectric effects.

For the family of applications which seek to use PMN and PMN:PT for precise position control or in agile piezoelectric transduction it has been most important to understand and control aging in these compositions. This understanding is particularly important for bias controlled electrostrictors where it has also been important to explore the frequency response in the biased piezoelectric sates and the manner in which piezoelectricity may be simply related to the dielectric and electrostrictive properties.

3.2 Fundamental Studies.

Transmission electron microscope studies of the PMN:PT system (Appendix 8) confirm the postulated nanoscale polar regions in the 0.93 PMN: 0.07% PT composition at very low temperature and the increasing size and perfection of polar regions as they mutate into a full domain structure at the 0.6 PMN:0.4 PT composition. The presence of the pseudo-morphotropic phase boundary between rhombohedral and tetragonal phases has been confirmed by dielectric and pyroelectric studies (Appendix 9).

In all normal proper ferroelectrics it is expected that the piezoelectric and electrostrictive constants in polarization notation are almost constant and only weakly dependent on temperature even in the vicinity of the Curie points. For crystals in centric prototypes, like the perovskite

$$s_{ij} = Q_{ijkl} P_k P_l$$

and the Q_{ijkl}, i.e., Q_{11}, Q_{12}, Q_{44} are only weak functions of temperature.

For PMN0.9:PT0.1 and for 9:65:35 PLZT relaxors, it is shown (Appendix 10) that Q_{11} and Q_{12} are quite strong functions of temperature near T_c due to the makeup of the polarization which involves both 180° (non-shape changing) and 90° (shape changing) reorientations of the micropolar regions. The unusual character of the

relaxors is also reflected in the stress dependence of the dielectric stiffness, which in simple non-polar solids is directly equivalent to polarization related electrostriction. In Appendix 11 simple relations are defined for ferroelectric and antiferroelectric crystals but it is shown that the relaxor is more complicated even above the mean Curie temperature, due to the coexistance of polar and non polar regions.

3.3 Agile Transducers.

In the report of studies carried out in 1988, the large possible piezoelectric effects in relaxor ferroelectric 0.9PMN:0.1PT were highlighted from an analysis of the slopes of the low frequency electrostrictive displacement vs field curves. Over the current contract period these results have been confirmed for a range of PMN:PT compositions which have been explored under DC bias using the MRL ultradilatometer facility.

Very high values of d_{33} up to 800 pc/N were confirmed for the frequency range from 0.1 Hz to 50 kHz (Appendix 12). It was also shown that in the non-dispersive composition/temperature domain $d_{33} \sim 2Q_{11}P_3\varepsilon_{33}$, where P_3 is the induced polarization and ε_{33} the permittivity at that polarization/field level. In a parallel study, using a lanthanum modified 0.93 PMN:0.07 PT composition, high values of piezoelectric d_{31} were confirmed by resonance methods (Appendix 13).

Clearly the PMN:PT system can provide agile piezoelectric materials which can be switched in both amplitude and phase by quite realizable DC fields. These materials could be applied directly to ultrasonic tomography as the resonance frequencies are such that the monolythic sample can be switched with reasonable voltage. Takeuchi, Masuzawa, Nakya, and Ito have described a 1:3 composite PMN:PT polyurethane array using just this principal. Companies in the USA are also interested but proprietary restrictions limit discussion.

For application of the agile sensors to lower frequency Navy applications, multilayer devices will be required and studies are now being developed upon simple inexpensive electrodes which could be co-fired with these compositions.

3.4 Aging Studies.

In PLZT relaxor compositions such as the 9.5:65:35, the defects arising from the lead vacancies which must compensate the trivalent lanthanum are such that all samples show aging. The aging does not, however, follow the normal log:linear form but takes a log:log character of the form $K = K_0 t^{-n}$ (Appendix 14). Aging affects dominantly the low frequency dispersive component of the response so that the Cole-

Cole arc shrinks continuous from the low frequency intercept, confirming and extending the original data of Schulze et. al.

In PMN:PT recent aging studies are summarized in Appendices 15 and 16. For this system ceramics which are carefully prepared on exact stoichiometry using very high purity chemicals can be completely free from aging (a most important result). Aging can, however, be re-introduced by non-stoichiometry or by doping with aleovalent ions. For doped materials the aging is very similar to that in PLZT, again affecting the dispersive low frequency component. Again, the effects of temperature change about the aging temperature are not symmetric, dispersion staying small at higher temperatures but being re-introduced by cooling the aged sample.

The model which explains all current aging results requires that the micro-polar regions which characterize the relaxor state be of slightly lower symmetry than the corresponding ferroelectric domain states. The polar vector then has a weakly preferred direction which becomes stabilized over time by readjustment of the dipolar defect structure. Qualitatively the model is very similar to that most recently proposed for aging in $BaTiO_3$ and PZT with the only exception that in PMN the whole micro polar region is dynamic whilst in the normal ferroelectrics it is only the domain wall region which is active.

3.5 Additional Relaxor Studies.

The ferroelectric literature is replete with all sorts and conditionals of surface layer both intrinsic and extrinsic for both the free and the electroded surfaces of ferroelectrics. In many instances the surface layer is diagnosed by a thickness dependence of the properties , but frequently the phenomena are confused by artifacts from the surface finishing. The problem of the ceramic:electrode interface is particularly important where large polarization charges are being switched, as in high strain actuators or thin film ferroelectrics for non-volatile memory applications .

PLZT ceramics which have been hot pressed to high optical transparency are free from internal macro-voids and offer an excellent vehicle for electrode interface studies. Data presented in Appendix 17 shows very clearly the existence of an extrinsic surface layer and how it is modified by polishing, lapping, or etching the surface. It also presents evidence that properties are also modified by internal stresses generated by the finishing process.

Data presented in Appendices 18 and 19 explore the properties in PMN:PT materials at compositions near 0.7PMN:0.3PT in the vicinity of the morphotropic phase boundary between rhombohedral and tetragonal ferroelectric phases, showing the large piezoelectric constants which occur in these compositions.

Dielectric studies on PMN:PT at the relaxor composition 0.9PMN:0.1PT have been extended into the region of microwave frequencies with measurements at 10 GHz (Appendix 20) showing continuation of the dielectric dispersion into this frequency range. Dielectric studies on high K materials at these frequencies are not at all simple and some of the techniques which can be applied are delineated in Appendix 21.

A general assessment of the importance of the relaxor ferroelectric families to the future of the multilayer ceramic capacitor (MLC) businesses is included for completeness as Appendix 22.

4. PHENOMENOLOGICAL THEORY.

Delineation of the Phenomenological Gibbs Free Energy functions for the $PbZrO_3$:$PbTiO_3$ family are now largely completed. Pre-prints of the work were included in the 1987 annual report. A final version of the phenomenology for $PbZrO_3$ is given in Appendix 23, and the complete set of five papers on the PZT solid solutions in Appendices 24, 25, 26, 27, and 28.

The derivation of the composition dependence of the electrostriction constants which were required for the phenomenology has been documented in Appendix 29, and an early exploitation of the phenomenological model to derive the electrostrictive, dielectric, and piezoelctric constants for lead titanate is given in Appendix 30. It is interesting to note from this study that the very large piezoelectric anisotropy which is evident in the lead titanate based ceramics has its origin in the unusually small value of Q_{12}, the averaged electrostriction constant.

It is interesting to note that in the tungsten bronze system, there is wide occurrence of solid solution systems which exhibit morphotropic phase boundaries (Appendix 31). Application of the phenomenological approach to the $Ba_{1-x}Sr_xNb_2O_6$ bronze, however, leads to equations in which both fourth power and sixth power terms in the order parameter are strong functions of temperature (Appendix 32), an interesting consequence of the relaxor behavior in this system. These two studies were accomplished in cooperative programs with the Rockwell Science Center in Thousand Oaks and are only included because of strong relevance to this program,

and through the participation of L. Eric Cross, part of whose support was from this program.

5. CONVENTIONAL PIEZOELECTRIC CERAMICS.

It was shown in earlier studies that in PZT ceramics of constant Zr:Ti ratio that are differently doped to produce soft, intermediate, or hard piezoelectric properties, the extensive extrinsic contributions freeze out at very low temperature so that all compositions have virtually identical properties at 4.2°K. In more recent studies we have explored the freeze out of the extrinsic property contributions in pure $PbZrO_3$:$PbTiO_3$ of different Zr:Ti ratio. This data was needed to determine coefficients in the phenomenology for PZTs and illustrates how the intrinsic properties change across the phase diagram (Appendix 33).

Following the modelling carried out on pure $PbTiO_3$ (Appendix 30) it was interesting to re-measure the properties of the Samarium doped lead titante over a wide temperature range (Appendix 34). From these studies it is clear that both ε_{33} and d_{33} appear mainly due to the average intrinsic property of the single domain. For d_{31} and Kp, the intrinsic contribution is very small and now extrinsic contributions can set the sign, even though the large anisotropy is again primarily due to the low value of Q_{12}.

For most of the studies carried out on ceramic samples, the materials were prepared here in the Laboratory and in many cases special preparation techniques had to be derived. These studies are however, largely subsumed into the experimental discussions in the earlier papers in these appendices.

In the extensive use of sol-gel methods to produce highly pure stoichiometric powder in the PZTs, it was necessary to study the chemistry of lead titante formation as a typical example and this work is separately reported in Appendix 35.

6. HIGH STRAIN ACTUATORS.

In general the elastic strain x_{ij} which may be induced in a polarizable deformable insulator may be characterized phenomenologically by the relation

$$x_{ij} = s_{ijkl}X_{kl} - b_{mij}P_m - Q_{mnij}P_mP_n$$

where X_{kl}, P_m, P_n are components of the elastic stress and electric polarizarion respectively, s_{ijkl} the elastic compliance, b_{mij} the piezoelectric coefficient in polarization notation, and Q_{mnij} the electrostriction tensor.

For all known materials, the b and Q constants are such that at realizable fields in bulk samples induced polarizations are such that the induced strains are limited to ~ 0.2%.

In ferroelectric polar states however, spontaneous polarization levels are such that strains up to ~ 15% occur spontaneously. Thus for high strain actuators it is clear that using present materials it is essential to manipulate the spontaneous polarization either by a phase change or by a domain change.

In two related studies the field forced antiferroelectric to ferroelectric phase change was investigated. In Appendix 36 it is shown that strains up to 0.85% can be induced electrically and that forward switching times of less than 1 μ sec are possible under high field. A major current topic of study is the fatigue effect which limits the number of switching cycles in these and in other high strain systems. In a second closely related study, the back switching from the induced ferroelectric into the stable antiferroelectric state was explored (Appendix 37). In some compositions back switching in times less than 2 μ sec was observed suggesting that in most compositions under a suitable back switching field very fast turn off will be possible.

7. APPRENTICE PROGRAM.

The apprentices who worked on the program during 1989 were:

Name:	Michael J. Hawkins
Birthdate:	March 30, 1971
Home Address:	940 Boundry Road
	Wenonah, NJ 08090
College:	Penn State

and

Name:	Tanika Robinson
Birthdate:	November 1, 1971
Home Address:	1672 N Wilton St.
	Philadelphia, PA 19131
College:	Ohio University

Michael Hawkins assisted S. Kumar who is working on smart materials. He was involved in the setting up of underwater acoustic tests in the MRL tank facility.

Tanika Robinson was involved with computer design and graphics for the 3:0 transducer materials and also assisted in the preparation for chemically derived perovskite powders.

THE PENNSYLVANIA STATE UNIVERSITY

MATERIALS RESEARCH LABORATORY

1989

Office of Naval Research
Apprentice Program Certification

for successful completion of the 7 week project/study program in Electronic Ceramica

Tanika Robinson

PENNSTATE

THE PENNSYLVANIA STATE UNIVERSITY

MATERIALS RESEARCH LABORATORY

1989

Office of Naval Research
Apprentice Program Certification

for successful completion of the 7 week project/study program in Electronic Ceramica

Michael J. Hawkins

PENNSTATE

Certificates for the two students are appended.

8. PAPERS PUBLISHED IN REFEREED JOURNALS

1. R.E. Newnham, "Electroceramics," Reports on the Progress in Physics 52:123-156 (1989).
2. L.E. Cross, "Piezoelectric and Electrostrictive Sensors and Actuators for Adaptive Structures and Smart Materials," Proc. AME 110th Annual Mtg., San Fransisco (December 1989).
3. R.E. Newnham, Q.C. Xu, S. Kumar and L.E. Cross, "Smart Ceramics," Ferroelectrics 102:77-89 (1990).
4. W.Y. Pan and L. Eric Cross, "A Sensitive Double Beam Laser Interferometer for Studying High Frequency Piezoelectric and Electrostrictive Strains," Rev. Sci. Inst. 60:2701 (1989).
5. Q.M. Zhang, S.J. Jang and L.E. Cross, "High Frequency Strain Response in Ferroelectrics and Its Measurement Using a Modified Mach-Zehnder Interferometer," J. Appl. Phys. 65:2807 (1989).
6. W.Y. Pan, H. Wang and L.E. Cross, "Laser Interferometer for Studying Phase Delay in Piezoelectric Response."
7. Dragon Damjanovic, "An Equivalent Electrical Circuit of a Piezoelectric Bar Resonator with a Large Piezoelectric Phase Angle," Ferroelectrics.
8. A.D. Hilton, C.A. Randall, D.J. Barber and T.R. Shrout, "TEM Studies of $Pb(Mg_{1/3}Nb_{2/3})O_3$-$PbTiO_3$ Ferroelectric Relaxtors," Ferroelectrics 93:379 (1989).
9. S.W. Choi, T.R. Shrout, S.J. Jang and A.S. Bhalla, "Dielectric and Pyroelectric Properties in the $Pb(Mg_{1/3}Nb_{2/3})O_3$-$PbTiO_3$ system," Ferroelectrics 100:29 (1989).
10. Q. Zhang, W. Pan, A. Bhalla and L.E. Cross, "Electrostrictive and Dielectric Response in Lead Magnesium Niobate-Lead Titanate (0.9PMN:0.1PT) and Lead Lanthanum Zirconate Titanate (PZT 9.5/65/35) Under Variation of Temperature and Electric Field," J. Am. Ceram. Soc. 72(4):599 (1989).
11. Q.M. Zhang, W.Y. Pan, S.J. Jang and L.E. Cross, "The Pressure Dependence of the Dielectric Response and Its Relation to Electrostriction," Ferroelectrics 88:147 (1989).

12. W.Y. Pan, W.Y. Gu, D.J. Taylor and L.E. Cross, "Large Piezoelectric Effect Induced by Direct Current Bias in PMN:PT Relaxor Ferroelectric Ceramics," Japanese J. Appl. Phys. 4:653 (1989).

13. D.J. Taylor, D. Damjanovic, A.S. Bhalla and L.E. Cross, "Complex Piezoelectric Elastic and Dielectric Coefficients of La doped $Pb(Mg_{1/3}Nb_{2/3})O_3$:0.07$PbTiO_3$ under DC Bias," Ferroelectric Letters.

14. W.Y. Gu, W.Y. Pan and L.E. Cross, "Effects of Thermal Treatment and DC Bias on Dielectric Aging in the PLZT 9.5:65:35 Relaxor Ferrolectric Ceramic," Ferroelectrics 89:47 (1989).

15. T.R. Shrout, W. Huebner, C.A. Randall and A.D. Hilton, "Aging Mechanisms in $Pb(Mg_{1/3}Nb_{2/3})O_3$-Based Relaxor Ferroelectrics," Ferroelectrics 93:361 (1989).

16. W.Y. Pan, T.R. Shrout and L.E. Cross, "Modelling the Aging Phenomenon in 0.9PMN:0.1PT Relaxor Ferroelectric Ceramic," J. Mat. Sci. 8:771 (1989).

17. Q.Y. Jiang, S.B. Krupanidhi and L.E. Cross, "Effects of the Lapped Surface Layer and Surface Stress on the Dielectric Properties of PLZT Ceramics," Proc. Symp. on Ceramic Dielectrics," Ed. H.C. Ling, Ceramic Soc. (1989).

18. S.W. Choi, T.R. Shrout, S.J. Jang and A.S. Bhalla, "Morphotropic Phase Boundary in $PbMg_{1/3}Nb_{2/3}O_3$-$PbTiO_3$ System," Materials Letters 8:253 (1989).

19. N. Kim, W. Huebner, S.J. Jang and T.R. Shrout, "Dielectric and Piezoelectric Properties of Lanthanum Modified Lead Magnesium Niobate-Lead Titanate Ceramics," Ferroelectrics 93:341 (1989).

20. M.T. Lanagan, N. Yang, D. Dube and S.J. Jang, "Dielectric Behaviour of the Relaxor $PbMg_{1/3}Nb_{2/3}O_3$-$PbTiO_3$ Solid Solution System in the Microwave Region," J. Am. Ceram. Soc. 72:481 (1989).

21. D.C. Dube, S.J. Jang and A. Bhalla, "Studying a Ferroelectric at Microwave Frequency," Ferroelectrics 87:303 (1988).

22. T.R. Shrout and J.P. Dougherty, "Lead Based $Pb(B_1B_2)O_3$ Relaxors vs. $BaTiO_3$ Dielectrics for Multilayer Capacitors," Proc. Symp. on Ceramic Dielectrics, Ed. H.C. Ling, Am. Ceram. Soc. (1989).

23. M.J Haun, T.J. Harvin, M.T. Lanagan, Z.Q. Zhuang, S.J. Jang and L.E. Cross, "Thermodynamic Theory of $PbZrO_3$," J. Appl. Phys. 65:3173 (1989).

24. M.J. Haun, E. Furman, S.J. Jang and L.E. Cross, "Thermodynamic Theory of the Lead Zirconate-Titanate Solid Solution System, Part I. Phenomenlogy," Ferroelectrics 99:13 (1989).

25. M.J. Haun, E. Furman, H.A. McKinstry and L.E. Cross, "Thermodynamic Theory of the Lead Zirconate-Titanate Solid Solution System, Part II. Tricritical Behavior," Ferroelectrics 99:27 (1989).

26. M.J. Haun, Z.Q. Zhuang, E. Furman, S.J. Jang and L.E. Cross, "Thermodynamic Theory of the Lead Zirconate-Titanate Solid Solution System, Part III. Curie Constant and Sixth Order Polarization Interaction Dielectric Stiffness Coefficients," Ferroelectrics 99:45 (1989).

27. M.J. Haun, E. Furman, T.R. Halemane and L.E. Cross, "Thermodynamic Theory of the Lead Zirconate-Titanate Solid Solution System Part IV. Tilting of the Oxygen Octahedra," Ferroelectrics 99:55 (1989).

28. M.J. Haun, E. Furman, S.J. Jang and L.E. Cross, "Thermodynamic Theory of the Lead Zirconate-Titanate Solid Solution System Part V. Theoretical Calculations," Ferroelectrics 99:63 (1989).

29. M.J. Haun, Z.Q. Zhuang, E. Furman, S.J. Jang and L.E. Cross, "Electrostrictive Properties of the Lead Zirconate-Titanate Solid-Solution System," J. Am. Ceram. Soc. 72:1140 (1989).

30. M.J. Haun, E. Furman, S.J. Jang and L.E. Cross, "Modeling of the Electrostrictive, Dielectric and Piezoelectric Properties of Ceramic $PbTiO_3$," IEEE Trans. on Ultrasonics, Ferroelectrics and Frequency Control 36:393 (1989).

31. J.R. Oliver, R.R. Neurgaonkar and L.E. Cross, "Ferroelectric Properties of Tungsten Bronze Morphotropic Phase Boundary Systems," J. Am. Ceram. Soc. 72:202 (1989).

32. J.R. Oliver, R.R. Naugaonkar and L.E. Cross, "A Thermodynamic Phenomenology for Ferroelectric Tungsten Bronze $Sr_{0.6}Ba_{0.4}Nb_2O_6$ (SBN60)," J. Appl. Phys. 64:37 (1988).

33. Z.Q. Zhuang, M.J. Haun, S.J. Jang and L.E. Cross, "Composition and Temperature Dependence of the Dielectric, Piezoelectric and Elastic Properties of Pure PZT Ceramics," IEEE Transactions on Ultrasonics Ferroelectrics and Frequency Control 36:413 (1989).

34. J.N. Kim, M.J. Haun, S.J. Jang, L.E. Cross and X.R. Xue, "Temperature Behavior of Dielectric and Piezoelectric Properties of Samarium-Doped Lead Titanate Ceramics," IEEE Transactions on Ultrasonics Ferroelectrics and Frequency Control 36:389 (1989).

35. T.W. Dekleva, J.M. Hayes, L.E. Cross and G.L. Geoffroy, "Sol-Gel Processing of Lead Titanate in Two Methoxyethanol Investigation into the Nature of the Prehydrolized Solutions," Comm. to Am. Ceram. Soc. 71:C280 (1988).

36. W.Y. Pan, Q. Zhuang, A. Bhalla and L.E. Cross, "Field Forces Antiferroelectrics to Ferroelectric Switching in Modified Lead Zirconate Titanate Stannate Ceramics," J. Am. Ceram. Soc. 72:571 (1989).

37. W.Y. Pan, W.Y. Gu and L.E. Cross, "Transition Speed on Switching From a Field Induced Ferroelectric State to an Antiferroelectric Upon the Release of the Applied Field in (PbLa)(ZrTiSn)O_3 Antiferroelectric Ceramics," Ferroelectrics 99:185 (1989).

9. INVITED LECTURES

1. The Fourth B.N. Singh Memorial Lecture, University of Delhi, January 25, 1989, L. Eric Cross, "Future Prospects in Electronic Ceramic Materials and Applications".
2. Indo-US Workshop on Electronic Ceramics and Materials, Pune India, January 14-16, 1989, L. Eric Cross, "At the Frontiers of Ceramic Science-Current Salients".
3. 91st Annual Meeting of the American Ceramic Society, Indianapolis, Indiana, April 23-27, 1989, L. Eric Cross, "High Permittivity Dielectrics for Multilayer Applications".
4. 1st Conference of the European Ceramic Society, Maastrict June 18-23, 1989, L. Eric Cross, "Electronic Ceramics: Current Issues and Future Prospects".
5. 1st US:USSR Seminar on Ferroelectricity, Boulder, Colorado, July 10-13, 1989, L. Eric Cross, "Relaxor Ferroelectrics".
6. 7th International Meeting on Ferroelectrics IMF7, Saarbrucken, F.R. Germany, August 28-September 1, 1989, L. Eric Cross, "Applications of Ferroelectrics".
7. First International Science and Technology Congress, Anaheim, California, October 31-November 3, 1989, L. Eric Cross, "Unusual Ferroic Phenomena and Their Potential Device Applications".
8. First International Science and Technology Congress, Anaheim, California, October 31-November 3, 1989, L. Eric Cross, "Ferroelectric Thin Films".
9. International Conference on Electronic Components and Materials, Beijing, China, November 7-10, 1989, L. Eric Cross, "Electronic Ceramics: Current Issues and Future Prospects".
10. 110th Annual Meeting of the American Society of Mechanical Engineers, San Francisco, California, December 10-15, 1989, L. Eric Cross, "Piezoelectric and

Electrostrictive Sensors and Actuators for Adaptive Structures and Smart Materials".

11. Indo-U.S. Workshop on Electronic Ceramics and Materials, Pune, India, January 14-16, 1989, R.E. Newnham, "Smart Composites".
12. CERAMTEC '89 Conference and Exposition, American Society of Metals, January 31, 1989, R.E. Newnham, "The Next Generation of Sensors and Microsensors".
13. Association for the Progress of New Chemistry, Tokyo-Oiso, Japan, February 6-10, 1989, R.E. Newnham, "Structure-Property Relationships in Nanocomposites".
14. Symposium on Integrated Ferroelectrics, Colorado Microelectronics Conference, Colorado Springs, Colorado, March 28-30, 1989, R.E. Newnham, Introduction to Ferroelectric Materials".
15. Symposium on Superconducting Oxides and Materials, American Chemical Society National Meeting, Dallas, TX, April 9-14, 1989, R.E. Newnham and W. Huebner, "Ferroic Phenomena in Oxides".
16. International Conference on coating and Sensors for Acoustic and Electromagnetic/Optical Applications, Pennsylvania State University, University Park, May 9-11, 1989, R.E. Newnham, "Smart Ceramics".
17. 117th Meeting of the Acoustical Society of America, Syracuse University, Syracuse, NY, May 22-26, 1989, R.E. Newnham and QiChang Xu, "Electrostrictive Materials".
18. American Crystallographic Association, University of Washington, Seattle, Washington, July 23-28, 1989, R.E. Newnham, "Phase Transformations in Composite Materials: Symmetry and Connectivity".
19. 32nd IUPAC Congress, Stockholm, Sweden, August 2-7, 1989, R.E. Newnham, "Integrated Electroceramics".
20. First International Ceramic Science and Technology Congress, Anaheim, California, October 31-November 3, 1989, R.E. Newnham, D. McLachlan, M. Blaskewicz and S. Yoshikawa, "Percolation Phenomena in Multifunction Composites".
21. R.E. Newnham, H. Ikawa and S.E. McKinstry, "Multifunctional Ferroic Nanocomposites."
22. 91st Annual Meeting of Am. Ceram. Soc., Indianapolis, Indiana, April 23-27, 1989, T.R. Shrout and J.P. Dougherty, "A World View on Lead Based $Pb(B_1B_2)$ Relaxors vs. $BaTiO_3$ Based Dielectrics for Multilayer Capacitors".

23. Indo:US Seminars on Electronic Materials, Pune, India, January 1989, A.S. Bhalla, "Pyroelectric Materials".
24. US:USSR Seminars on Ferroelectricity, Boulder, Colorado, July 1989, A.S. Bhalla, S.A. Markgraf and C.A. Randall, "Incommensurate Phases in $Ba_2TiGe_2O_8$ and $Ba_2TiSi_2O_8$".
25. Indo:US Seminars on Electronic Materials, Pune, India, January 1989, S.J. Jang, D.A. McHenry and A.S. Bhalla, "Electrooptic Properties of Relaxor PMN-PT".

10. CONTRIBUTED TALKS

Papers presented at the 91st Annual General Meeting of the American Ceramic Society, Indianapolis, Indiana, April 23-27, 1989:

1. "Relaxor Nature in the MPB Composition PZT-BT-PT Ceramics," U. Kumar, L.E. Cross, Pennsylvania State University, University Park, PA; A. Halliyal, E.I. duPont de Nemours, Wilmington, DE.
2. "Phase Relations, Dielectric and Piezoelectric Properties of Ceramics in the System Lead Zinc Niobate-BaTiO3-PbTiO3," J. Belsick, T.T. Srinivasan and R.E. Newnham, Pennsylvania State University, University Park, PA; A. Halliyal, E.I. duPont de Nemours, Wilmington, DE.
3. "Sintering Phenomena of Lead Magnesium Niobate," G.O. Dayton and J.V. Biggers, Pennsylvania State University, University Park, PA.
4. "Piezoelectric Relaxation in Lead Titanate Based Ceramics," D. Damjanovic and L.E. Cross, Pennsylvania State University, University Park, PA.
5. "Large Piezoelectric Effects Induced by Direct current Bias in PMN:PT Relaxor Ferroelectric Ceramics," W.Y. Pan, W.Y. Gu, D. Tayler and L.E. Cross, Pennsylvania State University, University Park, PA.
6. "Additional Damping and Wave Attenuation in 1-3 Piezoelectric Composites Due to Electric Conductivity," Z.Q. Bao, V.V. Varadan, V.K. Varadan, Pennsylvania State University, University Park, PA.
7. "Designing and Analyzing the Performance of PZT/Polymer Composite Probes I," J.H. Jeng, X.Q. Bao, V.V. Varadan and V.K. Varadan, Pennsylvania State University, University Park, PA.
8. "Designing and Analyzing the Performance of PZT/Polymer Composite Probes II," Z.Q. Bao, J.H. Jeng, V.V. Varadan and V.K. Varadan, Pennsylvania State University, University Park, PA.

9. "Surface Layers on Ferroelectric PLZT Ceramics," Q.Y. Jiang, S.B. Krupanidhi and L.E. Cross, Pennsylvania State University, University Park, PA.
10. "Static and Dynamic Values of the Piezoelectrid d31 Coefficient for PMN Based Ceramics and an Antiferroelectric PSnZT," D.J. Taylor, D. Damjanovic, W. Pan, A. Bhalla and L.E. Cross, Pennsylvania State University, University Park, PA.
11. "Ultrasonic Motor Using One Direction Poling," T. Ishii, J. Opalko, S.J. Jang and L.E. Cross, Pennsylvania State University, University Park, PA.
12. "Patterned Ceramics Through UV Curable Pastes," C.L. Haertling, S. Yoshikawa and R.E. Newnham, Pennsylvania State University, University Park, PA.
13. "dielectric Properties of Solids and Measurement Techniques at Microwave Frequencies," S.J. Jang, Pennsylvania State University, University Park, PA, D.C. Dube, Indian Institute of Technology, New Delhi, India.
14. "Microstructural Control of $BaTiO_3$ Ceramics by Surface Modification," B.L. Utech, J.H. Adair and T.R. Shrout, Pennsylvania State University, University Park, PA.
15. "Cresent-Shaped 3-O Transducers with Redistributed Stress,", Z.C. Xu, T. Meyer, K. Swain, S. Yoshikawa, T.T. Srinivasan and R.E. Newnham, Pennsylvania State University, University Park, PA.
16. "Hydroghermal Synthesis of Perovskite Ceramic Powders," J.H. Adair, T.R. Shrout and K. Osseo-Asare, Pennsylvania State University, University Park, PA.
17. "Preparaton and Low Frequency characterization of Order/Disorder $Pb(In_{1/2}Nb_{1/2})O_3$ (PIN) and $Ba(In_{1/2}Nb_{1/2})O_3$ (BIN)," F.G. Jones, T.R. Shrout, C.A. Randall and S.J. Jang, Pennsylvania State University, University Park, PA.
18. "Field Dependence of Internal Friction in Relaxors," D. Viehland, S.J. Jang, L.E. Cross and M. Wuttig, Pennsylvania State University, University Park, PA.

Papers presented at the International Conference on Electronic Components and Materials, Beijing, China, November 7-10, 1989.

19. "Large Piezoelectric Effect Induced by Direct Current Bias in PMN:PT Ferroelectric Ceramics," W.Y. pan and L. Eric Cross, Pennsylvania State University, University Park, PA.
20. "Electric Field Induced Antiferroelectric:Ferroelectric Switching in $(PbLa)(TiZrSn)O_3$ Ceramics for Large Amplitude Displacement Transducers," W.Y. Pan and L. Eric Cross, Pennsylvania State University, University Park, PA.

11. HONORS TO MRL FACULTY AND STUDENTS

Name of Person Receiving Award	Institution	Name of Award	Sponsor
R.E. Newnham	Materials Research Laboratory	Named to National Academy of Engineers	National Academy
L.E. Cross	Materials Research Laboratory	Senior Visiting Scientist JPL	California Inst. of Tech.
W.Y. Pan	Materials Research Laboratory	1989 Xerox Award Award Winner for best Ph.D. thesis in Materials at Penn State	Xerox Company

APPENDIX 1

Rep. Prog. Phys. 52 (1989) 123-156. Printed in the UK

Electroceramics

R E Newnham

Materials Research Laboratory, The Pennsylvania State University, University Park, PA 16802, USA

Abstract

Structure-property relationships in electronic ceramic materials are reviewed to provide insight into the behaviour of capacitors, thermistors, varistors, and other electroceramic components. Rapid progress in the integration and miniaturisation of ceramic components has led to the development of multipurpose electronic packages containing complex three-dimensional circuitry. At the same time, a wide variety of smart sensors, transducers, and actuators are being constructed utilising composite materials to concentrate fields and forces. At present the processing methods make use of tape casting the thick film techniques, but several upset technologies loom on the horizon. During the years ahead we can expect electroceramic devices to follow in the footsteps of semiconductor technology as the component sizes drop below 1 μm, and nanocomposite devices become a reality.

This review was received in September 1988.

Contents

1. Electroceramics market

The multibillion dollar electroceramics market (figure 1) includes Mn-Zn ferrites, PZT transducers, $BaTiO_3$ multilayer capacitors, ZnO varistors, Al_2O_3 packages, and SiO_2 optical fibres. Roughly speaking, the market is divided into six equal parts (Japan Electronics Almanac 1986). Rapidly developing technologies can be identified within each market segment: tellurium oxide coatings for video discs, barium hexaferrites for perpendicular recording, silver and copper electrode systems for multilayer capacitors, buried resistors and capacitors in ceramic packages, catalytic coatings for chemical sensors, and PZT piezoelectric motors. As in all rapidly evolving fields of science and engineering, there is a sense of excitement as a number of different technologies come together in a synergistic manner.

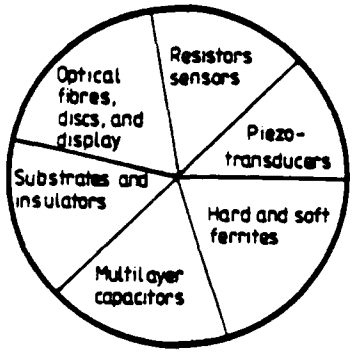

Figure 1. Electroceramics market.

2. Ceramic sensors

The cheapest and most widely used sensors are ceramic bodies (Kulwicki 1984). To illustrate structure-property relationships in ceramic sensors, six types of sensors will be described: three chemical sensors and three thermistors. The sensors make use of a variety of electrical phenomena sensitive to small changes in chemical composition or temperature.

2.1. Oxygen sensors

Superionic conductors are used to determine the air-fuel mixture in automobile engines (Eddy 1974). One surface of the conductor is in contact with exhaust gas through a porous electrode (figure 2), while the opposite surface is in contact with air. The diffusion of oxygen ions through the solid electrolyte causes a voltage to appear between the electrodes. Heating the sensor raises the conductivity level. Monitoring the composition of the air-fuel mixture results in greater fuel efficiency and reduced air pollution.

Stabilised zirconia is the most widely used ionic conductor for oxygen sensors. Partial substitution of Mg^{2+}, Ca^{2+}, or Y^{3+} for zirconium stabilises the cubic fluorite

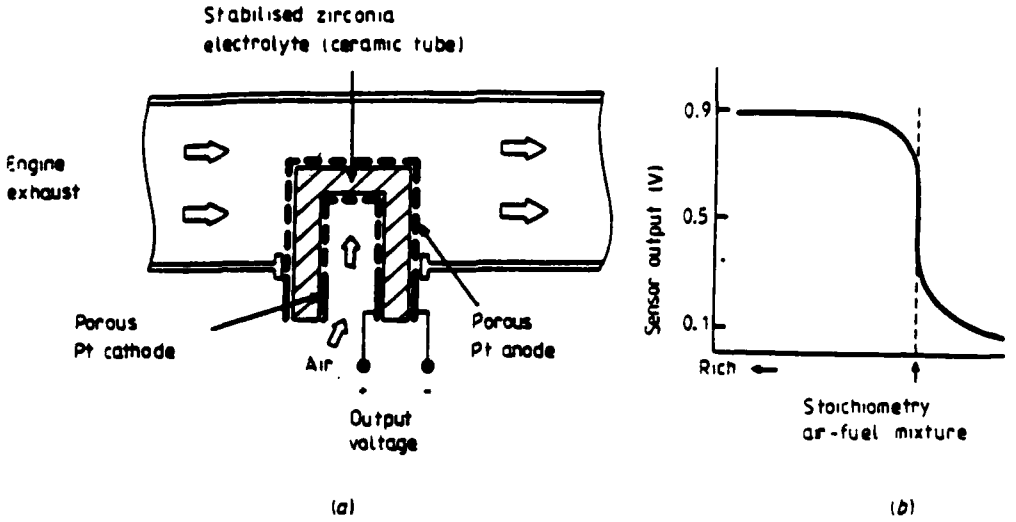

Figure 2. (*a*) Automotive exhaust sensor utilising an ionic conductor as a stabilised conductor. (*b*) Improved fuel efficiency is obtained by monitoring the sensor voltage and adjusting the air-fuel mixture.

structure with a sizeable concentration of oxygen vacancies. An oxygen vacancy is created for every zirconium replaced by magnesium, as indicated by the structural formula $(Zr_{1-x}Mg_x)(O_{2-x}\square_x)$. Magnesium replaces zirconium in the cubic cation sites of the fluorite structure (figure 3) with oxygen vacancies compensating for the lower cation charge. In the fluorite structure, the cations form a face-centred cubic lattice and the anions have a simple cubic arrangement. The anion sites are very close to one another (~2.5 Å) making it easy for oxygens to jump to an adjacent empty site. This promotes ionic conductivity in fluorite-family oxides with defect structure, making them useful as oxygen sensors (McGeehin and Hooper 1977).

2.2. Humidity sensors

Humidity sensors are used in microwave ovens and for electronic spark timing in automobile engines. The surface resistance changes by several orders of magnitude

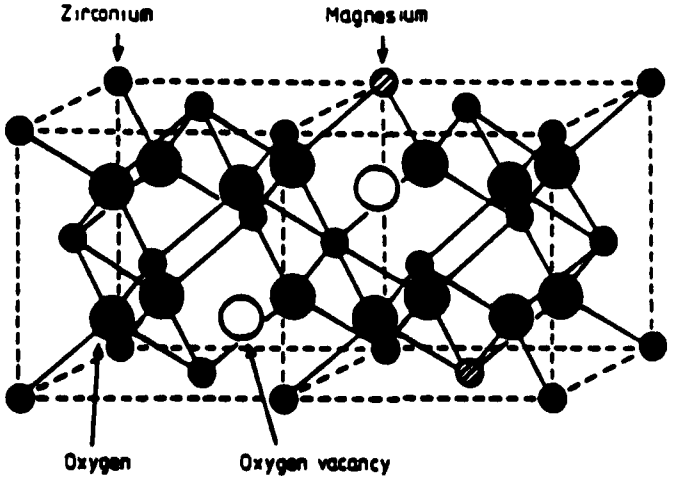

Figure 3. Stabilised zirconia is an excellent ionic conductor because of high concentration of oxygen vacancies and the close proximity of anion sites.

with humidity (figure 4). Metal oxide substrates of ($MgCr_2O_4$-TiO_2) with high surface area and salt-impregnated coatings are especially sensitive to small changes in humidity (Nitta 1981). The physical mechanism of surface conduction involves the adsorption of water vapour followed by dissociation into hydronium and hydroxyl ions:

$$2H_2O \Leftrightarrow (H_3O)^+ + (OH)^-.$$

Conduction takes place by means of the Grotthuss chain reaction in which protons are transferred from one water molecule to the next in the physisorbed water layer on the surface of the oxide, effectively passing along a hydronium ion in the direction of the current.

The process is illustrated in figure 5. As reported recently, hydroxyapatite ceramics make especially effective humidity sensors because of the attractive forces between surface hydroxyl groups and adjacent water molecules. The chemisorbed layer is

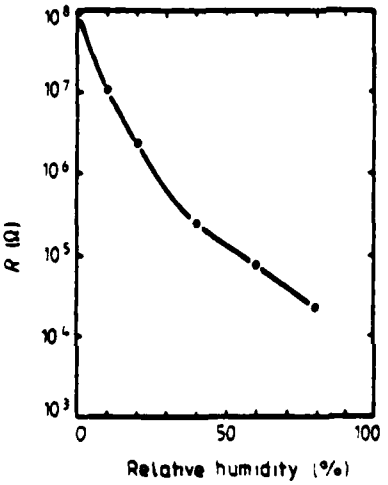

Figure 4. Electrical resistance of an oxide humidity sensor at 20 °C (Nitta 1981).

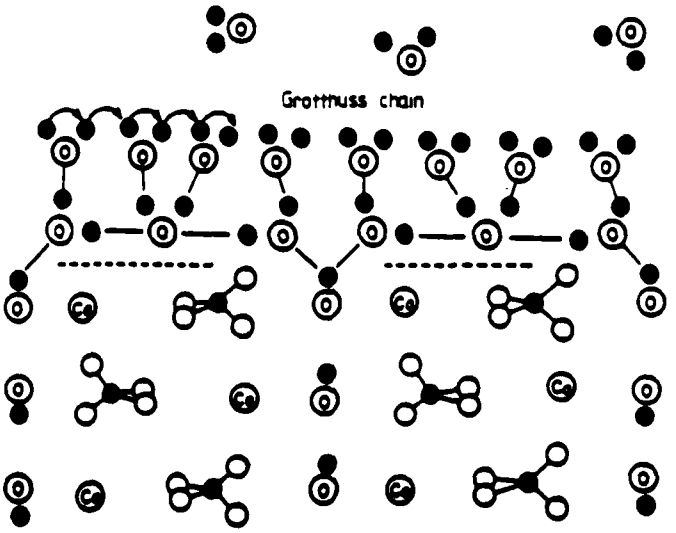

Figure 5. Pictorial view of the surface structure of a hydroxyapatite humidity sensor. Conduction takes place via a Grotthuss chain reaction in the adsorbed water layers.

surmounted by a physisorbed layer in which conduction takes place. At high humidity levels, a deeper, more fluid-like surface layer is formed and the conduction mechanism changes.

2.3. pH sensors

Oxide pH sensors are made from semiconducting transition-metal oxides such as RuO_2 and IrO_2 (Fog and Buck 1984). Both compounds are isostructural with rutile (figure 6). When protons approach the surface of the oxide, a chemical reaction takes place. Two protons combine with a surface oxygen to form a water molecule. The reaction is accompanied by valence changes of the ruthenium ions to maintain charge neutrality. Electrons liberated from the metal ions complete the reaction, and cause a current to flow in the solid. The resulting voltage depends on the hydrogen ion concentration (figure 6).

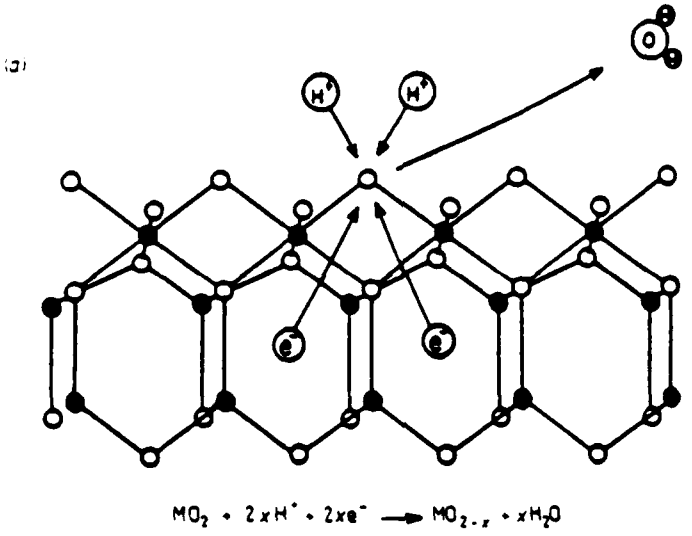

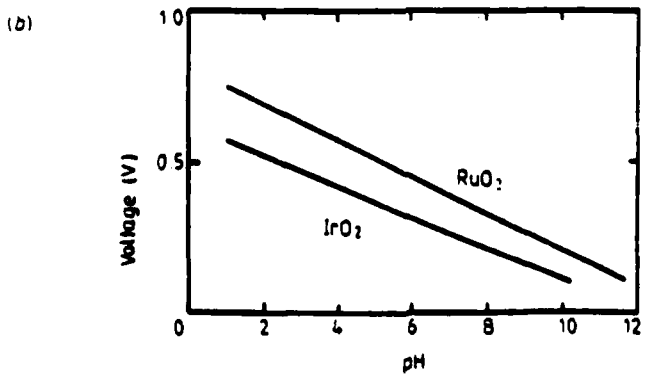

Figure 6. (*a*) **Transition-metal oxides are used as pH sensors in which protons react with surface oxygens to form water molecules. The reaction is accompanied by valence changes and current flow in the solid.** (*b*) **The resulting electric voltage is proportional to pH (Fog and Buck 1984).**

The three chemical sensors just described all involve ion motion, but in a different way. Bulk ionic conduction occurs in the zirconia oxygen sensor, whereas surface ionic conduction takes place in a humidity sensor. In the pH sensor, a chemical reaction takes place at the surface between protons and oxygen ions.

In the next section, we describe three temperature sensors, again with three different structure-property relationships, but this time the sensing involves electron motion rather than ion motion.

3. Thermistors

Three types of *ceramic thermistors* are in widespread use: NTC thermistors, PTC thermistors, and critical temperature thermistors. Typical resistance changes with temperature are illustrated in figure 7.

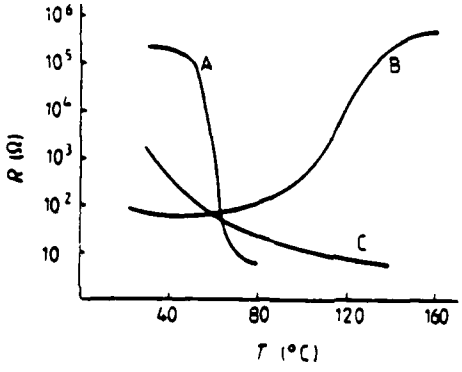

Figure 7. Typically the electrical resistance of thermistors changes by several orders of magnitude with temperature. In NTC thermistors the resistance decreases steadily with increasing temperature, but sudden changes at phase transitions are involved in PTC and critical temperature thermistors. A, critical temperature thermistor; B, PTC thermistor; C, NTC thermistor.

3.1. Critical temperature thermistors

Vanadium dioxide is often used in *critical temperature thermistors.* Below 80 °C, VO_2 is a semiconductor with a negative temperature coefficient of resistance. Above 80 °C it shows metallic behaviour with a great increase in conductivity (typically two orders of magnitude) and very little change with temperature. The critical temperature of 80 °C can be modified somewhat by changes in chemical composition.

The V^{4+} ion in VO_2 has a peculiar electron configuration with one 3d electron outside a closed shell. In the low temperature state, adjacent V^{4+} ions form electron-pair bonds giving rise to a band gap and semiconductor behaviour. A phase transition takes place at 80 °C in which the 3d electrons are liberated from the pair bonds and are free to conduct electricity. Changes in the crystal structure (figure 8) accompany the phase transformation. The rutile-like structure found at high temperatures transforms to a distorted monoclinic form below 80 °C. The formation of electron-pair bonds is reflected in the interatomic distances. In the rutile structure the V^{4+}-V^{4+} distance across shared octahedral edges is 2.9 Å. Below the transition, half are 2.7 Å

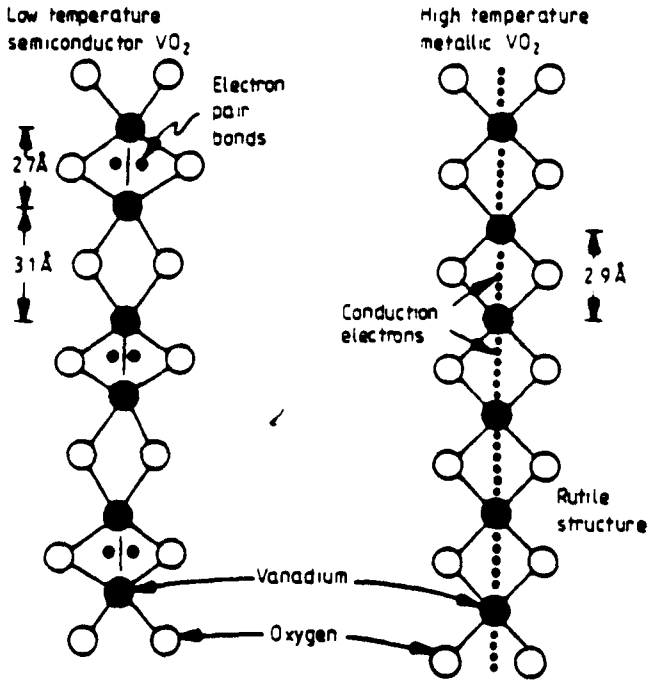

Figure 8. Structural changes take place in the VO_2 ceramics used as critical temperature thermistors. At the metal–semiconductor transition the resistance changes by several orders of magnitude and the bond lengths change. At high temperature the metal-like structure is isomorphous with tetragonal rutile, but changes to the semiconducting monoclinic state below 80 °C.

and half are 3.1 Å. This distortion in structures locks the electrons into localised states creating a band gap and semiconducting behaviour.

3.2. NTC thermistors

Electrical resistance decreases exponentially with increasing temperature in an NTC thermistor. Unlike critical temperature thermistors, there is no phase transition involved. Most NTC thermistors are composed of doped transition-metal oxides (Smit and Wijn 1959). Typical of these controlled valency semiconductors are Fe_2O_3:Ti and NiO:Li. Reacting Fe_2O_3 with TiO_2 in air yields

$$(1-x)Fe_2O_3 + xTiO_2 \rightarrow Fe^{3+}_{2-2x}Fe^{2+}_{x}Ti^{4+}_{x}O_3.$$

This is an n-type semiconductor in which electrons are transferred between iron atoms of different valence:

$$Fe^{3+} + e^- \Leftrightarrow Fe^{2+}.$$

The electron concentration and electrical resistivity are controlled by the titanium content.

p-type NTC thermistors are made from nickel oxide doped with lithium:

$$(1-x)NiO + \frac{x}{2}Li_2O \rightarrow Ni^{2+}_{1-2x}Ni^{3+}_{x}Li^{+}_{x}O.$$

The hole conduction process involves charge transfer between divalent and trivalent nickel ions:

$$Ni^{2+} + h^{+} \Leftrightarrow Ni^{3+}.$$

Doped nickel oxide has the rocksalt structure (figure 9(*a*)) with lithium partially replacing nickel in the cation sites. Ionic radii for Ni^{2+} (0.84 Å), Ni^{3+} (0.74 Å), and Li^{+} (0.88 Å) all favour octahedral coordination with oxygen. As shown in figure 9(*b*), resistivity decreases with increasing lithium content. Colour is another indication of increased conductivity. The green colour of pure nickel oxide deepens to black with increased doping.

For semiconducting compositions near $Ni_{0.95}Li_{0.05}O$, the band gap is about 0.15 eV. The physical origin of this band gap is attributed to the attractive forces between Li^{+} dopant ions and the compensating Ni^{3+} ions. Charge is neutralised best when these ions are next nearest neighbours (figure 9(*a*)). Polarisation of the surrounding structure also contributes to the band-gap energy.

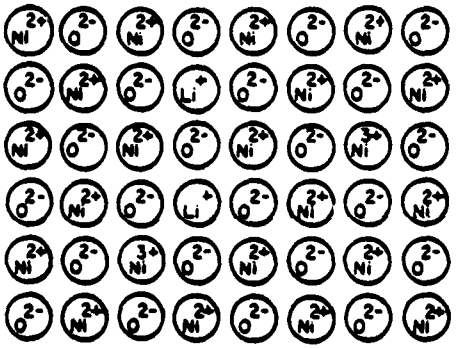

(*a*)

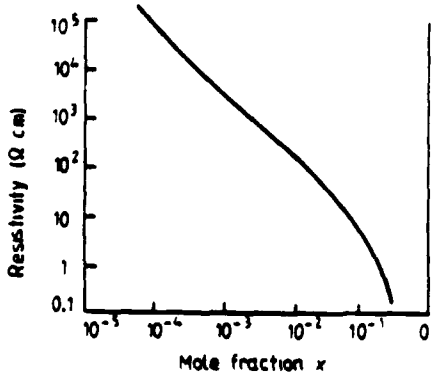

(*b*)

Figure 9. Doped nickel oxide thermistor. (*a*) The crystal consists of Ni^{2+}, Ni^{3+}, and Li^{+} ions in a rocksalt-like solid solution. (*b*) The electrical resistivity decreases with increasing lithium content.

Electrical conductivity is proportional to the charge carrier concentration n, the charge of each carrier q, and the mobility μ:

$$\sigma = nq\mu.$$

In thermistor materials, the temperature dependence of the conductivity is of great importance. Both n and μ depend on temperature. For a semiconductor, the carrier concentration varies exponentially with temperature, $n \sim \exp(-E/kT)$ where E is the energy required to liberate charge carriers. The temperature dependence of the mobility depends on its physical origin. For most scattering processes, mobility follows an inverse power law ($\mu \sim T^{-b}$) in which mobility decreases with increasing temperature because of atomic thermal vibration. A different temperature dependence is found for hopping processes. Here the mobility depends on thermal excitation, and increases exponentially with temperature, $\mu \sim \exp(E'/kT)$. Summing up, the temperature dependence of the electrical conductivity is

$$\sigma(T) \sim T^{-b} \exp[-(E+E')/kT] = T^{-b} \exp(-E''/kT).$$

Since exponentials tend to dominate, the electrical resistance of an NTC thermistor can be described by

$$R = A\,e^{B/T}.$$

For typical thermistors (figure 10), R lies in the range $1\text{-}10^4\ \Omega$, and B is 2000-6000 K. The temperature coefficient α describes the percentage change in resistance with increasing temperature:

$$\alpha = \frac{1}{R}\frac{dR}{dT} = \frac{1}{R}\frac{d}{dT}(A\,e^{B/T}) = \frac{-B}{T^2}.$$

If $B = 3600$ K and $T = 273$ K, α is approximately 4%/°C.

NTC thermistors are used in flowmeters in which the velocity is measured by monitoring the temperature difference between two thermistors. A heater positioned between the two thermistors provides the temperature difference.

Thermistors are also used as inrush limiters to protect diodes, fuses, switches, and light bulbs. The sudden surge of current which occurs when a light bulb is turned on often ruptures the bulb filament. With an NTC thermistor in series with the bulb, the energy of the initial surge is dissipated as heat in the thermistor.

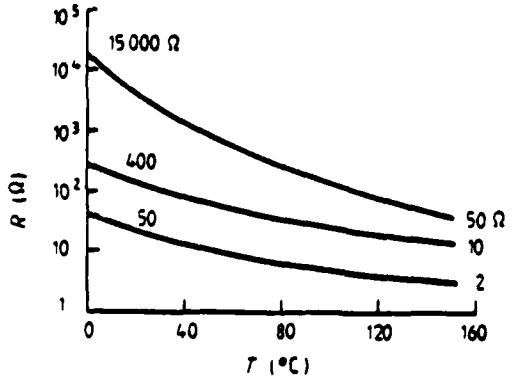

Figure 10. Dependence of resistance on temperature for typical NTC thermistors. R decreases by about 4% for each degree rise in temperature.

3.3. PTC thermistors

PTC thermistors differ from NTC thermistors in several important respects. The resistance of a PTC thermistor increases with temperature, but only over a limited temperature range near a phase transition. The resistance change is very large at this temperature because of grain boundary effects (Saburi 1964).

Barium titanate ceramics are widely used in PTC thermistors. When doped with donor ions such as La^{3+} or Ce^{3+} (for Ba^{2+}) or Nb^{5+} (for Ti^{4+}), the resistivity material shows a pronounced PTC effect (figure 11(*a*)). This low resistivity material shows a pronounced PTC effect (figure 11(*b*)) if fired in air. Only normal NTC behaviour is observed in ceramics prepared in reducing atmosphere.

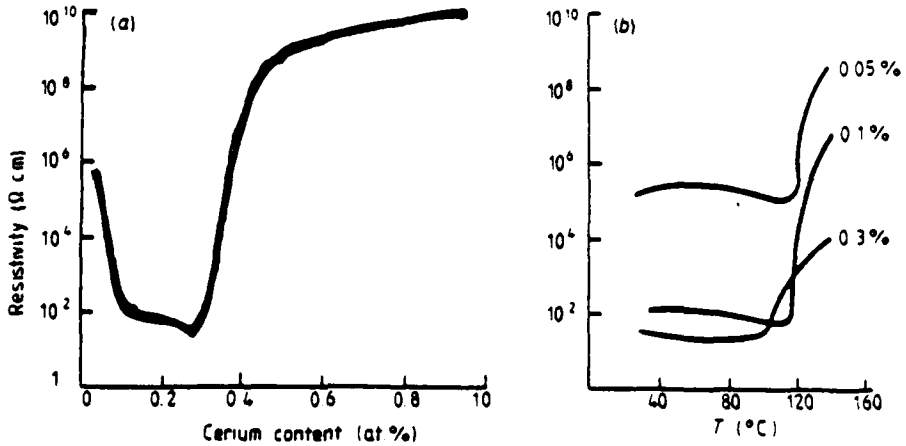

Figure 11. (*a*) Resistivity of cerium-doped barium titanate, $Ba_{1-x}Ce_xTiO_3$, plotted as a function of composition. (*b*) Resistivity of three cerium-doped barium titanate ceramics measured as a function of temperature. A large PTC anomaly occurs near the Curie temperature.

Explanation of the PTC effect rests upon understanding the defect structure. When sintered at high temperature, lanthanum-doped $BaTiO_3$ becomes an n-type semiconductor:

$$Ba_{1-x}La_xTiO_3 = Ba^{2+}_{1-x}La^{3+}_xTi^{4+}_{1-x}Ti^{3+}_xO^{2-}_3$$

with conduction taking place via transfer of electrons between titanium ions, $Ti^{4+} + e^- \leftrightarrow Ti^{3+}$. Thus the barium titanate grains in the ceramic are conducting, and remain conducting on cooling to room temperature.

But the grain boundary region changes during cooling. Oxygen is adsorbed on the surface of the ceramic and diffuses to grain boundary sites, altering the defect structure along the grain boundaries. The added oxygen ions attract electrons from nearby Ti^{3+} ions, thereby creating an insulating barrier between grains. If y excess oxygens are added per formula unit, the grain boundary region can be described as follows:

$$(Ba^{2+}_{1-x}La^{3+}_x)(Ti^{4+}_{1-x+2y}Ti^{3+}_{x-2y})O^{2-}_{3+y}.$$

A schematic illustration of the defect perovskite structure is shown in figure 12. The net result of this process is that the ceramic consists of semiconducting grain separated

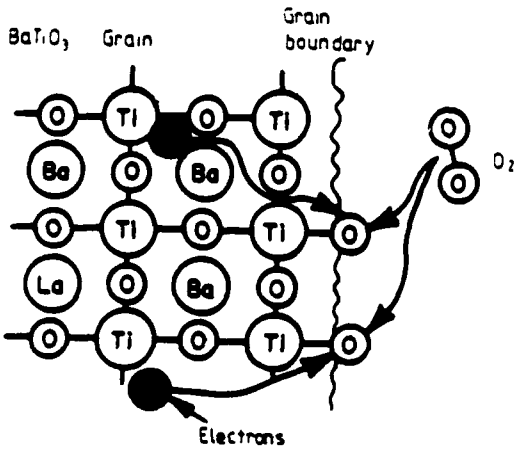

Figure 12. Schematic view of the $Ba_{1-x}La_xTiO_3$ structure near the surface of a grain boundary. Atmospheric oxygen dissociates and diffuses rapidly along a grain boundary where the atoms attract electrons and form insulating barriers.

by thin insulating grain boundaries. The electrical resistance of the ceramic is inversely proportional to grain size because smaller grains mean more insulating grain boundaries, and therefore higher resistance.

To explain the PTC effect it is necessary to consider the ferroelectric phase transition in $BaTiO_3$ and its effect on the insulating barriers between grains (Daniels *et al* 1978). Barium titanate is cubic and paraelectric above 130 °C, the Curie temperature. Below this temperature the perovskite structure distorts to a tetragonal ferroelectric state in which a large spontaneous polarisation P_s develops on the (001) faces. The dielectric constant reaches a maximum at T_c and then falls off in the high-temperature paraelectric state following a Curie-Weiss law

$$K \approx \frac{C}{T - T_c} \qquad (T > T_c).$$

The Curie constant C is about 10^5 °C.

The PTC anomaly in doped $BaTiO_3$ occurs at temperatures near T_c and is strongly affected by the appearance of ferroelectricity. Both the spontaneous polarisation and the Curie-Weiss law play an important role in the PTC effect.

At room temperature the resistance of a PTC thermistor is low because the electron charge trapped in grain boundary regions is partially neutralised by spontaneous polarisation. Wherever the domain structure is advantageously positioned, positive polarisation charge will cancel the negatively charged barriers between conductive grains, thereby establishing low resistance paths across the ceramic (figure 13(*a*)).

Above T_c the spontaneous polarisation disappears and the resistivity increases, giving rise to the PTC effect. At first the increase is very slow because of the high dielectric constant at the Curie point. The barrier height is inversely proportional to the dielectric constant of the surrounding medium; a highly polarisable medium shields the charges trapped at the grain boundary, reducing the height of the barrier and the electrical resistance. As the temperature increases further above T_c, the dielectric constant K decreases rapidly in accordance with the Curie-Weiss law. Decreases in K cause rapid increases in the barrier between grains and an increase in the electric resistance. Eventually the resistance increase levels off as the decrease in dielectric

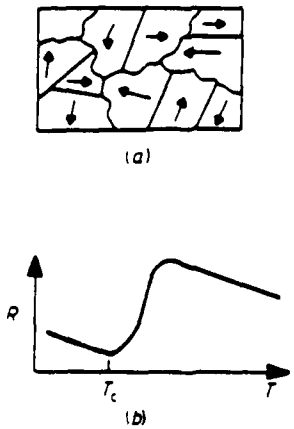

Figure 13. (*a*) At temperatures below T_c, spontaneous polarisation charges neutralise the potential energy barriers, creating low resistance paths through the ceramic. (*b*) Above T_c the dielectric constant decreases causing the electrical resistance to increase.

constant slows and the normal NTC effect of the semiconducting grains takes over (figure 13(*b*)).

PTC thermistors are used as protection against overvoltage and short circuits. When connected in series with the load, a PTC thermistor limits the current to safe levels. Large currents cause the temperature of the thermistor to rise into the PTC range, thereby raising the resistance and lowering the current. Additional applications include liquid-level indicators and thermostat control elements.

To summarise, the ceramic sensors just described make use of six different structure-property relations. The humidity sensor involves ionic conduction on surfaces with proton hopping between absorbed water molecules, whereas the zirconia oxygen sensor involves bulk ionic conduction through grains. In metal oxide pH sensors a chemical reaction takes place at the surface with protons reacting with surface oxygen atoms.

The three types of temperature sensors discussed in the last section make use of electronic phenomena in ceramics. Critical temperature thermistors employ a structural phase transformation in which the bulk electronic condition changes from metallic to semiconducting; a phase transformation is also involved in PTC thermistors, but grain boundaries are important here. Schottky barriers between the conducting ceramic grains are neutralised by the spontaneous polarisation associated with the ferroelectric phase transition in $BaTiO_3$. This is a much more complicated conduction phenomenon than that in an NTC thermistor. Bulk electronic conduction controls the resistivity of the transition-metal oxides used in NTC thermistors.

4. Metal oxide varistors

Varistors are ceramic semiconductors with a non-linear current-voltage relationship (figure 14). At low voltages, the varistor behaves like an NTC thermistor with small temperature-dependent currents. At a certain critical breakdown voltage V_B, however, the resistance diminishes suddenly and currents increase dramatically. The phenomenon differs from normal electric breakdown in that the $I-V$ characteristic is reversible and controllable by the ceramic microstructure. Like the PTC thermistor,

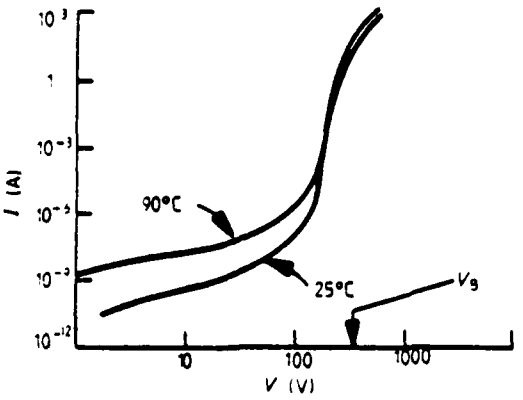

Figure 14. Typical I-V relation for ZnO varistor. The current increases very rapidly at the breakdown voltage V_B.

the electrical properties are governed primarily by thin insulating barriers at the grain boundaries. In the case of varistors, however, electron tunnelling is involved (Levinson and Philipp 1986).

Most varistors are made from zinc oxide with additives of several per cent. ZnO has the hexagonal wurtzite structure (figure 15) with tetrahedral ZnO bonds of 1.97 Å. A typical commercial composition for varistors is

$$(100-x)\mathrm{ZnO}+\frac{x}{6}(\mathrm{Bi_2O_3}+2\mathrm{Sb_2O_3}+\mathrm{Co_2O_3}+\mathrm{MnO_2}+\mathrm{Cr_2O_3})$$

where x is the mole per cent additives. Excellent varistor action is obtained for compositions with x in the range 3–10%. The phase relations are rather complex but when fired at 1350 °C, there are only two important phases. The varistor microstructure consists of doped ZnO grains separated by doped Bi_2O_3 grain boundary regions. TEM micrographs show that the bismuth oxide layer is extremely thin (<30 Å) in many places. This plays an important role in the conduction process. Electrically, the ceramic varistor consists of conducting ZnO grains with resistivities near 1 Ω cm, separated by insulating Bi_2O_3-rich grain boundaries. The grains are n-type and the boundaries p-type. Electrons near the boundaries are trapped in the intergranulate Bi_2O_3-rich

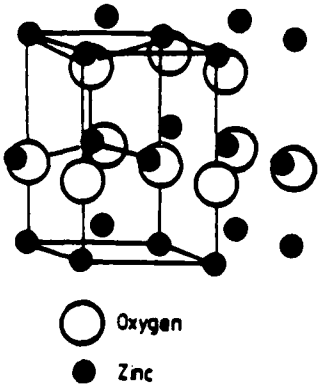

Figure 15. Unit cell of the hexagonal ZnO structure used in varistors. Lattice parameters are $a = 3.24$ Å, $c = 5.19$ Å.

regions leaving ionised donors on both sides of the boundary. The result is a symmetric Schottky barrier about 0.8 eV in height (figure 16(*a*)).

The non-linear I-V characteristic (figure 14) of a varistor can be explained in terms of the Schottky barrier model. At low voltages, in the pre-breakdown region, charge carriers surmount the Schottky barrier by thermal activation (figure 16(*b*)), giving rise to small temperature-dependent currents. As the applied voltage approaches V_B, the breakdown voltage, tunnelling from the filled states in the intergranular region begins (figure 16(*c*)). Further increases in voltage result in very large current flows through tunnelling.

Metal oxide ceramic varistors are used to protect circuit elements against inductive surges which often damage contacts, relays, and rectifiers. By connecting the varistor in parallel with the circuit element (figure 17), any voltage spikes greater than V_B cause

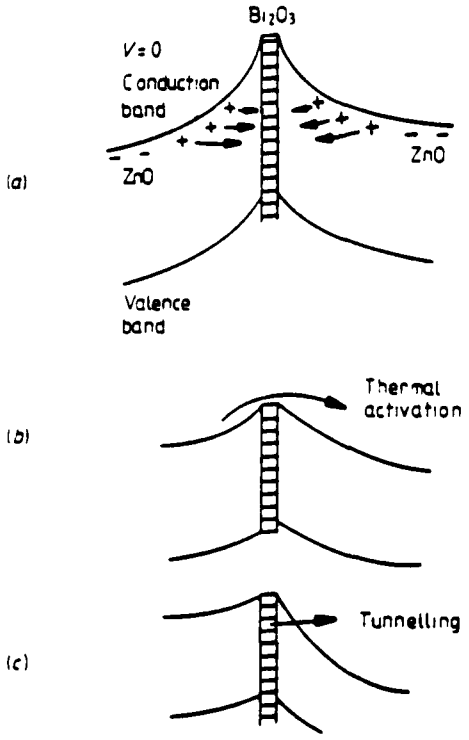

Figure 16. (*a*) Schottky barrier caused by double depletion layer in ZnO varistor. Band bending caused by donor electrons from the zinc oxide grains filling traps in the thin bismuth oxide-rich layer between grains. (*b*) At low voltages, conduction takes place by thermal activation, but (*c*) at the breakdown voltage tunnelling begins causing a very large increase in current.

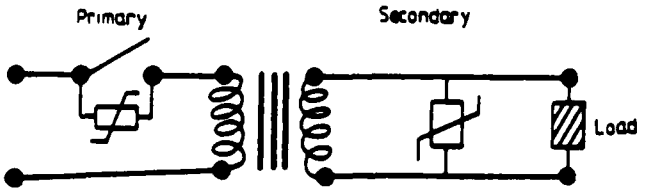

Figure 17. Varistors are used to protect electrical contacts and loads against inductive surges.

currents to flow through the varistor rather than the circuit element. Zinc oxide varistors have proved especially useful as lightning arrestors (Einzinger 1987).

5. Superconducting ceramics

Until two years ago it was taken for granted that superconducting transition temperatures were limited to 25 K. But with the discovery of lanthanum strontium cuprate (Bednorz and Müller 1986) the temperature doubled, and doubled again with $YBa_2Cu_3O_7$, the so-called 1-2-3 compound (Wu *et al* 1987). The triple perovskite unit cell (figure 18) contains seven oxygen and two empty oxygen sites.

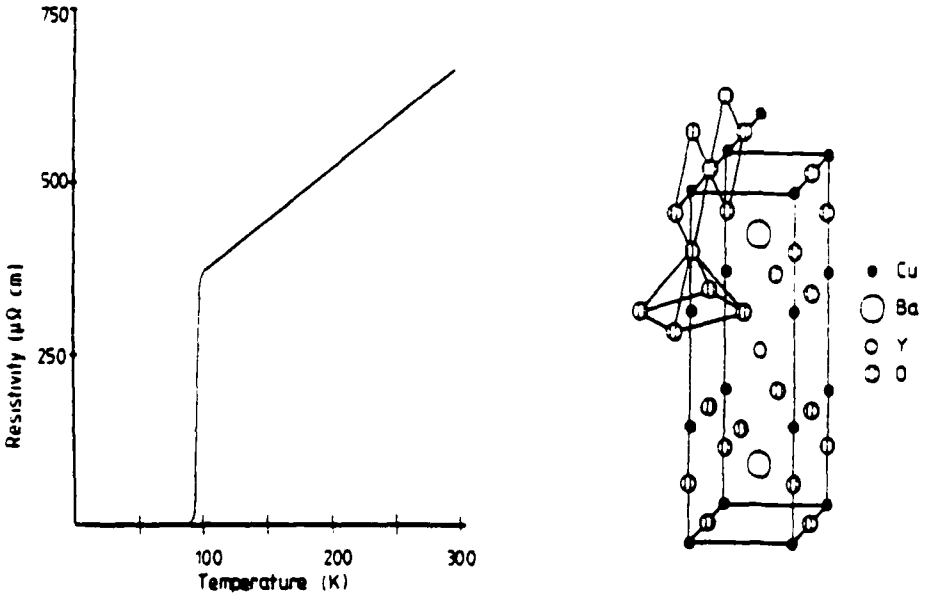

Figure 18. Resistivity of the newly discovered 1-2-3 cuprate ceramics; the structure contains many missing oxygen sites (Cava *et al* 1987).

The mechanism of superconductivity in the copper oxide family is not well understood. In the theory put forward for metallic superconductors, an electron moving through the lattice attracts or repels ions, causing them to vibrate. A quantum of vibration energy (phonon) attracts another electron with opposite magnetic spin and momentum in such a way that the two move in synchronised motion. The paired electrons may be far apart and separated by other particles, but they are indirectly linked, as if by a spring. Each and every motion, even a collision with the lattice, is cancelled by the partner's movement. Moreover, such Cooper pairs travel in concert with other pairs so that conduction electrons move together with remarkable orderliness.

The phonon links between electrons are so tenuous that they remain intact only at very low temperatures. Even a little heat is sufficient to overcome the phonon attraction and destabilise the superconducting state. The Bardeen-Cooper-Schrieffer (BCS) theory predicts an upper limit to the strength of the interaction with a T_c of 30–40 K.

This suggests that there must be another coupling mechanism in the high-T_c copper oxides. Isotope experiments have borne this out. The expected shift in T_c with isotopic substitution did not take place, thereby discrediting the phonon coupling mechanism. Attention is presently focused on the copper-oxygen planes and chains found in all

high-T_c ceramics. Most of the theories formulated during the past year involve the peculiar bonding between copper and oxygen atoms. Normally copper has a valence of +1 or +2 in minerals and oxide ceramics, but in the superconductors its valence exceeds two. Alternatively, an unusual valence of −1 can be assigned to some of the oxygen ions. The presence of 'excess' oxygen is crucial to the existence of superconductivity.

Three alternative mechanisms have been propounded to explain the coupling of Cooper pairs in superconducting cuprates. Closely related to the BCS theory is an excitonic model in which electron-hole pairs (excitons) perform the same function as phonons in superconducting metals. Another BCS-like model involves magnetic interactions as a coupling mechanism. Ferromagnetic regions within an antiferromagnetic matrix are responsible for the attractive forces between electrons. A third theory postulates the importance of resonating domain walls which are common in high-T_c ceramics. At the present time, theory seems to be of little value in guiding experimentalists.

Ceramic and thin-film specimens both exhibit superconductivity above liquid air temperatures, opening up a large number of possible applications: frictionless generators, motors and high-speed trains; levitating toys and gimmicks; electronic Josephson junctions and resistanceless interconnects; large magnetic fields for NMR medical diagnosis, nuclear accelerators and hydrogen fusion; power transmission lines and closed-loop energy storage for load levelling; radiation detectors for astronomy, oil exploration, and brain wave research. The feasibility of many applications rests upon improvements in the critical current density. Ways must be found for stabilising the superconducting phase under high magnetic fields and electric currents. Several interesting composite structures are under investigation.

But although ceramic superconductors have captured the imagination of thousands of scientists, the work is outside the mainstream of electroceramics. Until a major market is demonstrated, it will remain a curiosity. The main thrust in electroceramics research is not in the discovery of new materials but in the miniaturisation and integration of components already known.

6. Ferroelectric ceramics

Multilayer capacitors make use of ferroelectric oxides such as barium titanate (Herbert 1985). Ferroelectric oxides with the perovskite, tungsten bronze, pyrochlore, and bismuth titanate layer structures all have high dielectric constants and high refractive indices, and all contain corner-linked octahedral networks of Ti^{4+}, Nb^{5+}, or other d^0 ions. These transition-metal elements are the highly polarisable 'active' ions promoting ferroelectricity and the high permittivities required for capacitors.

With reference to the periodic system there are two major groups of active ions, and both are near electronic 'crossover' points where different types of atomic orbitals are comparable in energy, and where hybrid bond formation is prevalent. The first group typified by Ti^{4+}, Nb^{5+}, and W^{6+} are d^0 ions octahedrally coordinated to oxygen. For Ti^{4+}, the electronic crossover involves the 3d, 4s, and 4p orbitals which combine with the σ and π orbitals of its six O^{2-} neighbours to form a number of molecular orbitals for the $(TiO_6)^{8-}$ complex. The bond energy of the complex can be lowered by distorting the octahedron to a lower symmetry. This leads to dipole moments, ferroelectricity, and large dielectric constants.

A second group of active elements contributing to polar distortions in ceramic dielectrics are the lone-pair ions having two electrons outside a closed shell in an asymmetric hybrid orbital. Among oxides, the most important of these lone-pair ions are Pb^{2+} and Bi^{3+} which are involved in a number of ferroelectrics ($PbTiO_3$, $Bi_4Ti_3O_{12}$, $PbNb_2O_6$) with high Curie temperatures. In many of these compounds, Pb^{2+} and Bi^{3+} are in pyramidal coordination with oxygen and therefore contribute to the spontaneous polarisation.

6.1. $BaTiO_3$ capacitors

Many capacitor formulations are based on $BaTiO_3$, one of a number of ferroelectric substances crystallising with the perovskite structure. Barium atoms are located at the corners of the unit cell and oxygens at the face centres (figure 19). Both barium and oxygen ions have radii of about 1.4 Å and together they make up a face-centred cubic array having a lattice parameter near 4 Å. Octahedrally coordinated titanium ions located at the centre of the cubic perovskite cell are the active ions in promoting ferroelectricity. The low-lying d orbitals of titanium lead to unusual atomic arrangements and large electric polarisability.

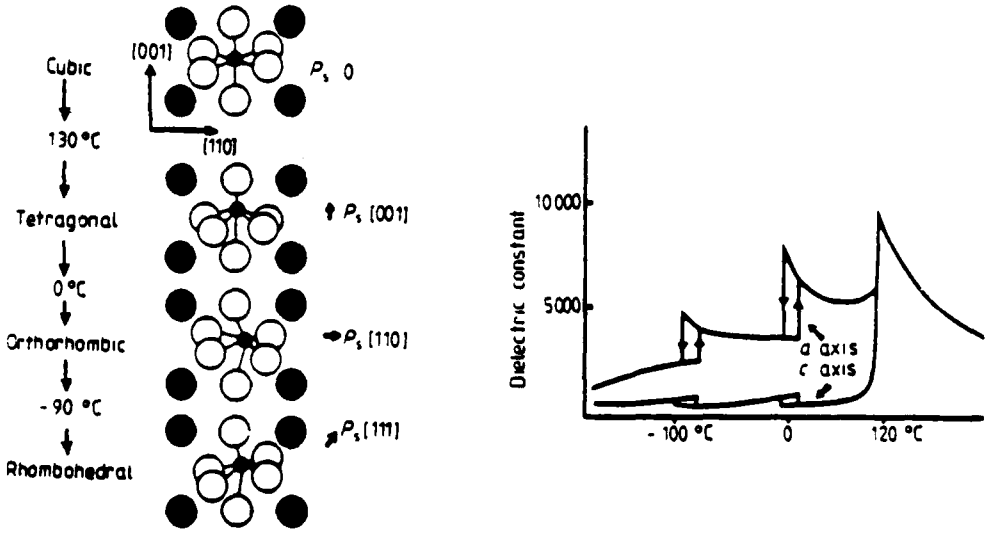

Figure 19. Structural changes occurring at the three ferroelectric phase transformations in $BaTiO_3$ result in large values of the dielectric constant over a wide temperature range.

On cooling from high temperature, the crystal structure of $BaTiO_3$ undergoes three ferroelectric phase transitions. All three are displacive in nature with atomic movements of 0.1 Å or less. The point symmetry changes from cubic m3m to tetragonal 4mm at the Curie temperature of 130 °C. The tetragonal state with its spontaneous polarisation along [001] persists down to 0 °C where it transforms to orthorhombic (mm2 symmetry) as P_s shifts to a [110] direction. On further cooling, the orthorhombic state transforms to rhombohedral (3m) near −90 °C. The structural changes are illustrated in figure 19. A peak in the dielectric constant occurs at each of the phase transitions (figure 19). In regard to capacitors, it is extremely important that the dielectric constant is high over a wide temperature range. The presence of the two lower ferroelectric transformations ensures that the dielectric constant remains high below the Curie temperature.

Note in figure 19 that the dielectric constant along the *a* axis is larger than that along the polar *c* axis. The instability of the structure makes it easy to tilt the spontaneous polarisation vector with a transverse electric field.

Since barium titanate is by far the most popular compound for multilayer ceramic capacitors, there have been many studies of its solid solutions. Substitutions for Ba^{2+} or Ti^{4+} are used to raise the permittivity, flatten its temperature dependence, and lower the losses.

Substituting a divalent cation for barium in $BaTiO_3$ modifies the transition temperatures. The three most commonly used 'Curie-point shifters' are Pb^{2+}, Sr^{2+}, and Ca^{2+}. Modest amounts of Pb^{2+} raise T_c, Sr^{2+} lower T_c, and Ca^{2+} has little effect. Divalent Pb is one of the very few additions which increases the transition temperature; the tetragonal pyramidal coordination favoured by Pb^{2+} stabilises the tetragonal phase with respect to the adjacent cubic and orthorhombic phases. All three Curie-point shifters destabilise the orthorhombic and rhombohedral phases of $BaTiO_3$ as the lower two transition temperatures drop when increasing amounts of Pb^{2+}, Sr^{2+}, or Ca^{2+} are added. The opposite effect is achieved by replacing titanium with larger tetravalent ions.

A pinching together of the phase transitions occurs when titanium is replaced with larger tetravalent ions. Typical of this type of behaviour is the $BaTi_{1-x}Zr_xO_3$ phase diagram. With increasing zirconium content, the Curie temperature drops while the lower two transition temperatures are raised, causing the three transition temperatures to converge near $x = 0.1$ and $T_c = 50\,^{\circ}C$. As a consequence the three peaks in the dielectric constant merge to give an immense peak of about $K = 8000$.

6.2. Domain walls and dielectric loss

Domain walls are an important source of dielectric loss for temperatures below T_c (Hardtl 1982). Under applied electric fields, domain wall motion takes place, dissipating energy. A number of different types of walls are found in $BaTiO_3$, with varying wall mobilities. Tetragonal $BaTiO_3$ has 180° walls, and both charged and uncharged 90° walls. Charged walls are important only in conducting $BaTiO_3$ where currents can flow, neutralising the charge. The 180° walls are generally more mobile than 90° walls because of the mechanical strain associated with 90° walls.

In general, the electrical loss of ferroelectric ceramics displays three identifiable temperature ranges (figure 20). Below T_c the losses are moderately high and are caused by domain walls. The magnitude of tan δ increases rapidly with the applied field, but does not depend strongly on frequency.

The second temperature range—typically extending 100–200° above the Curie temperature—has very low dielectric loss. Above T_c there are no domains to cause dielectric loss, and the temperature is too low for appreciable conductivity loss.

At high temperatures, the loss due to conductivity becomes important causing tan δ to increase rapidly with temperature. Conduction losses are inversely proportional to the measurement frequency.

Acceptor dopants such as K^+ or Fe^{3+} create oxygen vacancies in $BaTiO_3$: $(Ba_{1-x}K_x)Ti(O_{3-x/2}\square_{x/2})$ and $Ba(Ti_{1-x}Fe_x)(O_{3-x/2}\square_{x/2})$. Oxygen vacancies exert a much greater influence on the dielectric loss than do barium or titanium vacancies. The way in which oxygen vacancies affect tan δ depends on temperature and the dominant loss mechanism. Below T_c where domain wall losses predominate, oxygen vacancies lower tan δ. The explanation of why donors and acceptors affect the dissipation factor differently involves the pinning of domain walls. Donor-doped perovskite

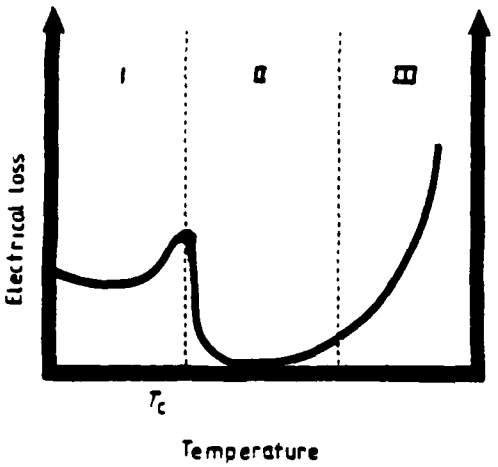

Figure 20. Temperature dependence of the electrical loss tan δ. At high temperatures the losses are caused by conduction, while domain walls are responsible at low temperatures. Region I, high loss caused by domain walls; region II, low loss; region III, high loss caused by conductivity.

ferroelectrics have lossy hysteresis loops and considerable domain wall motion whereas acceptor-doped perovskites do not.

The reason why domain walls are pinned more effectively in acceptor-doped perovskites can be seen from the crystal structure. Oxygen vacancies diffuse much faster than cation vacancies because of the proximity of oxygen sites. The distance between nearest-neighbour oxygens is only 2.8 Å compared to 4 Å for the shortest Ti–Ti or Ba–Ba interatomic distance.

Defect dipoles in acceptor-doped $BaTiO_3$ consisting of paired iron atoms and oxygen vacancies realign more easily than do the corresponding dipoles in donor-doped material. Thus the defect dipoles in acceptor-doped $BaTiO_3$ align with the spontaneous polarisation of the domain structure to pin domain walls, thereby lowering the dissipation factor in the low-temperature region below T_c.

6.3. Conduction losses and degradation

Oxygen vacancies are also important in the high-temperature region. The rapid increase of dissipation factor is caused by free carrier conductivity, and the concentration of free carriers depends on doping and temperature. The loss factor (tan δ) is inversely proportional to frequency in this temperature range.

Based on a number of experiments, the following picture has been developed for the DC degradation process in barium titanate ceramics. Polycrystalline titanates are appreciably reduced at the temperatures used in firing ceramic capacitors. On cooling, rapid reoxidation occurs above 1100 °C but effectively stops at some temperature between 600 and 900 °C. As a consequence the outside of the sample and, to some extent, the outside of each grain is well oxidised, but the interior of the grains remains oxygen deficient. Oxygen vacancies carry an effective charge of $+2e$, which is neutralised by 3d electrons on the titanium atoms, forming two Ti^{3+} ions for every oxygen vacancy. At low temperatures, the oxygen vacancies and Ti^{3+} ions are bound by a small energy of 0.1–0.2 eV, sufficiently large that only a few of the defects are separated. Electrons associated with the unattached Ti^{3+} ions are responsible for

conduction making use of the narrow 3d conduction band. Alternatively the conduction process can be described as electron hopping via $Ti^{3+} \leftrightarrow Ti^{4+} + e^-$ transfer. Unattached oxygen vacancies also contribute to the conductivity but their mobility is much smaller than that of electrons. Neutralised bound defects do not participate directly in the conduction process but experience a torque tending to align the dipole moment with the applied field. This in turn creates dielectric polarisation and dielectric loss. Oxygen vacancies are also important in the AC degradation of $BaTiO_3$ ceramics. Electrostrictive pumping of the oxygen vacancies to the grain boundary has been proposed as a mechanism.

Trivalent manganese plays an important role in a number of capacitor compositions by lowering conduction losses. Mn^{3+} has the $3d^4$ electron configuration and is widely known as a Jahn-Teller ion. It seems likely that the large tetragonal distortions associated with Jahn-Teller ions are effective in anchoring oxygen vacancies.

6.4. Relaxor ferroelectrics

Ordered perovskites generally have low dielectric constants because the linkage between 'active' ions is severed. In disordered structures such as the relaxor ferroelectrics the dielectric constant can be extremely large, making them useful as capacitor dielectrics. The monolithic Pb-based compositions under development in Japan (Yonezawa *et al* 1987) are excellent examples. Not only do the $Pb(Fe_{0.5}Nb_{0.5})O_3$-$Pb(Fe_{0.67}W_{0.33})O_3$ ceramics have dielectric constants in excess of 15 000 but they can be sintered in air at 850 °C with silver electrodes.

Relaxor ferroelectrics are characterised by temperature-sensitive microdomains resulting from the many different 'active' ion linkages in the disordered octahedral framework. Each (NbO_6) octahedron may be bonded to anywhere from zero to six other (NbO_6) octahedra. Connections between these octahedra are assumed to be essential to ferroelectricity and high K values. As temperature decreases from the high-temperature paraelectric state these microdomains gradually coalesce to macrodomains giving rise to a diffuse phase transformation. These polarisation fluctuations are also dependent on bias field and measurement frequency. The dielectric constant drops off rapidly with frequency (hence the name 'relaxor') because it takes time for the polarisation fluctuations to respond. DC bias fields favour coalescence, having the same effect as lowering the temperature.

Relaxor behaviour is very common among Pb-based perovskites, suggesting that Pb^{2+} and its 'lone-pair' electrons play a role in the microdomain process, possibly by adjusting the orientation of the lone pair.

Multilayer relaxor ferroelectrics are used as micropositioners as well as capacitors. The electrostrictive distortions are highly reproducible and have found widespread use in active optic systems (Uchino *et al* 1980).

6.5. Piezoelectric transducers

Piezoelectric transducers convert mechanical energy to electrical energy (the direct piezoelectric effect), or electrical energy to mechanical energy (the converse piezoelectric effect) (Herbert 1982). Ferroelectric ceramics such as lead zirconate titanate become piezoelectric when electrically poled. Poling is carried out under intense electric fields at temperatures just below the ferroelectric Curie point where the domains are most easily aligned.

The phase diagram of the $PbZrO_3$-$PbTiO_3$ system is shown in figure 21(*a*). A complete solid solution forms at high temperature with Zr and Ti randomly distributed over the octahedral sites of the cubic perovskite structure. On cooling, the structure undergoes a displacive phase transformation into a distorted perovskite structure. Titanium-rich compositions favour a tetragonal modification with sizeable elongation along [001] and a large spontaneous polarisation in the same direction. There are six equivalent polar axes in the tetragonal state corresponding to the [100], [$\bar{1}$00], [010], [0$\bar{1}$0], [001], and [00$\bar{1}$] directions of the cubic paraelectric state. A rhombohedral ferroelectric state is favoured for zirconium-rich compositions. Here the distortion and polarisation are along [111] directions, giving rise to eight possible domain states: [111], [$\bar{1}$11], [1$\bar{1}$1], [11$\bar{1}$], [1$\bar{1}\bar{1}$], [$\bar{1}$1$\bar{1}$], [$\bar{1}\bar{1}$1], and [$\bar{1}\bar{1}\bar{1}$].

The compositions which pole best lie near the morphotropic boundary between the rhombohedral and tetragonal ferroelectric phases. For these compositions there are fourteen possible poling directions over a very wide temperature range. This explains why the piezoelectric coefficients are largest near the morphotropic boundary (figure 21(*b*)).

Morphotropic boundaries are relatively common in Pb-based perovskites, more so than in other perovskite phase diagrams. In solid solutions based on $BaTiO_3$, a different sequence of phase transformations appears. On cooling from high temperatures the cubic phase undergoes transformations to tetragonal, orthorhombic, and rhombohedral. The intervening orthorhombic phase makes it possible for the tetragonal phase to transform to rhombohedral. Thus there is no morphotropic phase boundary in $BaTiO_3$-based ceramics.

It appears that morphotropic boundaries occur in $PbTiO_3$-based systems because of the suppression of the orthorhombic phase. The Pb^{2+} ion plays a major role in the suppression. Because of its lone-pair $6s^2$ electron configuration, Pb^{2+} favours pyramidal bonding. In the tetragonal and rhombohedral perovskites, such bonding occurs, but not in the orthorhombic ferroelectric form. Here Pb^{2+} is forced to move directly toward a neighbouring oxygen ion, an extremely unfavourable coordination (Heywang and Thomann 1984).

Poled ceramic transducers have conical symmetry (point group ∞m), the symmetry of a polar vector. By convention, the x_3 axis is chosen along the polar axis with the

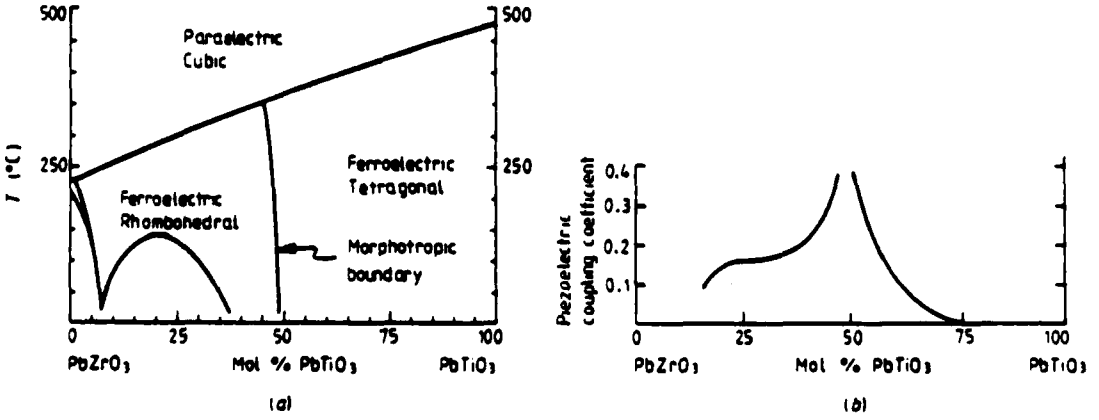

Figure 21. (*a*) **Binary phase diagram of the lead zirconate-lead titanate ceramics used in transducers.** (*b*) **Large piezoelectric coefficients are obtained for poled ceramics with compositions near the morphotropic phase boundary.**

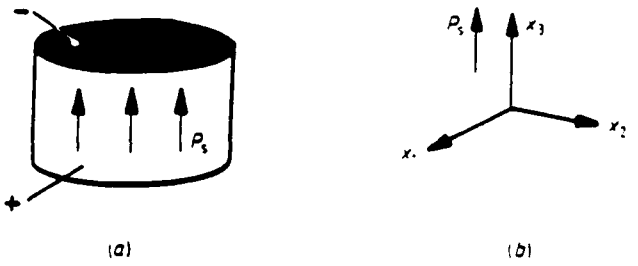

Figure 22. (*a*) Poled piezoelectric ceramics have the symmetry of the imposed electric field vector. This symmetry determines the form of the piezoelectric tensor which is referred to the axial system shown in (*b*).

orthogonal x_1 and x_2 axes perpendicular to x_3 (figure 22). The piezoelectric coefficients relate polarisation to mechanical stress. P_1, P_2, and P_3 are the components of the stress-induced polarisation along axes x_1, x_2, and x_3. In matrix notation, stress components σ_1, σ_2, and σ_3 are the applied tensile stresses parallel to x_1, x_2, and x_3. Shear stresses about x_1, x_2, and x_3 are designated σ_4, σ_5, and σ_6, respectively.

For poled ferroelectric ceramics, conical symmetry dictates that all piezoelectric coefficients are zero except $d_{31} = d_{32}$, d_{33}, and $d_{15} = d_{24}$. The direct piezoelectric effect can therefore be described by the following matrix expression:

$$\begin{pmatrix} P_1 \\ P_2 \\ P_3 \end{pmatrix} = \begin{pmatrix} 0 & 0 & 0 & 0 & d_{15} & 0 \\ 0 & 0 & 0 & d_{15} & 0 & 0 \\ d_{31} & d_{31} & d_{33} & 0 & 0 & 0 \end{pmatrix} \begin{pmatrix} \sigma_1 \\ \sigma_2 \\ \sigma_3 \\ \sigma_4 \\ \sigma_5 \\ \sigma_6 \end{pmatrix}.$$

Multiplying out,

$$P_1 = d_{15}\sigma_5 \qquad P_2 = d_{15}\sigma_4 \qquad P_3 = d_{31}(\sigma_1 + \sigma_2) + d_{33}\sigma_3.$$

Thus polarisation along x_1 can only be generated by shear stresses about x_2. For hydrostatic pressure p, $\sigma_1 = \sigma_2 = \sigma_3 = -p$, and $\sigma_4 = \sigma_5 = \sigma_6 = 0$. The resulting polarisation appears along x_3: $P_3 = (2d_{31} + d_{33})(-p)$.

Molecular mechanisms for piezoelectric coefficients d_{33}, d_{31}, and d_{15} are pictured and explained in figure 23. For PZT compositions near the morphotropic boundary, $d_{33} \simeq 400$ pC N^{-1}, $d_{31} \simeq -170$, and $d_{15} \simeq 500$. The magnitudes depend markedly on dopants and defect structure because of their influence on domain wall motion.

Donor ions create Pb vacancies in the PZT structure. As an example, when Nb^{5+} is substituted for Ti^{4+}, vacancies on the lead site result:

$$(Pb_{1-x/2}\square_{x/2})(Ti_{1-y-x}Zr_yNb_x)O_3.$$

Donor doping is not effective in pinning domain walls. Pinning is believed to result from the alignment of defect dipoles with the spontaneous polarisation within a domain. The defect dipoles come from the negatively charged Pb vacancies paired with dopant Nb^{5+} ions. Since the defect dipoles are formed at high temperature, the dipoles are not aligned with P_s initially because the spontaneous polarisation is zero in the cubic paraelectric state. Alignment can only take place below the Curie temperature (~350 °C for PZT) where diffusion rates are low. Such is the case for donor-doped PZT, a so-called 'soft' PZT. In a soft PZT, domain wall motion contributes to the size of the dielectric and piezoelectric coefficients. Hence soft PZT transducers are used as

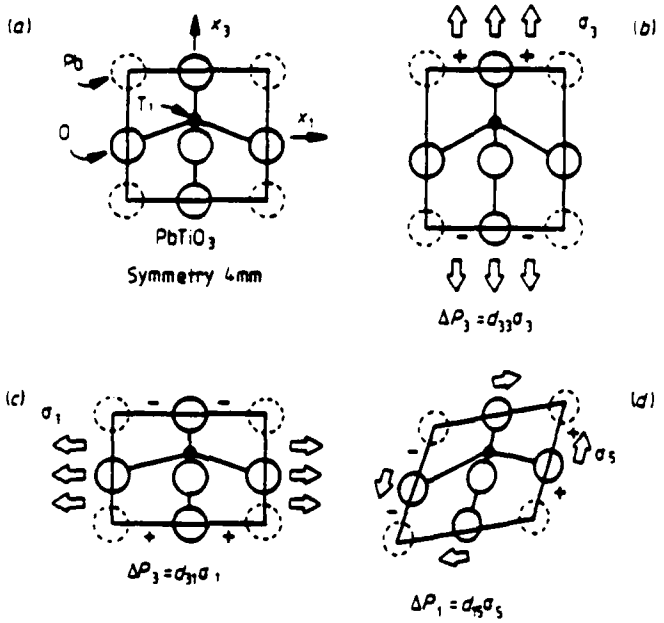

Figure 23. (*a*) Tetragonal $PbTiO_3$ is non-centrosymmetric with the titanium ion displaced from the centre of the unit cell. (*b*) When a tensile stress is applied parallel to x_3, the Ti^{4+} ion displaces further in its off-centre position, creating a positive polarisation in this direction: $P_3 = d_{33}\sigma_3$. (*c*) If the stress is applied along x_1, the dipole moment of the unit cell is diminished, and a negative polarisation appears. Hence d_{31} is negative while d_{33} is positive. (*d*) For a shear stress about x_2, the dipole moment is tipped, producing polarisation in the x_1 direction, $P_1 = d_{15}\sigma_5$.

hydrophones and ultrasonic detectors where high sensitivity to weak signals is needed. Adversely, however, soft PZT ceramics are easily depoled because the domain walls are not pinned. For this reason, soft PZT is not used for sonar transmitters or spark generators (Pointon 1982).

Acceptor doping with lower valent ions such as K^+ (for Ba^{2+}) or Fe^{3+} (for Ti^{4+}) is employed to produce 'hard' PZT. Oxygen vacancies are generated by acceptor doping:

$$(Pb_{1-x}K_x)(Ti_{1-y}Zr_y)(O_{3-x/2}\square_{x/2}).$$

Domain walls are pinned in hard PZT because the defect dipoles are able to align in accordance with the domain structure. Dipoles consisting of oxygen vacancies and associated dopant ions are able to re-orient more easily in a hard PZT. The explanation lies in the ease with which oxygen vacancies diffuse at temperatures below T_c.

Examination of the perovskite structure makes it clear why oxygen vacancies diffuse faster than cation vacancies. Cations are completely surrounded by oxygens and are separated from the nearest cation site by an entire unit cell (~4 Å), making diffusion very difficult. Oxygen sites, on the other hand, are adjacent to one another, only 2.8 Å apart. Hence oxygens can easily move into nearby oxygen vacancies, realigning defect dipoles and pinning domain walls.

7. Magnetism in oxides

Magnetic ordering occurs when the transition-metal atoms are nearest neighbours (metals) or next nearest neighbours (simple compounds) (Chikazumi 1964). Among

oxides and fluorides, antiferromagnetism is much more common than ferromagnetism or ferrimagnetism. The reason is the superexchange interaction. Direct exchange seldom occurs in such materials because the transition-metal ions are not in direct contact, but interact via an intermediate anion. Superexchange is a strong interaction, leading to magnetic transition temperatures comparable to metals. Ferromagnetic ordering in Fe occurs at 1040 K, antiferromagnetism in α-Fe_2O_3 at 950 K, and ferrimagnetism in magnetite at 860 K.

In the superexchange interaction two metal atoms M_1 and M_2 on opposite sides of an oxygen ion interact through a p orbital of oxygen (figure 24). Transition-metal ions with less than half full d shells will be considered first. Since the oxygen ion is not fully ionised, its outer electrons spend time on the neighbouring transition-metal ions. When it enters the d shell of a transition ion whose d orbitals are less than half full, the oxygen electron spin is parallel to those of the metal ion, in accordance with Hund's rule. Meanwhile the other electron in the same oxygen p orbital is on the opposite side of the oxygen ion because of the coulomb repulsion between two electrons in the same p orbital. While there, the second electron (whose spin is antiparallel to the first electron because of the Pauli exclusion principle) also interacts with transition-metal ions—and its spin will again be parallel to that of the metal ion if its d shell is less than half full. The antiferromagnetic superexchange thus arises from the alignment as shown in figure 24: the first metal atom accepts an electron with parallel spin from an oxygen neighbour; the spins of the two electrons in the same oxygen p orbital are antiparallel; and the second electron spends part of its time in parallel alignment with the d electrons of the second metal ion.

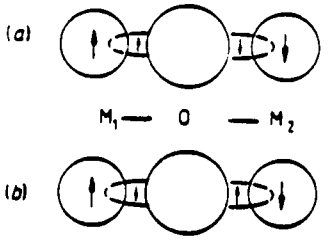

Figure 24. The 180° superexchange interaction when the transition-metal 3d shell is (*a*) less than half full and (*b*) half or more than half full.

A similar situation occurs when the d electron shell of the transition-metal ion is more than half full, again resulting in antiferromagnetic superexchange (figure 24). The oxygen electrons enter the metal atom d shell antiparallel to the net spin, but since the same thing happens to the other electron, the interaction remains antiferromagnetic. Superexchange is strongest when the angle M_1-O-M_2 is 180°, allowing maximum overlap of the p orbital with the two metal ions. The interaction weakens as the angle approaches 90°, even though the metal-metal distance may be shorter.

Long-range magnetic order disappears at high temperatures because of thermal disorder. The transition temperature is called the Curie point (T_c) in a ferromagnet or ferrimagnet, and the Néel point (T_N) in an antiferromagnet. T_c and T_N depend strongly on transition-metal concentration, as expected. The general trend is indicated by the transition temperatures for the following Fe^{3+} compounds, which are arranged in order of decreasing iron content: α-Fe_2O_3 (958 K), γ-Fe_2O_3 (743), FeOF (315), Fe_2MgO_4 (653), $Y_3Fe_5O_{12}$ (563), FeF_3 (394), $FeCl_3$ (10), Fe_2TeO_6 (219), $YFeO_3$ (643),

$FePO_4$ (25), $Fe_3(PO_4)_2 \cdot 4H_2O$ (15), $FeNH_4(SO_4)_2 \cdot 12H_2O$ (<1 K). Magnetic interactions weaken with increasing dilution, although some noticeable irregularities occur in the list. The transition temperature of $FeCl_3$ is surprisingly low, while that of $YFeO_3$ is rather high. These exceptions illustrate the influence of crystal structure on the exchange interactions. Ferric chloride has a layer structure with sequence -Cl-Fe-Cl-Cl-Fe-Cl-. Neither direct nor superexchange interactions are possible between layers, hence T_N is very low. In $YFeO_3$, the arrangement of iron and oxygen is nearly ideal for 180° superexchange. The compound crystallises in the perovskite structure with interconnected -O-Fe-O-Fe-O- chains in all three directions.

7.1. Spinel ferrites

Most magnetic ceramics make use of the trivalent iron, Fe^{3+}, with its five unpaired electrons. To take advantage of the large magnetic moment, it is necessary to couple the spins through superexchange. In ferrites with the spinel structure there is a strong antiferromagnetic superexchange coupling between the tetrahedral and octahedral sites. Each oxygen in the spinel structure is bonded to one tetrahedral cation and three octahedral cations (figure 25). The tetrahedral ion-oxygen-octahedral cation linkage subtends an angle of 125° at the oxygen ion which is large enough to make use of a 2p orbital in a strong superexchange interaction.

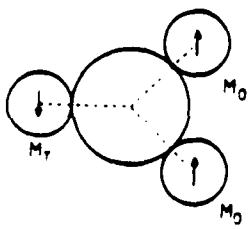

Figure 25. Oxygen nearest neighbours in the spinel structure. Superexchange coupling between the tetrahedral and octahedral sites is especially strong.

The complexity of the spinel structure is also important; there are twice as many octahedral as tetrahedral metal ions in spinel and this leads to magnetic imbalance and a net magnetisation. This is why magnetite (Fe_3O_4, spinel structure) is ferrimagnetic while hematite (α-Fe_2O_3, corundum structure) and wustite (FeO, rocksalt structure) are antiferromagnetic.

7.2. Magnetisation

In the spinel ferrites, the spontaneous magnetisation is equal to the *difference* between the sublattice magnetisations associated with the octahedral and tetrahedral sites. By judicious choice of ions, the difference can be made quite large, and leads to an unusual situation in which adding a non-magnetic ion *increases* the magnetisation. This type of substitution is used to maximise the remanent magnetisation of ferrites.

Zinc ferrite ($ZnFe_2O_4$) is a normal spinel whereas most other spinel ferrites have the inverse structure. In a normal spinel, divalent cations occupy the tetrahedral sites, in contrast to inverse spinels where the tetrahedral sites are filled with trivalent cations. In the nickel zinc ferrite solid solution ($Ni_{1-x}Zn_xFe_2O_4$), as x is increased Zn^{2+} replaces Fe^{3+} in the tetrahedral sites and Fe^{3+} fills the octahedral sites emptied by Ni^{2+}. Divalent

zinc has no unpaired electrons, divalent nickel has two, and trivalent iron five. The net magnetisation of nickel zinc ferrite is proportional to $5(1+x)+2(1-x)-0(x)-5(1-x)=2+8x$. Calculated magnetic moments for several of the zinc ferrite solid solutions are compared with experiment in figure 26. As predicted, the magnetisations rise with increasing zinc content until there are so few Fe^{3+} ions remaining in tetrahedral sites that the superexchange coupling between tetrahedral and octahedral sites breaks down. As a result, the Curie temperatures decline rapidly with increasing zinc content, eventually dropping below room temperature (figure 27). The ferrite changes from ferrimagnetic to paramagnetic as the composition nears pure zinc ferrite. The most useful compositions are those near $x=0.5$ where the magnetisation is a maximum.

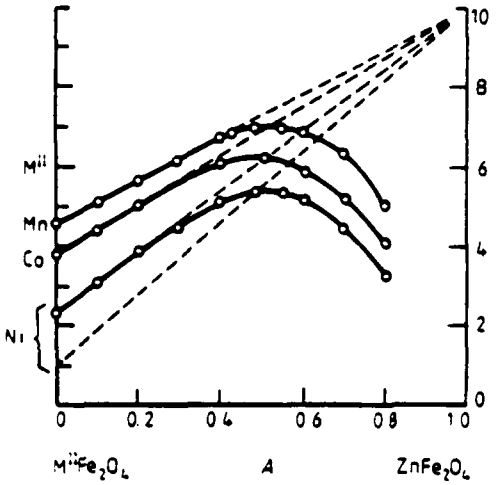

Figure 26. Addition of zinc raises the magnetisation of ferrites.

7.3. Soft ferrites

Soft ferrites are noted for their high magnetic permeability and high electrical resistivity (Slick 1980). Eddy current losses are of great importance, and compared to metals, the high resistivity of ferrites greatly reduces loss at high frequencies. Applications for soft ferrites include inductors, transformers, antenna rods, loading coils, deflection yokes, choke coils, recording heads, and magnetic amplifiers.

Manganese zinc ferrite and nickel zinc ferrite are the most widely used of the soft ferrites. Mn-Zn ferrite has the highest saturation magnetisation of any ferrite, and is a good soft magnetic core material, but Ni-Zn ferrite is superior at high frequencies because of its higher electrical resistivity and lower resonance losses.

The property of greatest interest in soft ferrites is the initial permeability μ_i and its frequency dependence. Permeability is a complex quantity, $\mu=\mu'-i\mu''$, with the magnetic loss factor defined as $\tan\delta=\mu''/\mu'$. Engineers often use $\tan\delta/\mu'$ as a figure of merit in comparing different ferrites at low frequencies. The lowest (best) figures of merit are obtained for Mn-Zn ferrites, and for Ni-Zn ferrites at high frequencies. The crossover frequency is approximately 1 MHz.

Figure 28 shows frequency spectra for several Ni-Zn ferrites. The permeability spectrum is characterised by a broad loss peak at f_r associated with domain wall losses. Note that the ferrites with high permeability have the worst frequency dependence; the product $\mu' f_r$ is approximately constant (Snoek's law).

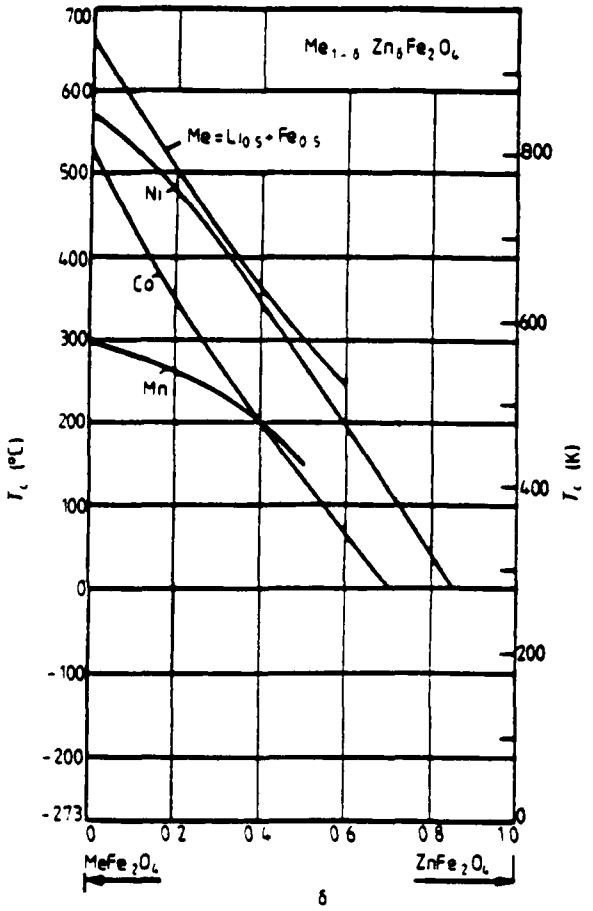

Figure 27. Addition of zinc lowers the Curie point of magnetic ferrites.

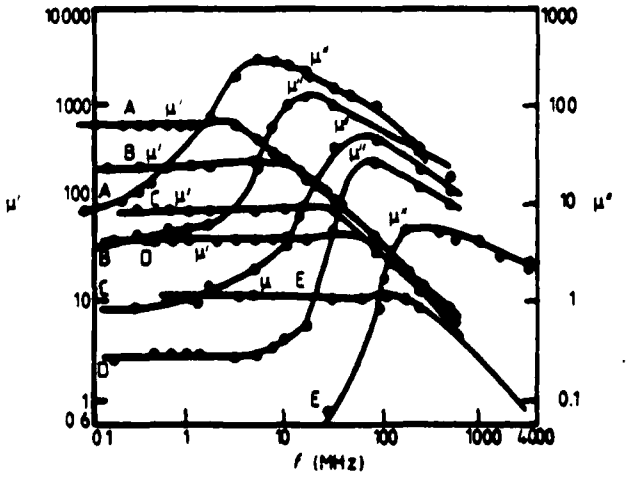

Figure 28. Permeability spectrum for Ni-Zn ferrites (Smit and Wijn 1959).

7.4. Anistropy, magnetostriction and microstructures

7.4.1. Anisotropy. To maximise the permeability of a soft ferrite it is necessary to eliminate restraints on domain wall motion. Crystal anisotropy and magnetostriction are two restraints which can be greatly reduced through control of chemical composition and microstructure. Mn-Zn ferrites are intrinsically soft because of their low anisotropy fields. Mn^{2+} and Fe^{3+} have half-filled 3d shells and Zn^{2+} has a completely filled shell. All three ions are spherically symmetric with little preference in spin orientation.

The anisotropy field affects both the rotational and domain wall contributions to the permeability. Since the spins in a low anisotropy ceramic are easily deflected by an applied field, the rotational permeability is greatly enhanced. Domain wall motion is also enhanced because of the nature of domain walls. Within the walls, spin orientations differ markedly in orientation from the easy axis directions. Thus wall energy and the ease with which walls can be created or displaced is influenced strongly by the anisotropy field.

7.4.2. Magnetostriction. The change in shape of a magnetic specimen during the magnetisation process is called magnetostriction. Domain wall motion is responsible for most of the strain. Strain measurements are made on unmagnetised specimens with randomised domain structure. When a field is applied, the specimen changes shape, and eventually both the magnetisation and the strain reach saturation values at very large fields. For ferrites the saturation strain λ ranges from 10^{-6} to 10^{-3}. Small values of λ are essential in a soft ferrite because strain mismatch impedes domain wall motion and magnetisation rotation.

Magnetostrictive coefficients have been measured for a number of ferrites including the manganese zinc ferrites shown in figure 29. Adding a few per cent Fe^{2+} reduces λ to zero, and it also decreases the anisotropy coefficient K_1.

7.4.3. Microstructures. Compositions near the intersection of the $\lambda = 0$ and $K_1 = 0$ lines are especially interesting. Magnetic permeabilities as large as 40 000 are measured

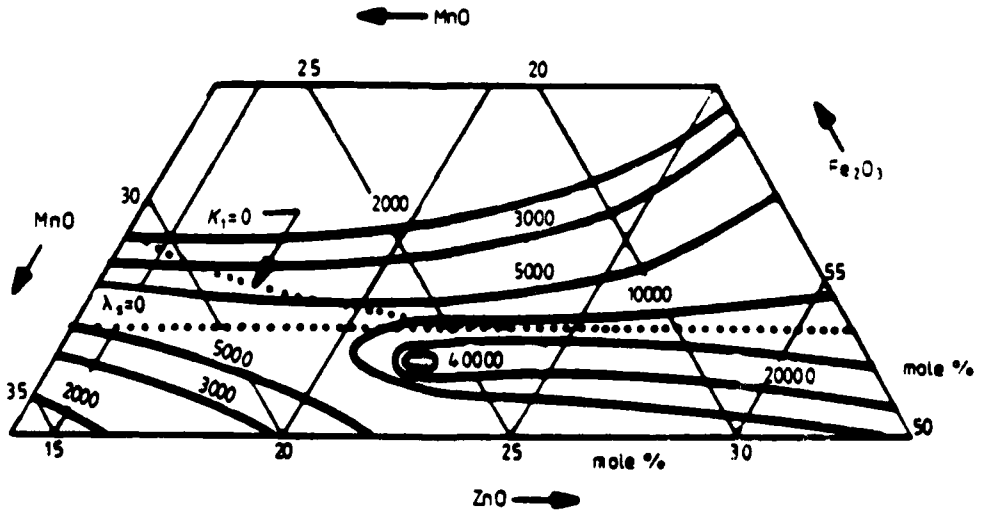

Figure 29. Constant permeability contours in the Mn-Zn-Fe ferrite system. Maximum permeability occurs near the point of zero magnetostriction and zero anisotropy.

near the point where magnetostrictive and anisotropy effects are absent. Domain wall and rotational contributions to the permeability are both enhanced at this composition.

In ceramic ferrites, a microstructure consisting of large, defect-free crystallites favours domain wall mobility and high magnetic permeability (Jonker and Stuijts 1971). Domain wall movements are suppressed in the fine-grained ferrites used in permanent magnets and in high frequency applications. Small grain microstructures and low porosity are also required for microwave ferrites to eliminate unwanted spin waves.

The distribution of pores in the microstructure is important. Tiny pores distributed uniformly throughout the grains are obtained in ferrites slightly deficient in oxygen. The pores pin domain walls and lower the magnetic permeability. A different pore structure is obtained in ferrites deficient in cations. In this case the pores are swept together at the grain boundaries during sintering, leaving behind relatively perfect crystallites. Very high permeabilities can then be achieved provided the grain size is large (Jonker and Stuijts 1971).

Microstructure also controls magnetic losses. Substituting Fe^{2+} in Mn-Zn ferrites raises the permeability but it also lowers the electrical resistivity as the extra electron hops easily between iron atoms: $Fe^{2+} \leftrightarrow Fe^{3+} + e^-$. The increased conductivity leads to eddy current losses which can be controlled by adding a small amount of silica to the starting material. During the sintering operation, silica forms a grain boundary phase which raises the resistance and eliminates eddy currents. This results in a decrease in the electrical loss tan δ and an increase in the figure of merit, $\mu/\tan\delta$.

Eddy currents are the most important source of loss at low frequencies (kHz range) but ferrimagnetic resonance and domain wall damping are the controlling mechanisms in the MHz range. Mn-Zn ferrites are not used at these frequencies because the Larmor precession frequency is too low. Ni-Zn ferrites have stronger internal fields and higher resonant frequencies (10-1000 MHz). This lowers resonance losses in the 1-10 MHz range. Eddy current losses are also small because of the higher resistivity of the Ni-Zn compositions, although the permeability μ' is somewhat smaller.

Domain wall damping contributes to loss at frequencies just below resonance. To limit this factor, it is necessary to minimise wall displacements by making the grain size very small. Hot pressing procedures or the addition of grain growth inhibitors keep the grain size small and lower losses.

Small grain size is also an advantage in microwave ferrites which operate in the GHz range. When operated at high power levels, parametric excitation of spin waves becomes the dominant loss mechanism. Reductions in grain size to below 2 μm increase the power handling capability by several orders of magnitude.

7.5. Permanent magnets

Hard magnets are characterised by high coercive field strength and high remanent magnetisation (Becker *et al* 1968). The $(BH)_{max}$ energy product (figure 30) is used as a measure of magnetic 'hardness'.

Processing methods to maximise the BH product are magnetic annealing and the texturing of crystallites by magnetic pressing. Precipitation hardening, superlattice formation, and work hardening also increase the coercive field by restricting domain wall movement.

Some oxide magnets utilise particles small enough to have single domain structure. The oxide powder (OP) magnet with composition $3CoFe_2O_4 \cdot Fe_3O_4$ invented 50 years

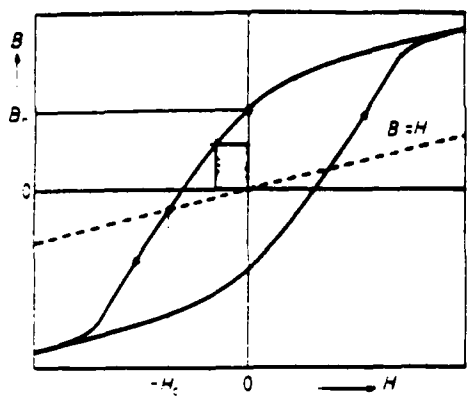

Figure 30. Hysteresis in magnetic ceramics.

ago has large magnetocrystalline anisotropy and large magnetostrictive coefficients as well as small particle size. Overfiring can cause grain growth, resulting in a reduced coercive field.

One of the most widely used permanent magnet materials is barium ferrite, a ferrimagnetic oxide with the magnetoplumbite structure. The large Ba^{2+} ions form a close-packed array with the O^{2-} anions in a mixed sequence of hexagonal and cubic close-packing. Trivalent iron ions occupy three types of sites within the magnetoplumbite structure: octahedral, tetrahedral, and an unusual five-coordinated trigonal bipyramid site.

Magnetic interactions between the iron ions take place via the same -Fe-O-Fe- superexchange mechanism found in spinel ferrites. Four of the twelve irons in $BaFe_{12}O_{19}$ align opposite to the other eight, giving a net saturation magnetisation of $(8-4)5 = 20\,\mu_B$ per formula unit. Spin alignments for the various magnetic ions in the unit cell are illustrated in figure 31, pointing out the similarity to the spinel structure. The saturation magnetisation is also similar to the spinel ferrites, but the crystalline anisotropy is much larger because of the lower symmetry. In $BaFe_{12}O_{19}$ the Fe^{3+} spins are locked tightly to the [001] direction giving a high anisotropy coefficient.

Compared to the best metallic permanent magnets, the ferrite magnets are characterised by a high coercive field (H_c) and low residual magnetic induction (B_r). The origin of the high coercive field is the high magnetocrystalline anisotropy which locks the spins into the *c* axis orientation. Representative properties for the OP magnet, and for barium and strontium hexaferrite are listed in table 1. The ferrites are best used in applications that take advantage of the high H_c values; DC motors, holding devices, and magnetic separators. Flexible rubber-bonded ferrites are used as stators and as magnetic latching devices.

7.6. Preparation and applications

Barium ferrites are generally made by calcining $BaCO_3$ with $BaFe_{12}O_{19}$. The oxide is then ground to micrometre-size powder, compacted in a die, and sintered at 1200 to 1300 °C to about 95% theoretical density.

To obtain grain alignment with a threefold improvement in properties, the powder is pressed in the presence of a magnetic field before sintering. Barium ferrite has a platey morphology with the easy axis of magnetisation perpendicular to the hexagonal plates. The combined action of parallel stress and magnetic field during the forming

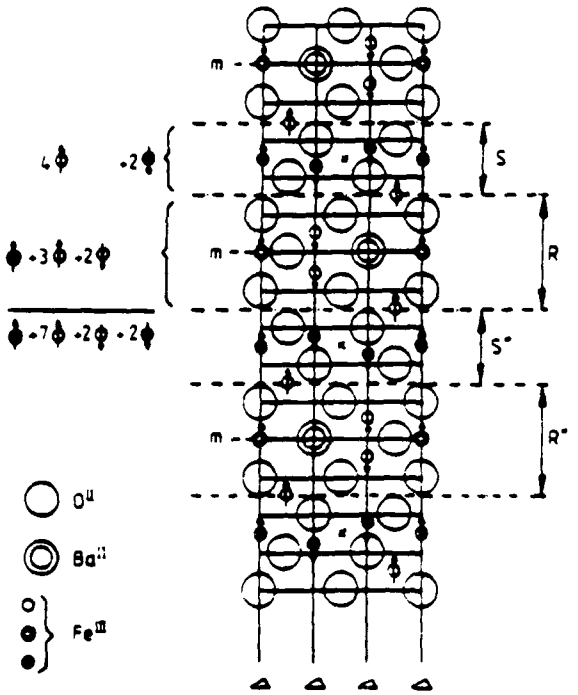

Figure 31. Cross section of the magnetoplumbite structure M, with the *c* axis vertical. The arrows indicate the spin orientations. The vertical lines are axes of threefold symmetry and the cross denotes a centre of symmetry. All layers containing barium are mirror planes, and are denoted by m. The structure consists of spinel-like blocks separated by the layers containing barium. The asterisk indicates a rotation of a block by 180° about the *c* axis (Smit and Wijn 1959).

Table 1. Properties of ferrite permanent magnets (Becker *et al* 1968).

Material	B_r (W m^{-2})	H_c (10^6 A m^{-1})	$(BH)_{max}$ (10^3 J m^{-3})
$BaFe_{12}O_{19}$			
Isotropic	0.22	0.148	4.0
Oriented (high B_r)	0.384	0.160	14.0
Oriented (high H_c)	0.32	0.204	10.4
Rubber bonded	0.22	0.118	4.4
$SrFe_{12}O_{19}$			
Oriented (high B_r)	0.40	0.176	14.8
Oriented (high H_c)	0.355	0.252	12.0
OP magnet			
$Co_{0.5}Fe_{0.25}Fe_2O_4$	0.25	0.052	4.8

operation produces a highly oriented grain structure with spins parallel to the magnetic field. To obtain a high remanent magnetisation, it is important to avoid grain growth during sintering. Silicate mixtures are used as grain growth inhibitors.

The uses for permanent magnets are surprisingly numerous and frequently go unnoticed. Among the applications are telephones, electric clocks, television, radio, hearing aids, watt-meters, phonographs, and thermostats. Portable appliances such as the electric knife, automobile accessories, and the electric toothbrush use low voltage

DC motors with permanent magnets. In industry, they are used in magnetic separators, microwave systems, magnetic chucks, and computers.

The design of a permanent magnet is as important as the choice of materials. Through improved materials and computer-aided design, the performance of permanent magnets has often surpassed electromagnets in lower cost and volumetric efficiency. The performance is governed by the demagnetisation curve, the nature of the magnetic circuit, and the dimensions of the magnet.

The basic function of a permanent magnet is to generate a useful magnetic field in an air gap. In a well designed circuit, the field is concentrated across the gap with the aid of soft magnet pathways for the flux.

The applications for permanent magnets can be subdivided into static and dynamic functions. Static functions include separators, latches, compasses, and chucks where the magnet gives a mechanical force, and magnetrons and beam-focusing devices in which the magnet controls an electron beam.

Dynamic devices generally involve electric to mechanical energy conversion. Examples are microphones, phonograph pick-ups, telephone bells, and loudspeakers.

8. Summary

In this brief review, many interesting topics in electroceramics have been omitted or given only cursory attention. More complete discussions can be found in the recent books edited by Buchanan (1986) and by Levinson (1988).

An overview of structure-property relationships in electroceramics is given in figure 32 which illustrates the various atomistic mechanisms utilised in ceramic circuit components. Multilayer capacitors, piezoelectric transducers and PTC thermistors make

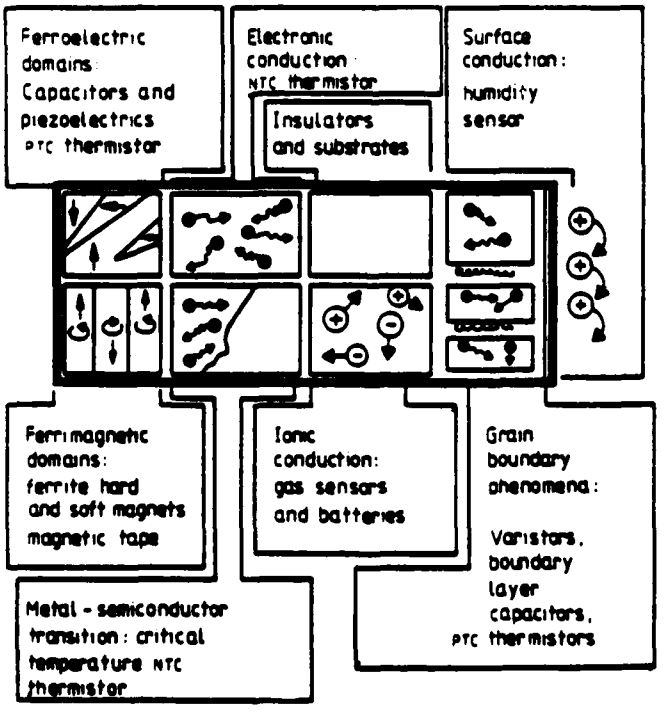

Figure 32. An overview of the various atomistic mechanisms involved in electroceramic components.

use of the properties of ferroelectric perovskites with their high dielectric permittivity, large piezoelectric coefficients, and anomalous electric conductivity. Similar domain phenomena are observed in ferrimagnetic oxide ceramics such as $NiFe_2O_4$. Hard and soft ferrites are analogous to hard and soft PZT, and have found substantial markets in magnetic tape and electric motors.

Several kinds of mechanisms are operative in thermistors and other ceramics used as sensors. Most are based on changes in electrical resistivity, but the causes are different. The critical temperature thermistor involves a semiconductor-metal phase transition. NTC thermistors make use of the semiconducting properties of doped transition-metal oxides. Ionic conductivity is used in oxygen sensors and batteries. Stabilised zirconia is an excellent anion conductor, and β-alumina is one of the best cation conductors.

Humidity sensors make use of surface conduction. Adsorbed water molecules dissociate in hydroxyl in hydronium ions which alter the electrical resistivity.

Grain boundary phenomena are involved in boundary layer capacitors, varistors, and PTC thermistors. The formation of thin insulating layers between conducting grains is crucial to the operation of all three electroceramic components. Lastly, the importance of electroceramic insulators and substrates should not be overlooked. Here one strives to eliminate most of the interesting effects just described, but this is not always easy.

References

Becker J J, Luborsky F E and Martin D L 1968 *IEEE Trans. Magn.* MAG-4 84–98

Bednorz J G and Müller K A 1986 *Z. Phys.* B **64** 189–93

Buchanan R C (ed.) 1986 *Ceramic Materials for Electronics* (New York: Marcel Dekker)

Cava R J, Batlogg B, VanDoner R B, Murphy D W, Sunshine S, Siegrist T, Remeika J P, Reitman E A, Zahurak S and Espinosa G P 1987 *Phys. Rev. Lett.* **58** 1676–9

Chikazumi S 1964 *Physics of Magnetism* (New York: Wiley)

Daniels J, Hardtl K H and Wernicke R 1978 *Philips Tech. Rev.* **38** 73–82

Eddy D 1974 *IEEE Trans.* VT-**23** 125–8

Einzinger R 1987 *Ann. Rev. Mater. Sci.* **17** 299–321

Fog A and Buck R P 1984 *Sensors and Actuators* **5** 137–46

Hardtl K H 1982 *Ceram. Int.* **8** 121–7

Herbert J M 1982 *Ferroelectric Transducers and Sensors* (London: Gordon and Breach)

—— 1985 *Ceramic Dielectrics and Capacitors* (London: Gordon and Breach)

Heywang W and Thomann H 1984 *Ann. Rev. Mater. Sci.* **14** 27–47

Jonker G H and Stuijts A L 1971 *Philips Tech. Rev.* **32** 79–95

Kulwicki B M 1984 *J. Phys. Chem. Solids* **10** 1015–31

Levinson L M (ed.) 1988 *Electron Ceramics* (New York: Marcel Dekker)

Levinson L M and Philipp H R 1986 *Ceram. Bull.* **65** 639–46

McGeehin P and Hooper A 1977 *J. Mater. Sci.* **12** 1–27

Nitta T 1981 *Ind. Eng. Chem. Prod. Res. Dev.* **20** 669–74

Pointon A J 1982 *IEE Proc.* **129** 285–307

Saburi O 1964 *J. Am. Ceram. Soc.* **44** 54–63

Slick P I 1980 *Ferromagn. Mater.* **2** 189–241

Smit J and Wijn H P J 1959 *Ferrites* (New York: Wiley)

Uchino K, Nomura S, Cross L E and Newnham R E 1980 *J. Phys. Soc. Japan* **49** suppl. B 45–8

Wu M K, Ashburn J R, Torng C J, Hor P H, Meng R L, Gao L, Huang Z J, Wang Y Q and Chu C W 1987 *Phys. Rev. Lett.* **58** 908–10

Yonezawa M, Miyauchi M, Utsumi K and Saito S 1987 *NEC Res. Dev.* **85** 1–6

APPENDIX 2

Piezoelectric and Electrostrictive Sensors and Actuators for Adaptive Structures and Smart Materials.

L. Eric Cross
Evan Pugh Professor of Electrical Engineering
Materials Research Laboratory
Pennsylvania State University
University Park, PA 16801

ABSTRACT

For stress, vibration, and acoustic pressure sensing piezoelectric and electrostrictive ceramic and composite materials provide unusual versatility. In this talk the design principles for piezoelectric composites will be briefly reviewed and the immense advantages possible in ceramic/polymer composites highlighted. Polarization biased electrostrictive compositions are shown to give interesting switchable transduction capability both for receiving and sending modes. In actuator systems, the evaluation of multilayer actuator materials will be traced and new possibilities for ultra high strain materials explored. Again, the theme will be electric polarization control to exploit the major dimension changes which occur in micro-domain to macro-domain and antiferroelectric to ferroelectric phase transitions.

In the composite systems, a very logical extension of current work is to examine possible systems which could incorporate both a sensor and a responder in the same material together with active solid state electronics coupling the two elements. Preliminary data is presented for a piezoelectric sensor/actuator combination which mimics an ultra soft material (five times softer than rubber) for weak AC stress, but has the properties of a stiff ceramic, even under very high DC pressure.

Possible extensions of this concept to other types of "smart systems" are briefly reviewed.

1. INTRODUCTION

Over the last decade increasing interest has been evidenced in sensor systems to detect sub-acoustic, acoustic, and ultrasonic waves. At the low frequency end of the spectrum, Navy needs for ever more sensitive and larger area sensors has pushed new developments in both polymer and ceramic/polymer composite systems. At higher frequencies, the electromedical community has needs for very high receive sensitivities so that ultrasonic stress levels may be kept well below the threshold for tissue damage. In the electromedical field also, composites offer significant advantage both in receive and sending modes. For the large sensor arrays in use in both fields it becomes important to explore simple ways of switching transducers both in sensitivity and in phase so as to distinguish in one case global from local noise sources, and in another case, to do beam steering and beam focusing from a static array structure. Several different types of electrostrictive systems offer the possibility of polarization controlled piezoelectricity with exceptionally large induced piezoelectric d_{ij} and coupling coefficients k_{ij}. In several of these which will be discussed, the polarization has remnance so that by charge control, specific phase and sensitivity can be induced and remains remnant over long periods. Both switching speeds and decay character will be discussed.

In actuator systems the potential application areas are much broader, ranging from the very simple "drop on demand" actuators for ink jet printers to the highly sophisticated and precise position control actuators for large-area, surface-deformable mirrors. The demands encompass a very wide range of force/displacement requirements and widely different precisions and reproducibility needs. In this paper the focus will be upon the materials available and characteristics which can be achieved. For large shape change (beyond 0.1%) it is essential to begin to manipulate the spontaneous polarization in ferroic crystals. Several techniques for encompassing such polarization controlled systems will be examined. At very high levels repeated switching of the strain leads to fatigue and possible origin for the fatigue will be briefly examined.

The switchable agile transducers represent one family of "smart" solids in which the piezoelectric response is under control from the polarization state induced. A second type of smart solid is a logical next step in the composite approach in which both sensor and responder are coupled in the materials with embedded solid state control electronics. To demonstrate the principle a piezoelectric sensor/actuator combination which permits the control of the elastic compliance S_{33} is examined. Using a negative feedback from the sensor, which causes the actuator to shirk its three dimension under a 33 stress (X_{33}) applied to the sensor, large strain can be induced by very small stress mimicking the elastic property of a very soft solid. In the demonstration experiment discussed, the amplification is

such that the compliance S_{33} is larger than that of a soft rubber and is maintained over the frequency range from 10 to 150 Hz. Since the sensor is piezoelectric, DC pressure does not give feedback and the sensor/actuator stack just displays the property of a stiff ceramic.

2. PIEZOELECTRIC AND ELECTROSTRICTIVE SENSORS.

For many sensor systems which are based upon the transduction of stress to electric signal using a piezoelectric solid it is possible to develop a figure of merit for the materials parameters of the piezoelectric. A typical example would be the figure of merit for sensing weak hydrostatic pressure waves which takes the simple form

$$F = d_h g_h / \tan \delta.$$ Where:

F is the figure of merit which should be as large as possible.

d_h is the hydrostatic piezoelectric charge coefficient.

g_h the hydrostatic piezoelectric voltage coefficient.

$\tan \delta$ the dielectric loss tangent in the piezoelectric.

For uniaxial poled ferroelectric crystals or ceramics or the PVF2 copolymer with PTFE. The non-zero d and g constants are:

0	0	0	0	d_{15}	0	0	0	0	g_{15}	0	
0	0	0	d_{15}	0	0	0	0	0	g_{15}	0	0
d_{31}	d_{31}	d_{33}	0	0	0	g_{31}	g_{31}	g_{33}	0	0	0

$$\text{Thus } d_h = d_{33} + 2d_{31} \qquad g_h = \frac{d_{33} + 2d_{31}}{\varepsilon_{33}}$$

$$\text{so that } F = \frac{d_h g_h}{\tan \delta} = \frac{(d_{33} + 2d_{31})^2}{\varepsilon_{33} \tan \delta.}$$

To maximize the figure of merit it is clear that one would wish to maximize certain tensor components to minimize others, and this is true for most sensing applications.

In a monolythic single phase material, the non-zero constants are set by the symmetry and their magnitudes by the nature and arrangements of the constituent atoms. In a composite however the mean constants can be modified by the mutual arrangement of the components and the fields and fluxes can be steered to desired paths by the self-connectivity of the compliant component. For polymer/PZT ceramic composites the flux steering can be particularly effective since the polymer is dielectrically stiff but elastically compliant, whilst the ceramic is just the converse, i.e., elastically stiff but dielectrically highly compliant (fig 1).

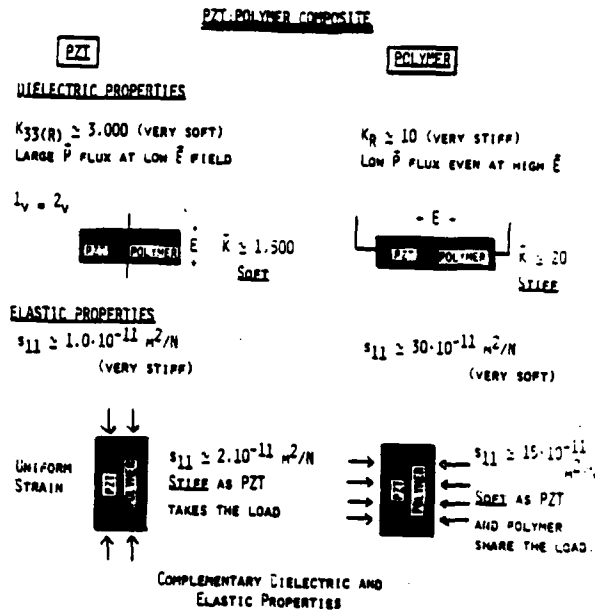

Fig. 1 Contrasting dielectric and elastic properties in series and parallel combinations of PZT ceramic and a polymer.

A rather simple qualitative way of describing connectivity for a two phase system is the simple cubes model of Newnham et al[1, 2, 3] illustrated in fig. 2. The proposed notation indicates the presence or absence of connected area for flux along any of the three orthogonal axes, where, by convention, the piezoelectric phase is described first. Connectivities which are of most interest in hydrostatic stress sensors are 0:3, 1:3, and 3:3. For actuator systems, the 2:2 connectivity is most important.

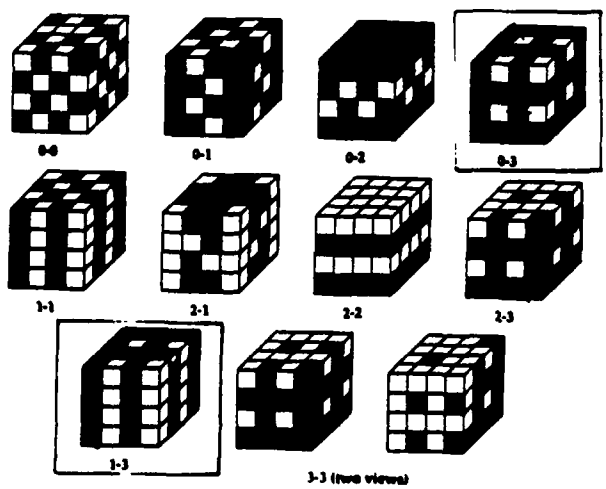

Fig. 2 Ten different connectivity patterns of a diphasic solid.

Many different ways of fabricating polymer/ceramic transducers using different modes of connectivity have been explored and are illustrated in fig. 3, and the sort of improvement in the simple hydrostatic figure of merit $d_h g_h$ which can be obtained is demonstrated in fig. 4, which compares a range of two phase composites to the best single phase materials.

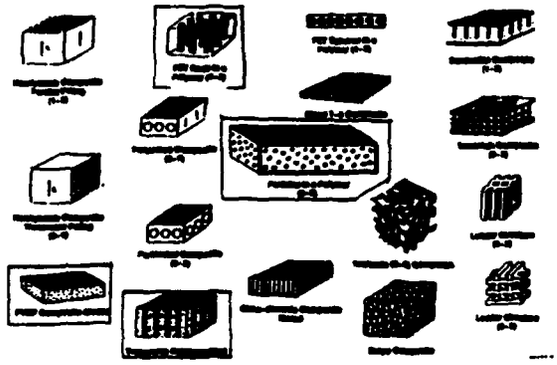

Fig. 3 Examples of several types of PZT polymer composites for piezoelectric applications.

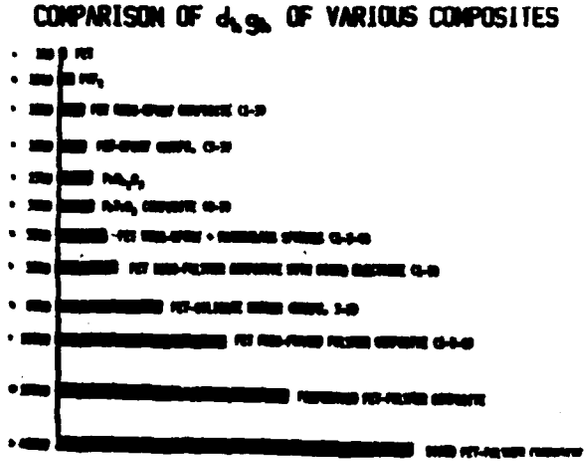

Fig. 4 Figure of merit $d_h g_h$ for hydrophone composites compared to single phase materials.

In electro-medical tomography it is often desirable to use the transducer both as a sender and as a sensitive sensor of ultrasonic waves. For this purpose, the 1:3 connectivity can be significantly advantageous. The problem has been discussed by Smith et al[4] who show that high values of k_t, the piezoelectric thickness coupling, are essential. In this case the 1:3 connectivity uncouples the normal transverse clamping of d_{31} with consequent significant improvement of k_t (fig. 5). It is surprising to note that significant reduction in the volume fraction of the active PZT phase in fact enhances the k_t and since at the same time this improves the impedance match to tissue and reduces the system Q, the composite has significant advantage.

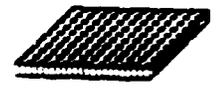

Fig. 5 a. 1:3 PZT polymer composite transducer.

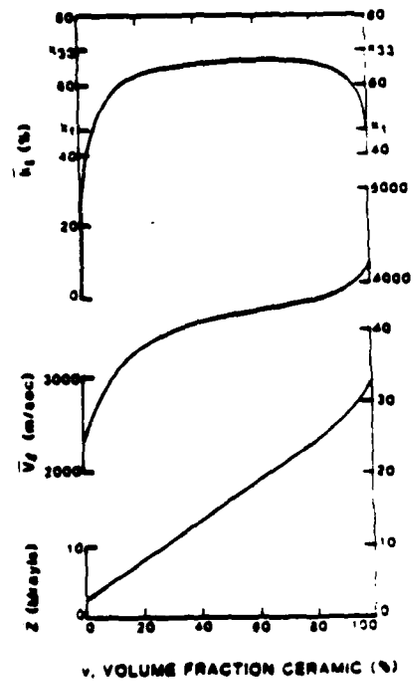

Fig. 5 b. Coupling coefficient k_t, acoustic velocity, and acoustic impedance as a function of volume fraction of the ceramic phase.

Obviously in the 1:3 configuration the composite is an array of individual elemental senders and receivers. If the activity of each sender/receiver could be controlled in a simple manner then the array could be used as a phased array with the possibility of beam forming and beam scanning which is inherent is such arrays. A step in this direction would be to make each element agile(switchable) under DC field control. In electrostrictive ceramics such as lead magnesium niobate ($PbMg_{1/3}Nb_{2/3}O_3$) summarized as PMN and in solid solutions with lead titanate ($PbTiO_3$) summarized PMN:PT, the deformation field curve is as in fig. 6.[5]

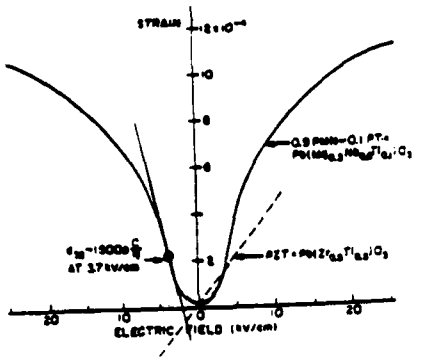

Fig. 6 Deformation x_3 vs electric field E_3 in PMN:PT relaxor ferroelectric ceramic showing induced piezoelectric d_{33} compared to a soft PZT.

Clearly, on this curve, the slope at any point ($\delta x_{33}/\delta E$) is just the piezoelectric constant d_{33}. Three features are of major interest.

(1) The maximum slope which occurs for fields near 3.8 kv/cm gives $d_{33} \backsim 1{,}500$, more than three times the value of a good soft PZT.

(2) At zero bias the slope is zero so that $d_{33} = 0$.

(3) By reversing the bias, the sign of d_{33} is changed and thus the phase of a transmitted or received signal is inverted.

Fig. 6 is a near-static curve taken at 1/10 Hz, but measurements have now been made over a wide field range and confirm that the high values of d_{33} persist to high frequency.(6) In these polarization biased electrostrictors it is expected that $d_{33} = 2\,Q_{11}\,P_3\,\varepsilon_{33}$ and this relation is in fact found to be in good agreement with the measured d_{33} values.

In the lead lanthinum zirconate titanate (PLZT) family it is possible to find unusual electrostrictive solids which can be switched electrically into a series of polar states which persist remnantly down to zero field. However, unlike simple ferroelectric ceramics these materials exhibit double loops and can be switched back to a zero polarization state.

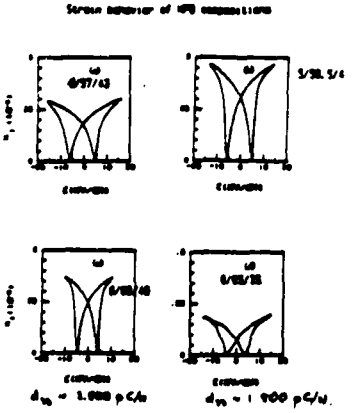

Fig. 7 Strain vs field curves for PLZT compositions close to the morphotropic phase boundary showing very high induced piezoelectric effects.

Examination of the strain/field curves (fig. 7) show exceedingly high slopes at zero field yielding d_{33} values up to 2,500. Switching times in these ceramics are short (~1-5 μ seconds) and the remnant state set up by a switchable pulse persists (fig. 8).(7) Studies are now under way to explore the high frequency behavior and the construction of arrays of elements with tunable d constants.

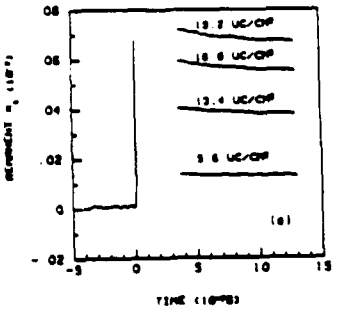

Fig. 8 a. Remnant polarization after pulse switching.

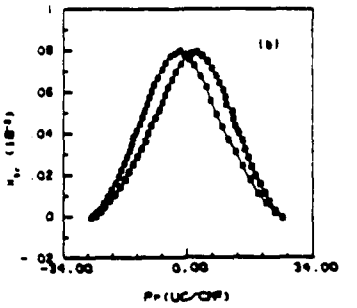

Fig. 8 b. Magnitude of remnant strain as a function of switched charge Pr.

3. ACTUATOR MATERIALS.

For conventional piezoelectric actuators which use compositions in the lead zirconate titanate (PZT) family it is possible to establish load lines (fig. 9) which exhibit the trade-off between displacement and force for any given driving field.

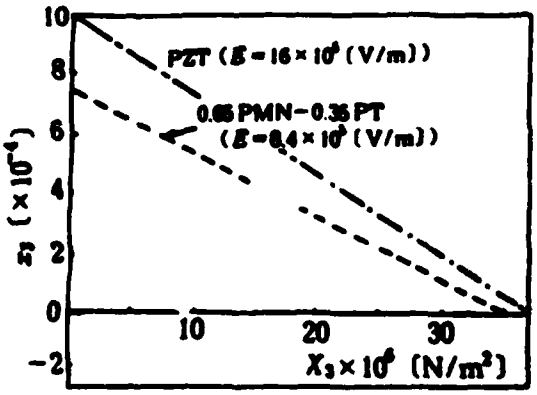

Fig. 9 Load lines for PZT and PMN:PT type piezoelectric actuators.

It is evident that the transducer can generate very large forces ~30 x 10^6 N/m^2, but only rather small displacements ~ 10 μm/cm for field levels of the order 20 kv/cm. To avoid high terminal voltages it is necessary to make the actuator very thin, i.e., E = V/d, so that to keep V tractable d must be made very small, and the actuator made up from a stack of electroded sheets (fig. 10).

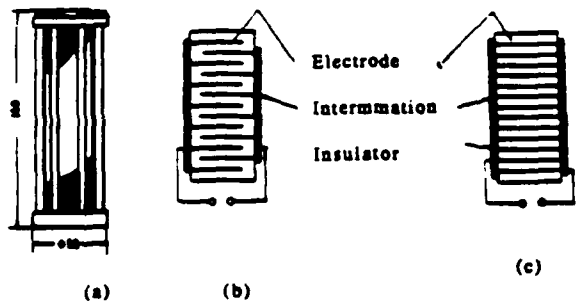

Fig. 10 a. Typical stacked single sheet actuator.
b. Capacitor type structure.
c. Actuator structure.

In some actuators the stack is assembled from individual sheets which must be lapped and polished and electroded before assembly. More recently the techniques used by the multilayer ceramic capacitor houses are being adapted to produce tape cast sheets of green ceramic which can be co-fired with integral electrode structures.

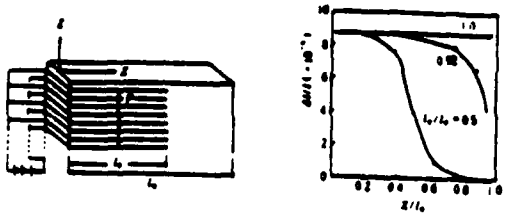

Fig. 11 Effect of dead space in capacitor type structure upon actuator performance.

Electrode pickup is more complex in these actuator structures than in the simple MLC (fig.11) as the dead space which can be used in the capacitor leads to large unwanted shear stress concentrations and consequent failure. For the stacked actuator a number of different methods have been used to provide strain amplification. A simple lever system used by Nippon Electric Company in their dot matrix printer is delineated in fig. 12.

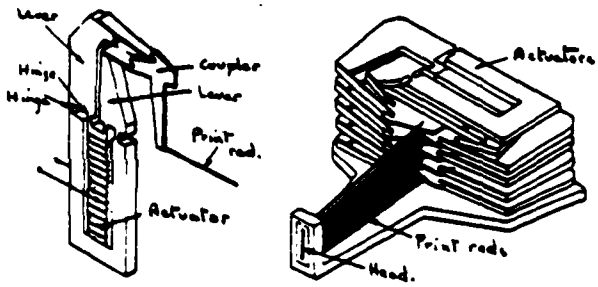

Fig. 12 Strain amplifier used in the NEC actuator for a dot matrix printer.

For the simple piezoelectric or electrostrictive actuator strain levels are limited to order 10^{-3}. If, however, one looks at the spontaneous strains which occur at the phase change into the ferroelectric state, i.e., strains induced by P_s, the spontaneous polarization, they reach up to more than 10% in some systems. It may be argued from simple fracture mechanics that strains of order 0.1% would be the upper limit for brittle solids like the ceramic actuators, however, it must be remembered that unlike the normal fracture mechanics situation, the electro-elastic strains are generated at ZERO STRESS by internal body forces. Thus if the polarization change can be engineered to be continuous and homogeneous there is no intrinsic reason that larger strains should not be engendered.

Polarization change mechanisms which could be used in ferroelectric crystals and ceramics to control electrostrictive strain are delineated in Table 1 in increasing order of the polarization change, and thus of the induced strain.

POLARIZATION CHANGE MECHANISMS USED TO CONTROL ELECTROSTRICTIVE STRAIN.

INDUCED POLARIZATION INCREASING →

(a) **Homogeneous polarization of a Perselectric Phase**

$E = 0 \quad \bar{P} = 0 \quad \sqrt{\overline{P^2}} = 0 \quad P \propto E.$
Stable zero strain state.

• (b) **Induced polarization in a Relaxor ferroelectric**

$E = 0 \quad \bar{P} = 0 \quad \sqrt{\overline{P^2}} \neq 0 \quad P \propto E$
Stable zero strain state.

• (c) **Induced Polarization change in Poled Ceramic**

$E = 0 \quad \bar{P} = P_R \quad \sqrt{\overline{P^2}}_{ind} = 0 \quad P_{ind} \propto E.$
Unstable zero strain state (Aging change of P_R).

(d) **Micro ⇒ Macrodomain Poled Relaxor**

$E = 0 \quad \bar{P} = 0 \quad \sqrt{\overline{P^2}} \neq 0$ **P vs E Hysteretic**
Stable zero strain state

(e) **Field forced Phase Change**

$E = 0 \quad \bar{P} = 0 \quad \sqrt{\overline{P^2}} = 0$ **P vs E Double Hysteretic**
Stable or unstable depending on system

(f) **Field Forced Domain Change**

$E = 0 \quad \bar{P} = 0 \quad \sqrt{\overline{P^2}} \neq 0$ **P vs E Hysteretic**
Unstable zero strain state

Table 1 Polarization change mechanisms which can be used to control electrostrictive strain.

The type B which uses the induced polarization change in a relaxor ferroelectric like PMN:PT is now widely used in optical systems such as surface deformable mirrors[8] where the stable zero field dimensions and very low thermal expansion are critical and make up for the complexity of a non-linear strain vs field relation. The conventional poled piezoceramic (type C) is certainly the most widely used in actuators, with many companies using proprietary soft PZT compositions or PMN:PT with enough lead titanate to induce the ferroelectric phase. The disadvantage for such materials is that slow aging associated with internal re-arrangement of the poled domain structure leads to a continuous drift of dimensions so that servo-control is essential if these actuators are to be used in precise position control.

Recent studies[9,10] have focused upon micro to macro domain polarization change in PLZT compositions, and upon antiferroelectric to ferroelectric phase change in lead zirconate titanate stannate (PLSnZT) compositions.

comp.	T_m(°C)	K_m	K_{25}	E_m (Oersted)	P_r (coul/cm^2)	x_l (10^{-3})	x_t (10^{-3})	$^{\%}w_{x_l}$
8/67/35	99	12000	5500	3.6	31	81	2.5	1
9/65/35 *	105	11500	4600	3.6	30	82	2.1	32
9/63/37	114	11300	4500	4.7	31	76	1.9	32
7/65/35	140	15000	3000	4.5	28.4	1	3.1	7
7/62.5/37.5*	169	16000	2900	5	27.2	1.2	3.7	66
7/60/40	172	17000	3000	6.3	26.2	1.2	3.8	4
7/58/42	189	17500	2800	8	22	1.1	3.5	39
7/56/44	199	17200	2200	10	22	94	2.3	4
6/63/38	196	19000	2100	5	31	1.45	4.1	58
6/60/40 *	206	18000	2000	5.6	29.5	1.35	4.7	57
6/58/42				7.45	29	1.33	3.9	53
5/60/40	230	19000	1600	6.52	32	79	4.2	53
5/58.5/41.5*				6.41	36	1.24	4.5	29
5/56/44				8.5	32.1	1.6	5.6	56
4/57/43 *				7.47	35.2	1.26	3.0	4
4/55/45				10	29.5	1.21	2.9	55

* MPB compositions — T_m: Temp. of dielectric maximum
x_t: Transverse strain induced at 1 kV/mm — E_m: Maximum dielectric constant
x_l: Longitudinal strain induced at 1 kV/mm — K_{25}: Dielectric constant at 25°C
$^{\%}w_{x_l}$: Temporary remanent strain

Table 2 Maximum longitudinal x_l and transverse x_t strains for a family of PLZT ceramics with compositions close to the MPB.

In table 2, maximum strain realizable for a range of PLZT compositions are given. For these compositions the strain is polarization controlled so that charge control rather than field control must be used. The actuator however has the advantage that the strain state can be set by a very short current pulse which will bring the actuator to a precise position where it will remain in a remnant state until updated by another positive or negative current pulse. For large systems then, a whole bank of actuators could be serviced by one power supply in a "dial-a-displacement" mode.

For antiferroelectric to ferroelectric switching, the major advantage is that the induced strain is primarily a volume strain which is far less disruptive than the predominantly shear strains of the straight electrostriction. Compositions which have been examined in the modified PZSnT family are documented in table 3,

No	Composition
4	$Pb_{.97}La_{.02}(Zr_{.68}Ti_{.05}Sn_{.25})O_3$
5	$Pb_{.97}La_{.02}(Zr_{.53}Ti_{.12}Sn_{.35})O_3$
6	$Pb_{.97}La_{.02}(Zr_{.68}Ti_{.11}Sn_{.23})O_3$
7	$Pb_{.97}La_{.02}(Zr_{.68}Ti_{.105}Sn_{.235})O_3$
8	$Pb_{.97}La_{.02}(Zr_{.64}Ti_{.09}Sn_{.27})O_3$
9	$Pb_{.97}La_{.02}(Zr_{.64}Ti_{.11}Sn_{.25})O_3$
10	$Pb_{.97}La_{.02}(Zr_{.62}Ti_{.11}Sn_{.27})O_3$

11	$Pb_{.97}La_{.02}(Zr_{.88}Ti_{.09}Sn_{.29})O_3$
12	$Pb_{.97}La_{.02}(Zr_{.80}Ti_{.1}Sn_{.2})O_3$
13	$Pb_{.97}La_{.02}(Zr_{.575}Ti_{.1125}Sn_{.3125})O_3$
14	$Pb_{.97}La_{.02}(Zr_{.55}Ti_{.1}Sn_{.35})O_3$

Table 3 Compositions in the PSnZT family examined for antiferroelectric to ferroelectric switching.

their induced polarization changes are sketched in fig. 13 and the associated strain in one composition is shown in fig. 14. Strain levels up to 0.8% can be achieved in the antiferroelectric:ferroelectric switching but the electric fields required are high.

NO	D (g/cm)	$\Delta E/E_c$	P (uc/cm²)	Ec (kv/cm)	Eapp (kv/cm)	x1
4	8	.35	43	50	75	.55%
5	8	.8	30	30	35	.18%
6	8	1.1	40	21	46	.87%
7	7.7	1.2	36	22	58	.52%
8	7.7	.4	30.5	52	68	.37%
9	7.7	1.16	36	27	60	.59%
10	7.7	1.16	36	19	60	.6%
11	7.7	.9	33	38	70	.45%
12	7.4	.33	31.6	49	59	.51%
13	7.4	.5	28	30	43	.45%
14	7.2	.28	30	44	56	.52%

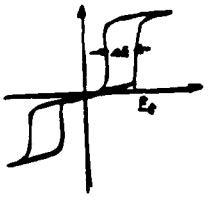

Table 4 Strain levels and switching fields for the compositions in the PSnZT system given in Table 3.

For actuator applications these compositions will be of most interest in pumping and in injection applications such as ink jet printing, diesel engine control, fuel injection, etc., and for actuating hydraulic control systems and hydraulic amplifiers.

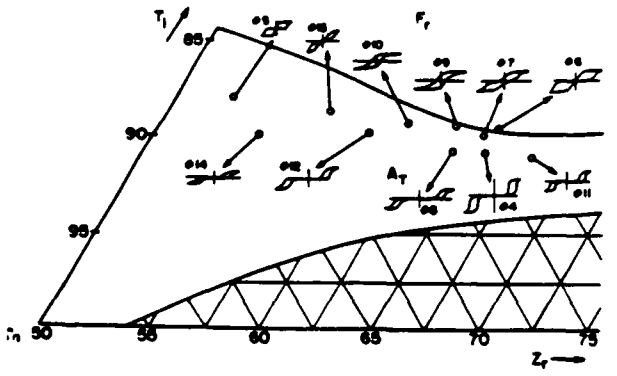

Fig. 13 Schematic of the types of hysteresic behavior observed for the compositions delineated in Table 3 and their approximate location on the phase diagram.

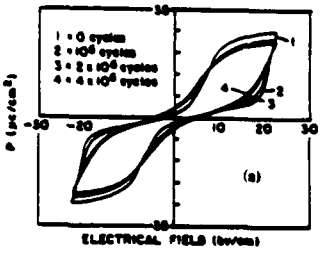

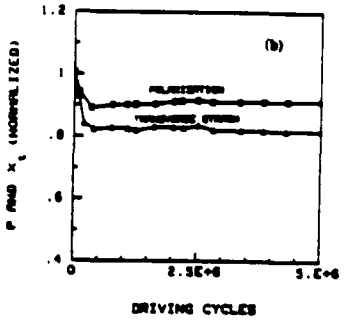

Fig. 14 Dielectric hysteresis and normalized transverse strain as a function of the number of switching crystals in a PSnZt composition.

4. SMART MATERIALS

In this paper, the term smart material is used to delineate a material or composite in which the response function of the material can be controlled either in response to the environment or by some externally applied signal. On this definition, it is clear that the PMN:PT relaxor ferroelectric described in section 2 is smart in the sense that its piezoelectric response either for sensing or for sending ultrasonic pulses can be controlled by an externally applied

bias field, with the response being field tuneable both as to phase and amplitude.

More generally, the type of material envisaged is a composite which encompasses a sensing element, a compact solid state electronics package, and a responder element. Thus, the material itself is really an adaptive control system in which the "smart function" is primarily the responsibility of the electronic package which controls the response to signals incident upon the sensor. A particular example which has been the subject of research in our laboratory is a piezoelectric sensor/piezoelectric actuator combination (fig. 15) interconnected by a small (millwatt) linear amplifier.

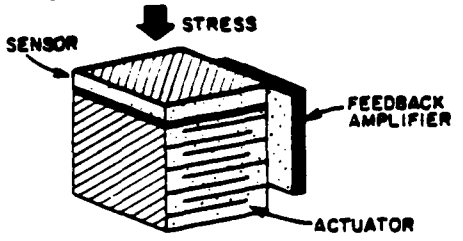

Fig. 15 Schematic diagram of the sensor/actuator combination for an elastic compliance control composite.

The objective of the exercise is to develop a combination of stiff pressure insensitive materials which could mimic a highly compliant rubber for very small AC stress, i.e., a system with very large compliance S_{33}.

Conceptually, the combination is particularly simple, but effectively illustrates the more general principle. For a small AC stress, the piezo-sensor detects an AC voltage which is amplified and applied to the actuator in such a sense that when the stress is increasing the actuator is shrinking its three-axis dimension. For a suitable gain then, a small positive stress gives rise to a large positive strain, thus mimicking a highly compliant solid.

To test the concept, two identical sensor/actuator combinations were fabricated and mounted in a rigid jig (fig 16).

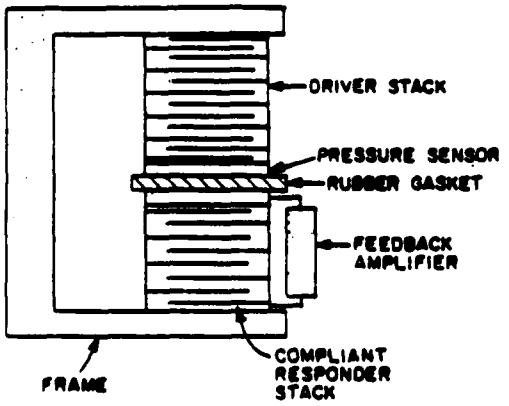

Fig. 16 Test structure for the elastic compliance control composite.

The coupling between the two being via a soft rubber gasket. The upper actuator is driven by an AC signal to produce a reciprocating stress wave. The upper sensor determines the stress level whilst the lower combination provides compliance control. With the amplifier switched off, the stress level monitored by the upper sensor is set by the soft rubber which is the most compliant element in the system. However, when the lower amplifier is turned up the sensor reading drops at maximum gain by a factor of more than five, indicating that the compliant stack is now more than five times softer than the rubber (fig. 17).

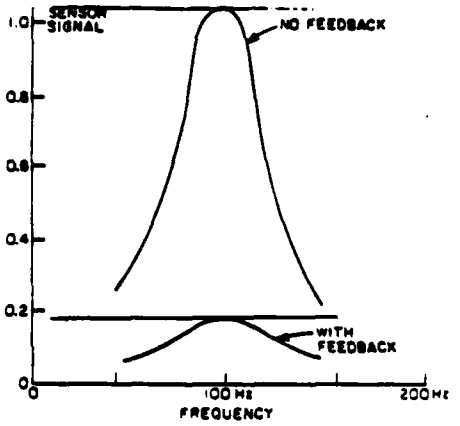

Fig. 17 Stress levels recorded in the pressure sensor of fig. 16 with and without feedback.

The tuned source could be moved over the range from 10 Hz to 150 Hz which was the passband of the feedback amplifier without changing the effective enhanced compliance.

Preliminary tests show that the high compliance is maintained over the frequency range from 10 Hz to 150 Hz, limited by the pass band of the amplifier used. Clearly since the sensor is a piezoelectric ceramic, it does not respond to DC pressure, and the stack behaves as a normal rigid ceramic under DC loading.

From this simple experiment it is natural to speculate as to the possibility of more refined compliance control, for example in fig. 18, the possibility of using a non-linear amplifier to give non-linear elastic response (fig. 18b) or a tuned amplifier to give high compliance at a single frequency(fig. 18c) or a phase shifting amplifier to raise the imaginary part of the compliance (fig. 18d).

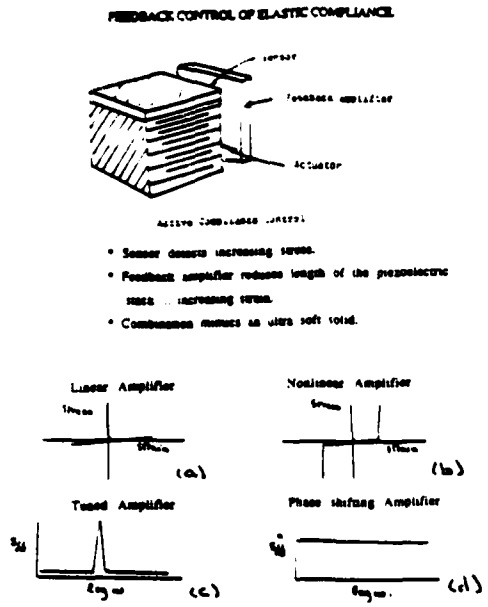

Fig. 18 a. Elastic response for a linear feedback amplifier.
b. Response for a non-linear limiting amplifier.
c. Response for a tuned amplifier.
d. Response for a phase shifting amplifier.

The target for these initial studies was the problem of providing high compliance under deep submergence conditions for Navy systems, however, possibilities for control of vibration transmission from heavy rotating machinery and from other active sources will certainly be interesting.

Perhaps, however, the most important feature is the demonstration of what could be a much wider application to other smart systems using different combinations of sensor and responder components.

5. CONCLUSIONS.

In this paper an attempt is made to summarize the status of development of composite materials for piezoelectric sensors and to point up new possible agile systems which can be developed using bias field control of the piezoelectric response in relaxor ferroelectric compositions in the PMN:PT and in the PLZT family materials. For actuator applications, conventional electrostrictive and piezoelectric multilayer actuators are discussed and the advantages and limitations of each family delineated. Work upon new high strain material systems which use control of field induced phase transitions to provide much larger switchable strains are briefly described. A logical extension of the composite work is the evolution of families of "smart" materials which incorporate sensor and responder functions together with solid state interconnect electronics into the material. To illustrate the principle a simple piezosensor/piezoactuator system for active elastic compliance control is briefly discussed. With this combination it is possible to mimic the AC performance of a very soft rubber whilst maintaining the load bearing capability of a stiff ceramic.

References:

1. R.E. Newnham, D.P. Skinner, L.E. Cross. Connectivity and Piezoelectric-Pyroelectric Composites. Mat. Res. Bull., 13, 525, 1978.

2. D.P. Skinner, R.E. Newnham, L.E. Cross. Flexible Composite Transducers. Mat. Res. Bull., 13, 599, 1978.

3. R.E. Newnham. Composite Electroceramics. Annual Rev. Mat. Sci., 16, 47, 1986.

4. W.A. Smith, A.A. Shaulov, M.E. Rosar, B.M. Singer. Composite Piezoelectrics for Ultrasonic Transducers. Proc. 6th IEEE Symp. on Appl. of Ferroelectrics, Lehigh Univ., 8-11 June 1986, p. 231, p. 249.

5. L.E. Cross, Relaxor Ferroelectrics--Polarization and Strain Behavior. Solid State Studies in Ceramics, 27, 31, 1987.

6. W.Y. Pan, W.Y. Gu, D.J. Taylor, L.E. Cross. Large Piezoelectric Effect Induced by Direct Current Bias in PMN:PT Relaxor Ferroelectric Ceramics. Jap. J. of Appl. Phys., 28, 4, 653, 1989.

7. W.Y. Pan, Q.M. Zhang, Q.Y. Jiang, L.E. Cross. Electric Field Induced Strain in $(PbLa)(TiZr)O_3$ Ferroelectric Ceramics Near the Tetragonal-Rhombohedral Morphotropic Phase Boundary. Ferroelectrics, 88, 1, 1988.

8. Mark Ealy, C Wheeler. A Standardized Electrodisplacive Transducer. S.P.I.E. Symp. on Aerosp. Sensing, Orlando, FL, March 1989.

9. W.Y. Pan, L.E. Cross. Piezoelectric and Electrostrictive Materials for Transducer Applications. Annual Report ONR Contract N00014-82-K0339, Appendix 10.

10. W.Y. Pan, L.E. Cross. Antiferroelectric to Ferroelectric Switching in Lead Zirconate Titanate Stannate Ceramics. Proc. of 6th IEEE Symp. on Appl.s of Ferroelectrics, Lehigh Univ., 8-11 June 1986, p. 648.

APPENDIX 3

Ferroelectrics, 1990, Vol. 102, pp. (000–000)
Reprints available directly from the publisher
Photocopying permitted by license only

SMART CERAMICS

R. E. NEWNHAM, Q. C. XU, S. KUMAR and L. E. CROSS
Materials Research Laboratory, The Pennsylvania State University, University Park, PA 16802

(Received January 15, 1989)

Recent progress in the integration and miniaturization of electroceramic conponents has led to the development of multipurpose electronic packages containing complex three-dimensional circuitry. At the same time, a wide variety of sensors, transducers, and actuators have been fabricated for automotive, military, and consumer electronics applications. By bringing together the ceramic sensors and ceramic actuators in multilayer packages, a new generation of smart ceramics can be developed.

INTRODUCTION

Webster's dictionary gives several definitions for the word SMART, including "to feel mental distress or irritation", "alert, clever, capable", and "stylish". All three meanings are appropriate to the currently fashionable subject, "Smart Materials". It causes one mental distress to think a ceramic can in any way be smart but with the help of a feedback system it is possible.

The Piezoelectric Pachinko machine illustrates the principle of a smart material. Pachinko Parlors with hundreds of vertical pinball machines are very popular in Japan. The Piezoelectric Pachinko game constructed by engineers at NipponDenso is made from PZT multilayer stacks which act as both sensors and actuators. When a ball falls on the stack the force of impact generates a piezoelectric voltage. Acting through a feedback system, the voltage pulse triggers a response from the actuator stack. The stack expands rapidly throwing the ball out of the hole, and the ball moves up a spiral ramp during a sequence of such events. Eventually it falls into a hole and begins the spiral climb all over again.

The video tape head positioner operates on a similar principle. A bilaminate bender made from tape-cast PZT ceramic has a segmented electrode pattern dividing the sensing and actuating functions of the positioner. The voltage across the sensing electrode is processed through the feedback system resulting in a voltage across the positioning electrodes. This causes the cantilevered bimorph to bend, following the video tape track path. Articulated sensing and positioning electrodes near the tape head help keep the head perpendicular to the track. The automatic scan tracking system operates at 450 Hz.

These two examples illustrate how a smart ceramic operates. A *smart material senses a change in the environment, and using a feedback system, makes a useful response. It is both a sensor and an actuator.*

The definition can be extended to even more clever materials. A *very smart material senses a change in the enviroment and responds by changing one or more of its property coefficients. Such a material can "tune" its sensor and actuator functions in time and space to optimize behavior.* The distinction between smart and

very smart materials is essentially one between linear and nonlinear properties. The physical properties of nonlinear materials can be adjusted by bias fields or forces to control response.

The difference between a smart and a very smart material can be illustrated with piezoelectric and electrostrictive ceramics. A plot of strain as a function of electric field for lead zirconate titanate (PZT) and lead magnesium niobate (PMN) ceramics is shown in (Figure 1). PZT is a piezoelectric ceramic in which ferroelectric domains are aligned in a poling field. Strain is linearly proportional to electric field in a piezoelectric material which means that the piezoelectric coefficient is a constant and cannot be electrically tuned with a bias field.

PMN is not piezoelectric at room temperature because its Curie temperature lies near 0°C. Because of the proximity of the ferroelectric phase transformation, however, PMN ceramics exhibit very large electrostrictive effects. As a result a large nonlinear relationship between strain and electric field is observed (Figure 1). Electromechanical strains comparable to PZT can be obtained with electrostrictive ceramics like PMN, and without the troubling hysteretic behavior shown by ferroelectric PZT. The nonlinear relation between strain and electric field can be used to tune the piezoelectric coefficient. The piezoelectric d_{33} coefficient is the slope of strain—electric field curve. Its value for PMN is zero at zero field and increases to a maximum value of 1500 pC/N (about three times larger than PZT) under a bias field of 3.7 kv/cm (Figure 1).

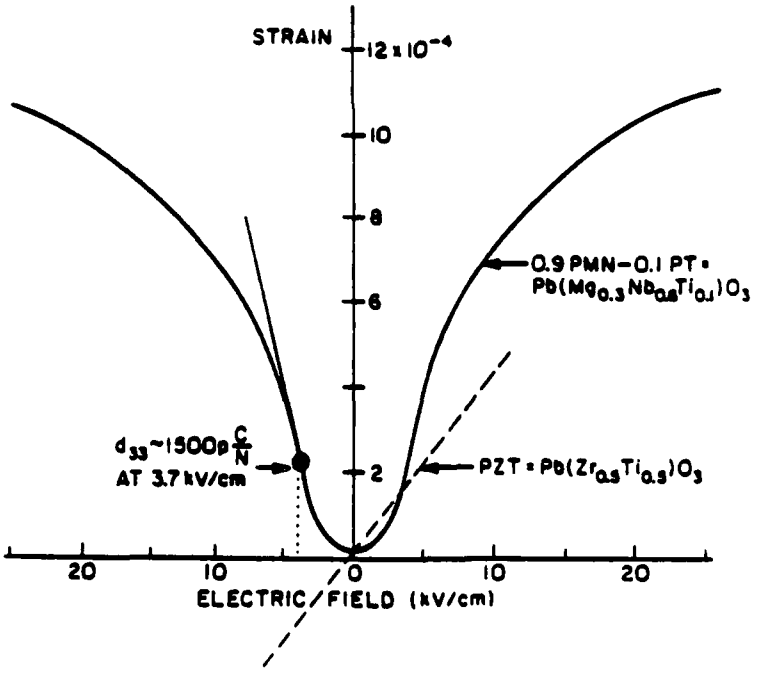

FIGURE 1 Electromechanical coupling in electrostrictive (PMN-PT) and piezoelectric (PZT) ceramics.

There is another type of very smart material which makes use of a phase change. Transducers made from certain compositions in $PbZrO_3$-$PbTiO_3$-$PbSnO_3$ ternary system display electrically induced transformations from an antiferroelectric phase to a ferroelectric phase.

The ferroelectric phase is favored under high electric fields because of its large spontaneous polarization. The phase change is accompanied by strain changes of 10^{-3} which are very large for a ceramic. Dielectric and mechanical hysteresis loops are shown in Figure 2. Bistable behavior can be achieved by working with phase change materials.

Eventually, of course, we would like to include a feedback system within a smart ceramic, but there seems to be no simple way to do this at present. The integrated ceramic circuitry being developed in the Penn State Dielectric Center may provide a method of doing this in the future. Another approach is to deposit ceramic films on silicon chips. Limited success has been achieved with lead titanate and lead zirconate-titanate films on silicon for long-term ferroelectric random access memories (FRAM). By utilizing these ferroelectric films as sensors and actuators, a

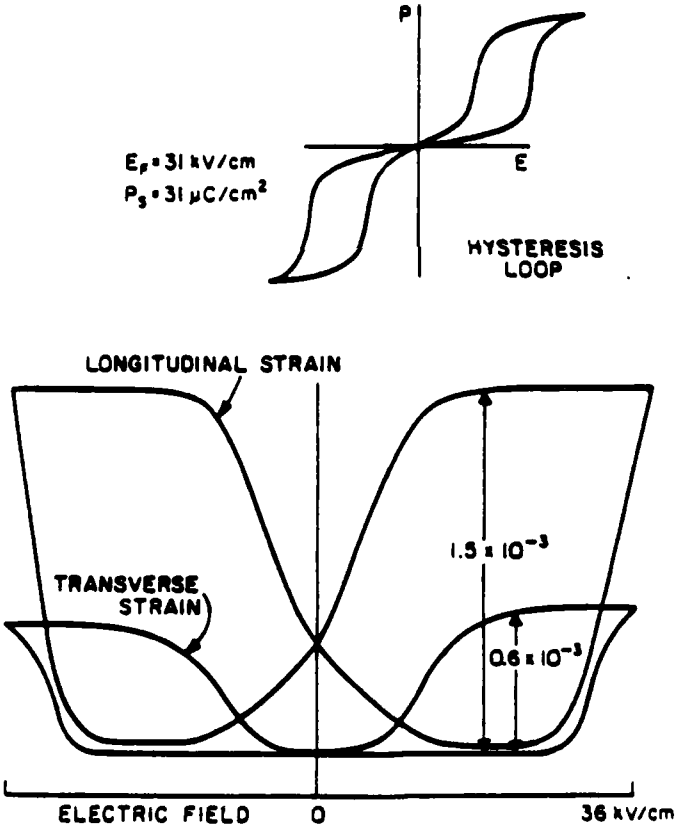

FIGURE 2 Electrical and electromechanical hysteresis in $(Pb_{0.97}La_{0.03})(Zr_{0.95}Ti_{0.12}Sn_{0.35})O_3$ ceramics with antiferroelectric-ferroelectric phase change.

family of extremely intelligent materials could be obtained in which the feedback electronics could be fully integrated in the material. The time is not far off for such intelligent composites.

Ceramic Sensors and Actuators

More than thirty electroceramic sensors are used in recent automobile models. The 1987 Nissan Cedric has PZT piezoelectric knock sensors, barium titanate raindrop sensors, NTC thermistors for sensing the temperature of cooling water and exhaust gas, zirconia air/fuel oxygen sensors, zinc oxide blower motor varistors, aluminum phosphate dew point sensors, and more than twenty other ceramics with an electrical function. As shown in Table I, these sensors involve several different physical principles. Many of these are part of smart systems but have yet to be utilized as smart or very smart materials because they have not been used as actuators or responders.

When considering actuators, the piezoelectric devices listed in Table II come to mind. Under electric excitation the piezoelectric material changes shape, causing the adjacent material to move, whether it be solid, liquid or gas.

This is the physical principle of speakers, ink jets, and micropositioners. But the word actuator can be used in a more general sense to include other types of response such as display, signal transmission, magnetic or electric field modification, and

TABLE I

Ceramic Sensors

Sensor Type	Chemical Composition	Active Property
Oxygen	$Zr_{1-x}Ca_xO_{2-x}$	Bulk Ionic Conductivity
Humidity	$MgCr_2O_4$-TiO_2	Surface Ionic Conductivity
Acidity	IrO_{2-x}	Surface Chemical Reaction
Pressure	$Pb\,Zr_{1-x}Ti_xO_3$	Piezoelectricity
Temperature	$Pb\,Zr_{1-x}Ti_xO_3$	Pyroelectricity
Voltage	ZnO-Bi_2O_3	Grain Boundary Tunneling
PTC Thermistor	$Ba_{1-x}Ce_xTiO_3$	Grain Boundary Transition
NTC Thermistor	$Fe_{2-x}Ti_xO_3$	Bulk Electronic Conductivity
CT Thermistor	VO_2	Electronic Phase Transformation
Chemical	ZnO-CuO	Surface Electronic Conductivity
Optical	CdS	Photoresistance

TABLE II

Actuator Applications

Tracking Optical and Magnetic Heads
Drivers for Relays and Switches
Wire-Dot Printers and Via Punches
Fuel Injection Valves
Adaptive Optic Systems
Micropositioners for Robots and Machine Tools
Cone Vibrators for Speakers
Fans and Conical Air Movers
Ink Jet Printers

thermal control. Hundreds of possible sensor-actuator combinations are possible when a matrix of electrical, mechanical, magnetic, optical and thermal phenomena is considered. In the following section we describe a few possible applications of smart materials to underseas systems. Electromechanical actuators for compliant walls or ink jet configurations capable of injecting polymers, microbubbles or pressure bursts appear to be of special interest for reducing turbulence in the boundary layer.

Controlled Compliance Experiments

Smart materials capable of responding to pressure or temperature changes are expected to have several interesting industrial and military applications. A "smart skin" which can reduce flow noise and streamline the flow of moving liquids is of special interest in chemical engineering and oceanographic applications. Such a skin might consist of a piezoelectric sensor together with an electronic feedback system and an electrostrictive or a piezoelectric actuator designed to counteract turbulence (Figure 3).

In a demonstration experiment we have shown that for external pressure fluctuations, the smart material can become more compliant than the medium in which the pressure variations take place. This has the direct consequence of reducing acoustic reflection from the surface of the smart material.

In our test experiment (Figure 4), one actuator is used as a driver (noise source), and the other as the responder. PZT disks are used as the actuator elements. Sandwiched between the two actuators are two sensors and a layer of rubber. The upper actuator is driven at a frequency of 100 Hz and the vibrations are monitored with the upper sensor. The pressure wave emanating from the driver passes through the upper sensor and the rubber separator and impinges on the lower sensor. The resulting signal is amplified using a low noise amplifier and fed back through a phase shifter to the lower actuator to control the compliance.

A smart sensor-actuator system can mimic a very stiff solid or a very compliant rubber. This can be done while retaining great strength under static loading, making the smart material especially attractive for underseas applications.

To illustrate compliance control, consider the case of a positive pressure pulse incident on the lower sensor of the test experiment (Figure 4). The sudden increase

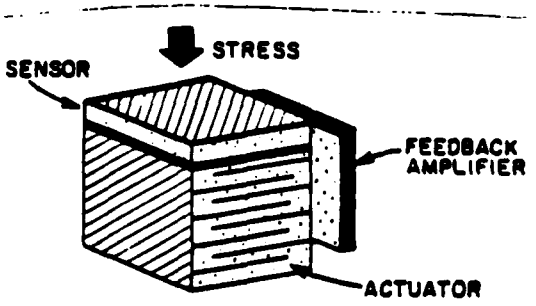

FIGURE 3 Smart piezoceramic material for supporting smart skin.

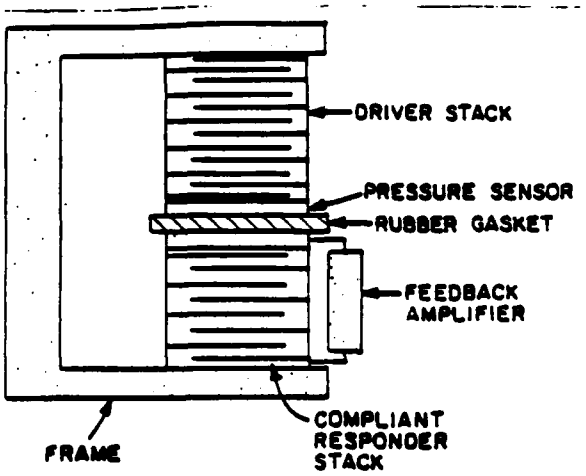

FIGURE 4 Test experiment for evaluating smart materials with controlled compliance.

in pressure results in a voltage pulse being fed to the amplifier and lower actuator. If the phase of the feedback is such that the actuator expands in length then the sensors will be further compressed, leading to amplified oscillations. Under these conditions the responding actuator is acting like a very stiff material since its motion prevents compression by the positive pressure pulse.

On the other hand, if the phase of the feedback voltage is adjusted to cause the responder to contract in length rather than expand, then the smart material mimics a very soft, compliant substance. This reduces the force on the sensors and partially eliminates the reflected signal. The reduction in output signal of the upper sensor is a measure of the effectiveness of the feedback system. As shown in Figure 5, we can reduce the compliance of our actuator-sensor material by a factor of six compared to rubber.

Smart Composite-Composites

No single piezoelectric material possesses the optimum properties for send-receive transducers, and the statement is probably true for sensor-actuator devices as well. Putting together the best sensor with the best responder makes a lot of sense. During the past year we have been experimenting with the send-receive transducer shown in Figure 6. It is a four-layer device consisting of a polyvinylidene fluoride piezopolymer, a 3-3 fried PZT-polymer composite, a poled PZT ceramic, and a 0-3 tungsten-polymer backing layer. In connectivity notation the transducer can be described as 2-2(3-3)-2-2(0-3). Metal electrodes are inserted between all four layers to give control over the three piezoelectric layers.

There are several interesting properties of this transducer. The acoustic impedances are graded from the stiff PZT ceramic to the PZT composite to the compliant PVDF polymer. This eliminates much of the reflection loss in transmitting ultrasound from PZT to water. A second possible advantage is in interrogating the

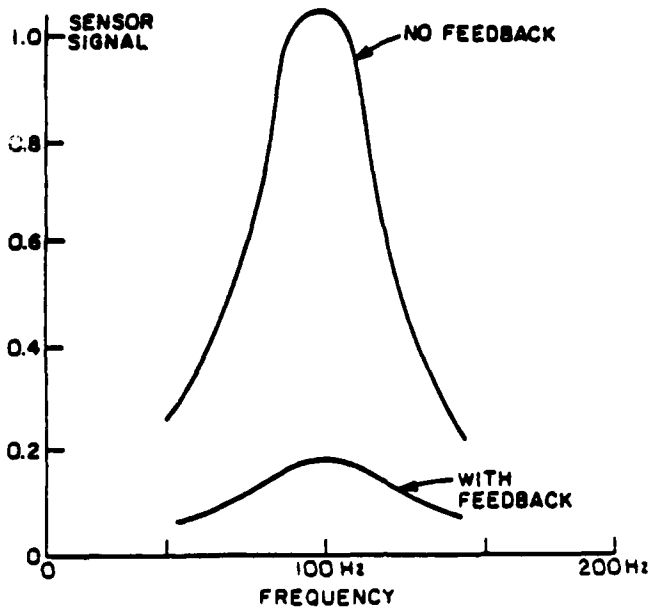

FIGURE 5 Reduced subsonic reflectance from smart piezoceramic experiment in Figure 4.

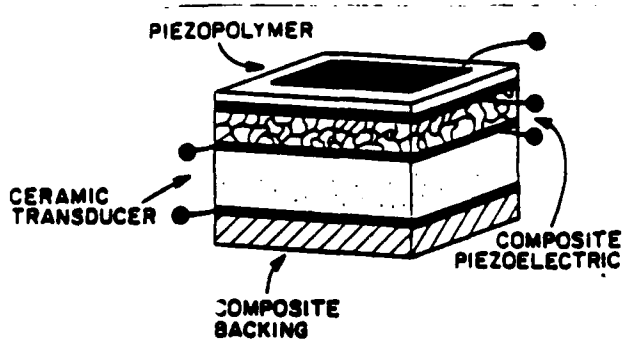

FIGURE 6 Composite-composite transducer for send-receive sonar transmission.

outgoing signal and comparing it to the return signal. With the PZT as transmitter and the composite and polyvinylidene fluoride layers as sensors, the outgoing beam can be sampled as it leaves the ceramic. Since no two transmissions are identical, it is important to monitor the outgoing signal in order to calibrate the intensity and frequency spectrum of the return signal.

Based on the physical properties of the constituent materials, the equivalent circuit of the trilaminate composite transducer has been established. The frequency response of transmitting, receiving and voltage transition gain for different layers and their hybrid connection have been computed and compared with the experimental results. The frequency response of the composite transducer is considerably

improved by changing the connecting modes between the layers. Experimental results show that different layers make different contributions to the frequency dependence of the sensitivity. The transducer impedance, sensitivity and bandwidth can be adjusted according to the application.

CONCLUSION

During the next decade, we can expect to see a large number of smart ceramic devices combining ceramic sensors and actuators in multicomponent multifunction packages. Through feedback systems, these devices will be capable of responding to changes in the environment by means of linear and nonlinear actuators.

APPENDIX 4

A sensitive double beam laser interferometer for studying high-frequency piezoelectric and electrostrictive strains

W. Y. Pan and L. E. Cross

Materials Research Laboratory, The Pennsylvania State University, University Park, Pennsylvania 16802

(Received 14 February 1989; accepted for publication 17 April 1989)

A double beam laser interferometer is built up to study high-frequency piezoelectric and electrostrictive strains. The system is capable of resolving a displacement of 10^{-2} Å using lock-in detection and measuring the strain all the way to the piezoelectric resonance frequencies using a digital oscilloscope for detection. The interference of sample bending to the detected signal is effectively avoided.

INTRODUCTION

The study of piezoelectric and electrostrictive properties of materials involves the measurement of strain induced by the external driving forces. There are several methods which are used to measure the strains precisely. Among these methods, the laser interferometer technique is the most sensitive.[1-4] More recently, a laser interferometer was built in this laboratory which is capable of resolving an ac electric field induced displacement of the order of 10^{-3} Å.[5] However, there are still two drawbacks with this system. First, the driving frequency of the electric field is limited to about 1 kHz, above which the "back motion" significantly reduces the detected displacement. In this technique, only one of the two sample major surfaces is facing the probing laser beam, while the other is bonded to a sample holder. Under the ac driving electric field, the sample deforms repeatedly due to the piezoelectric and electrostrictive effects. As a result, the center of mass of the sample oscillates along the direction of the beam. Under high driving frequencies, the force needed to support the sample is so large that the bonding material is not rigid enough to prevent the sample from moving against the bonding material. If this occurs, the displacement detected is less than the total displacement. Using a more rigid bonding material is not a good solution because it tends to produce clamping in the transverse direction. The second drawback is that a bending effect may occur if the sample is not properly bonded, causing the detected displacement that is significantly larger than the displacement due to the deformation of the sample. Thus, a further improvement to overcome these drawbacks is necessary.

The basic principle of the laser interferometer is that, for a monochromatic light of wavelength λ interfering with a reference beam, the interference light intensity at a detection point is

$$I = I_p + I_r + 2\sqrt{I_p I_r}\cos(4\pi\Delta d/\lambda), \quad (1)$$

where I_p is the light intensity for the probing beam, where the sample is placed, and I_r is the light intensity for the reference beam, respectively, and Δd is the optical path-length difference between the two beams. For convenience, Eq. (1) can be rewritten as

$$I = 1/2(I_{max} + I_{min}) + 1/2(I_{max} - I_{min})\cos(4\pi\Delta d/\lambda), \quad (2)$$

where I_{max} and I_{min} are the maximum and minimum interference intensities which can be measured from the instrument conveniently.

The interferometer discussed below adopts the ac signal detection technique used in the earlier work.[5] The change [illegible] that the motions of the two sample surfaces are detected simultaneously. The system is capable of measuring an ac displacement of the order of 10^{-2} Å by lock-in detection. When the displacement is greater than 1 Å, it can be detected using a high bandwidth oscilloscope, the strain can be properly measured all the way to the piezoelectric resonance frequencies. The interference of the sample bending effect to the detected signal is effectively avoided.

I. DOUBLE BEAM AC STRAIN MEASURING SYSTEM

A. Optical system

The schematic drawing of the double beam laser interferometer as well as the electronic system is shown in Fig. 1. The incident laser beam is split into two beams by PBS1 (PBS: polarized beam splitter). The beam polarized vertically is reflected to the reference arm and that polarized horizontally is transmitted into the probing arm. The laser used here is a polarized laser with a rotatable plane of polarization (Spectra-Physics Stabilite™, Model 124 A Helium-Neon laser). Since the light intensity loss in the probing arm is much greater than that in the reference arm, the plane of the polarization of the laser is rotated to increase the intensity of the beam entering into the probing arm until the two beams are equally intense at the detection plane. The visibility of the interference, $(I_{max} - I_{min})/(I_{max} + I_{min})$, is improved this way. In the probing arm, the beam first hits the sample surface, then bounces back with the plane of polarization rotated by the quarter wave plate to the vertical direction. Therefore the beam is totally reflected by PBS1, two reflecting mirrors, and PBS2 to hit the sample surface at the same point but from the other side. The beam bounced back from the second sample surface is horizontally polarized and thus transmits through the PBS2 without reflection. In the reference arm, the beam is first completely reflected by PBS3 into the reference mirror, the reflected beam transmits through PBS3 and joins the probing beam in the beam splitter. The

 0034-6748/89/082701-05$01.30

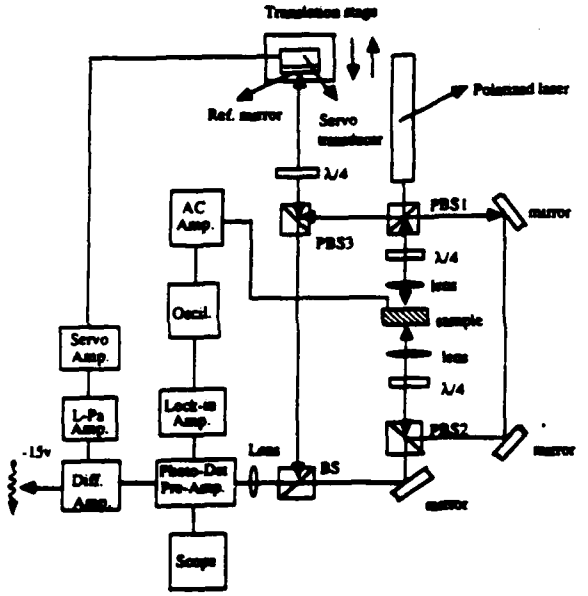

FIG. 1. Schematic drawing of the double beam laser interferometer.

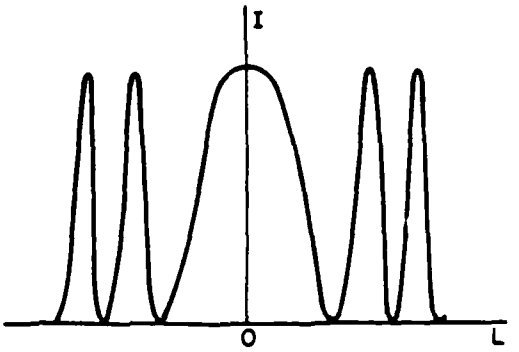

FIG. 2. Interference pattern in the detection plane for a finite beam diameter of laser and a large Δd. I is the intensity and L is the distance from the center of the spot.

two beams both polarized horizontally are recombined by the neutral beam splitter.

In the positioning of optical components, it is very important to keep the optical path-length difference between the probing arm and the reference arm as small as possible. Because of the great reflection and transmission loss of the beam intensity, especially in the probing arm, a laser with power larger than 10 mW is necessary. For a multimode laser with such a power level, the coherence length of the laser beam is typically only 20–30 cm long because of the simultaneous oscillation of many modes which satisfy the cavity resonance condition. Only when the difference of the optical path lengths of the probing arm and the reference arm is less than the coherence length of the laser beam, is the interference possible. Even when the optical path-length difference is already less than the coherence length of the laser beam, the difference is still harmful to the sensitivity. In the real experimental situation, due to the finite diameter of the laser beam, if the optical path-length difference Δd is not small enough, the interference pattern behind a condenser lens will show a distribution in the light intensity at the detection plane, such as that shown in Fig. 2. If the photo detector aperture is larger than the central fringe diameter, the sensitivity of the system can be greatly reduced. Since this central fringe diameter is inversely proportional to Δd, effort has been made in the system setup process to reduce this Δd, so that in the detection screen the central fringe occupies the whole illuminated area and the view spot shows uniform light intensity distribution, indicating that the central fringe diameter is much larger than the aperture of the photodetector. Unfortunately, the optical path length of the probing arm is fixed, and the adjustment can be made only in the reference arm. Thus, the servo transducer is positioned on a translation stage which can more forward and backward along the beam direction to vary the optical path-length of the reference arm in a very fine scale. In order to further improve the sensitivity, a condenser lens is inserted in front of the photodetector to further expand the diameter of the central fringe. Under this condition, the light intensity is that described by Eq. (1).

The optical path-length is also important for the sensitivity of the system. It was found in the real adjustment that the shorter the optical path-length, the higher the sensitivity. This must be due to the fact that the laser beam is not absolutely monochromatic, the incoherence increases as the optical path-length increases. In the present system, the optical components were placed as close as possible and the optical path length was kept under 130 cm long.

B. Electronic system

For small displacement measurement, it is desirable to set the interference between the two beams at a point about the $(2n+1)\lambda/8$ $(\pi/2)$ point, where the light intensity change will be maximized for the same displacement change in Δd. Near this point, we can write Δd as

$$\Delta d = d_{ac} + (2n+1)\lambda/8, \tag{3}$$

and Eq. (1) can be reduced to

$$I = I_p + I_r + 2\sqrt{I_p I_r}\sin(4\pi d_{ac}/\lambda)$$

$$= I_p + I_r + 2\sqrt{I_p I_r}\,4\pi d_{ac}/\lambda, \tag{4}$$

In Eq. (4), the sign " + " or " − " depends on whether n is an even or odd number. The approximation $\sin x = x$ is valid for small x and in our case, the error associated with this approximation is less than 1% if d_{ac} is less than 130 Å. Equation (4) indicates that the light intensity change is linearly proportional to the change d_{ac} for small displacement.

The stabilization of the interferometer at the $\pi/2$ point is achieved by introducing a feedback loop in the reference arm as shown in Fig. 1. The configuration used can set the system at any reference point by adjusting the voltage level at the differential amplifier reference input. The set voltage is compared with the output voltage of the photodetector, the difference of the two voltages is amplified by the L-Pa ampli-

fier and servo amplifier to drive the servo-transducer. The reference mirror is then driven by the servo transducer to change the optical path length of the reference arm and to bring the output voltage of the photodetector to the set voltage. This feedback loop responds only on the low-frequency signal (< 10 Hz), it does not affect the measurement at high frequencies. The L-Pa amplifier can also generate a sinusoidal wave to drive the servo transducer. If the displacement of the reference mirror is larger than the wavelength of the light, the interference intensity curve can be obtained. The $V_{max} - V_{min}$ or $V_{p\text{-}p}$ value may be measured using a digital oscilloscope.

C. Sample mounting

The way in which the sample is mounted is shown schematically in Fig. 3. The two major surfaces of the sample are very smoothly polished. Gold is then sputtered to the surfaces for both electric conduction and optical reflection purposes. The sample is bonded to the sample holder by epoxy. It is confirmed by the measurement of admittance vs frequency that the resonance frequencies of the sample mounted this way are very close to those of the free sample especially when the ratio of the sample length (vertical direction) to cross section (horizontal plane) is large. The sample holder is able to move in the y and z directions (x is the direction of the laser beam and z is the vertical direction) and also rotate in x-z plane.

II. PIEZOELECTRIC STRAIN MEASUREMENT

A. Ultra-low displacement measurement

For sinusoidal displacement $d_{ac} = d_0 \cos(\omega t)$, the optical signal is converted by the photodetector to a voltage change and then amplified. This voltage signal is detected by a two-phase lock-in analyzer (EG&G Princeton Applied Research, Model 5208) as V_{out} which is a rms value of the detected signal corresponding to the displacement $d_0/\sqrt{2}$. From Eq. (4) it can be shown that

$$d_0 = (\lambda/\sqrt{2}\pi)(V_{out}/V_{p\text{-}p}), \tag{5}$$

where $V_{p\text{-}p}$ is the peak-to-peak value of the interference signal, which corresponds to the change in the interference signal ($I_{max} - I_{min}$). The lock-in detection offers excellent noise rejection and is the key to the sensitivity. Figure 4 shows the field induced displacement vs the applied voltage (1 kHz) for an x-cut quartz measured using lock-in detection. The displacement is linearily proportional to the applied voltage due to the pure piezoelectric effect. Under a very quiet environment, the system response to an applied field as weak as 1.5 V/cm for a $V_{p\text{-}p}$ value of about 1 V. Such a response gives a displacement resolution 10^{-2} Å. However, compared with that of the single beam system,[5] the sensitivity of the double beam system is an order of magnitude less. Several things are responsible for the degraded sensitivity. First of all, the light intensity loss ($> 70\%$ in general) due to the reflection and transmission in the double beam system is much greater than that in the single beam system because there are more optical components and one more reflecting sample surface in the double beam system. The conversion of the light intensity to voltage is accomplished by an inversely biased photodiode. The photoexcited current flows to the ground through a resistor, the voltage across the resistor is enlarged by an operational amplifier with a gain of 100. Obviously, the smaller the resistance of the resistor, the faster the response speed of the photodiode and the less the signal-to-noise ratio. A 1-kΩ resistor is selected in order to raise the response frequency of the photodiode to MHz range. When the noise level is kept constant, the smallest measurable voltage signal $(V_{out})_{min}$ is subsequently fixed, and hence the smallest detectable displacement is determined by $I_{p\text{-}p}(I_{max} - I_{min})$ or $V_{p\text{-}p}(V_{max} - V_{min})$ value according to the relation

$$(d_0)_{min} = (\lambda/\sqrt{2}\pi)(V_{out})_{min}/V_{p\text{-}p}.$$

If the sample surfaces are not very reflecting, the $V_{p\text{-}p}$ value can be only 50–100 mV. The $(V_{out})_{min}$ measured by the lock-in is set by the electronic and mechanical noises and is in the range of 0.01–0.1 mV depending on the environment. Therefore, the sensitivity is in the range of 0.1–3 Å. For quartz, the sample surfaces can be polished so well that the reflectivity of the surfaces yields a $V_{p\text{-}p}$ value above 0.7 V.

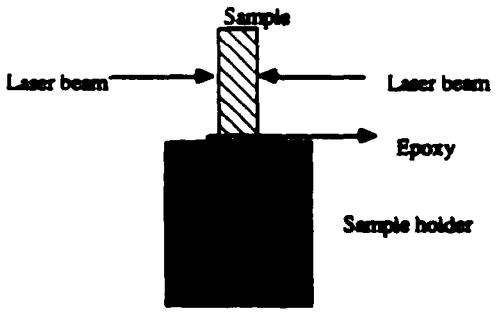

FIG. 3. Schematic drawing of sample mounting.

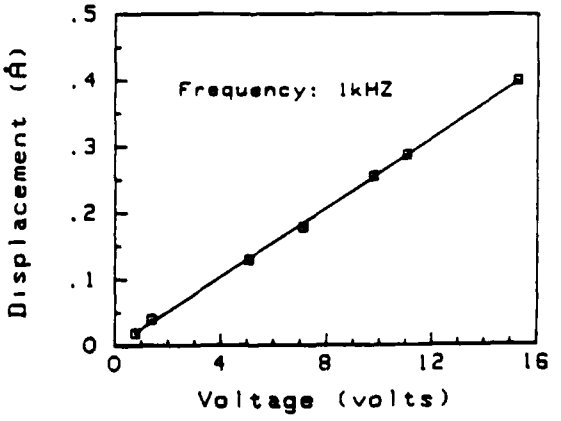

FIG. 4. Voltage scan of x-cut quartz at the frequency of 1 kHz.

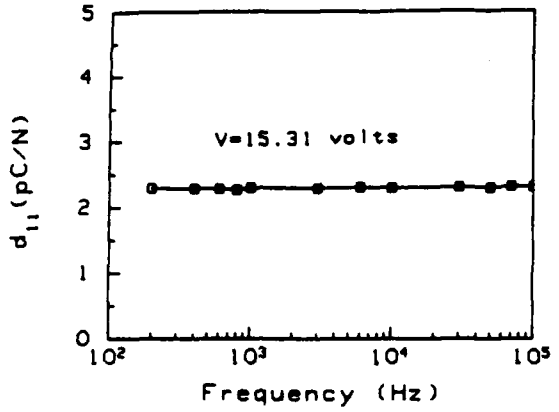

FIG. 5. Frequency scan of x-cut quartz at applied voltage of 15.31 V.

such a $V_{p\text{-}p}$ value yields the reported sensitivity of 0.01 Å. For the single beam system, even the polished ceramic sample surfaces can yield a $V_{p\text{-}p}$ value above 1 V, this is one of the reasons for the degraded sensitivity in the double beam system. Second, wave-front distortion is much more severe in the double beam system than that in the single beam system because of the elongated optical path lengths and increased optical components, consequently, in the detection plane the reference beam and the probing beam would be less coherent. Finally, as mentioned earlier, because of the lack of absolute monochromaticity of the laser light, the coherence of the light decreases with increasing optical path length. In the present setup, it is impossible to keep the optical path-length under 130 cm which is much longer than that of the single beam system.

Figure 5 shows the displacement versus the driving frequency of applied voltage 15.31 V for the x-cut quartz. The d_{11} value is constant with respect to the frequency up to 100 kHz which is the limit of the bandwidth of the lock-in amplifier used (5208 two phase lock-in analyzer, EG&G Princeton Applied Research), the absence of the dispersion is a characteristic of nonferroelectric piezoelectric.

B. High-frequency displacement measurement

Although the lock-in detection provides high sensitivity, the driving frequency of the applied electric field is limited by the bandwidth of the lock-in amplifier. An oscilloscope does not have as good noise rejection capability as the lock-in amplifier, but the bandwidth can be much higher. A digital oscilloscope (Hewlett Parkard 54201A) was used for the high-frequency displacement detection. The bandwidth of the oscilloscope is, under the repetitive mode, 200 MHz which is well above the fundamental resonance frequencies for a regular sample size. When the signal from the photodetector is greater than 1 mV, the signal-to-noise ratio under a quiet environment is large enough to allow the signal to be measured by the digital oscilloscope. According to Eq. (5), the sensitivity is about 1 Å for a $V_{p\text{-}p}$ value of about 1 V.

If the induced signal is larger than 130 Å, Eq. (5) is no longer valid because of the nonlinearity between the displacement and interference light intensity. But, when the displacement is less than $\lambda/4$, it can be calculated as

$$d_0 = (\lambda/4\pi)\sin^{-1}(2V_0/V_{p\text{-}p}), \tag{6}$$

where d_0 is the displacement amplitude induced by the applied electric field and V_0 is the voltage signal amplitude measured from the stabilization point $1/2(V_{max} + V_{min})$ by the oscilloscope. Figure 6 shows the displacement of PZT5 induced by an applied ac voltage amplitude 15.31 V versus the driving frequency. The voltage amplitude generated by the piezoelectric effect of the sample versus the driving frequency was measured by a spectra-analyzer (Hewlett Parkard, 3585A). The amplitude is a relative value to the excitation voltage level and is proportional to the admittance of the sample. The amplitude versus frequency is also shown in

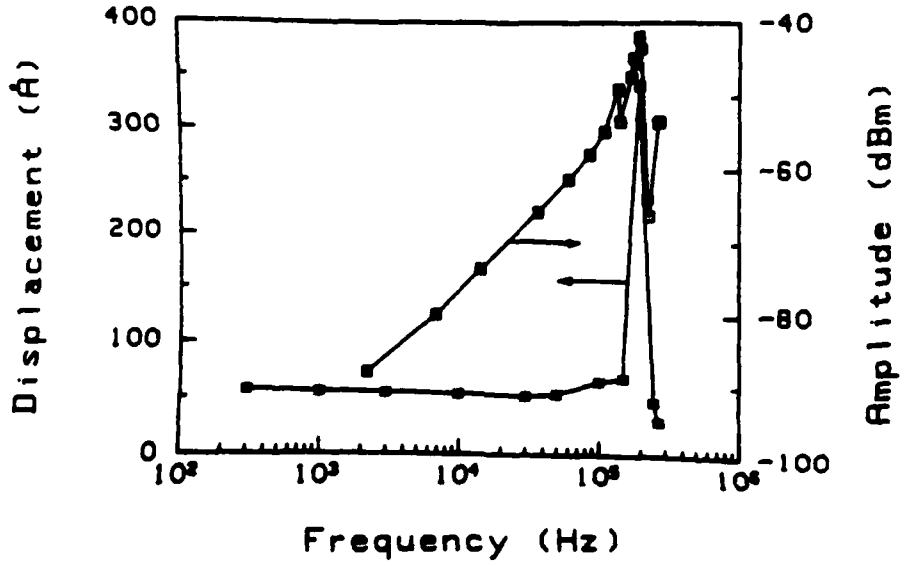

FIG. 6. Frequency scan of field induced displacement and voltage amplitude generated by the piezoelectric effect for PZT5. The applied voltage for displacement measurement is 15.31 V. The voltage amplitude is measured by the spectra analyzer.

Fig. 6. It is observed that the resonance peaks measured by the two different methods agree quite well. As shown in Figure 3, the mass center of the sample is not oscillating under the driving ac field. The "back motion" is no longer a concern here, thus the displacement can be measured properly to high-frequency range.

C. Elimination of bending effect

The present detection system can be free from the interference of a bending effect. As shown in Fig. 3, if the top of the sample bends toward the left beam and the optical path length of the left beam decreases, then the optical path length of the right beam increases, offsetting the decrease of the optical path length in the left beam. This is, of course, based on the assumption that the beam spots on the sample surfaces are very small and the beams on the two sides of the sample are collinear. In the present system, the reduction of the beam spots is accomplished by two condenser lens on the two sides of the sample and the collinearity of the beams on both sides of the sample is made possible by adjusting the beam to pass the collinear pinholes on both sides of the sample. The pinholes are removed after the beam adjustment.

ACKNOWLEDGMENTS

The interferometer described in this paper is modified from that built up by Dr. Q. M. Zhang for the measurement of the response speed of the field induced strain. The authors wish to thank him for initiating this work.

[1]D. Volkomerson, Appl. Phys. Lett. 29, 183 (1976).
[2]D. L. Allenswoth, Rev. Sci. Instrum. 51, 1330 (1980).
[3]Th. Kwaaital, Rev. Sci. Instrum. 45, 399 (1974).
[4]V. E. Bottom, J. Appl. Phys. 41, 3941 (1970).
[5]Z. M. Zhang, W. Y. Pan, and L. E. Cross, J. Appl. Phys. 63, 2492 (1988).

APPENDIX 5

High-frequency strain response in ferroelectrics and its measurement using a modified Mach-Zehnder interferometer

Q. M. Zhang,[a] C. J. Jang, and L. E. Cross
Materials Research Laboratory, The Pennsylvania State University, University Park, Pennsylvania 16802

(Received 9 August 1988; accepted for publication 29 November 1988)

In this paper we report on a modified Mach-Zehnder interferometer which is capable of measuring the ultrashort time strain response of a sample. Using this instrument, the dispersion of piezoelectric and electrostrictive coefficients of several commonly used ferroelectrics was measured. The strain switching behavior of lead lanthanum zirconate titanate (PLZT) 9/65/35 driven by a square pulse electric field was studied. The results show that the switching rise time of the strain response for PLZT 9/65/35 can be much shorter than 5 μs at a pulse field strength near 25 kV/cm and that the fall time of the strain response is considerably shorter than the rise time in the experimental field strength range.

I. INTRODUCTION

The dispersion and switching properties of ferroelectric materials are of great importance for the practical application of the materials and for a basic understanding of ferroelectricity. In the normal frequency range (< 100 MHz) where ferroelectrics are used, the dispersion of response functions and switching behavior are closely related to the defect structure of the materials, domain nucleation, and domain boundary motions.[1,2] Using modern electronic techniques, the dielectric dispersion and polarization related switching can be easily studied. Abundant experimental information can be found in the literature.[3–9] However, concerning the study of strain related properties in ferroelectrics, especially in the high-frequency domain, experimental information based on direct measurement on the strain response is lacking.

The piezoelectric and electrostrictive coupling in the ferroelectrics provide a convenient and effective means to convert an electric signal to mechanical signal (strain or stress) and vice versa. This conversion is actually a two-step process: the electric-field-induced polarization changes and consequently the polarization related strain level change. Since this later process can also be frequency dependent, an independent study of the strain response up to high frequency is highly desirable.

In this paper we report on a modified Mach-Zehnder interferometer which is capable of measuring the ultrashort time strain response of a sample. Using this instrument, the dispersion of piezoelectric and electrostrictive coefficients of several commonly used ferroelectrics was examined. The strain switching behavior of PLZT 9/65/35 under a square pulse electric field was also studied. These results will be reported in the following paper and their implications discussed.

II. THE APPARATUS AND ITS OPERATION PRINCIPLE

Although the laser interferometer has been widely used in precise displacement measurement and is capable of measuring these displacements to ultrahigh frequencies (> 10 MHz),[10,11] its application is still limited to lower frequencies as a dilatometer. The major obstacle which prevents this instrument as a high-frequency dilatometer is the single surface displacement detection scheme in the currently used interferometer, as discussed in an earlier publication.[12] Using this scheme, where only one face of the sample is detected (in later discussion, this face is denoted as the front face of the sample), the strain level of the sample can be obtained only by assuming the possible motion of the undetected face of the sample (denoted as the back face) resulting from the strain change. In most cases, the back face is assumed to be fixed and hence the front face displacement is equal to the sample dilatation due to the strain change. It is clear that such an assumption is valid only at low frequency. As the frequency is increased, the holding force on the back face of the sample to prevent its motion will increase as the square of the frequency.[12] Thus, the back face of the sample will certainly be set into motion due to the finite size of the holding force and this back face motion is usually unpredictable. Hence, it is not possible to use this single face detection interferometer to follow the sample strain response to high frequency.[12] Of course, increasing the strength of the holding force can raise the operation frequency. But this will also result in an increase on the sample clamping which is not desirable. Normally, under unrestrained conditions to the sample a single face detection laser interferometer can only be operated below several kHz for a small strain amplitude measurement (< 100 Å). At a fixed frequency, the holding force is also proportional to the amplitude of the sample dilatation. Thus, the operation frequency for the study of polarization related strain response which involves a large displacement measurement (> 1000 Å) is limited below several hundred Hz.

Based on these facts, a correct strain measurement at high frequency requires one to probe the motion of both faces of a sample. Shown in Fig. 1 is the schematic drawing of a modified Mach-Zehnder interferometer recently built to fulfill these requirements. By the arrangement of the optical path in the measuring arm as shown in the figure, the setup is insensitive to the motion of the sample as a rigid body, which is actually the major cause of errors in the single face detec-

[a] Present address: Building 555, Brookhaven National Laboratory, Upton, NY 11973.

 0021-8979/89/072807-07$02.40

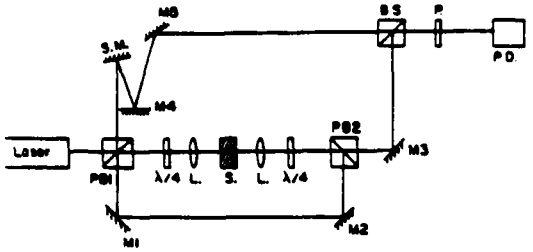

FIG. 1. Schematic drawing of the optical part of the modified Mach-Zehnder interferometer. PB1 and PB2 are two polarized beam splitters, SM is a servomirror which is driven by a PZT actuator, P is a polarizer, $\lambda/4$ is quarter wave plate, L is condenser lens, and S is the test sample.

tion interferometer for strain measurement. The change in the optical path length in the measuring arm is equal to the dilatation of the sample from the strain change.

The operation principle of this interferometer is as follows: The laser light is equally divided by a polarized beam splitter (PB1) into the measuring arm and the reference arm with mutually perpendicular polarization directions. In the measuring arm, where the sample is located, the linearly polarized laser beam hits the first face of the sample and is reflected back to PB1. The quarter wave plate ($\lambda/4$) in that path rotates the polarization direction of this beam by 90° before it is sent back to PB1. As a result, the returning beam will be totally reflected by PB1 to the reflection mirrors M1, M2, and the second polarized beam splitter PB2. Totally reflected by PB2, the laser beam is directed to the second face of the sample. The function of the quarter wave plate in this path is the same as the previous one and ensures that the laser beam reflected from the second face of the sample will be totally transmitted through PB2 to reflection mirror M3. The probing beam and the reference beam meet at the beam splitter (BS), and with the help of a polarizer (P) these two beams form the interference pattern to be detected by the photodetector.

The purpose of the two lenses in the measuring arm is to reduce the effect of tilting of the sample reflection face with respect to the laser beam, as discussed in Ref. 12. It is expected that if the reflection face tilting becomes large, errors will be induced. Therefore, care in sample holding should be practiced to reduce the reflection face tilting in the high-frequency measurement.

In the reference arm, the additional mirrors M4 and M5 are used to compensate the optical path length of the arm so that it is equal to the measuring arm optical path length. This reduces the interference signal noise. In this setup, the total length of the reference arm is about 2.3 m.

An accurate measurement of the sample strain requires that the laser beams hitting the first and the second sample faces are colinear. The first face of the sample, therefore, has to be oriented precisely with respect to the incident beam. In order to achieve that, a three-point aligner was designed, as schematically shown in Fig. 2. The three pinholes on the aligner are adjusted to be colinear with the help of a laser beam. Using this aligner, the laser beams on the two sides of the sample can be adjusted to be colinear.

The interference signal seen by the photodetector is

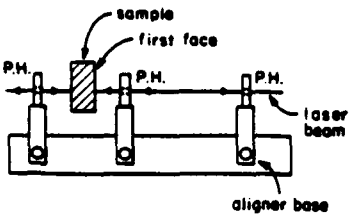

FIG. 2. Schematic drawing of the three-point aligner which is used to aid the sample alignment to ensure that the laser beams on the two faces of the sample are colinear. PH stands for pinhole.

$$I = \tfrac{1}{2}(I_{max} + I_{min}) + \tfrac{1}{2}(I_{max} - I_{min})\cos(4\pi\Delta d/\lambda)\,, \quad (1)$$

where I_{max} and I_{min} are, respectively, the interference light intensity at the maximum and minimum points, and Δd is the optical path length difference between the two arms. In case $\Delta d/\lambda \ll 1$ and the interference signal is biased at the middle point between I_{max} and I_{min} where the maximum sensitivity is achieved, a linear relationship between ΔI and Δd exists as given by

$$\Delta d = (\lambda/2\pi)\Delta I/(I_{max} - I_{min})\,. \quad (2)$$

III. SAMPLE MOUNTING PROBLEMS

As we pointed out in the preceding section, a proper sample holding is an important factor in obtaining accurate data. In our measurement, three different sample holding methods were used as shown in Fig. 3. Method (a) has a clamping effect on the sample. Therefore, it is only suitable for small strain measurement (strain $< 10^{-7}$) even with the position of the probing laser beam located away from the holding position. This is the easist holding method and will not induce a large clamping effect, as has been tested when the sample is thick (> 3 or 4 mm). Method (b) has very small clamping effect. When the center of mass of the sample is overlapped with the sample holding point, the tilting of the reflection face of the sample can be minimized. In both (a) and (b), the sample under test is glued to the sample holder by epoxy (either conductive or nonconductive) and they are suitable for the measurement of the sample strain under both cw and pulse field driving. It is obvious that if the sample becomes thin, a bending or flexure motion of the sample will be excited. At the flexure resonance of the sample, large tilt-

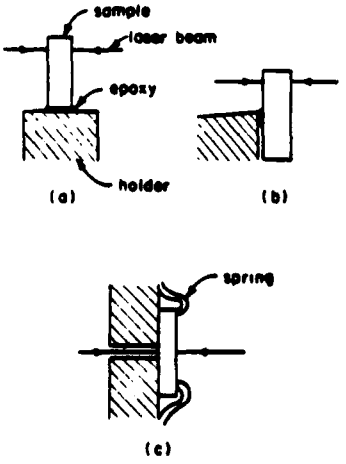

FIG. 3. Three different ways of mounting the sample for high-frequency strain measurements.

ing of the sample reflection face will be induced [the frequency of the flexure mode for most of the ferroelectrics with a bar shape as supported in our experiment is about 0.5 (h/l^2) MHz or higher, where h and l are the bar thickness and the length in units of mm, respectively].[13] Therefore, a relatively thick sample is needed (>0.5 mm) to minimize the sample bending.

In method (c), one face of the sample is placed against the holder with a hole in the middle with a diameter just large enough to pass the laser beam and two springs (or two rubber bands) are used on the other face to press the sample to the holding surface. This sample holding method is not very suitable for the strain measurement under cw driving to high frequency (<10 Hz) since the two springs are usually not identical. However, in studying the switching rise time behavior of the sample strain under pulse driving, this holding method is superior to methods (a) and (b). Especially when the sample is very thin, the support of the sample holder prevents the sample from bending during the sample expansion near the rising edge of the pulse. When the sample contracts (as the applied voltage decreases), the mass center motion of the sample will pull the whole sample away from the holding surface and the sample is in a mechanically unstable position. As a result, if the forces from the two holding springs are not equal, an irregular sample tilting will occur. This holding method, therefore, does not work for cw strain measurement.

Depending on the experimental situation and purpose, other types of sample holding methods should be considered to achieve the best results.

IV. DISPERSION OF PIEZOELECTRIC AND ELECTROSTRICTIVE COEFFICIENTS OF SEVERAL SELECTED FERROELECTRICS

The piezoelectric and electrostrictive coefficients of x-cut quartz (d_{11}), hard PZT (PZT-8) (d_{33}), soft PZT (PZT-5) (d_{33}), and PLZT 9.5/65/35 (M_{11}) were measured as a function of frequency. The measurement of the x-cut quartz single crystal was performed for the purpose of calibration. In the piezoelectric constant measurement, all the samples used had a thickness of 2 mm or more and the areas of the samples were about 4×4 mm^2 or more. In the electrostrictive coefficient measurement, PLZT samples were about 0.5 mm thick and 5×5 mm^2 or larger in area. All the samples were polished to optical flat on both faces.

Both the soft and hard PZT were commercially available ceramic samples. PLZT samples were hot-pressed transparent samples. PZT samples are poled and they show piezoelectric strain response, whereas PLZT 9.5/65/35 is a ferroelectric relaxor, and at room temperature it is an electrostrictive material.

The piezoelectric and electrostrictive coefficients were measured by applying an ac field on the sample, and the strain response signal from the photodetector was detected by a lock-in amplifier (EG&G Princeton Applied Research 5208) and a digitized oscilloscope (HP 54201A). For a sample thickness t with an applied voltage V_0 (amplitude), the piezoelectric constant is given by

$$d_{11(\text{or }33)} = \Delta d / V_0 \tag{3}$$

and the electric-field-related electrostrictive coefficient by

$$M_{11} = 2\Delta d(2f)t/V_0^2, \tag{4}$$

where $\Delta d(2f)$ is the sample's dilatation at frequency $2f$ measured by the lock-in amplifier.[12] The frequency doubling ($2f$) in the sample strain is due to the electrostrictive coupling of the sample strain response to the electric field.

It was observed, however, that more reliable data can be acquired more rapidly by using a two-signal comparison method. In this method, two voltage signals with frequencies f_0 and f_1 were applied simultaneously to the sample, as shown in Fig. 4. The response signals from the sample were measured by using two lock-in amplifiers tuned at f_0 and f_1, respectively. By fixing f_0 and varying f_1, the dispersion of the piezoelectric or electrostrictive coefficient can be obtained through the relation

$$\frac{d_{33}(f_1)}{d_{33}(f_0)} = \left(\frac{\Delta d(f_1)}{\Delta d(f_0)}\right)\left(\frac{V(f_0)}{V(f_1)}\right), \tag{5}$$

where $\Delta d(f_1)$ and $\Delta d(f_0)$ are the dilatations of the sample at frequencies f_1 and f_0, $V(f_1)$ and $V(f_0)$ are the applied voltage amplitude with frequencies f_1 and f_0, or

$$\frac{M_{11}(f_1)}{M_{11}(f_0)} = \left(\frac{\Delta d(2f_1)}{\Delta d(2f_0)}\right)\left(\frac{V(f_0)}{V(f_1)}\right)^2. \tag{6}$$

where $\Delta d(2f_1)$ and $\Delta d(2f_0)$ are the dilatations of the sample at frequencies $2f_1$ and $2f_0$.

The measured dispersions of the piezoelectric constants for x-cut quartz, soft PZT, and hard PZT are shown in Fig. 5. For quartz, d_{11} did not vary up to 100 kHz. Above that, the sample mechanical resonance (piezoelectric resonance) causes d_{11} value deviate from its intrinsic value. Whereas for both soft PZT and hard PZT, d_{33} decreases slightly as the frequency is increased. This decrease, as seen from the figure, is the result from the dispersion of the dielectric permittivity. This indicates that for weak field excitation, in the frequency domain, poled ferroelectrics can be described as polarization biased electrostrictive materials with $d_{33} = 2P_0\epsilon\epsilon_0 Q_{11}$, where P_0 is the bias polarization. The change in d_{33} is the result of the dispersion of the dielectric permittivity, ϵ. Hence, for both hard and soft PZT, Q_{11}, the polarization related electrostrictive constant measured in the weak field limit, is frequency independent. At frequencies near and above 100 kHz, the measurement was affected by the sample's piezoelectric resonance. Therefore, to pur-

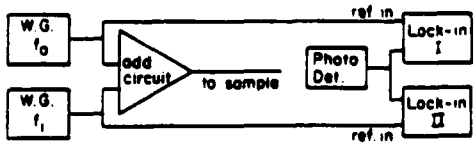

FIG. 4. Schematic drawing of the power supply and signal detection arrangement for the two-signal comparison method. Voltages from the two waveform generators (WG) are added by an add circuit. Depending on the experimental situation, a power amplifier may be used following the add circuit to supply a high-voltage signal to the sample.

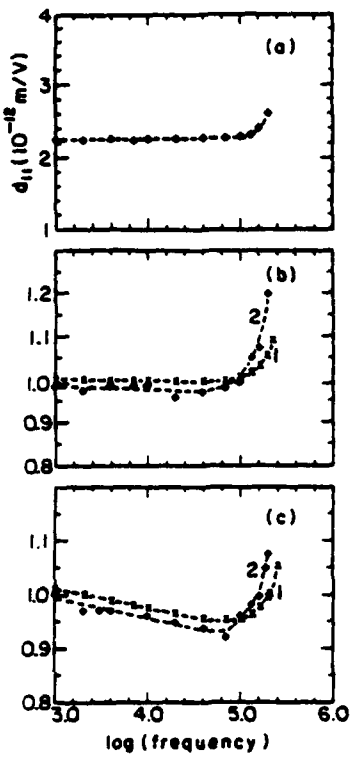

FIG. 5. (a) d_{11} for x-cut quartz; (b) $d_{33}(f)_{33}$ (1 kHz) (curve 2) and $\epsilon_{33}(f)/\epsilon_{33}$ (1 kHz) (curve 1) for hard PZT; (c) $d_{33}(f)/d_{33}$ (1 kHz) (curve 2) and $\epsilon_{33}(f)/\epsilon_{33}$ (1 kHz) (curve 1) for soft PZT as a function of frequency.

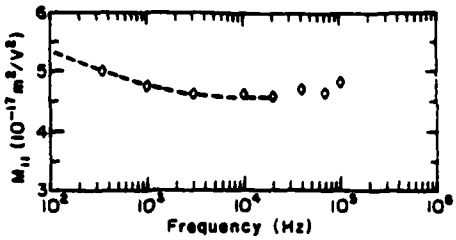

FIG. 7. The electric-field-related electrostrictive coefficient M_{11} for PLZT 9/65/35. The field strength is 440 V/cm. The mechanical resonance of the sample causes the increase of M_{11} at frequencies above 50 kHz.

sue the measurement to even higher frequencies, it is necessary to suppress the sample mechanical resonance or reduce the sample dimension to move the resonance to even higher frequencies.

For comparison, in Fig. 6 the piezoelectric constant is shown for x-cut quartz and hard PZT measured using a single face detection interferometer.[12] The measurement is apparently limited to below 2 kHz.

The electrostrictive coefficient M_{11} for PLZT 9.5/65/35 as a function of frequency is shown in Fig. 7. The applied field amplitude was 440 V/cm. The data above 50 kHz are affected by the mechanical resonance of the sample (the oscillation frequency for electrostrictive materials is $2f$ where f is the applied field frequency). However, this resonance is much weaker than the piezoelectric resonance since there is no anomaly in the real part of dielectric constant at this resonance region. The resonance observed for this electrostrictive material is purely mechanical resonance.

V. STRAIN RESPONSE OF PLZT 9/65/35 UNDER HIGH FIELD WITH cw AND SQUARE PULSE DRIVING

The strain response at a fixed electric field amplitude (16.3 kV/cm) as a function of frequency was measured for PLZT 9/65/35 ceramics (hot pressed transparent samples). The measured strain hysteresis loops are shown in Fig. 8 and summarized in Fig. 9. All the data were taken under cw driving and recorded by a digitized oscilloscope. The limitation on the measured frequency is caused by the power amplifier. In our experiment, a Kepco bipolar power amplifier (model BPO 1000M) was used which has a bandwidth of about 1 kHz. The dispersion of the strain response can be clearly seen and is larger than the dispersion of the weak field electrostrictive coefficient.

Switching characteristics of PLZT 9/65/35 under square pulse driving were also studied. The sample thickness

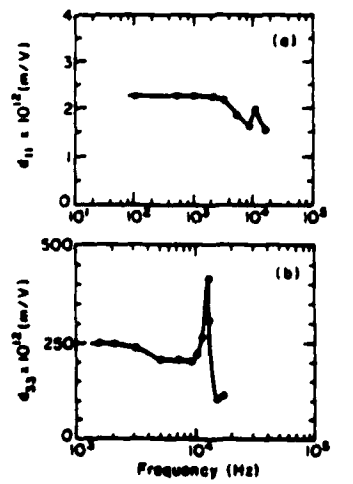

FIG. 6. (a) d_{11} for x-cut quartz; (b) d_{33} for hard PZT measured using a single-face detection interferometer.

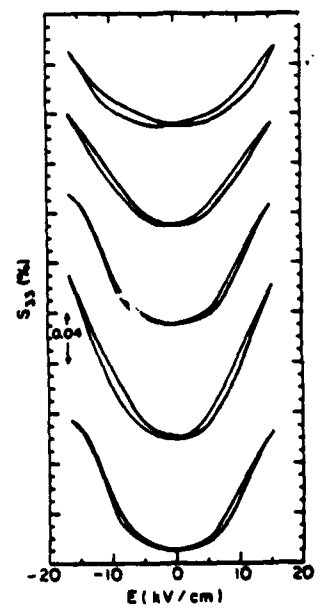

FIG. 8. Strain hysteresis loops for PLZT 9/65/35 as a function of frequency, from bottom to top: 1 Hz, 10 Hz, 100 Hz, 300 Hz, and 1 kHz.

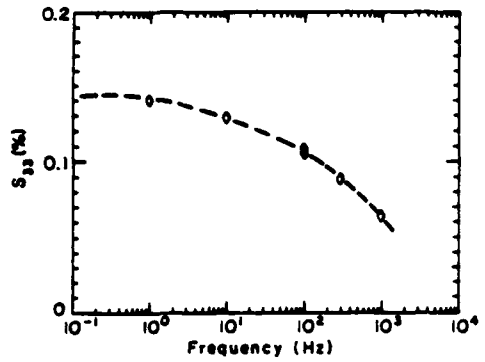

FIG. 9. The dispersion of the strain response of PLZT 9/65/35 under 16.3-kV/cm cw driving field.

used is 0.365 mm. In this measurement, a high-power pulse generator (HP 214B and Cober Model 604A) with rising time shorter than 20 ns and a maximum output power of 9 kW was used. The response strain signal was recorded on a digitized oscilloscope. The photodetector used has a flat response up to 1 MHz and a bandwidth of more than 5 MHz. Typical data record is shown in Fig. 10. Figure 10(a) shows both the strain response and the applied square pulse.

Figure 10(b) shows the response of the current and strain of the sample to a square pulse with 5-μs duration. The polarization response $P(t)$ of the sample can be obtained by integrating the current with respect to time

$$P(t) = \int_0^t i(t')dt' .$$

One can observe immediately that the rise time for the strain response is longer than the fall time. Part of the reason is as follows: When an electric field is applied to a sample, the primary response of the sample is the polarization change. The strain change of the sample is a consequence of the polarization change. For an electrostrictive material, $s_{11}(t) = Q_{11}P^2(t)$, assuming that Q_{11} is not strongly frequency dependent. If we assume that the polarization response to a square electric pulse is symmetric at the rising and the falling edges of the pulse and has an exponential dependence on time, then at the rising edge,

$$P(t) = P_0[1 - \exp(-t/\tau)] , \tag{7a}$$

and at the falling edge,

$$P(t) = P_0 \exp(-t/\tau) , \tag{7b}$$

where τ is a constant characterizing the response time of the sample polarization to a pulse. Equation (7) describes that the rising and falling edges of the polarization response function have the same response time τ. Therefore, the strain response at the rising edge would be

$$s_{11}(t) = Q_{11}P^2(t)$$
$$= s_0[1 - 2\exp(-t/\tau) + \exp(-2t/\tau)] , \tag{8a}$$

and at the falling edge would be

$$s_{11}(t) = s_0 \exp(-2t/\tau) . \tag{8b}$$

Equation (8) shows that the fall time of the sample strain response should be much shorter than the rise time and that they have different time-dependent forms. Approximately speaking, the falling edge has a characteristic time of $\tau/2$, which is shorter than the rise time of about τ. The argument presented above demonstrates that even a symmetric polarization response to the square pulse will result in an asymmetric strain response. Apart from that, there is no prior reason to assume that the sample polarization response to the square pulse should be symmetric at the rising and falling edges and that they have the same time-dependent functional form. In fact, a careful inspection of Fig. 10 reveals that even in the polarization response curve, the fall time is also shorter than the rise time. The experimental data presented below show that the fall time of the strain response curve is shorter than half of the rise time.

For the pulse switching, the sample strain shows mechanical resonance. Such a resonance effect is very small when the pulse field is small, as shown in Fig. 10(a). For a field of 25 kV/cm, as shown in Fig. 11, a strong mechanical

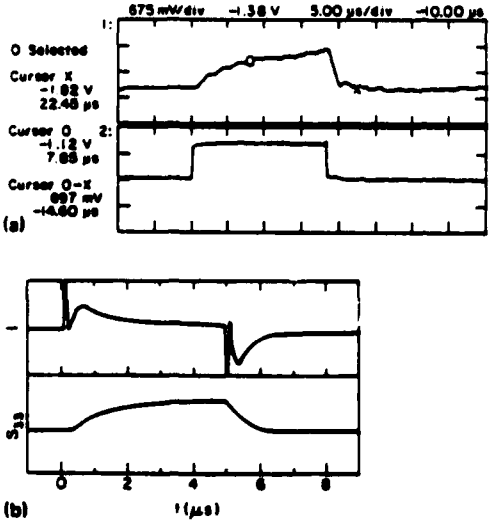

FIG. 10. (a) The strain response signal and the applied square pulse (11.2 kV/cm) as recorded from the digitized oscilloscope for PLZT 9/65/35; (b) the current and the strain response signals recorded from a digitized oscilloscope. The field strength in 11.2 kV/cm.

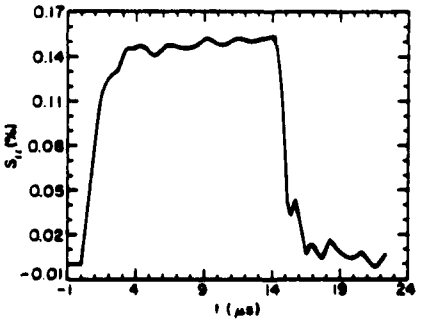

FIG. 11. Strain response curve for PLZT 9/65/35 under 25-kV/cm field. The data show the resonance at the rising and falling edges.

resonance appears at both the rising and falling edges. The overall resonance amplitude (peak-to-peak value) is less than 15% of the total strain change in all the strain data measured.

A series of measurements were taken while varying the applied field strength and pulse width and some of them are presented in Fig. 12. In these data, the sample strain resonance was averaged out.

In order to look at the general trends, we plot in Fig. 13 the strain level of the sample at a fixed pulse width of 30 μs as a function of applied field strength. The data demonstrate that at an elevated field level (24.7 kV/cm), a relatively high strain level (0.15% strain) can be obtained from this material under a short pulse (equivalent to 33 kHz). At low frequency, for example, 0.1 Hz, this strain level is achieved by a field strength lower than 17 kV/cm. These data indicate that the strain loss due to the reduced pulse duration can always be compensated by increasing the applied field strength for the pulse driving mode. This would generally be true for most of the relaxor materials.

The situation may not be the same if the sample is driven by a cw field. In the pulse driven case as in our experiment, there is always enough time between the two pulses for the sample to relax back to its initial state (we are not concerned with the aging effect and in this case, the aging effect at high field is negligible[14]). Hence, to a reasonable approximation the sample prior to the pulse can be taken as having been in thermal depoled state. The driving electric field strength and the duration of the pulse should not affect this initial state. As a result, the only limitation to the final strain response of the sample is the finite relaxation time for micropolar domains to align statistically with the applied electric field as well as the finite domain wall traveling speed. Increasing the electric field strength of the pulse will speed up these processes,[7] compensating for the shortened duration of the pulse. However, in the cw driven case, the strain response would also depend on the relaxational processes of the sample for switching back under thermal agitation to the $E = 0$ state after having been excited. Increasing the applied field will not speed up this returning process. At high frequency, the sample is not able to relax back to its thermal random state when $E = 0$. This will certainly cause an additional reduction in the strain response of the sample besides the limitation due to the finite switching rise time. We refer to this as recovery limitation. Therefore, there is a limit on the operating frequency for cw driving; beyond this limit, the strain loss of the sample due to increased operating frequency cannot be compensated for by increasing the applied electric field strength. Hence, the recovery speed should be an important criterion for high-frequency material applications.

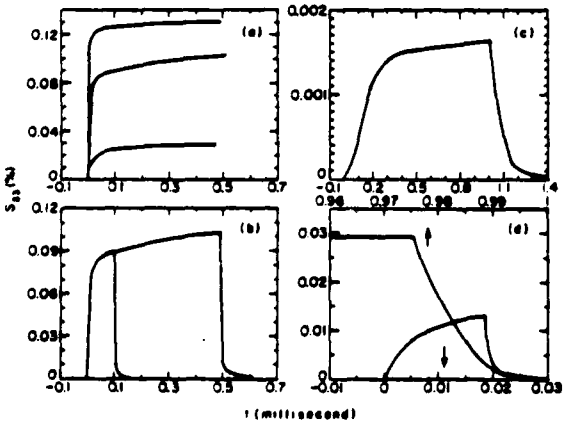

FIG. 12. (a) Strain response to an applied square pulse with increasing field strength: 11.2, 18, and 22 kV/cm; (b) strain response for square pulses of 18 kV/cm with different time durations; (c) strain response at relatively weak field level (4.4 kV/cm) and long time duration (1 ms); (d) the falling edges of the strain response curves to square pulses of 11.2 kV/cm with 19-μs and 1-ms time durations.

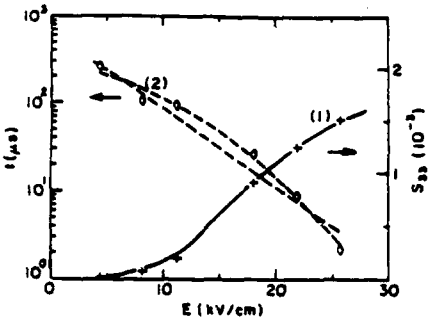

FIG. 13. The strain level of PLZT 9/65/35 as a function of the field strength for the square pulse with 30-μs duration (curve 1) and the switch rise time t_r of the strain response curve as a function of applied field strength E (curve 2). The dashed straight line for curve 2 is a linear fitting to the data, and the dashed curved line is the fitting to the data by using linear and quadratic two terms.

For PLZT 9/65/35, as shown in Fig. 12, the fall time of the strain response curve is relatively short. At high field level, it can be much shorter than 3 μs. At frequencies near or below 100 kHz, the dispersion in the strain response is mainly caused by the rising edge of the curve. For cw driving with a 16-kV/cm field, a strain of 0.065% was obtained at 1-kHz frequency. While with square pulse driving with 1-ms duration, the same strain level could be obtained with a field strength of about 15 kV/cm. The field levels between the two cases do not differ too much. Hence, for PLZT 9/65/35 at high field level, the falling edge does not impose a strong limitation on the strain response at a cw field of moderately high frequencies (near 100 kHz). In other words, the recovery limitation for this material is located above 100 kHz.

In relaxor materials, the polarization change of the sample to the applied field involves both 180° domain related phenomena (180° micropolar domain flipping, as well as 180° domain boundary motion) and non-180° domain related phenomena (non-180° micropolar domain rotation and their boundary motion, as well as the micropolar domains expanding into the paraelectric region). Only the later phenomena contribute to the sample strain response. In the normal case, the response time for these different phenomena are not the same. It is expected that as the operation frequency changes, both the dielectric constant and polarization related electrostrictive coefficient (Q_{ij}) would show dispersion. The dielectric constant will decrease with frequency;

however, the dispersion of Q_{ij} may not be so simple. It may show some irregular changes with frequency depending on the relative response times between the 180° domain-related change and non-180° domain-related change. The ultimate limitation on the strain response time is the speed for acoustic signal propagation through the medium. Near this limit, the electrostrictive coefficient will drop to zero. For most of the samples with dimensions on the orders of mm, this limit seems to be in the frequency range of MHz or above.

Also shown in Fig. 13 is the curve of the relative switch rise time as a function of applied field strength for pulse driving, where the relative switch time t_r is defined as the time needed for the strain level to reach 80% of the total level for a 0.5-ms duration square pulse. Among the various simple functional forms between t_r and electric field E, it is found that both expressions $t_r \propto \exp(-\text{const}\,E)$ and $t_r \propto 1/E$ can fit the data points relatively well. As can be seen from the figure, at a field above 20 kV/cm, the switching rise time can be shorter than 10 μs (at 25 kV/cm it is about 2 μs).

The dependence of the switching rise time on applied field strength for PLZT 9/65/35 is apparently different from that observed in normal ferroelectrics,[3,7,8] where the switching time is controlled by a two-dimensional nucleation process and by the speed of transverse expansion of the domain. At low field levels, $t_r \propto \exp(-\text{const}/E)$ and at high field level, $t_r \propto 1/E$. In relaxor ferroelectrics, there exists a large number of thermally active micropolar domains.[14] If we assume that polarization switching in these materials is through the microdomain flipping and their boundary expansion into the paraelectric matrix, under an applied field E, the probability for these micropolar domains to line up close the field direction is proportional to $\exp(\text{const}\,E)$ when the field level is below the saturation field. This implies $t_r \propto \exp(-\text{const}\,E)$ as observed. A close inspection of Fig. 13 also reveals that the switch rise time t_r actually falls off a little bit faster than that described by the function $\exp(-\text{const}\,E)$. In other words, the coupling constant [proportional to the "const" in function $\exp(-\text{const}\,E)$] is weakly field strength dependent and increases slightly as the field strength increases. This may be related to the ferroelectric cooperative effect as more micropolar domains line up with the applied electric field. The relationship $t_r \propto 1/E$ also indicates that the polarization switch in this relaxor material is strongly affected by the micropolar domain. Therefore, in relaxor materials, by inceasing the micropolar domain activities, the response time of a sample can be greatly increased. This has been demonstrated in literature.[15,16]

VI. SUMMARY

In this paper we demonstrated that by using a modfied Mach-Zehnder interferometer, the strain response of a sample can be measured up to [illegible] the dispersion of the piezoelectric constant for soft PZT and hard PZT and the dispersion of electrostrictive coefficient of PLZT 9.5/65/35 were measured. The piezoelectric resonance found in both PZT samples affected the dispersion of the dielectric and piezoelectric constants. The pure mechanical resonances in the relaxor material affect the dispersion of the electrostrictive coefficient, but did not have an anomalous effect on the dielectric dispersion at frequencies below 1 MHz. The switching behavior of the sample strain for PLZT 9/65/35 under square pulse driving was investigated. It was shown that for a high field level (>20 kV/cm), the switch rise time for the sample strain can be much shorter than 10 μs. The fall time of the strain response curve is shorter than the switch rise time ($<3\,\mu$s) and shows less field amplitude dependence than the switch rise time, except at low field levels (<5 kV/cm).

ACKNOWLEDGMENTS

The authors wish to thank Dr. W. Y. Pan and Yuemin Sun for their valuable assistance during this experiment and D. McHenry for making corrections in the manuscript. This work was supported partly by Rome Air Development Center through ITEK Optical Systems, Division of Litton, Inc. and partly by the Office of Naval Research.

[1] E. Fatuzzo and W. J. Merz, *Ferroelectricity* (Wiley, New York, 1967).
[2] M. E. Lines and A. M. Glass, *Principles and Applications of Ferroelectrics and Related Materials* (Clarendon, Oxford, 1977).
[3] Q. Li, W. Y. Pan, and L. E. Cross, Mater. Lett. 5, 51 (1986).
[4] T. Furukawa and G. E. Johnson, Appl. Phys. Lett. 38, 1027 (1981).
[5] J. M. Geary, Appl. Phys. Lett. 32, 455 (1978).
[6] G. Arlt and H. Peusens, Ferroelectricity 48, 213 (1983).
[7] W. J. Merz, Phys. Rev. 95, 690 (1954); J. Appl. Phys. 27, 938 (1956). H. L. Stadler, J. Appl. Phys. 29, 1485 (1958).
[8] R. C. Miller and A. Savage, Phys. Rev. 115, 1176 (1959).
[9] E. A. Little, Phys. Rev. 98, 978 (1955); J. Fousek and B. Brezina, J. Phys. Soc. Jpn. 19, 830 (1964).
[10] V. E. Bottom, J. Appl. Phys. 41, 3941 (1970); D. L. Allensworth, Rev. Sci. Instrum. 51, 1330 (1980).
[11] D. Royer and E. Dieulesaint, Appl. Phys. Lett. 49, 1056 (1986); D. Vilkomerson, Appl. Phys. Lett. 29, 183 (1976).
[12] Q. M. Zhang, W. Y. Pan, and L. E. Cross, J. Appl. Phys. 63, 2492 (1988).
[13] J. M. Herert, *Ferroelectric Transducers and Sensors* (Gordon and Breach, New York, 1982).
[14] W. A. Schulze, J. V. Biggers, and L. E. Cross, J. Am. Ceram. Soc. 61, 46 (1978); W. Y. Pan, E. Furman, G. O. Dayton, and L. E. Cross, J. Mater. Sci. Lett. 5, 647 (1986).
[15] L. E. Cross, Ferroelectricity 76, 241 (1987).
[16] M. Ozolinsh, Mater. Res. Bull. 17, 741 (1982).

APPENDIX 6

Laser Interferometer for Studying the Phase Delay of Piezoelectric Response

W.Y.Pan, H.Wang and L.E Cross

Materials Research Laboratory

The Pennsylvania State University

University Park, PA 16802

A laser interferometer is used to study the phase delay of the piezoelectric response. The real and imaginary part of the piezoelectric d coefficients are calculated from the measured strain amplitude and the phase delay with respect to the applied electric field for PZT-5. The same coefficients are also measured using Smits's iterative method. The results are in good agreement. The phase delay with respect to the applied electric field is also studied near resonance frequencies, the result is in excellent agreement with the classic vibration theory.

§1 Introduction

A very sensitive single beam laser interferometer was built up in this laboratory in 1987. The system is capable of resolving the displacement down to 10^{-3}Å in the frequency range of 20-2000 Hz[1]. Very recently, a double beam laser interferometer was built up in this laboratory to measure the displacement under higher frequencies. The system is capable of resolving displacement 10^{-2}Å from 50 Hz to MHz range[2]. The high sensitivity is largely due to the phase sensitive detection to discriminate the noise. However, for all the previous works, effort was only made to measure the amplitude of the strain. In the this paper we report the measurement of phase delay of the piezoelectric response using the double beam laser interferometer.

§ 2 Fundamental Principles and Experimental Technique

2.1 Measuring system and fundamental principles

The schematic diagram of the double beam laser interferometer is shown in Figure 1. The general principles and the description of the system were illustrated in an earlier paper[2]. When the two beams (reference beam and the probing beam) interfere with each other, the light intensity at a detection point vs the differential optical path of the two arms can be schematically illustrated by Figure 2. To achieve high sensitivity, we stabilize the system at A or B points of the curve. Under ideal situation, the signal at one stabilized point is in phase with the applied electric field while that at the other point has 180^0 phase shift with respect to the applied electric field.

In the real situation, even if the sample mounting does not introduce any extra phase shift, the phase shift can be caused by both the imaginary part of the piezoelectric strain coefficient and the detecting system. To separate the the contribution of the phase delay due to the imaginary part of the piezoelectric strain coefficient, we have to subtract the contribution to the phase shift from the detecting system. Quartz has a mechanical Q well above 1000 and virtually no dielectric loss in the radio frequency range[3]. Therefore, the phase delay of the piezoelectric response of the Quartz can be negleted compared with that of other materials with higher electric and mechanic loss. If a quartz sample is mounted properly so that the mounting does not introduce any extra phase shift, the phase shift measured by the system can be regarded as the phase shift due to the detecting system. We can then separate the contribution to the phase shift due to imaginary part of the piezoelectric response from the total phase shift:

$$\theta_P=\theta_T-\theta_C \qquad (1)$$

where θ_P *is* due to the imaginary part of the piezoelectric response, θ_T is the total detected phase shift and θ_C is the calibrated phase shift using quartz.

If a sinusoidal field is applied to the sample, the complex piezoelectric coefficient can be expressed as:

$$d^*=d'+jd''=S_0e^{j(\omega t+\theta)}/E_0e^{j\omega t}=(S_0/E_0)e^{j\theta} \qquad (2)$$

Separating the real and imaginary part of the piezoelectric coefficient, we have:

$$d' = (S_0/E_0)\cos\theta \qquad d'' = (S_0/E_0)\sin\theta \qquad (3)$$

where (S_0/E_0) is the amplitude of the d constant and θ is θ_P.

Using a Lock-in amplifier, we can measure both amplitude and phase shift of the induced displacement , hence we can separate the real and imaginary parts of the piezoelectric coefficient.

2.2 Critical experimental elements

2.2.1 Coherence improvement of the laser light

For a multimode He-Ne laser laser, the coherence length of the laser is limited (~30 cm) due to the simultaneous oscillation of many modes which satisfy the cavity resonce condition. It appeared that the coherence length of the light and the overlapping in space of the coherent wave packets from the reference and probing arm were very important for the sensitivity and stability of phase detection.

The coherence length of the light was improved by increasing the monochromacity of the light . A heavy filter was used to reduce the component of the lights with wavelength other than 6328Å. The loss in the intensity of the outcoming beam due to the filtering was compensated by increasing the driving field to raise the signal above the noise level.

The overlapping of the coherence wavepackets from probing and reference arms was improved by carefully matching the optical path lengths of probing and reference arms. The lengths of the two arms were measured and matched by adjusting the translation stage. In the experiment, we found that the sensitivity and stability of the phase detection was improved as the differential optical path length decreased.

2.2.2 Overlapping in space of reference and probing beams

In the space between the beam splitter and photodetector, the reference and probing beams are recombined by the beam splitter. Under the static condition (reference mirror and sample do not deform), It is relative easy to overlap the two beams between the BS and the detection plane. Even this is done perfectly, the two beams may still dislocate with respect to each other during the deformation of the sample or reference mirror if the two beams are not arranged properly in the

reference and probing arms. Clearly, this is caused by the fact that the beams are not strickly perpendicular to the reflecting surfaces. When the surfaces deform, not only the optical path lengths change, but the beams deviate from the original positions. If this happens, difficulty arises in the stability of phase detection. It is very difficult to prevent such a deviation from occuring under the repeated deformation of the sample and the reference mirror. The two reflecting surfaces of the sample have to be made strickly parallel and careful alignment of the beams is necessary to accomplish that.

2.2.3 Sample preparation and mounting

The samples were cut into bar shape with the length of the bar more than four time the width and thickness. The two ends of the bar were carefully polished and partially electroded by gold sputtering for the purpose of light reflection. Small coated mirrors could also be attached to the ends of the bar for the reflection purpose. The sample was mounted in a manner shown in Figure 3. The length of the contact between the sample and the sample holder was kept under 10% of the length of the bar. It was found that when the contact length was larger than this ratio, the clamping effect would affect the phase shift . For the sample measured at the resonance frequencies the length of the bar was made more than six time the width and thickness of the bar to obtain the pure mode. Epoxy was used to adhere the sample to the sample holder.

2.3 Smits's iterative method

To confirm the result obtained by the optical method, we used Smits's iterative method to determine the real and imaginary parts of the piezoelectric strain coefficients. In this technique, the admittance of the resonator was measured as a function of frequency, the values near the resonance frequencies were used to calculated the real and imaginary piezoelectric, elastic and dielectric constant by solving the simultaneous equations using the iterative method. The detail of this technique was clearly described by Smits[4]. In our experiment, the sample was cut to plate shape (length:width: thicknes=10:2:1), the admittance of the ceramic resonator was measured by an impedance analyzer (Hewlett Packard). A computer program was written to calculate the coefficients using the iterative method[5].

§3 Measurement on PZT-5 Ceramic Samples

Figure 4 shows the phase shift θ_p of PZT-5 as a function of frequency. Since the values are negative, the strain lags behind the driving electric field. It must be remembered that there is another 180^0 phase difference between the applied electric field and the strain due to the negative value of d_{31}. This is obvious and thus not included in θ_p. For frequency above 1kHz, the errors for the measurement with attached mirrors and without mirrors are 5% and 10% respectively. Below 1kHz, the error is larger due to the low frequency noise. Clearly the sample with mirrors attached to the ends exhibits greater phase shift than that without mirrors. Symbol Δ stands for the value measured by Smits's methods, clearly the value is in a better agreement with the measurement without the attached mirrors, the mass of the mirrors affects the phase shift although it does not affect the amplitude significantly .

Figure 5 shows the real and imaginary parts of the d_{31} coefficient as a function of frequency. Again, both the real and imaginary parts of the piezoelectric coefficients from the strain measurement and Smits method are in good agreement.

Figure 6 (a) shows the amplitude of the tranverse displacement (the displacement perpendicular to the applied electric field) and phase shift as a function of frequency at piezoelectric resonance frequencies for a long PZT5 piezoelectric ceramic bar (l=5.6cm). The amplitude peaks appear at fundamental and third harmonic resonance frequencies. The peak at the third harmonic frequency is much lower than that at the fundamental frequency because of the increased damping at higher frequency. θ_p decreases 180^0 at the fundamental frequency, then comes back at the second harmonic frequency and drops again by 180^0 at third harmonic frequency. It appears that the phase shift drops at the odd harmonic and rises at even harmonic frequencies.

To confirm that the phase delay at resonance frequencies is as illustrated in Figure 6(a). we calculate the phase shift of the displacement at the end of the bar with respect to the applied electric field in terms of vibration theory. Very similar to the derivation of Cady[3], we derive the phase shift to be determined by :

$$\cot\theta_p = -\sin(\omega l/V^E)/(\alpha l/V^E) \quad (4)$$

where V^E is the wave velocity under constant electric field and $\alpha=\omega/2Q_m$(Q_m is the mechanic quality factor). For PZT-5, V^E and Q_m are 2794 m/s and 70 respectively[6]. For the bar (l=5.6cm) used for the measurement, the phase shift was calculated according to eq. (4). The calculated pahse shift and measured phase shift are illustrated in Figure 6(b), they are in excellent agreement.

Acknowledgements

We wish to thank Dr. D. Damjonovic for providing us with computer program and assistance in the iterative method calculation.

Referencs

1 Q.M. Zhang, W.Y Pan and L.E.Cross, J. Appl.Phys. 63 (1988) 2429

2 W. Y. Pan and L.E.Cross, Rev. Sci. Instrum. 60 (1989) 2701

3 W. G. Cady , Piezoelectricity (Dover Publication, Inc. 1964)

4 J.G. Smits, IEEE Transaction on Sonic and Ultrasonic SU23 (1976) 393

5 D. Damjonovic, Ph.D thesis, The Pennsylvania State University (1987)

6 W.Y.Pan, L.E.Cross and B.R.Li, (Sumitted to IEEE Trans. on Sonics and Ultrasonics.)

LIST OF FIGURES

Figure 1: The Schematic diagram of the double beam laser interferometer.

Figure 2: The light intensity vs the differential arm length. A and B are the stabilization points.

Fugue 3: Sample geometry and mounting.

Figure 4: θ_p of PZT-5 ceramic as a function of frequency. Δ stands for the value calculated from Smits's method.

Figure 5 : d_{31} coefficients as a function of frequencies of PZT-5 ceramic :(a) real part and (b) imaginary part. Δ stands for the values calculated by Smits's method.

Figure 6 (a): The transverse displacement amplitude u and θ_p as a function of the driving frequency at high frequecy range for a long (l=5.6cm) PZT-5 ceramic bar.

Figure 6(b): θ_p as function of frequency at resonance frequency range. The continous curve is calculated from the vibration theory using modified Cady equation and the data points are measured using the laser interferometer.

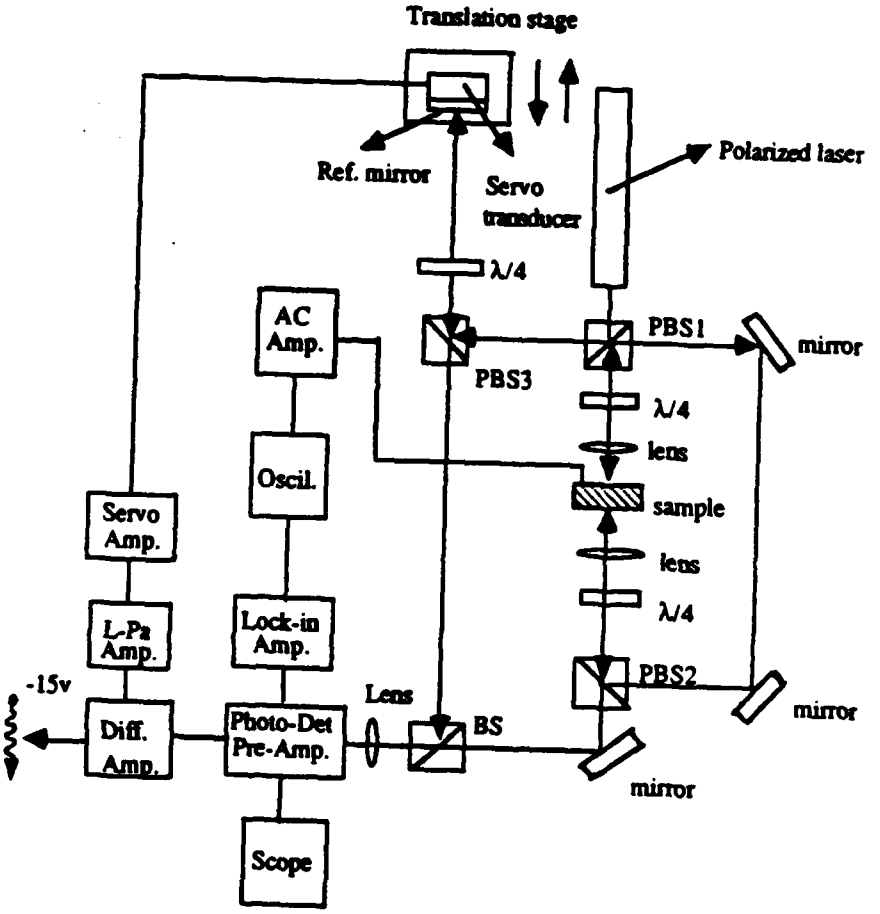
Translation stage
Ref. mirror
Servo transducer
Polarized laser
λ/4
AC Amp.
PBS1
mirror
PBS3
λ/4
lens
Oscil.
sample
Servo Amp.
lens
λ/4
L-Pa Amp.
Lock-in Amp.
PBS2
-15v
Lens
mirror
Diff. Amp.
Photo-Det Pre-Amp.
BS
mirror
Scope

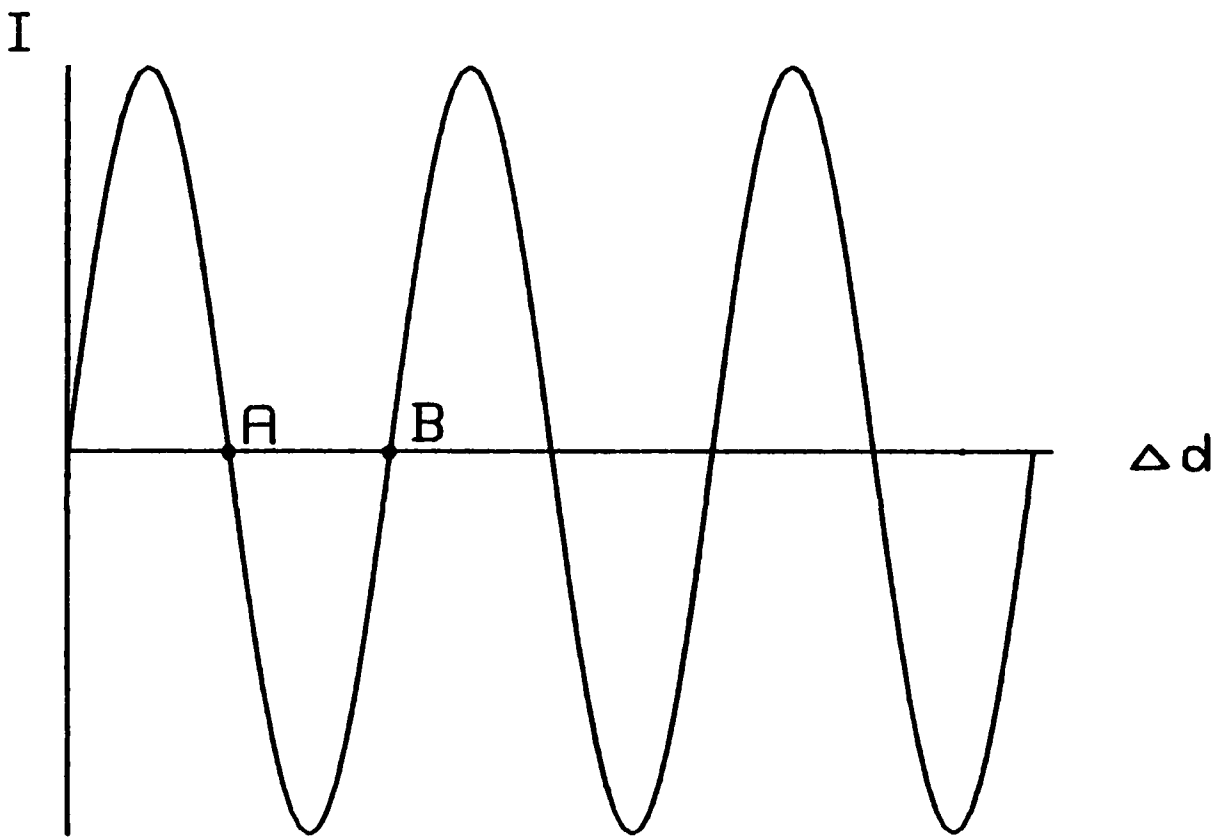
I
A
B
Δd

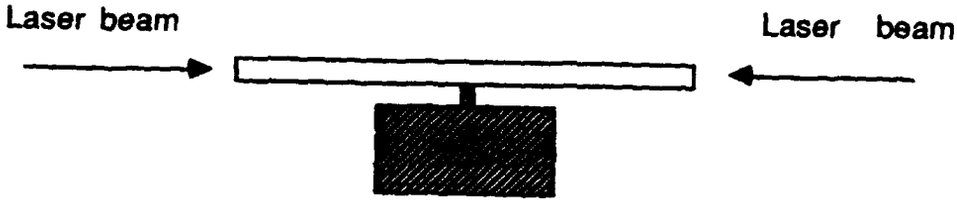
Laser beam
Laser beam

Fig 1

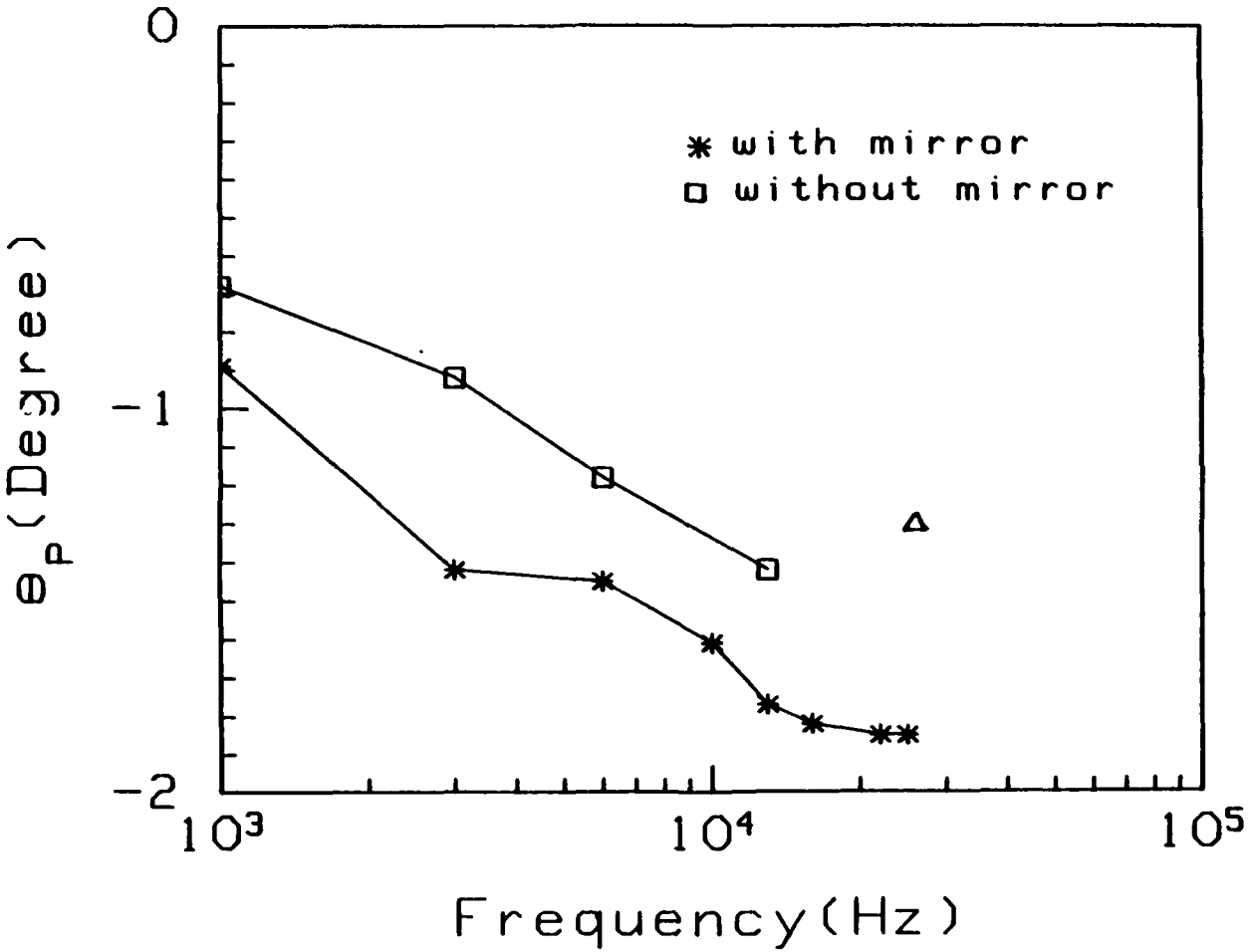
0
−1
−2
θ_p (Degree)
* with mirror
□ without mirror
Δ
10^3
10^4
10^5
Frequency (Hz)

Fig. 5

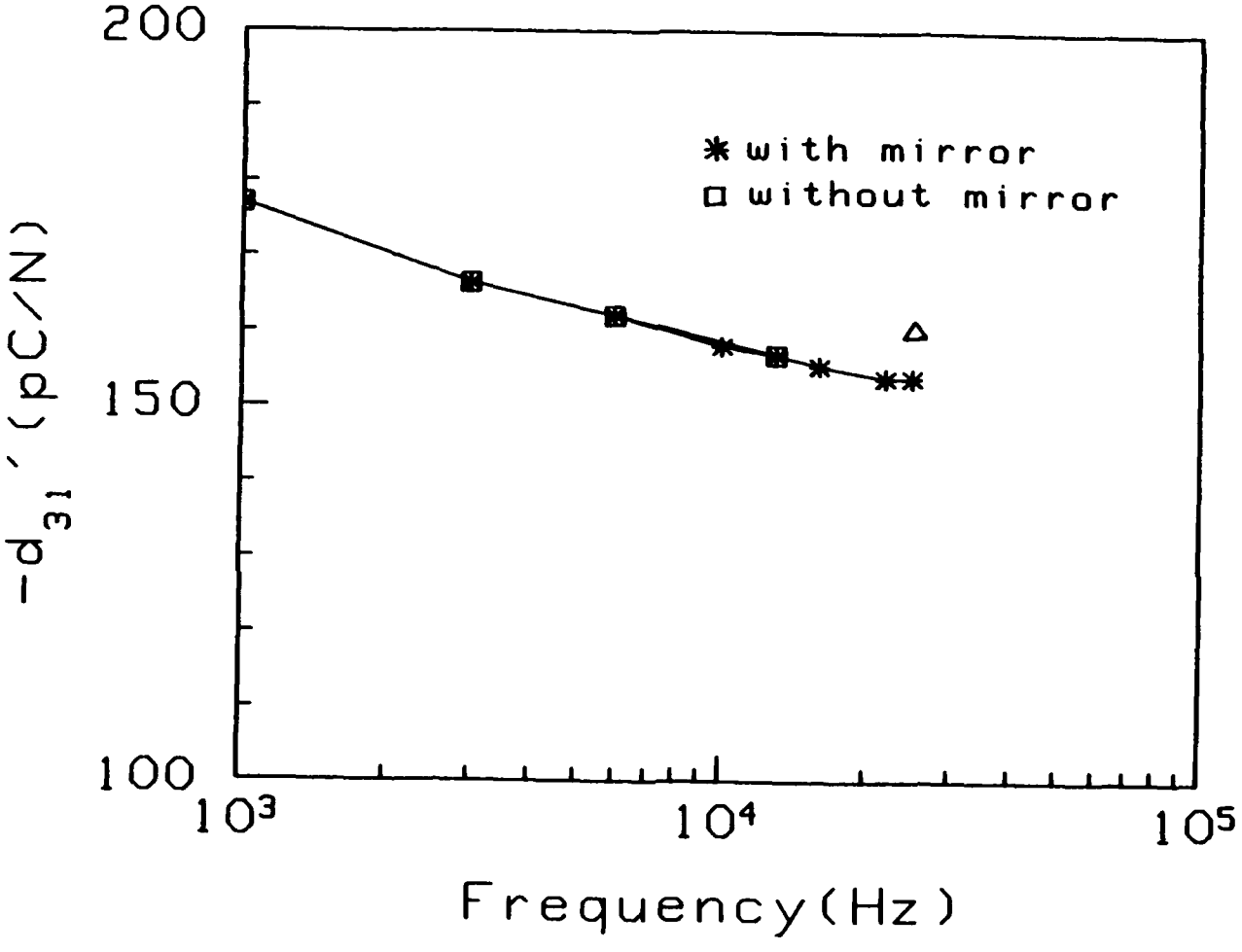
200
150
100
$-d_{31}'$ (pC/N)
* with mirror
□ without mirror
△
10^3
10^4
10^5
Frequency(Hz)

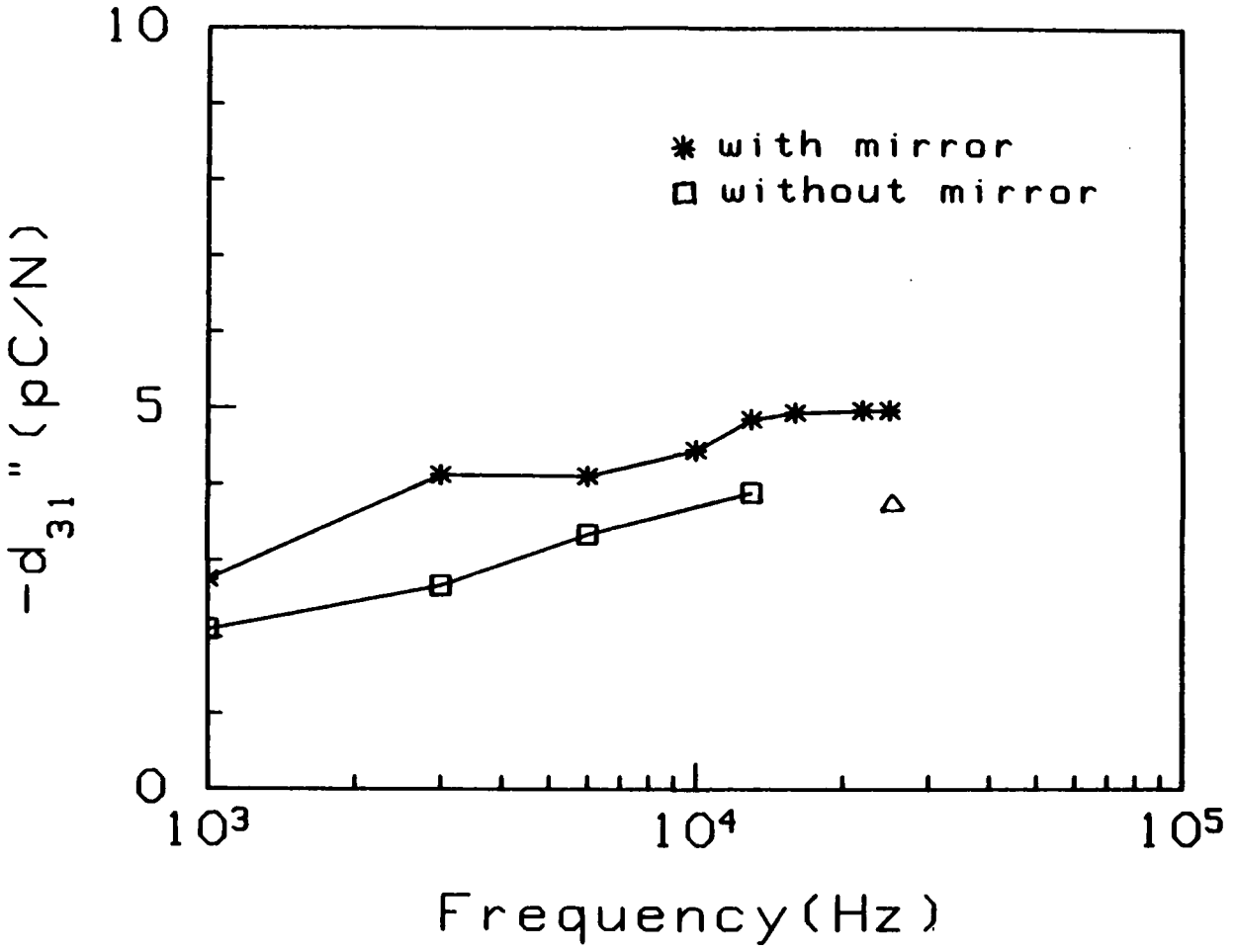
10
5
0
$-d_{31}$" (pC/N)
* with mirror
□ without mirror
△
10^3
10^4
10^5
Frequency(Hz)

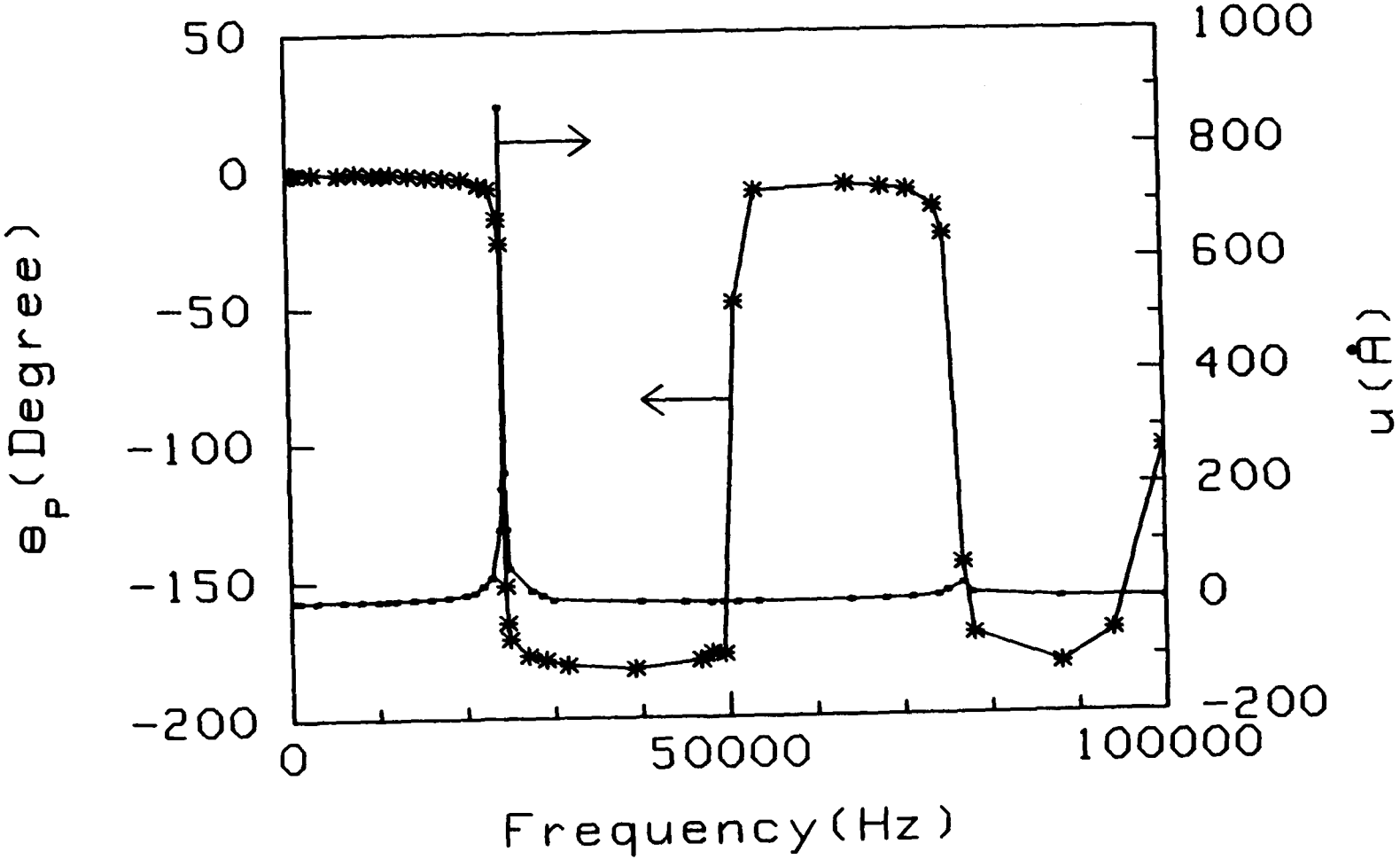
50
0
-50
-100
-150
-200
θ_p(Degree)
1000
800
600
400
200
0
-200
μ(Ω)
0
50000
100000
Frequency(Hz)

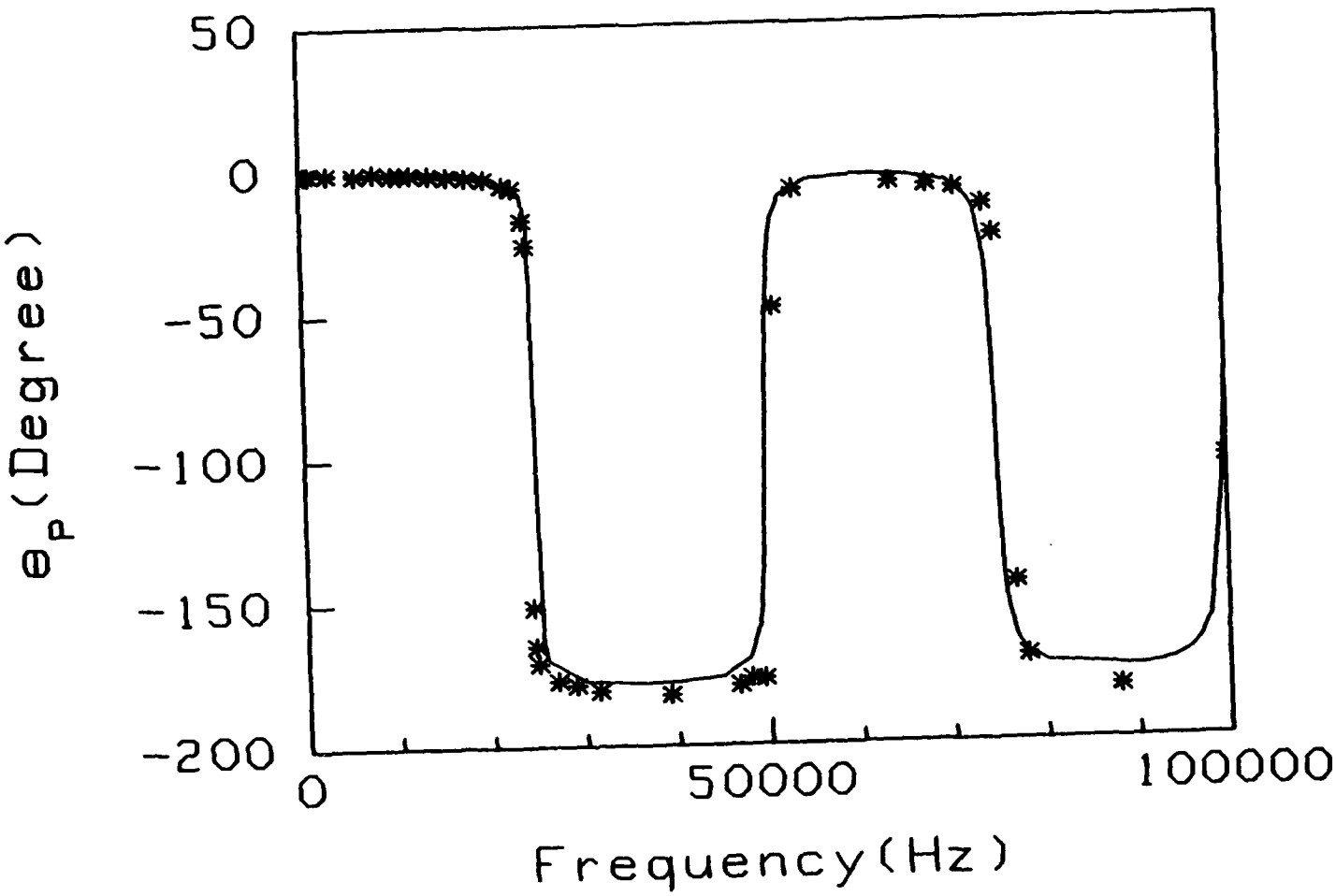
50
0
-50
-100
-150
-200
θ_p(Degree)
0
50000
100000
Frequency(Hz)

APPENDIX 7

Ferroelectrics, 1990, Vol. 109, pp. 000–000
Reprints available directly from the publisher
Photocopying permitted by license only

AN EQUIVALENT ELECTRIC CIRCUIT OF A PIEZOELECTRIC BAR RESONATOR WITH A LARGE PIEZOELECTRIC PHASE ANGLE

DRAGAN DAMJANOVIC
Materials Research Laboratory, The Pennsylvania State University, University Park, Pa 16802 USA

(Received October 21, 1989; in final form January 26, 1990)

The effect of the piezoelectric phase angle on an equivalent electric circuit of a piezoelectric resonator is discussed. A new equivalent circuit is derived which contains components associated with the piezoelectrically coupled energy losses. The impedance of the derived equivalent circuit is in excellent agreement with the experimentally determined impedance of a piezoelectric ceramic resonator having a significant piezoelectric phase angle.

Keywords: equivalent electric circuit, piezoelectric relaxation

1. INTRODUCTION

In the past several years there has been increased interest in relaxation of the piezoelectric properties of some single crystals,[1] ceramics,[2] and composite materials.[3] Although the piezoelectric relaxation in these materials is not yet fully understood, it is clear that it does not originate from an independent loss mechanism in the material, but is a result of an electromechanical coupling between the dielectric and mechanical losses operating in the material.[4] A particularly interesting consequence of this coupling is that the piezoelectric contributions to the total energy dissipation in a material may be either positive or negative, depending on the sign of the piezoelectric phase angle.[5]

In the vicinity of the resonant frequency, the relevant properties of a piezoelectric resonator may be described by an equivalent electric circuit. In practice, the usage of equivalent circuits greatly simplifies the analysis and design of piezoelectric transducers. The equivalent circuit, in standard form, for an unloaded resonator is shown in Figure 1a, and contains components which are associated with the mechanical losses (R_1) and dielectric losses (R_2) in the resonator.[6,7] Land *et al.*,[7] have noted that a resonator with a nonzero piezoelectric phase angle can no longer be represented by the standard equivalent circuit or its simple generalization in which the resistors R_1 and/or R_2 are replaced by a series of two resistors, one of which would then account for the piezoelectrically coupled energy losses. Martin[8] also discussed the effect of the piezoelectric losses on an equivalent circuit of a resonator, however, a new equivalent circuit which would contain elements associated with the electromechanically coupled energy dissipation processes was not derived.

In a recent study of ceramics based on lead titanate, which exhibit highly anisotropic piezoelectric properties,[9] a significant piezoelectric phase angle associated

EPS #8867 Paper Ref. No. 89 P110

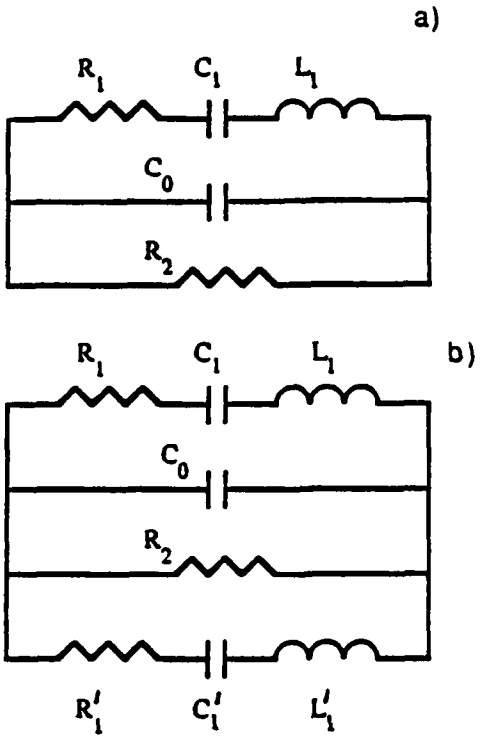

FIGURE 1 a) Standard equivalent circuit of an unloaded piezoelectric resonator. b) Equivalent circuit of a piezoelectric bar resonator with significant piezoelectric phase angle. All symbols are identified in the text. Components of the standard circuit are identical to the corresponding components of the new circuit in the limit $d_i \rightarrow 0$.

with the transverse (d_{31}) piezoelectric coefficient was observed. Some relevant material properties of the lead titanate ceramics modified with samarium used for this study are given in Table I. In the course of this work an attempt was made to derive an equivalent circuit which included the elements that represented the piezoelectrically coupled energy losses. With the relatively large piezoelectric phase angle of our lead titanate based ceramics, we were able to compare the impedance of the derived equivalent circuit with the measured impedance of the resonator. In addition, these modified lead titanate ceramics exhibit a change of sign of the real component of d_{31} with temperature, while the imaginary component of d_{31} remains the same in sign.[10] Thus, the piezoelectric phase angle changes its sign with temperature, permitting us to observe whether the derived circuit is sensitive to the sign of the piezoelectric phase angle.

2. DERIVATION OF THE CIRCUIT AND DISCUSSION

For simplicity, the bar-shaped resonator (Figure 2), with an electric field perpendicular to the length of the resonator is considered. For a ceramic resonator, the

TABLE I

Selected properties of modified lead titanate ceramics used for this study. The data are for ceramic samples in a shape of a thin disk and a bar, at 25°C and poled at 60 kV/cm.

Property	Symbol (units)	
Composition	$(Pb_{0.94}Sm_{0.06})(Ti_{0.98}Mn_{0.02})O_3$	
Lattice constants[1]	a (Å)	3.902
	c (Å)	4.072
Density[2]	ρ (kg/m^3)	7420
Transition temperature[3]	T_c (°C)	310
Elastic properties		
Poisson ratio	σ (–)	0.177
Elastic compliance	s^E_{11} (m^2/N)	7.65×10^{-12}
Mechanical quality factor[4]	Q_m	900
Dielectric properties		
Relative dielectric permittivity[5]	$\varepsilon^T_{11}/\varepsilon_0$ (–)	175
Dielectric loss factor[6]	$\tan\delta_\varepsilon$ (–)	0.01
Piezoelectric properties		
Transverse coefficient	d_{31} (C/N)	0.27×10^{-12}
Longitudinal coefficient	d_{33} (C/N)	60×10^{-12}
Piezoelectric loss factor[7]	$\tan\delta_{d_{31}}$ (–)	0.15
Planar coupling coefficient	k_p (–)	0.0038
Transverse coupling coefficient	k_{31} (–)	0.0025
Thickness coupling coefficient	k_t (–)	0.45

[1] Point group $4mm$
[2] 97% of the theoretical
[3] Cubic ($m3m$) to tetragonal ($4mm$)
[4] $Q_m = s^E_{11}/s^T_{11}$
[5] at 1 kHz: $\varepsilon_0 = 8.85 \times 10^{-12}$ F/m
[6] at 1 kHz: $\tan\delta_\varepsilon = \varepsilon^T_{11}/\varepsilon^T_{11}$
[7] $\tan\delta_{d_{31}} = d^T_{31}/d^T_{31}$

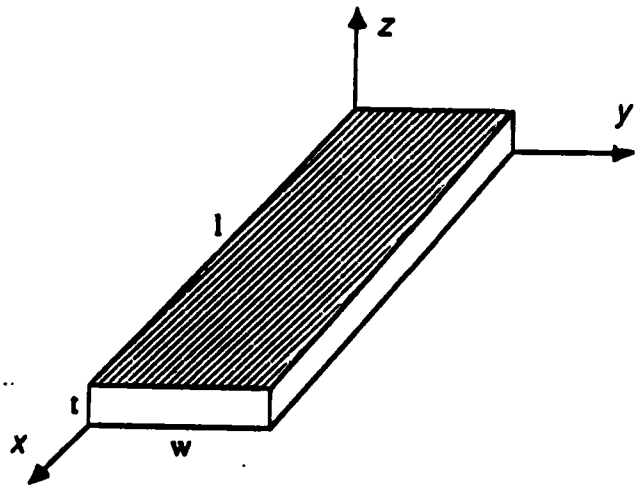

FIGURE 2 Piezoelectric bar resonator. The top and bottom surfaces are electroded.

direction of polarization is parallel to the driving electric field which is applied parallel to z-axis. The admittance Y of such a resonator which oscillates in the transverse mode is given by:[11]

$$Y = i\frac{\omega wl}{t}\left(\varepsilon_{33}^{T} - \frac{d_{31}^{2}}{s_{11}^{E}}\right) + i\frac{2wd_{31}^{2}}{\sqrt{\rho s_{11}^{E}}s_{11}^{E}t}\tan\frac{\omega l\sqrt{\rho s_{11}^{E}}}{2} \tag{1}$$

where l, t and w are the length, thickness and width of the bar, respectively, and ρ its density. ε_{33}^{T} is the dielectric permittivity at constant stress T and s_{11}^{E} is the elastic compliance at constant electric field E. The superscripts E and T are omitted hereafter for simplicity. Near the resonant frequencies, Equation (1) can be approximated by:[12]

$$Y = i\frac{\omega wl}{t}\left(\varepsilon_{33}^{T} - \frac{d_{31}^{2}}{s_{11}^{E}}\right) + i\frac{8wd_{31}^{2}}{\rho ls_{11}^{2}t}\sum_{n}\frac{1}{\frac{n^{2}\pi^{2}}{\rho s_{11}l^{2}} - \omega^{2}} \tag{2}$$

where summation goes over $n = 1, 3, 5, \ldots$ and n is the number of the overtone. In order to describe the effects of energy loss on the resonator's impedance, it is necessary to introduce the complex elastic and dielectric coefficients: $s_{11} = s_{11}' - is_{11}''$ and $\varepsilon_{33} = \varepsilon_{33}' - i\varepsilon_{33}''$. Similarly, in order to account for the effects of piezoelectric coupling on total energy losses, the piezoelectric coefficient is also assumed to be complex: $d_{31} = d_{31}' - id_{31}''$. The ratio d_{31}''/d_{31}' then defines the tangent of the piezoelectric phase angle. Equation (2) can be simplified by defining the fundamental resonant frequency as $\omega_0^2 = \pi^2/l^2\rho s_{11}'$ and writing $d_{31}^2/s_{11} = Reds + iImds$. Thus, one obtains, near the fundamental resonance ($n = 1$):

$$Y = i\omega(\varepsilon' - Reds)\frac{lw}{t} + \omega(\varepsilon'' + Imds)\frac{lw}{t} + i\omega\frac{8wl}{t\pi^{2}}(Reds + iImds)\left(\frac{\Omega - iM}{\Omega^{2} - iM^{2}}\right) \tag{3}$$

where $\Omega = (\omega_0^2 - \omega^2)/\omega_0^2$, $M = s_{11}''/s_{11}'$ and assuming $\omega^2/\omega_0^2 \approx 1$. A further manipulation of Equation (3) leads to:

$$Y = i\omega(\varepsilon' - Reds)\frac{lw}{t} + \omega(\varepsilon'' + Imds)\frac{lw}{t} + i\omega\frac{8wl}{t\pi^{2}}Reds\left(\frac{\Omega - iM}{\Omega^{2} + iM^{2}}\right) + i\omega\frac{8wl}{t\pi^{2}}(iImds)\left(\frac{\Omega - iM}{\Omega^{2} + iM^{2}}\right) \tag{4}$$

The third term in Equation (4) can be written in terms of the components of an electric circuit in the following way:

$$Y_3 = \frac{1}{R_1 + i\left(\omega L_1 - \frac{1}{\omega C_1}\right)} \tag{5}$$

where $R_1 = M/\omega C_1$, $C_1 = 8wl Reds/t\pi^2$ and $L_1C_1 = 1/\omega_0^2$. As expected, the resistance R_1 is associated with the mechanical losses,[11] and the product of the inductance L_1 and the motional capacitance C_1 defines the resonant frequency ω_0. Similarly, the first term defines the clamped capacitance $C_0 = (\varepsilon'_3 - Reds)lw/t$ and the second term, related to the dielectric losses, is represented by $1/R_2 = \omega(\varepsilon''_3 + Imds)lw/t$.

The last term in Equation (4) is proportional to the third term with the proportionality constant being $i(Imds/Reds)$. Therefore, one can use the following abbreviations: $R'_1 = R_1/i(Imds/Reds)$, $L'_1 = L_1/i(Imds/Reds)$ and $C'_1 = i(Imds/Reds)C_1$ and the last term in Equation (4) may be, then, rewritten as:

$$Y_4 = \frac{1}{R'_1 + i\left(\omega L'_1 - \frac{1}{\omega C'_1}\right)} \tag{6}$$

A simple calculation shows that the admittance in Equation (4) is identical to the admittance of the electric circuit shown in Figure 1b, with its components defined as in the text above. In the limit $d''_{31} \to 0$, the impedances of the standard equivalent circuit, Figure 1a, and the new one, Figure 1b, coincide, assuming $\omega^2/\omega_0^2 \approx 1$. It is interesting to note that, although the values of the "resistance" R'_1, "capacitance" C'_1 and "inductance" L'_1 are purely imaginary numbers, the total impedance $Z_4 = 1/Y_4$ of the corresponding branch of the new equivalent circuit may still be expressed in the same form as the impedance $Z_3 = 1/Y_3$ of the R_1-C_1-L_1 branch (compare Equations 5 and 6). In fact, the imaginary part of the Z_4, $R'_1 = i(Imds/Reds)R_1$, is now simply a reactive component added in parallel to the

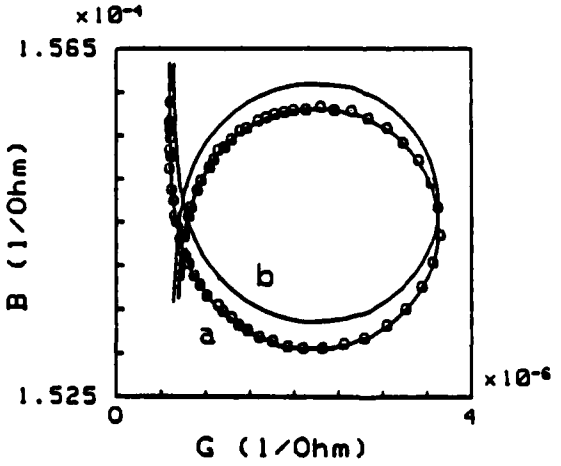

FIGURE 3 Admittance loop for a (Pb, Sm)TiO_3 resonator at 60°C. The circles represent experimental data, and the curves a) and b) correspond to admittance of the standard and new equivalent circuit, respectively. Dimensions of the resonator are: $l = 1.435 \times 10^{-2}$ m, $w = 1.454 \times 10^{-3}$ m, $t = 1.99 \times 10^{-4}$ m, $\rho = 7420$ kgm^{-3}. The values of the relevant coefficients are: $s'_{11} - is''_{11} = 7.694 \times 10^{-12} - i1.171 \times 10^{-14}$ m^2/N, $d'_{31} - id''_{31} = 6.703 \times 10^{-13} - i6.318 \times 10^{-14}$ C/N, $\varepsilon'_{33} - i\varepsilon''_{33} = 1.612 \times 10^{-9} - i6.764 \times 10^{-12}$ F/m.

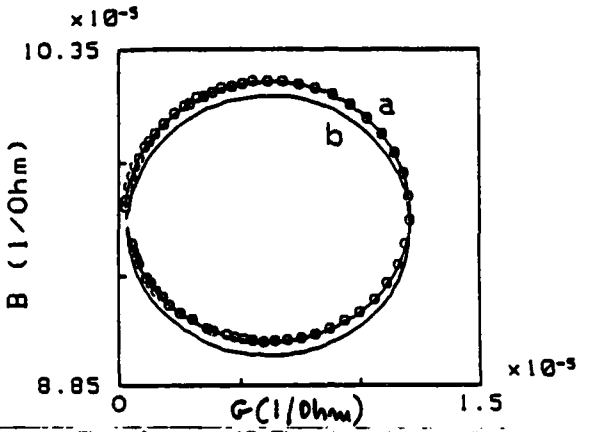

FIGURE 4 Same as for Figure 3, at −180°C. The values of the coefficients are: $s_{11}^{E} - is_{11}^{E}$ = 7.544 × 10^{-12} − i8.569 × 10^{-13} m²/N, $d_{31} - id_{31}^{\prime}$ = − 1.133 × 10^{-10} − i5.712 × 10^{-14} C/N, $\varepsilon_{33}^{T} - i\varepsilon_{33}^{\prime T}$ = 9.869 × 10^{-10} − i3.747 × 10^{-12} F/m.

impedance of the standard circuit. The real component of Z_4, which now contains $C_1^{\prime}$ and $L_1^{\prime}$, is a frequency dependent resistive term, added in parallel to the impedance of the standard circuit, in which the resistance R_1 also depends on frequency ($R_1 = M/\omega C_1$).[11]

Two examples were chosen to illustrate the validity of the new equivalent circuit. The admittance of a piezoelectric resonator made of lead titanate ceramics modified with samarium is measured at two different temperatures.[13] The sample was poled at 80 kV/cm. At these temperatures, +60°C and −180°C, the piezoelectric phase angle of the examined resonator was positive and negative, respectively. Figures 3 and 4 show the admittance ($Y = G + iB$, G − conductance, B − susceptance) loops of this resonator. The circles represent experimental points. Curve (a) is calculated using the new equivalent circuit in Figure 1b while curve (b) is obtained using the standard equivalent circuit shown in Figure 1a. The values of the complex piezoelectric d_{31}, elastic s_{11} and dielectric ε_{33} coefficients were calculated using an iterative method[14] from the experimental data[13] and these coefficients were used to calculate the components of the equivalent circuits in Figures 1a ($d_{31}^{\prime} = 0$) and 1b. It is clear that the derived circuit, as opposed to the standard, accurately describes the admittance of the investigated resonator, by taking into consideration the piezoelectric phase angle. The new equivalent circuit is also sensitive to the sign of the piezoelectric phase angle.

Finally, it is interesting to see the effect of the piezoelectric phase angle on the power dissipation of the derived circuit. The power dissipation P over one cycle is given by $P = (U_0 I_0 \cos\phi)/2$, where $U = U_0 \exp(i\omega t)$ and $I = I_0 \exp(i\omega t + \phi)$ are the AC driving voltage and current across the resonator, respectively. It follows that $P = \frac{1}{2} U_0^2$ Real $(1/Z_{tot})$, where the Z_{tot} is the total impedance of the circuit. Then:

$$P \alpha \text{Real}(1/Z_{\omega i}) = \frac{R_1}{R_1^2 + \left(\omega L_1 - \frac{1}{\omega C_1}\right)^2} + \frac{1}{R_2} - \frac{1}{\frac{Imds}{Reds}}\left(\frac{\omega L_1 - \frac{1}{\omega C_1}}{R_1^2 + \left(\omega L_1 - \frac{1}{\omega C_1}\right)^2}\right) \quad (7)$$

The origin of the last term in Equation (7) is in the piezoelectric coupling between the dielectric and mechanical losses in the resonator. Depending on the sign of the ratio *Imds/Reds* (which in turn depends on the sign of the piezoelectric phase angle, d_3^1/d_3^1) and frequency, this piezoelectric contribution to the power dissipation may be either positive or negative. The above result agrees with the predictions made by Holland[5] and Mezheretskii[15] that the electromechanically coupled losses in a piezoelectric material may increase or *decrease* the total energy dissipation.

3. SUMMARY

In summary, we have derived an equivalent circuit of a piezoelectric bar resonator which exhibits a significant piezoelectric phase angle. It is experimentally verified that the new circuit is necessary for an accurate description of the impedance of such a resonator near its resonance. The predictions that the piezoelectric contributions to the total energy losses in a piezoelectric resonator may be either positive or negative are confirmed by calculating the power dissipation in the derived circuit. The new equivalent circuit is sensitive to the sign of the piezoelectric phase angle.

REFERENCES

1. T. Yamaguchi and K. Hamano, *J. Phys. Soc. Japan*, **50**, 3956 (1981).
2. G. Arlt, *Ferroelectrics*, **74**, 37 (1987).
3. H. Ueda, E. Fukada and F. E. Karasz, *J. Appl. Phys.*, **60**, 2672 (1986).
4. G. Arlt, *Ferroelectrics*, **40**, 149 (1982).
5. R. Holland, *IEEE Transactions on Sonics and Ultrasonics*, **SU-14**, 18 (1967).
6. G. Arlt, *J. Acoust. Soc. Am.*, **37**, 151 (1965).
7. C. E. Land, G. W. Smith and C. R. Westgate, *IEEE Transactions on Sonics and Ultrasonics*, **SU-11**, 8 (1964).
8. G. E. Martin, *Proceedings of the 1974 IEEE Ultrasonics symposium*, Milwaukee, WI, Nov. 11–14, p. 613.
9. D. Damjanovic, T. R. Gururaja, S. J. Jang and L. E. Cross, *Mat. Lett.*, **4**, 414 (1986).
10. D. Damjanovic, T. R. Gururaja, and L. E. Cross, *Am. Ceram. Soc. Bull.*, **66**, 699 (1987).
11. D. Berlincourt, D. R. Curran and H. Jaffe, "Piezoelectric and Piezomagnetic Materials and Their Function in Transducers," in *Physical Acoustics* Vol. 1, Part A., ed. by W. P. Mason, Academic Press, New York 1964, P. 226 and 243.
12. R. Holland and E. P. EerNisse, *IEEE Transactions on Sonics and Ultrasonics*, **SU-16**, 173 (1969).
13. For experimental details and materials properties see References 9 and 10 and D. Damjanovic, PhD Thesis, The Pennsylvania State University, 1987.
14. J. Smits, *IEEE Transactions on Sonics and Ultrasonics*, **SU-23**, 393 (1976).
15. A. V. Mezheretskii, *Elektrikchestvo*, **10**, (1984).

APPENDIX 8

Ferroelectrics, 1989, Vol. 93, pp. 379–386
Reprints available directly from the publisher
Photocopying permitted by license only

TEM STUDIES OF $Pb(Mg_{1/3}Nb_{2/3})O_3$-$PbTiO_3$ FERROELECTRIC RELAXORS

A. D. HILTON, C. A. RANDALL,† D. J. BARBER and T. R. SHROUT†
Dept. Physics, University of Essex, Wivenhoe Park, Essex, U.K.

(Received August 29, 1988)

TEM was used to observe nanoscale microstructural changes which occur over a range of PMN-PT compositions. Increasing PT additions to the PMN-PT solid solution modify ferroelectric and structurally ordered domains. The relevance of nanostructural changes to the corresponding dielectric properties are briefly discussed.

Keywords: transmission electron microscopy, ordering, perovskite, ferroelectric, morphotropic phase boundary.

1. INTRODUCTION

$Pb(Mg_{1/3}Nb_{2/3})O_3$-$PbTiO_3$(PMN-PT) solid solutions exhibit a range of ferroelectric properties dependent on composition. Solid solutions low in PT content show diffuse frequency dependent Paraelectric (PE)—Ferroelectric (FE) phase transitions characteristic of relaxor ferroelectrics. Such compositions have potential applications in electrostrictive and piezoelectric devices. The behavior of relaxor ferroelectrics is usually attributed to an underlying heterogeneous distribution of B site cations over the perovskite lattice. Microregions of varying B cation composition have different transition temperatures and cause a 'smearing out' of the PE→FE phase transition.[1] A size distribution of microregions gives rise to a dielectric dispersion within the radio frequency range, a feature also characteristic of relaxor ferroelectrics. Microregions which have undergone the PE→FE transition spontaneously polarize parallel to ⟨111⟩ crystallographic directions (when the low temperature ferroelectric symmetry is rhombohedral) and are then referred to as polar microregions. Polarization vectors in each region are randomly oriented in the bulk and can be thermally switched to any of the 8 equivalent ⟨111⟩ directions.[2] If the thermal energy of the system is sufficiently reduced, the polarization vectors of the polar microregions can be stabilized and polar microdomains develop. Unpoled relaxor ferroelectrics exhibit optical macroscopic isotropy below the Curie temperature. However, when an external field is applied, a relaxor becomes anisotropic and macroferroelectric domains are observed to form.

Increasing the PT content to the PMN-PT solid solution is accompanied by the onset of more 'normal' ferroelectric behavior. 'Normal' ferroelectrics exhibit a sharp PE→FE phase transition at the Curie temperature. On cooling through the Curie temperature spontaneous dipoles form and align within macroferroelectric

†Materials Research Labs., Pennsylvania State University, University Park, PA USA

domains to give regions of uniform polarization. These domains arrange themselves within the bulk in order to minimize the free energies associated with depolarization fields and strain.

At about 35 mole % PT† the PMN-PT phase diagram exhibits a morphotropic phase boundary (MPB). Below 35 mole % PT, the transition to the ferroelectric phase is accompanied by a lowering of symmetry from cubic to rhombohedral. Above 35 mole % PT, the low temperature ferroelectric phase is tetragonal. However, the MPB composition varies with temperature.[3] Thus on cooling compositions which lie close to the MPB, tetragonal and rhombohedral symmetries can develop successively. PMN-PT compositions near the MPB are both of technical and scientific interest since anomalously high electrostrictive coefficients are known to exist in such compositions.[4]

PMN-PT solid solutions have the perovskite crystal structure. The possibility for structural ordering in many $Pb(B^{I}_{x}B_{1-x}^{II})O_3$ perovskites exists since more than one cation shares the B site. The tendency to order arises if B^{I} and B^{II} cations vary in ionic size and valance. In this case ordering tends to reduce the total strain and electrostatic energy respectively of the lattice.[5] Ordering takes place by the diffusion of constituent B cations to neighboring B sites. The $2a_0 \times 2a_0 \times 2a_0$ (where a_0 is the lattice parameter) FCC superstructure which results can be detected by electron diffraction. In addition, the distribution of structural order can be revealed by TEM dark field (DF) imaging of superlattice reflections. The existence of short range 1:1 order of B^{I} and B^{II} cations in PMN has already been established using TEM high resolution[6] and DF techniques.[7]

Though the dielectric and piezoelectric properties of PMN-PT solid solutions have been thoroughly investigated, few studies on the associated nanostructures have been reported. This paper aims to correlate the results obtained on the nanostructures, observed by TEM, in various PMN-PT compositions, to the relevant dielectric properties.

2. EXPERIMENTAL

Ceramic discs were prepared via the Columbite route in order to minimize pyrochlore formation.[8] These discs were mechanically polished to a thickness of about 30 μm prior to atom beam milling at 5KV in order to obtain thin TEM samples. Microstructural observations were made on a JEOL 200 CX TEM. Low temperature observations were possible using a Hexland liquid nitrogen cooled stage.

3. RESULTS AND DISCUSSION

3.1 Ferroelectric Domains

Figure 1(a) exhibits a bright field (BF) image of the relaxor composition 0.93 PMN–0.07PT at −170°C. On heating the mottled contrast quickly disappears. Figure 1(b) is a bright field image of the same area as shown in Figure 1(a) after a short

†This value is dependent on processing history.

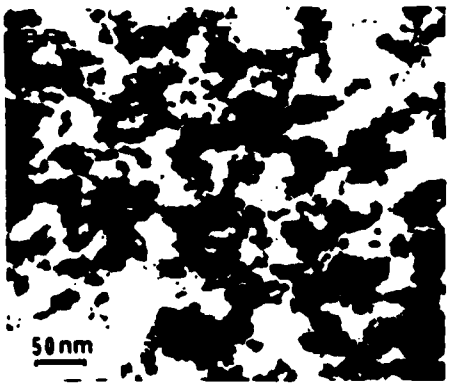

FIGURE 1(a) Mottled contrast observed at −170°C in 0.93PMN-0.07PT. Dark area (~80 nm in size) are associated with polar microdomains.

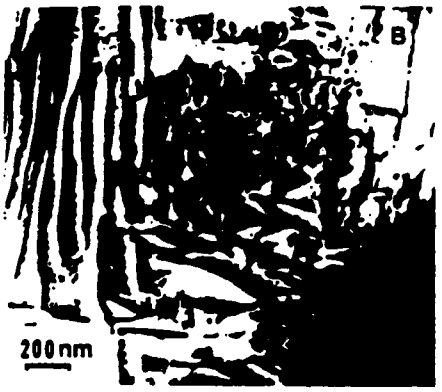

FIGURE 1(b) Macropolar-domains observed in 0.93PMN-0.07PT at −170°C.

period of being radiated by the electron beam. This exhibits a complex array of macro-ferroelectric domains. High contrast x-ray film was required to record the mottled contrast in Figure 1(a) since the transformation to the macro-domains observed in Figure 1(b) took place almost instantaneously under the electron beam irradiation. The dark areas (~80nm in size) observed in Figure 1(a) are believed to originate from the dynamical contrast associated with the stabilization of micro-polar regions. Radiation with the electron beam is believed to both locally heat and strain the sample. Heating the sample causes the micropolar domains to become thermally unstable and the contrast disappears. The simultaneous application of stress (caused by the electron beam bending the specimen foil) aligns polar vectors and macro-ferroelectric domains develop (1(b)). A similar micropolar–macropolar transition has also been observed in a TEM study of 8.2/70/30 PLZT.[9]

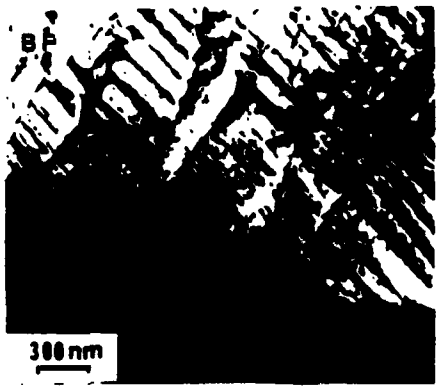

FIGURE 2 Complex macropolar domain structure observed in 0.8PMN-0.2PT at −170°C.

It is interesting to note that no polar microdomains were observed in relaxor PMN at low temperatures. This is possible if the micropolar domains are thermally switching or if the spontaneous distortions of the dipoles are too small to be detected.

Figure 2 shows a BF image of complex macrodomain structures observed in 0.8PMN-0.2PT. No polar microdomains could be imaged in this composition. However the complex configuration of the macrodomains may imply the existence of many nucleation sites and thus the early presence of polar microdomains. This situation may also be complicated further by surface depolarization effects that exists in thin foils.

Figure 3 shows a BF micrograph of macro ferroelectric domains observed at room temperature in 0.6PMN-0.4PT. This composition is close to the MPB and exhibits a 'normal' PE→FE phase transition. Both 90° and 180° domains are present. The 90° domains are twinned on {110} planes and alternate domains have different widths.

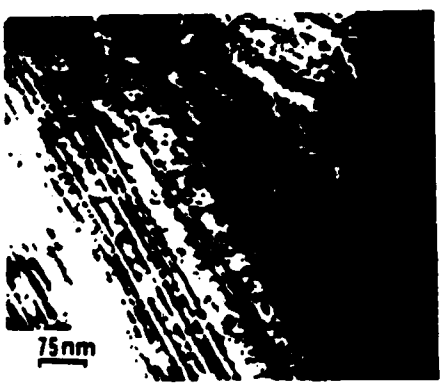

FIGURE 3 90° and 180° domains observed in 0.6PMN-0.4PT at room temperature. Alternate 90° domain widths are approximately 20nm and 40nm respectively.

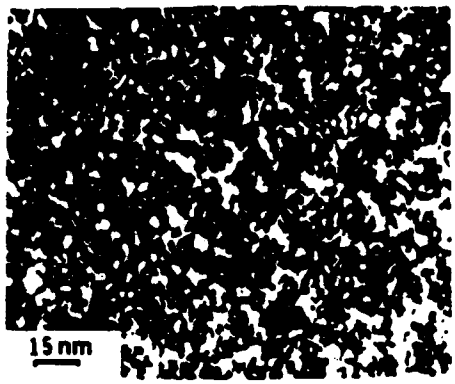

FIGURE 4(a) Structurally ordered domains observed in PMN (~6nm in size).

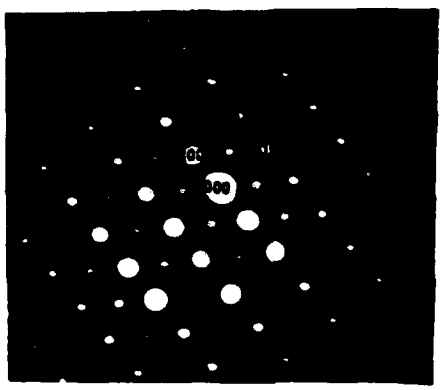

FIGURE 4(b) ⟨110⟩ SADP associated with Figure 4(a). The superlattice F spots are indicated.

3.2 Structurally ordered domains

Figure 4(a) exhibits light domain contrast ~6nm in size, observed by dark field (DF) imaging the {3/2, 3/2, 3/2} superlattice reflection in PMN. These domains are believed to be associated with regions of short range 1:1 ordering of magnesium and niobium cations on the perovskite lattice. The superlattice reflections (F spots) are indicated in the ⟨110⟩ selected area diffraction pattern (SADP) shown in Figure 4(b). With increasing PT content to PMN the ordered regions are observed to reduce in size. Associated with this reduction in size is a weakening of intensity of the F spot. Figure 5 exhibits the ⟨110⟩ SAPD observed in 0.6 PMN-0.4PT. In this composition the F spot is undetectable which signifies a statistically homogeneous disorder of magnesium and niobium cations over the lattice.

The implications of 1:1 B cation order in $Pb(B^{I}_{x}B^{II}_{1-x})O_3$ perovskites when $x = 1/3$ (as in the case for PMN) are unclear. In $x = 1/2$ perovskites 1:1 ordering of B^{I} and B^{II} cations is expected to reduce the variation between local chemistry and bulk stoichiometry. In PMN, regions of 1:1 short range order of Mg and Nb ions

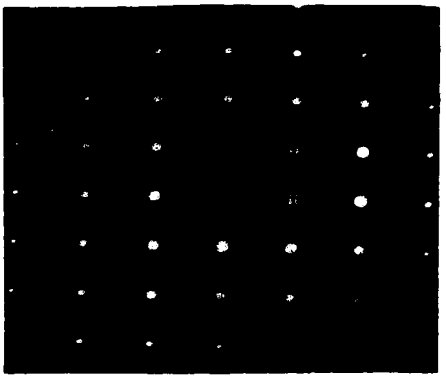

FIGURE 5 (110) SADP in 0.6MN-0.4PT. The F spots are absent.

deviate from bulk stoichiometry and necessarily result in volumes rich in Mg (ordered) and separate regions rich in Nb (presumably statically disordered). Thus, in the absence of compensating charge effects, huge space charges would be generated in the lattice between ordered and disordered regions (with effective positive and negative charges respectively). Even though it would appear that it is energetically favorable for Mg and Nb ions to order (from electrostatic and strain considerations) only limited short range order is observed, even after prolonged annealing. It is proposed that any space charges generated, during the 1:1 ordering of Mg and Nb ions, limit the degree of order obtainable and an equilibrium size of ordered domains is reached when the lattice is no longer able to compensate for such charges.

Titanium ions also occupy B sites in the PMN-PT solid solution, and since PMN-PT compositions exhibit a progressive decrease in B site order with increasing PT additions it is possible that Ti ions dilute the electrostatic and strain interactions between Nb and Mg ions, thus reducing their tendency to order.

3.3 Microstructural: dielectric property relations

Figure 6 shows the dielectric behavior near the PE→FE transition temperature for a range of PMN-PT compositions. Clearly more 'normal' ferroelectric behavior is associated with increasing PT content. The existence of polar microdomains observed by TEM in the 0.93 PMN-0.07PT relaxor composition supports early theories regarding polarization mechanisms in relaxor materials. In the same composition the micropolar—macropolar domain transition has been observed and followed 'in situ'. This serves to simulate the isotopic/anisotopic behavior observed in such compositions on application of an electric field.

With increasing PT content only macroferroelectric domains are observed, characteristic of 'normal' ferroelectrics. This trend is reflected in the dielectric curves shown in Figure 6.

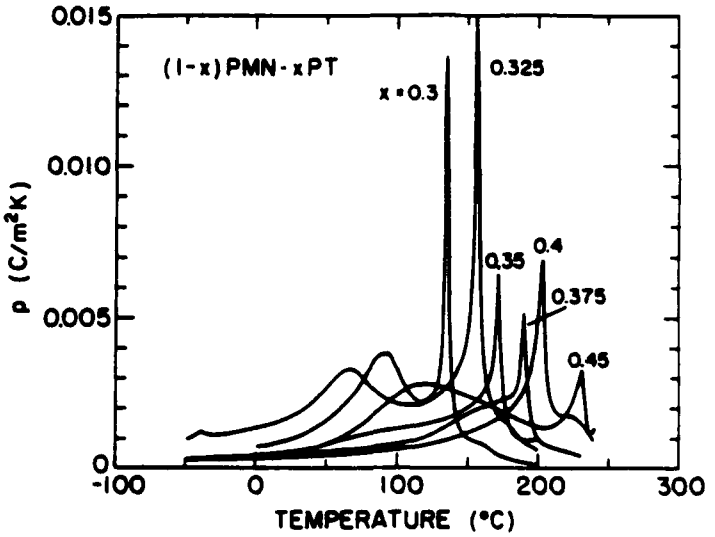

FIGURE 5 Pyroelectric coefficient vs temperature for various compositions in the (1-x) PMN:xPT solid solution.

PMN:PT can be suitably adjusted for the room temperature pyroelectric applications. In the present studies we focussed on the MPB compositions especially.

In most cases like in the dielectric data, two major anomalies corresponding to the phase transitions cubic → tetragonal → rhombohedral, were observed.

Figures 5 and 6 show the pyroelectric coefficient and the plots of polarization, respectively, for various compositions in the (1-x) PMN-xPT solid solutions as a function of temperature. Pyroelectric coefficient increases with mole% PT. However, for x more than ~ 0.325, the pyroelectric coefficient decreased. The composition with the maximum pyroelectric coefficient and polarization P_s (Figure 7) might be at the morphotropic phase boundary similar to that observed in the K vs

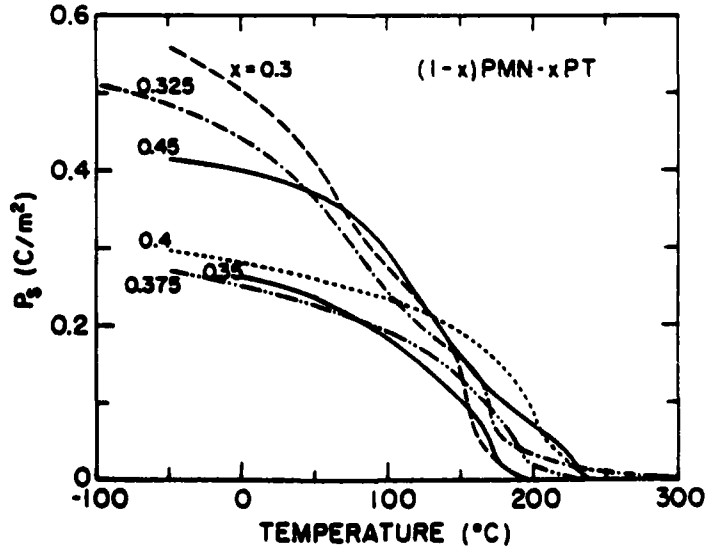

FIGURE 6 P_s vs T plots for (1-x) PMN:xPT system.

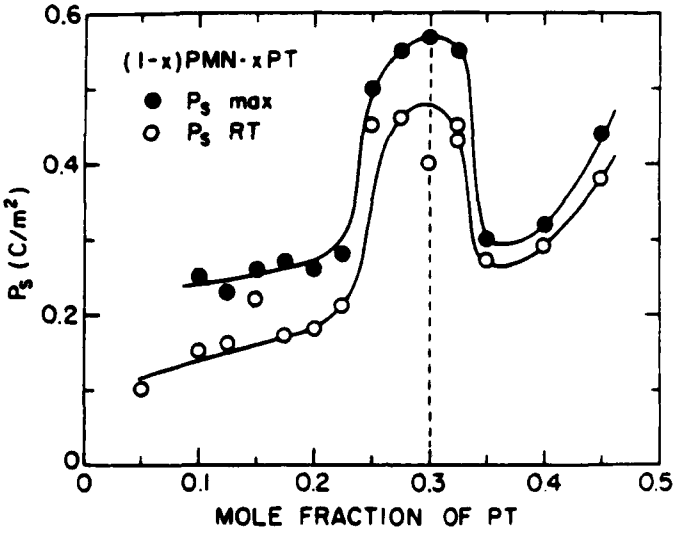

FIGURE 7 Maximum and room temperature polarization values as a function of mole fraction of PT.

T studies. The broadening of the peaks in the pyroelectric coefficient vs temperature plots may be due to the coexistence of the ferroelectrics and paraelectric phases. The presence of two peaks in the p vs T similar to that of K vs T (Figure 8) data could be due to the slight curvature in the MPB boundary. The spontaneous polarization decreases gradually with increasing temperature, but does not vanish at the transition temperature of the solid solution. This is typical of a relaxor ferroelectric. It is expected that the micro-regions of ferroelectric and paraelectric coexist in the transition region near the transition temperature. The maximum pyroelectric coefficient is observed at the compositions $x \sim 0.3$–0.325 as shown in Figure 5.

CONCLUSIONS

The largest dielectric constants are found at the composition $x \sim 0.30$–0.325 mole% of $PbTiO_3$. The magnitude of dielectric constant before and after poling changes very little for the composition near the MPB. Anomaly in the plot of the transition temperature vs mole fraction of $PbTiO_3$ was observed at the composition $x = 0.30$–0.325.

Maximum peak value to the pyroelectric coefficient was observed for $x \sim 0.325$. The pyroelectric coefficient vs temperature plots showed two anomalies similar to those of dielectric data. This suggests the possibility of the curvature in the morphotropic phase boundary in the PMN:PT system.

Maximum values of the spontaneous polarization was observed for $x \sim 0.30$–0.325. It has been shown in the present study that ferroelectric solid solution of PMN:PT with composition close to the morphotropic phase boundary exhibit the high dielectric constant and relatively superior pyroelectric properties.

Based on the present dielectric and pyroelectric studies the morphotropic phase boundary in the system PMN:PT possibly exists at $x \sim 0.30$–0.325.

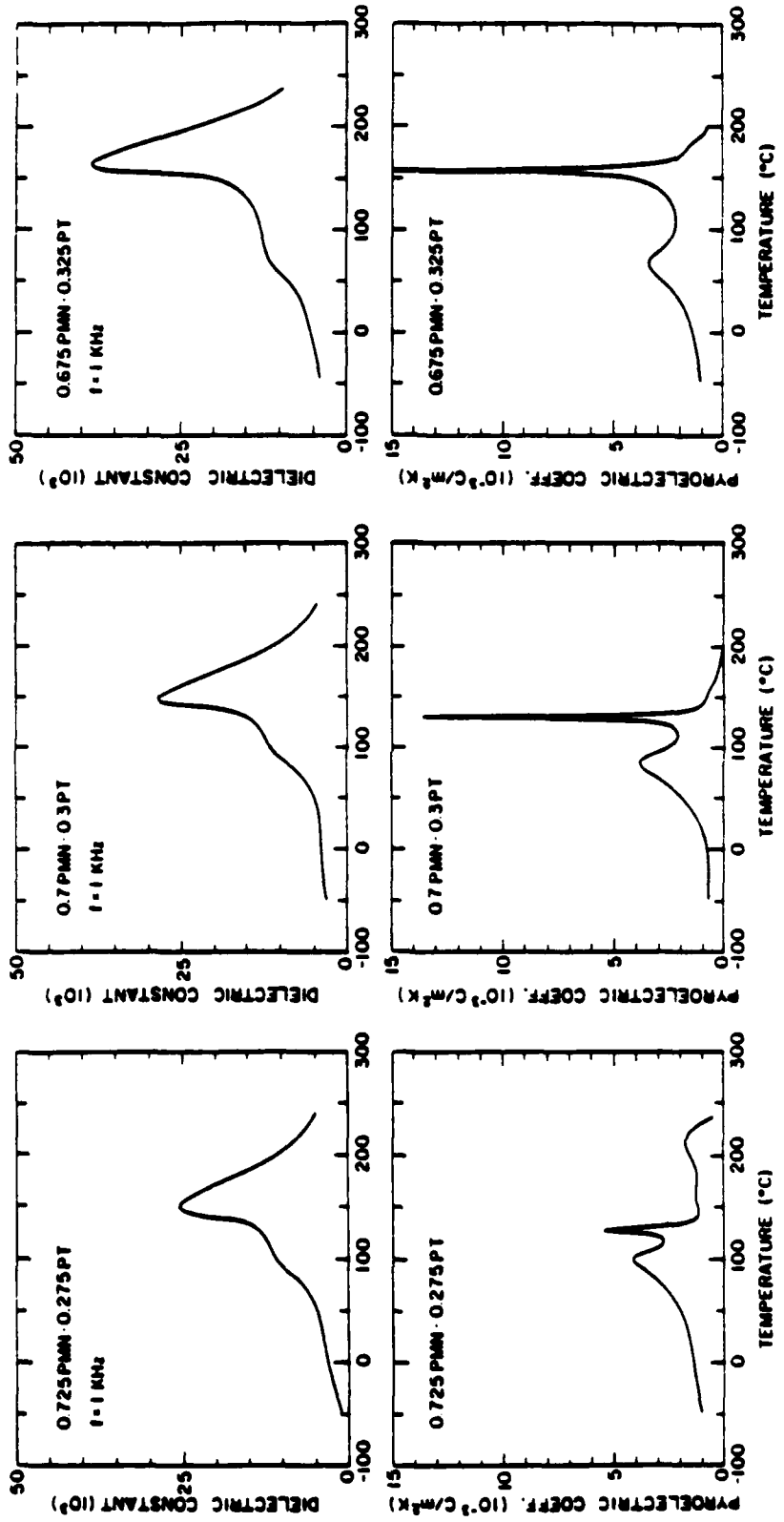

FIGURE 8 ε p vs T and K vs T plots for the compositions 0.725 PM:0.275 PT, 0.70 PMN:0.3 PT and 0.675 PMN:0.325 PT. Both sets of measurement indicate the presence of two peaks.

X-ray studies in an attempt to establish the proposed curvature in the morphotropic phase boundary is in progress.

ACKNOWLEDGEMENT

The authors wish to thank Professor L. E. Cross for various stimulating discussions and Mr. N. Yang for many samples preparations.

REFERENCES

1. G. A. Smolenskii and A. I. Agranovskaya, *Sov. Phys. Tech. Phys.*, **3**, 1380–82 (1958).
2. S. J. Jang, Ph.D. Thesis, The Pennsylvania State University (1979).
3. V. A. Bokov and I. E. MyL'nikova, *Sov. Phys.-Solid State*, **3**, 613 (1961).
4. G. A. Smolenskii, V. A. Isupov, A. I. Agranovskaya and S. N. Popov, *Sov. Phys.-Solid State*, **2**, 2584 (1961).
5. W. Wersing, *Ferroelectrics*, **7**, 163–165 (1974).
6. Lu Hahn, Kenji Uchino and Shoichiro Nomura, *Japan J. Appl. Phys.*, **17**, 637–641 (1978).
7. H. M. Barnett, *J. Appl. Phys.*, **33**, 1606 (1962).
8. J. Kuwata, K. Uchino and S. Nomura, *Ferroelectrics*, **37**, 579–582 (1981).
9. S. L. Swartz and T. R. Shrout, *Mat. Res. Bull.*, **17**, 1245 (1982).
10. R. L. Byer and C. R. Roundy, *Ferroelectrics*, **3**, 333 (1972).
11. B. Jaffe, R. S. Roth and S. Marzullo, *J. Res. NBS*, **55**, 239–253 (1955).
12. A. Reisman, Academi Press, New York (1970).
13. K. Carl and K. H. Hardtl, *Phys. Stat. Sol. (a)*, **8**, 87–98 (1971).
14. V. A. Isupov, **12**, 1084–1088 (1970).
15. A. F. Devonshire, *Phil. Mag.*, **40**, 1040 (1949).

APPENDIX 10

Reprinted from the Journal of the American Ceramic Society Vol. 72, No. 4 April 1989

journal

J. Am. Ceram. Soc., 72 [4] 599–604 (1989)

Electrostrictive and Dielectric Response in Lead Magnesium Niobate–Lead Titanate (0.9PMN · 0.1PT) and Lead Lanthanum Zirconate Titanate (PLZT 9.5/65/35) under Variation of Temperature and Electric Field

Qiming Zhang, Wuyi Pan, Amar Bhalla,* and Leslie E. Cross*

Materials Research Laboratory, The Pennsylvania State University, University Park, Pennsylvania 16802

In situ measurements of electrostrictive strain and effective dielectric constant for two ferroelectric relaxor materials, lead magnesium niobate–lead titanate (0.9PMN · 0.1PT) and lead lanthanum zirconate titanate (PLZT 9.5/65/35), were performed in the temperature ranges near their respective mean Curie points under the variation of applied electric field. The measurement results show that the polarization-related electrostrictive coefficients Q_{ij} are not constant under variation of temperature and electric field. The observed anomaly in Q_{ij} indicates the dynamic behavior of the existing micropolar domains and its coupling to local defect structure. The data also support the idea that at temperatures far above the mean Curie point, there is still a substantial amount of micropolar domain and the response of the relaxor materials at the experimental temperature range is from the combined contributions due to induced polarization and micropolar domain flipping. [Key words: lead, lanthanum, zirconate, titanate, dielectric materials.]

I. Introduction

UNLIKE normal ferroelectrics, which have well-defined Curie temperatures to separate the ferroelectric and paraelectric phases, relaxor ferroelectrics exhibit a broad transition peak in the weak-field dielectric constant. This kind of transition behavior is often referred to as diffused phase transition (DPT) in the literature.[1,2] A distinct feature of DPT in the case of ferroelectric relaxor materials is the frequency dependence of the weak-field dielectric constant maximum T_m, and upon increasing the frequency, T_m shifts upward with a reduced dielectric constant maximum. This apparently cannot be related to the intrinsic phase transition of phonon softening. It is proposed that the relaxor materials can be viewed as having a strong breakdown of the translational symmetry arising from local compositional fluctuations, and related to it there is a distribution of the Curie temperature over a wide temperature range from different individual microvolumes.[1-3] Each microvolume is ferroelectric in nature at a temperature below its T_c and at a given temperature a relaxor material is an assembly of ferroelectric and paraelectric microregions. Thus the DPT in such materials can be recognized as a relaxor phase transition (RPT).

Direct experimental evidence which supports this interpretation is from the measurement of the temperature dependence of the refractive index $n(T)$ and strain $s(T)$ of ferroelectric relaxors.[4,5] These results show that both $n(T)$ and $s(T)$ deviate from the expected linear temperature dependence of pure paraelectric behavior and such deviations occur at temperatures far above T_m. Therefore, it is interesting to ask what is the dynamic behavior of the system and to what extent does it depend on the existing micropolar domains.

In this paper, we report an in situ electrostrictive and dielectric study of two typical relaxor materials: lead lanthanum zirconate titanate (PLZT) of composition 9.5/65/35 and lead magnesium niobate–lead titanate (0.9PMN · 0.1PT). These measurements were carried out at temperatures from below T_m to far above that, in a region of great interest from both a theoretical and practical point of view, and with variation in the amplitude of the measured electric field. We will show that, related to the dielectric anomaly, there is an anomaly in the strain response behavior. On the basis of the concept of RPT, we will discuss the function of different components in the relaxor materials, the dynamics of the micropolar domains, as well as the effect of local defects on polarization vector flipping.

The electrostrictive coefficients are defined by

$$s_{ij} = M_{ijkl} E_k E_l \tag{1a}$$

$$s_{ij} = Q_{ijkl} P_k P_l \tag{1b}$$

where s_{ij} are the strain components and M_{ijkl} and Q_{ijkl} are the electrostrictive coefficients related to the electric field E and polarization P of the sample. In the later discussion, these electrostrictive coefficients are represented by M and Q. Using the convention that M_{ijkl} or $Q_{ijkl} = M_{mn}$ or Q_{mn} ($m, n = 1, 2, 3$), in our experimental case where only M_{11} (Q_{11}) and M_{12} (Q_{12}) were measured, the following equations are used:

$$s_{33} = M_{11} E_3^2, \qquad s_{33} = Q_{11} P_3^2 \tag{2a}$$

$$s_{11} = M_{12} E_3^2, \qquad s_{11} = Q_{12} P_3^2 \tag{2b}$$

The effective dielectric constant in our measurement is defined as

$$\varepsilon = P_{max} / \varepsilon_0 E_{max} \tag{3}$$

Hence, in a weak field, it is the dielectric constant in the normal sense, and in a strong field, it is a measure of the averaged dielectric response of the sample when there are a polarization hysteresis loop and a nonlinearity.

II. Experimental Procedure

0.9PMN · 0.1PT ceramic samples used in our experiment were made by the conventional sintering process and these samples were free from an aging effect. PLZT 9.5/65/35 samples were transparent (hot-pressed) ceramics, which showed an aging effect. We chose these two materials for this investigation because both samples have T_m near and above room temperature,[5,6] which is suitable for the study using our experimental setup. Also these materials are widely used in actuator and electrostrictive devices. Hence knowledge of the electrostrictive response of these samples at various temperatures and in various electric fields is desirable.

In the strain measurements, all of the samples were polished on one surface to optical quality and sputtered with gold on both sides to form electrodes and reflection surfaces. These samples were mounted on a temperature stage capable of varying temperature from room temperature to about 200°C. The temperature stability of the system is about 0.5°C. Because of a sample bond-

R. T. McSweeney—contributing editor

Manuscript No. 199195. Received April 13, 1988; approved September 9, 1988. Supported by the Office of Naval Research.
*Member, American Ceramic Society.

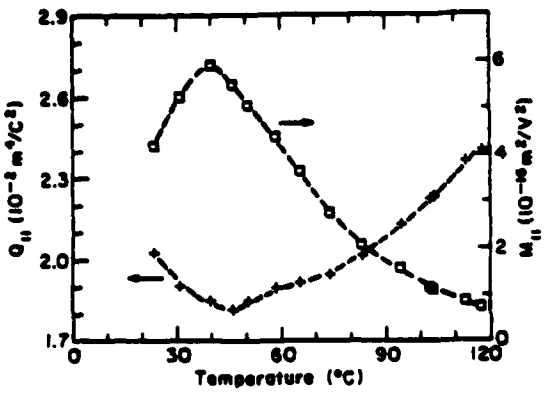

Fig. 1. Q_{11} (+) and M_{11} (□) as a function of temperature for 0.9PMN · 0.1PT ceramics. The measurements were made at a frequency of 400 Hz and an electric field amplitude of 190 V/cm.

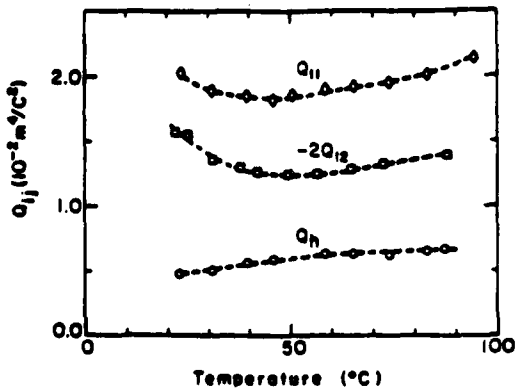

Fig. 3. Q_{11} (◇), $-2Q_{12}$ (□), and Q_h (○) for 0.9PMN · 0.1PT as a function of temperature.

ing problem at high temperatures, our experiment was limited to temperatures below 150°C. A laser interferometer was used for the strain measurements, which has been described in an earlier paper.[7] The high resolution of the interferometer reduces the data scattering in the electrostrictive coefficient measurement compared to that taken with other techniques and this makes accurate, quantitative measurements possible.

[6]Model 393, Ithaco, Ithaca, NY.

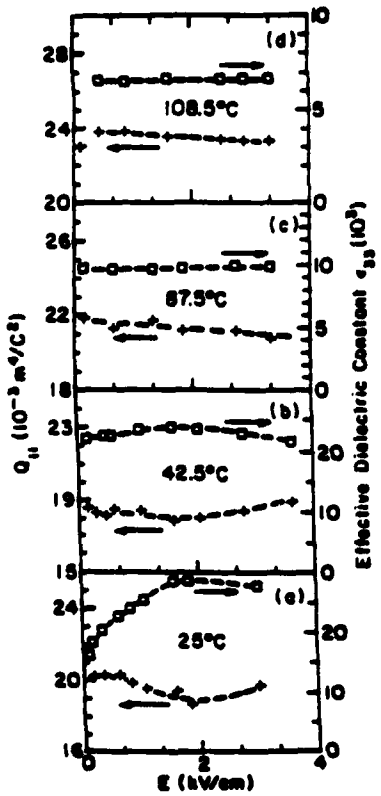

Fig. 2. Field amplitude dependence of electrostrictive coefficient Q_{11} (+) and effective dielectric constant ϵ (□) at (a) 25°, (b) 42.5°, (c) 87.5°, and (d) 108.5°C for 0.9PMN · 0.1PT. The measuring frequency was 200 Hz.

The measurement of the dielectric response was made with a modified Sawyer–Tower circuit. In the weak-field case, a lock-in amplifier[6] was used, and in the strong-field case, a digitized oscilloscope was used to read the data.[5] Both the strain and the dielectric response of the sample were measured simultaneously to avoid the problems of temperature uncertainty, sample aging, and an electric field poling effect.

In the weak-field measurements, the typical sample thickness was 2 mm for both PLZT 9.5/65/35 and 0.9PMN · 0.1PT samples. For the strong field, thinner samples were used and the thickness of the samples was 0.4 mm. In the measurements with variation in the amplitude of the electric field, all of the data were taken following a sequence from a low-field level to a high-field level to avoid a possible hysteresis effect. However, we found that in some cases even if M_{11} and ϵ change because of hysteresis at temperatures below T_m, the Q_{11} obtained seem not to show any obvious change from the in situ measurement.

III. Results

(1) *Results for 0.9PMN · 0.1PT*

The weak-field Q_{11} and M_{11} as a function of temperature are shown in Fig. 1. The measuring field level was 190 V/cm. The induced strain corresponding to that was below 10^{-7}. The choice of such a measuring field amplitude was for the reason of experimental convenience. Upon reducing the field level, we did not observe changes in either Q_{11} or M_{11}. But large changes in both M_{11} and Q_{11} with temperature were observed. For M_{11}, this behavior was expected because of its coupling to the dielectric constant, which has a large variation near T_m. The maximum of M_{11} coincides with weak-field dielectric constant maximum T_m and has a value of 5.95×10^{-16} m²/V². The minimum of Q_{11} lies about 10°C above T_m (≈35°C) and its value is 18×10^{-3} m⁴/C². The values may be reproduced within 2% error.

Q_{11} and ϵ, subjected to a change in the ac field level, were measured at temperatures below T_m, near T_m, and above T_m. These data are plotted in Fig. 2. At 25°C, the dielectric constant increased with an increase in the field amplitude, and near 3 kV/cm, it almost doubled. After that, the effective dielectric constant decreased. Correspondingly, Q_{11} showed a decrease with field and then an increase. At a field level of 16 kV/cm, Q_{11} had a value of 21.5×10^{-3} m⁴/C², close to the earlier measured value.[5] In the other temperature scans, changes in both Q_{11} and ϵ were much smaller in the field range, as shown in Fig. 2. At 108.5°C, Q_{11} was measured to be 26.5×10^{-3} m⁴/C² at a field level of 18.6 kV/cm compared with the weak-field value of 23×10^{-3} at the same temperature. Therefore, in 0.9PMN · 0.1PT both the weak-field and strong-field Q_{11} vary with temperature and an increase in dielectric constant causes a decrease in Q_{11}.

The weak-field Q_{12} was also measured from room temperature to 90°C. In Fig. 3, Q_{11}, Q_{12}, as well as Q_h, which is defined as

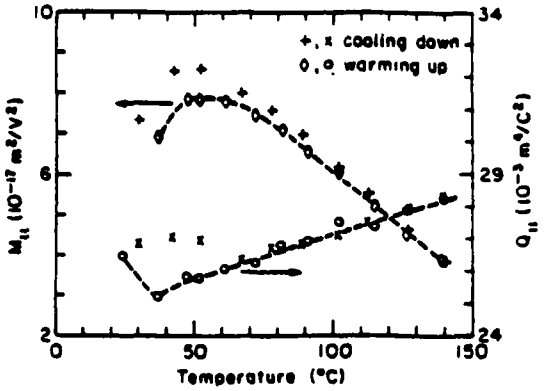

Fig. 4. Q_{11} and M_{11} as a function of temperature for PLZT 9.5/65/35. The data were taken at a frequency of 400 Hz and a field amplitude of 210 V/cm. The curve labeled ○ (◇) is Q_{11} (M_{11}) and data points were taken on warming up and the curve labeled × (+) is Q_{11} (M_{11}) and data were taken on cooling the sample from the high temperature. The difference between the two curves is due to the aging effect.

$Q_h = Q_{11} + 2Q_{12}$, are plotted with temperature. Q_h is the electrostrictive coefficient associated with sample volume strain. It is evident from the figure that, unlike Q_{11} and Q_{12}, Q_h does not show an anomaly at temperatures near the minimum of Q_{ij} ($i, j = 1, 2$).

(2) *Results for PLZT 9.5/65/35*

The weak-field ($E_{ac} = 210$ V/cm) M_{11} and Q_{11} coefficients versus temperature are shown in Fig. 4. The induced strain level s_{33} under this field is of the order of 1.5×10^{-8}. It is interesting to note that, besides the variation of M_{11} and Q_{11} with temperature, the data taken from warming up and cooling down showed different values below 80°C. This is apparently related to the aging of the sample.[9] The warming data were taken on a well-aged sample (aged at room temperature for several months). The minimum for

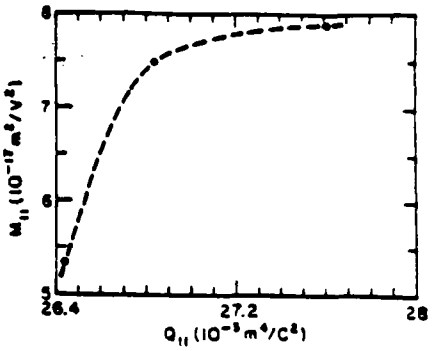

Fig. 5. Effect of sample aging on the relation between Q_{11} and M_{11} for PLZT 9.5/65/35 at 32°C using 210 V/cm ac field at 400 Hz.

Q_{11} in the heating cycle occurred near 40°C, lower than T_m. However, the minimum in the cooling cycle was shifted to a temperature above T_m. Since it took about 20 min to record a data point, the data taken in the cooling cycle were in a constant aging process. In Fig. 5, we plot the aging effect on M_{11} and Q_{11} at 32°C. It can be seen that Q_{11} compared to M_{11} decreases faster at first and then M_{11} decreases faster than Q_{11}. The implication of this will be discussed later.

The measurement of Q_{11} under a strong electric field was also performed for frequencies from 0.1 to 100 Hz at several temperatures. In Fig. 6, strain versus square of the polarization is plotted. The linear relation indicates that the strain is electrostrictive in nature. Q_{11} taken from the slope is plotted as a function of frequency for the three temperatures in Fig. 7. A very weak temperature and frequency dependence can be seen and this change is similar to the behavior observed in the case of weak-field measurements.

Compared with 0.9PMN·0.1PT data, the change in both Q_{11} and M_{11} with temperature for PLZT 9.5/65/35 is much smaller.

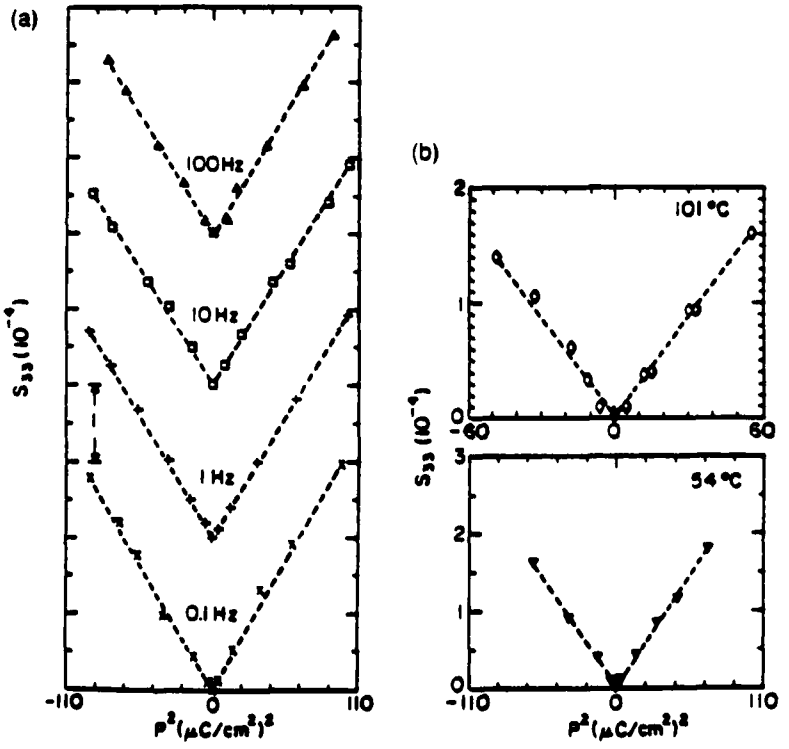

Fig. 6. (a) Strain s_{33} versus the square of polarization for PLZT 9.5/65/35 at 22°C at different frequencies. (b) Strain s_{33} versus the square of polarization at 54° and 101.5°C. The measuring frequency was 100 Hz.

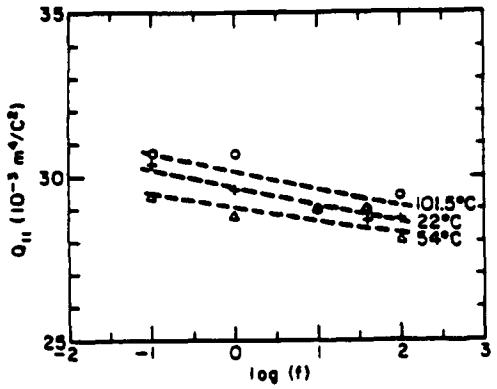

Fig. 7. Electrostrictive coefficient Q_{11} as a function of frequency at a strong field level.

This is related to the smaller changes in the dielectric constants with temperature.

The evolution of the electrostrictive coefficients from weak field to strong field for several temperature points is shown in Fig. 8. Again, in contrast with 0.9PMN · 0.1PT, where the dielectric constant and the electrostrictive coefficient change in opposite directions, the PLZT 9.5/65/35 sample showed an increase in Q_{11} as the effective dielectric constant increased. It is most obvious in the room-temperature scan, where an abrupt increase in Q_{11} occurred in fields between 2 and 3 kV/cm. We did not observe saturation in the effective dielectric constant at a field level above 17 kV/cm. Q_{12} was also measured at room temperature with variation in field. An increase in the magnitude of Q_{12} with field, similar to that in Q_{11}, was also observed, as shown in Fig. 8. The value of Q_{12} is close to the values reported by Meng *et al.*[10] However, because of the limitation of the instrument, the measurement did not give a reliable Q_{11} value.

In Table I, some of the Q_{ij} coefficients are listed for the two samples with the weak-field (WK) and strong-field (SF) measurements at several temperatures.

IV. Discussion

The observed anomalous behavior of Q_{ij} with temperature and field appears not to be due solely to the intrinsic properties of the sample. By assuming that there exist micropolar domains which are actively coupled to the external field and contribute to the various response functions of the sample, the data can be understood consistently.

From the idea of local Curie temperature distribution, we expect that the samples in our experimental temperature range will be composed of three different micro regions: region I, where the local Curie temperature is far below the measuring temperature T_0; region II, where the local T_c is near but below T_0; and region III, with the local $T_c > T_0$. Region I is the pure paraelectric phase region where no phase transitions can be induced by the external field. Region II will show a kind of field-induced transition,[10] even if in the relaxors, such transition may be highly smeared in nature. Region III is the region with micropolar domains. The response behavior of a sample from the first two regions is usually called intrinsic and the response due to existing domain flipping (or tunneling) is called extrinsic.

If we are concerned only with the response from the first two regions of the sample, taking 0.9PMN · 0.1PT as an example, it would be reasonable to think that Q_{11} should increase with temperature in the temperature range from just below T_m to the highest local Curie temperature. The overall response of the sample from these regions is a statistical averaging over all of the local regions. Region II will have a large weight factor since it is more softened to the external field than region I. From recent refractive index measurement results, the highest local Curie temperature of 0.9PMN · 0.1PT is approximately equal to T_c of pure $PbTiO_3$.[11] For regions rich in PMN, there will be a large resistance to the appearance of spontaneous polarization and these regions will have a lower local Curie point (T_m for PMN is below 0°C).

The two end members of 0.9PMN · 0.1PT have quite different Q_{ij} coefficients. Q_{11} for PMN ceramics is about 19×10^{-3} m^4/C^2.[12] For ceramic $PbTiO_3$, no direct data are available. Based on averaging of the single-crystal data, Haun *et al.*[14] calculated the value of Q_{11} for ceramic $PbTiO_3$ to be between 22.8×10^{-3} and 56.5×10^{-3} m^4/C^2. Regions with higher Curie temperatures will have a larger Q_{11} compared to the regions with lower Curie temperatures. This consideration is consistent with the earlier work reported by Jang[5] on PMN–PT compositions with various $PbTiO_3$ contents. On the average, an increase in the value of Q_{11} with temperature from the intrinsic regions for 0.9PMN · 0.1PT may be expected. In general, an intrinsic Q_{ij} distribution will exist in the relaxor materials. Such distribution should affect the strain response of the sample with temperature.

For the micropolar domains, there are two different polar-vector flipping processes taking part in the mechanical strain properties: (i) 180° flipping, which does not produce any strain change, and (ii) non-180° flipping, which changes the strain of the sample. If the polarization change involves induced polarization (P_i) plus pure 180° domain flipping, using Eqs. (1) or (2) to calculate the observed Q (Q_{obs}), a smaller value will be obtained, i.e.

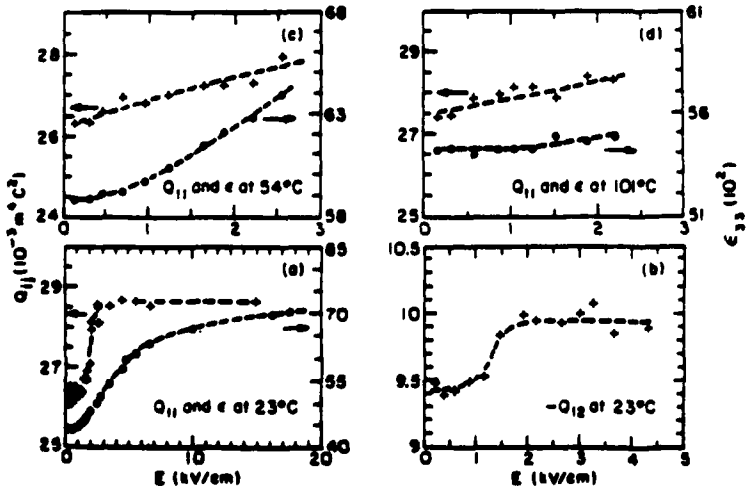

Fig. 8. Field amplitude dependencies of Q_{11} and Q_{12} and the effective dielectric constant ε for PLZT 9.5/65/35: (a) Q_{11} and ε at 23°C, (b) Q_{12} at 23°C, (c) Q_{11} and ε at 54°C, and (d) Q_{11} and ε at 101°C.

$$Q_{ob} = s/P_r^2 = (s/P_r^2)(P_r/P_r)^2 = Q_m(P_r/P_r)^2 \quad (4)$$

where P_r is the total polarization change, s is the induced strain, and Q_m is the intrinsic Q. Since $P_r > P_r$, therefore $Q_{ob} < Q_m$. In the relaxor materials used in our experiment, both 180° and non-180° domain flipping should be present. For the sake of simplicity, we start with a single crystal of tetragonal structure. Assuming its prototypic cubic phase has a lattice parameter a, in the tetragonal ferroelectric phase, the lattice parameters are $c = a + \Delta l_1$ and $b = a - \Delta l_2$. Corresponding to that, the strain will be $s_{33}^s = \Delta l_1/a$, and $s_{11}^s = -\Delta l_2/a$. For domain flipping from a fully thermally depoled state, the initial $P = 0$ state has an averaged lattice constant: $a_{av} = a + (1/3)\Delta l_1 - (2/3)\Delta l_2$. If we assume that all of the domains are aligned along the field direction after switching (along one of the c axes), then it is a single domain crystal. The strains produced by domain flipping from a fully thermally depoled state, therefore, are

$$s_{33} = (2/3)s_{33}^s + (2/3)s_{11}^s \quad (5a)$$

$$s_{11} = -(1/3)s_{33}^s + (1/3)s_{11}^s \quad (5b)$$

It is clear that $\Delta l_1 > 2\Delta l_2$. Even for a fully poled single-crystal relaxor material, Q_{11} should be smaller than that of the intrinsic one and the Q_{12} will be larger in magnitude than the intrinsic value of Q_{12}. For ceramics, averaging from the single-crystal Q coefficients is the same for the intrinsic Q_{ij} and the domain flipping produced Q_{ij}. The conclusion obtained above should still be valid.

The observed strain and the dielectric responses are the combined contributions (a weighted averaging) of two parts, the intrinsic and the extrinsic, and they are coupled to each other through the structure of the relaxors. The anomaly observed in the Q_{11} curve (Fig. 1) is a clear indication of strong micropolar domain activities. Therefore, those domains are in a dynamic state. However, in 0.9PMN · 0.1PT, in the temperature range studied, the observed Q_{11} has a minimum value around 18×10^{-3} m⁴/C² and a maximum value of 26.5×10^{-3} m⁴/C² when using the strong field. This maximum may not be the highest value of Q_{11} for 0.9PMN · 0.1PT. This kind of increasing trend in Q_{11} values is difficult to explain if we assume only extrinsic contribution changes with temperature. It may involve an increase in the intrinsic Q_{11} with temperature as discussed above and it may also be due to the different barrier distribution for 180° and non-180° microdomain flipping processes, as will be discussed below. The variation of Q_{11} in the highest temperature (108.5°C) scan with field is consistent with the refractive index measurements and at $T > T_m$ there still exist substantial amounts of micropolar domains forming so-called polar glassy states.[3]

The variation in both Q_{11} and ε for PLZT 9.5/65/35 is much smaller compared with that of 0.9PMN · 0.1PT. This may be due to the less active micropolar domains in PLZT near T_m. As shown in Fig. 9, there is an energy barrier distribution for micropolar domain tunneling (flipping). A sharp distribution in the barrier may correspond to what has been observed in the case of 0.9PMN · 0.1PT and a broad distribution apparently reduces the weight of the micropolar domain contributions to the total response of the sample near T_m. This results in a smaller change in the quantities measured. This may also offer an explanation for the high saturation field observed in the PLZT samples.

At a measuring temperature T_0, one of the factors affecting the energy barrier distribution for the micropolar domain tunneling is the local Curie temperature distribution. It is conceivable that the domains with a $T_c \gg T_0$ will have a higher barrier than that of the domains with T_c near T_0 if they have the same microvolume. From this scenario, we would expect that maximum domain activity (micropolar domain tunneling) occurs at a temperature just below the local Curie temperature peak. This may produce a minimum of $T_m Q$ of Q_{ij} near but below T_m. However, the observation of 0.9PMN · 0.1PT and nonaged PLZT 9.5/65/35 seems inconsistent with this consideration, where $T_m Q$ lies above T_m. We believe that this discrepancy is caused by the fact that in these samples, there is both 180° and non-180° micropolar domain flipping. Since the former process has a larger polarization vector change and the latter process involves ferroelastic switching, it is possible that the tunneling barriers for the two processes are different and this difference in the barrier distribution may also be temperature dependent. Therefore, a maximum ratio of 180° domain flipping to non-180° domain flipping may produce a minimum in observed Q_{ij} $(i, j = 1, 2)$ and this minimum does not necessarily coincide with T_m. On the other hand, the domain flipping process does not produce a volume change. This makes Q_h insensitive to how the micropolar domain reorients and Eq. (4) is valid for Q_h.

The aging effect observed in PLZT 9.5/65/35 is possibly another manifestation of this barrier difference for the two processes. The flipping barrier for the non-180° process is higher than that of the 180° process. At the first stage of aging, there are more non-180°

Table I. Q_{ij} for 0.9PMN · 0.1PT and PLZT 9.5/65/35 at Selected Temperatures

(A) 0.9PMN · 0.1PT

Coeff*	Q_{ij} (×10⁻³ m⁴/C²)			
	25°C	42.5°C	87.5°C	108.5°C
WF Q_{11}	20.3	18.6	21.8	23
WF Q_{12}	−7.7	−6.3	−7.0	
WF Q_h	4.9	6	7.8	
SF Q_{11}	21.5 (16 kV/cm)			26.5 (18.6 kV/cm)

(B) PLZT 9.5/65/35

Coeff*	Q_{ij} (×10⁻³ m⁴/C²)			
	22°C	51.5°C	54°C	101.5°C
WF Q_{11}	26.4	26.3		27.4
WF Q_{12}	−9.5			
SF Q_{11}	28.7 (15 kV/cm)			28.5 (15 kV/cm), 29.2 (17 kV/cm)

*WF stands for weak field and SF for strong field. The field levels are indicated in parentheses following the Q_{11} values.

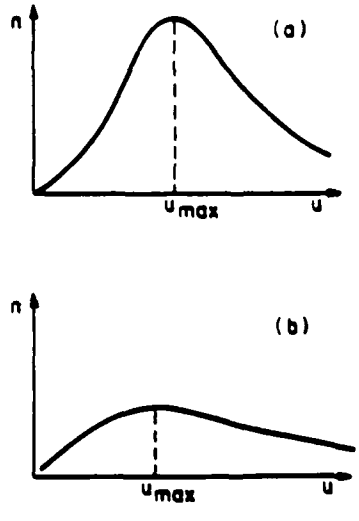

Fig. 9. Schematic drawing of the energy barrier distribution for the micropolar domain in the relaxors. (a) shows a relatively sharp distribution which may correspond to the state in 0.9PMN · 0.1PT; (b) a broad distribution will reduce the contribution from the micropolar domain to the response of the sample near T_m.

polar domain flipping processes involved, causing larger change in Q_{11} compared with the later stages of the aging process. In the temperature scan, aging causes reduced non-180° polar-vector flipping and this takes the minimum in Q_{11} to below T_m. In the voltage scan, as the applied field amplitude increases, this ferroelastic-related flipping can gain enough energy to overcome the barrier and contributes to the response of the sample. The increase in Q_{11} with increased ε seems to be consistent with this picture. From earlier study of the aging effect in relaxors,[9] the local defect structures pin the micropolar domains and in the PLZT sample studied this pinning effect is different for different domain reorientation processes.

Based on the data presented above and our analysis, it is clear that the small value of Q observed in relaxor materials, to a large extent, is due to the existing micropolar domains. From the discussion here, it seems to be possible to separate the micropolar domain contribution to the response of the sample from the intrinsic one. Further experiments on simpler relaxor materials like SBN, where only 180° domain flipping exists, will be interesting and worthwhile.

References

[1](a) V. A. Bokov and I. E. Myl'nikova, "Electrical and Optical Properties of Single Crystals of Ferroelectrics with a Diffused Phase Transition," *Sov. Phys.—Solid State (Engl. Transl.)*, 3, 613 (1961). (b) G. A. Smolenskii, Ferroelectrics and Related Materials, Gordon and Breach Science Publishers, New York, 1984.
[2]L. E. Cross, "Relaxor Ferroelectrics," *Ferroelectrics*, 76, 241 (1987).
[3]R. Clark and J. C. Burfoot, "The Diffuse Phase Transition in Potassium Strontium Niobate," *Ferroelectrics*, 8, 505 (1974).
[4]G. Burns and F. H. Dacol, "Crystalline Ferroelectrics with Glassy Polarization Behavior," *Phys. Rev. B*, 28, 2527 (1983); "Glassy Polarization Behavior in $K_3Sr_3(NbO_3)_9$-type Ferroelectrics," *ibid.*, 30, 4012 (1984).
[5](a) S. J. Jang; Ph.D. Thesis, Pennsylvania State University, University Park, PA, 1979. (b) A. S. Bhalla, R. Guo, L. E. Cross, G. Burns, F. H. Dacol, and R. R. Neurgaonkar, "Measurements of Strain and the Optical Indices in the Ferroelectric $Ba_{0.4}Sr_{0.6}Nb_2O_6$: Polarization Effect," *Phys. Rev. B*, 36, 2030 (1987).
[6]G. H. Haertling, "PLZT Electrooptic Materials and Applications—A Review," *Ferroelectrics*, 75, 25 (1987).
[7]Q. M. Zhang, W. Y. Pan, and L. E. Cross, "Laser Interferometer for the Study of Piezoelectric and Electrostrictive Strains," *J. Appl. Phys.*, 63, 2492–96 (1988).
[8]Q. M. Zhang, W. Y. Pan, S. J. Jang, and L. E. Cross, "Domain Wall Excitations and Their Contribution to the Dielectric and Piezoelectric Response of PZT Samples", unpublished work.
[9]W. Y. Pan, E. Furman, G. O. Dayton, and L. E. Cross, "Dielectric Aging Effects in Doped Lead Magnesium Niobate: Lead Titanate Relaxor Ferroelectric Ceramics," *Mater. Sci. Lett.*, 5, 647 (1986).
[10]Z. Y. Meng, U. Kumar, and L. E. Cross, "Electrostriction in Lead Lanthanum Zirconate-Titanate Ceramics," *J. Am. Ceram. Soc.*, 68 [8] 459–62 (1985).
[11](a) L. E. Cross, "Properties of Barium Titanate Single Crystals," *Philos. Mag., Ser. 7*, 4 (337) 1161 (1953). (b) W. Y. Pan, Q. M. Zhang, A. S. Bhalla, and L. E. Cross, "Field-Induced Strain in Single-Crystal $BaTiO_3$," *J. Am. Ceram. Soc.*, 71 [6] C-302–C-305 (1988).
[12]D. McHenry; private communication.
[13]W. Y. Pan and L. E. Cross, "Direct and Converse Electrostrictive Effects in $Pb(Mg_{1/3}Nb_{2/3})O_3$": unpublished work.
[14]M. J. Haun, E. Furman, S. J. Jang, and L. E. Cross, "Modeling of the Electrostrictive, Dielectric, and Piezoelectric Properties of Ceramic $PbTiO_3$", to be published in *Trans. IEEE. Sonic. Ultrason.* □

APPENDIX 11

Ferroelectrics, 1988, Vol. 88, pp. 147–154
Reprints available directly from the publisher
Photocopying permitted by license only

THE PRESSURE DEPENDENCE OF THE DIELECTRIC RESPONSE AND ITS RELATION TO THE ELECTROSTRICTION

Q. M. ZHANG, W. Y. PAN, S. J. JANG, and L. E. CROSS
Materials Research Laboratory, The Pennsylvania State University, University Park, PA 16802 USA

(Received 15 March 1988)

Based on Landau–Devonshire theory, the effect of elastic stress upon the dielectric response is analyzed for ferroelectric, antiferroelectric, and relaxor ferroelectric materials. It is shown that besides the direct coupling between stress and polarization which leads to the thermodynamic equivalence to direct electrostriction, an extra coupling occurs in systems with non-zero polarization. In ferroelectric and antiferroelectric materials the effect is quite straightforward and relations are derived between stress coefficients and direct electrostriction. For relaxor ferroelectrics the relation cannot be defined thermodynamically because of the dispersive contribution to the response from switching of polar micro regions, however, the qualitative trends can be predicted and are in concert with measured properties.

I. INTRODUCTION

Electrostriction is the basic electromechanical coupling for all substances regardless of their symmetry group. In this phenomenon the strain is proportional to the square of the electric field E or the polarization P of the material. It is expressed as:

$$x_{ij} = Q_{ijkl} P_k P_l \tag{1}$$

or more precisely:

$$Q_{ijkl} = \frac{1}{2} \frac{\partial^2 x_{ij}}{\partial P_k \partial P_l} \tag{2}$$

The proportional constant Q_{ijkl} is the electrostrictive charge coefficient. Using the Maxwell relations, the Q coefficients can be related to the change of the dielectric stiffness with respect to the stress:

$$Q_{ijkl} = -\frac{1}{2} \frac{\partial \chi_{ij}}{\partial X_{kl}} \tag{3}$$

Where χ_{ij} and X_{kl} are the dielectric stiffness and stress respectively. The converse electrostrictive effect offers a convenient way of measuring the Q coefficient of various materials. By plotting the curve of χ vs stress, one can find Q coefficient from the slope. Since Q coefficient can be approximately taken as constant over temperatures and stresses,[1] the χ vs stress curve (converse curve) will be a straight line. As observed in most of the experimental systems, this is indeed the case.[2] However, for relaxor ferroelectrics, the converse curve is not a straight

line.[3] For normal ferroelectrics, it is found that the slope of the converse curve can change sign when the temperature increases beyond the curie point and vise versa, which seems to indicate a sign change of the Q coefficient.[3,4] This is, of course, not consistent with the directly measured Q value using Equation (2). Therefore, a further consideration of the converse electrostrictive effect in these materials seems to be necessary.

In this paper, the conditions under which the Q coefficient can be measured correctly in the converse method will be discussed based on Landau–Devonshire theory. For simplicity, we will concentrate our discussion on the pseudo-cubic system and it is assumed that the spontaneous polarization occurs only along one of the original axes.

II. FERROELECTRIC CRYSTALS

For ferroelectrics derived from a centric cubic point group, the Gibbs free energy density can be written as:[5]

$$\begin{aligned} G(T, X, P) = G_0(T, X) &+ 1/2\alpha(P_1^2 + P_2^2 + P_3^2) + 1/4\alpha_{11}(P_1^4 + P_2^4 + P_3^4) \\ &+ 1/4\alpha_{12}(P_1^2P_2^2 + P_2^2P_3^2 + P_3^2P_1^2) + 1/6\alpha_{111}(P_1^6 + P_2^6 + P_3^6) \\ &- Q_{11}(X_1P_1^2 + X_2P_2^2 + X_3P_3^2) - Q_{12}(X_1(P_2^2 + P_3^2) \\ &+ X_2(P_1^2 + P_3^2) + X_3(P_1^2 + P_2^2)) \end{aligned} \quad (4)$$

where $G_0(T, X)$ includes all the terms which do not depend on P, the polarization vector. In the later discussions, these terms do not affect the result and can be neglected. The subscripts for stresses X_{ij} are reduced to matrix notation. We first discuss the case where the dielectric constant is measured along z axis. This allows us to omit all the terms involving P_1 and P_2 if we assume that the spontaneous polarization is along z axis. The coefficients are: $\alpha = \alpha_0(T - T_0)$ where T is temperature, α_{ij}, α_{111}, and Q_{ij} are approximately temperature and stress independent. For a first order transition, $\alpha_{11} < 0$ and $\alpha_{111} > 0$, and for a second order transition, $\alpha_{11} > 0$ and P^6 term can be neglected near the transition point. The introduction of the negative sign in front of the terms involving electromechanical coupling for the convenience of the discussion. It is clear that Q_{ij} in Equation (4) are the same as that introduced in Equations (1) and (2).

The thermodynamic stable state corresponds to the minimum of the free energy density G. These conditions yield that a first order transition will occur at $T_c > T_0$ (Curie–Weis temperature) and a second order transition at $T_c = T_0$. From Equation (4), it is clear that the coupling between the stress and the polarization causes the shifting of the transition temperature. As will be seen later, it is this secondary effect that gives rise to a large change in the slope of the converse curve in the ferroelectric crystals.

To make the notations simpler and still have the generality, we only consider the situation where the stress is a hydrostatic pressure, that is: $X_1 = X_2 = X_3 = -p$. Replacing X's in Equation (4) gives:

$$G = (\alpha/2)P_3^2 + (\alpha_{11}/4)P_3^4 + (\alpha_{111}/6)P_3^6 + Q_hpP_3^2 \quad (5)$$

where $Q_h = Q_{11} + 2Q_{12}$. With an electric field along z axis,

$$(\partial G/\partial P)_T = E = \alpha P_3 + \alpha_{11} P_3^3 + \alpha_{111} P_3^5 + 2Q_h p P_3 \tag{6}$$

$$(\partial^2 G/\partial P^2)_T = \chi = \alpha + 3\alpha_{11} P_3^2 + 5\alpha_{111} P_3^4 + 2Q_h p \tag{7}$$

Therefore:

$$(\partial/\partial p)(\chi)_{T,P} = 2Q_h \tag{8}$$

which is just the relation for the converse method. The above derivation shows that the partial derivative condition for Equation (8) is P = constant, which means that as long as P is held constant in the pressure change process, the converse method can be used in both the systems with $P_s = 0$ and $P_s \neq 0$ (P_s the spontaneous polarization).

If the experiment is carried out above the curie temperature, the above condition is automatically satisfied since that phase, $P_s = 0$ at all the time. However, for the measurement within the ferroelectric temperature region, $P_s \neq 0$. A change of the stress will induce a change in P which will in turn cause a change in χ as shown by Equation (7). Denote the experimentally measured slope of the converse curve as Q_h^c:

$$Q_h^c = (1/2)(\partial/\partial p)(\chi) = Q_h + (3\alpha_{11} + 10\alpha_{111} P_3^2) P_3 (\partial P_3/\partial p)_T \tag{9}$$

With $E = 0$, Equation (6) gives $(\partial P_3/\partial p)_T$:

$$P_3(\partial P_3/\partial p)_T = -Q_h/(\alpha_{11} + 2\alpha_{111} P_3^2) \tag{10a}$$

or

$$(\partial P_3/\partial p)_T = -2Q_h P_3 \epsilon\epsilon_0 \tag{10b}$$

Substituting to Equation (9) gives the final result:

$$Q_h^c = Q_h(1 - (3\alpha_{11} + 10\alpha_{111} P_3^2)/(\alpha_{11} + 2\alpha_{111} P_3^2)) \tag{11a}$$

or

$$Q_h^c = Q_h(1 - (6\alpha_{11} + 20\alpha_{111} P_3^2) P_3^2 \epsilon\epsilon_0) \tag{11b}$$

where P_3 and ϵ are the spontaneous polarization and relative dielectric permittivity at the measuring point which will depend on the pressure and temperature. Equation (11b) shows that when $P_3 = 0$, then $Q_h^c = Q_h$.

For a first order transition $(6\alpha_{11} + 20\alpha_{111} P_3^2)$ is positive. Therefore in some materials, we would expect a sign change in the slope of the converse curve when the material measured passes the transition point from $P_3 \neq 0$ to $P_3 = 0$ state even if Q_h does not change at above and below the transition point. For a second order transition, Equation (11a) with $\alpha_{111} = 0$ shows that $Q_h^c = -2Q_h$, a constant but with a negative slope for the converse curve below the transition point.

It is also interesting to see how this affects the converse curve for the dielectric constant measured in the direction perpendicular to the spontaneous polarization. Assuming the E field is along the x axis, terms with P_1 should be added in our derivation from Equation (4). The spontaneous polarization is P_3 and P_1 is the induced polarization which is small. There is no need to keep all the higher order

terms in P_1 in Equation (4). Following the same derivation procedure shown above, the slope of the converse curve in this direction:

$$Q_h^c = Q_h(1 - \alpha_{12}/(2(\alpha_{11} + 2\alpha_{111}P_3^2))) \tag{12a}$$

or

$$Q_h^c = Q_h(1 - \alpha_{12}P_3^2\varepsilon_{33}\varepsilon_0) \tag{12b}$$

here ε_{33} is the dielectric constant along z axis. Comparison between Equations (11) and (12) indicates that the result of the converse method will depend on the direction along which the dielectric constant is measured.

The above discussions clearly demonstrate that besides the direct coupling between stress and polarization which leads to the thermodynamic equivalence to direct electrostriction, an extra coupling occurs in systems with non-zero polarization.

Comparison of Equation (11) with experiments is made on $BaTiO_3$ single crystal. $BaTiO_3$ is a ferroelectrics with a first order paraelectric-ferroelectric transition in the vicinity of 120°C. The data by G. A. Samara for the pressure and temperature dependence of the dielectric constant of $BaTiO_3$ single crystal along the c-axis (the spontaneous polarization axis) are used here.[4] For $BaTiO_3$, there is another transition near 0°C. However, unlike ε_{11} which follows Curie–Weis law near this second transition, ε_{33} is not affected except very near this transition. Furthermore, the hydrostatic pressure moves the second transition towards low temperature. At room temperature and relatively high pressure, the expression (11) should be satisfied. From the condition of a first-order transition near 120°C, the following relations can be found.[5]

$$\alpha = \chi,\ \alpha_{11} = -4\chi_1/P_0^2,\ \alpha_{111} = 3\chi_1/P_0^4 \tag{13}$$

where χ_1 and P_0 are the dielectric stiffness and the spontaneous polarization at the transition temperature with zero stress. Hence, for $BaTiO_3$:

$$Q_h^c = Q_h\left(1 - 3\left(\frac{5P_3^2 - 2P_0^2}{3P_3^2 - 2P_0^2}\right)\right) \tag{14}$$

The data are shown in Figure 1. Both the spontaneous polarization and the dielectric constant measured along the c axis as a function of pressure at 23°C are

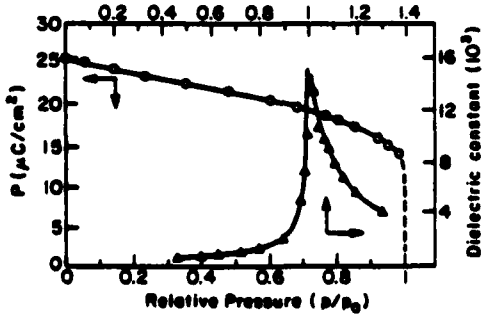

FIGURE 1 Pressure dependence of the spontaneous polarization (O) and dielectric constant (Δ) measured along the c-axis of single crystal $BaTiO_3$ at 23°C.

shown. At $p = 10$ Kbar, Q_h^c found from the converse curve is -0.0045. From Equation (14), Q_h is found to be $0.02\,m^4/C^2$, which is in reasonable agreement with the accepted value of $Q_h = 0.011$ (m^4/C^2) ($Q_{11} = 0.123$ and $Q_{12} = -0.056$)[6] at room temperature. We believe that the error related is due to the existing "a" domains in the crystal. The dielectric constant measured at the lowest pressure is about 700, as shows in the figure, which apparently contains "a" domain contribution.[7] As the sample approaches the transition point, the increased "a" domain activity will certainly cause a large error.

III. ANTIFERROELECTRIC SYSTEM

In order to expand the above discussion to antiferroelectric phases, a free energy function which carries the polarization at the two sublattice should be used.[8,9] Using the convention adapted (sublattice spontaneous polarization along z direction)

$$G = f(P_a^2 + P_b^2) + gP_aP_b + h(P_a^4 + P_b^4) + r(P_a^6 + P_b^6) + qp(P_a^2 + P_b^2 + 2\Omega P_aP_b) \quad (15)$$

where P_a and P_b are the two sublattice polarizations, g and Ω are introduced to describe the sublattice coupling, and p is the hydrostatic pressure. We neglect the higher order terms in the two sublattice coupling for the sake of simplicity.

Introducing the notations:

$$P_A = (P_a - P_b) \quad \text{and} \quad P_F = (P_a + P_b) \quad (16)$$

In the case when the external field is zero, P_A and P_F describe the spontaneous antiferroelectric and ferroelectric polarization in antiferroelectric and ferroelectric phase respectively. Equation (15) can be rewritten as

$$\begin{aligned} G = {} & (1/2)(f + g/2)P_F^2 + (1/2)(f - g/2)P_A^2 + (1/8)h(P_A^4 + P_F^4) \\ & + (1/32)r(P_A^6 + P_F^6) + (3/4)hP_F^2P_A^2 + (15/32)r(P_F^4P_A^2 + P_F^2P_A^4) \\ & + (1/2)qp(P_A^2 + P_F^2 + \Omega(P_F^2 - P_A^2)) \end{aligned} \quad (17)$$

It is clear from this expression that the Q coefficient for the ferro- and antiferroelectric phase can be expressed as follows:

$$Q_{fh} = (1/2)q(1 + \Omega) \quad \text{and} \quad Q_{ah} = (1/2)q(1 - \Omega) \quad (18)$$

In the preceeding section, Q_{fh} is expressed as Q_h. It is experimentally observed that the antiferroelectric to paraelectric transition temperature moves upwards as the pressure increases.[10] Corresponding to it, Q_{ah} is expected to be negative.

In the antiferroelectric phase, if there is no external electric field, $P_a = -P_b$. When a field is turned on, an induced ferroelectric polarization P_F will be non-zero, $P_F = P_a + P_b$. Hence P_a is no longer equal to $-P_b$ and the magnitude of the antiferroelectric polarization should be expressed

$$P_A = 2\min\{|P_a|, |P_b|\} \quad (19)$$

which is just Equation (16) if $P_a = -P_b$.

For the spontaneous antiferroelectric polarization P_A, Equation (17) allows us

to find:

$$(\partial G/\partial P_A)_T = 0 = (f - g/2) + (1/2)hP_A^2 + (3/16)rP_A^4 + q(1 - \Omega)p \quad (20)$$

which relates the P_A to the change of temperature and pressure. In the general case, Equation (15) has to be used:

$$(\partial G/\partial P_a)_T = E = 2fP_a + gP_b + 4hP_a^3 + 6rP_a^5 + 2qp(P_a + \Omega P_b) \quad (21a)$$

and for P_b, we can get Equation (21b) with the same form except that the subscripts "a" and "b" change the position.

Equation (21a) + Equation (21b) yields:

$$2E = (2f + g)(P_a + P_b) + 4h(P_a^3 + P_b^3) + 6r(P_a^5 + P_b^5) + 2qp(P_a + P_b)(1 + \Omega) \quad (22a)$$

and Equation (21a)–Equation (21b) yields:

$$0 = (2f - g)(P_a - P_b) + 4h(P_a^3 - P_b^3) + 6r(P_a^5 - P_b^5) + 2qp(P_a - P_b)(1 - \Omega) \quad (22b)$$

For a small field measurement, P_F will be small. In the following discussion, we only keep the lowest order terms in P_F ($P_F = P_a + P_b$). Therefore, we can have from Equation (22):

$$(\partial E/\partial P_F)_T = \chi = (f + g/2) + (3/2)hP_A^2 + (15/16)rP_A^4 + q(1 + \Omega)p \quad (23)$$

where P_A is given by Equation (20). Therefore the slope of the converse curve is:

$$(\partial/\partial p)(\chi)_T = q(1 + \Omega) + (3/4)(4h + 5rP_A^2)P_A(\partial P_A/\partial p)_T \quad (24)$$

and from Equation (20)

$$Q_h^c = Q_{fh} - 3Q_{ah}\frac{4h + 5rP_A^2}{4h + 3rP_A^2} \quad (25)$$

Due to the introduction of the two sublattice polarizations, Equation (25) seems to be different from Equation (11). However, if the same notation is used, Equation (25) can be changed to the form of Equation (11). For a continuous transition

$$Q_h^c = Q_{fh} - 3Q_{ah} \quad (26)$$

This is a constant. Since $Q_{ah} < 0$, Q_h^c will be always positive.

In the direct method, both the strain and induced ferroelectric polarization P_F can be measured. Therefore

$$\Delta S = Q_h P_F^2 \quad (27)$$

ΔS is a generalized strain. In this discussion, it is volume strain. In the $P_A \neq 0$ phase, an initial strain S_0 exists as ($S = \partial G/\partial p$):

$$S_0 = (1/2)q(1 - \Omega)P_{A0}^2 \quad (28)$$

The strain after a field E is applied is

$$S = q(P_a^2 + P_b^2 + 2\Omega P_a P_b) \quad (29)$$

Here, P_A also deviates from P_{A0}. ΔS in Equation (27) is

$$\Delta S = S - S_0 \quad (30)$$

For the purpose of simplicity, use Equation (22b) without the terms containing r and p. That is, it is a system with a continuous transition and no external stress. Equation (22b) gives

$$(2f - g) + 4h(P_a^2 + P_aP_b + P_b^2) = 0 \tag{31}$$

Using $P_a + P_b = P_F$ and substituting $P_b = P_F - P_a$ to Equation (31):

$$(2f - g) + 4h(P_F^2 + P_a^2 - P_FP_a) = 0 \tag{32}$$

The solution for P_a is

$$P_a = (1/2)(P_F \pm \sqrt{P_F^2 - (2f - g)/h}) \tag{33}$$

which will be reduced to the spontaneous antiferroelectric polarization $P_{A0} = 1/2\sqrt{(g - 2f)/h}$ if $P_F = 0$.

Therefore, the two sublattices will have the polarizations:

$$P_a = (1/2)(P_F + \sqrt{-3P_F^2 - (2f - g)/h}) \tag{34a}$$

and

$$P_b = (1/2)(P_F - \sqrt{3P_F^2 - (2f - g)/h}) \tag{34b}$$

With a nonzero P_F, the magnitude of the antiferroelectric polarization is $(\sqrt{-3P_F^2 - (2f - g)/h} - P_F)$. Substituting Equation (34) into Equation (29) and using Equation (30):

$$\Delta S = q(2\Omega - 1)P_F^2$$

Hence,

$$Q_h = Q_{fh} - 3Q_{ah}$$

which is the same as Equation (26). If the higher order terms are included, Q_h will be the same as Equation (25) Q_h^c. In the sense that the direct and converse methods give the same Q coefficients, the antiferroelectric system can be taken as a paraelectric phase with an effective Q coefficient in the measurement. Experimental results on antiferroelectric lead zirconate titanate stannate ceramics confirmed this conclusion.[11]

IV. THE FERROELECTRIC RELAXOR MATERIALS

The converse method is used widely in relaxor materials to determine the Q coefficients. It is found that even in the region where the macroscopic polarization is zero, the converse curve still does not show a straight line. Some emperical expressions are tried to correct the data to give a constant Q. From our discussion above, we see that χ vs p needs not to be a straight line even if Q is a constant. It has been proposed that, in the relaxor materials, at the temperature region where the macroscopic polarization is zero, there are still micro-regions with non-zero polarization.[12] Above the temperature where $P_s = 0$, experiment results seem to be convincing that $P_s^2 \neq 0$ and P_s^2 persists up to very high temperature.[13] Therefore, in the microscopic scale, the relaxor material is a mixture of polar

regions and non-polar regions. In the polar region, Equations (11) and (12) should be used to describe χ vs p result. The complication of the system makes it difficult to find a correct expression for the converse curve in the region with $P_s^2 \neq 0$. However, as the pressure or temperature increases, P_s^2 should decrease. The anomalous effect discussed above will become small and should make Q_h^c gradually increase as either the pressure or temperature increases. This kind of trend is actually observed in the experiment data[3] which in turn supports the idea of the micro-polar domains in the relaxor material at temperatures above the average Curie point. Since the relaxor materials, a large part of the dielectric constant is from the reorientation of the polar region,[12] this will also be stress dependent and may also give an extra effect on the converse curve. The available data on the relaxor materials seem to indicate that this is the case.[3] Therefore, it is fair to say that at present there is no firm basis for the interpretation of the converse method to give a reliable Q coefficient. Of course, the pressure dependent of the dielectric response will provide interesting information about the relaxor materials. Further work is needed to relate this to conventional direct electrostriction.

V. SUMMARY

Using Landau–Devonshire theory, we showed that in the ferroelectric phase, due to the fact that the dielectric constant depends on the spontaneous polarization which is pressure dependent, the pressure dependence of the dielectric response will deviate from the behavior of the pure electrostriction coupling effect. Taking all these into account, we derived the expression which relates the slope of the converse curve to the electrostriction coefficients. In the antiferroelectric phase, both the direct and converse method do not give the pure electrostrictive coefficient. In the relaxor materials, the existence of micro-polar region will cause a change of the converse curve from the pure electrostriction coupling effect even in the high temperature region when the macroscopic polarization is zero.

The authors wish to express their thanks of the financial support from the Office of Naval Research.

REFERENCES

1. M. J. Haun, Z. Q. Zhuang, E. Furman, S. J. Jang, L. E. Cross. submitted to *J. Amer. Ceram. Soc.*
2. Z. Y. Meng and L. E. Cross. *J. Appl. Phys.* **57**, 488 (1985).
3. K. Uchino, S. Nomura, L. E. Cross, S. J. Jang, and R. E. Newnham. *J. Appl. Phys.* **51**, 1142 (1985).
4. G. A. Samara. *Phys. Rev.* **151**, 378 (1966).
5. A. F. Devonshire. *Phil. Mag.* **40**, 1040 (1949); **42**, 1065 (1951); *Advan. Phys.* **3**, 85 (1954).
6. F. Jona and G. Shirane. Ferroelectric Crystals (McMillan Co., NY, 1962).
7. W. J. Merz, Phys. Rev. **76**, 1221 (1949); L. E. Cross, *Phil. Mag. Ser. 7*, **4**, 1161 (1953).
8. C. Kittel. *Phys. Rev.* **82**, 729 (1951).
9. L. E. Cross. *J. Phys. Soc. Jpn.* **23**, 77 (1967); K. Uchino, L. E. Cross, and R. E. Newnham. *Jpn. J. Appl. Phys.* **19**, L425 (1980).
10. G. A. Samara. *Phys. Rev.* **B1**, 3777 (1970).
11. Unpublished data from the authors.
12. P. Asadipour, A. S. Bhalla, and L. E. Cross. *Jpn. J. Appl. Phys.* (suppl.) (1986); L. E. Cross. *Ferro.* **76**, 241 (1987).
13. G. Burns and F. H. Dacol. *Sol. State Comm.* **48**, 853 (1983); *Phys. Rev.* **B28**, 2527 (1983).

APPENDIX 12

JAPANESE JOURNAL OF APPLIED PHYSICS
VOL. 28, NO. 4, APRIL, 1989, pp. 653-661

Large Piezoelectric Effect Induced by Direct Current Bias in PMN:PT Relaxor Ferroelectric Ceramics

W. Y. PAN, W. Y. GU, D. J. TAYLOR and L. E. CROSS

Materials Research Laboratory, The Pennsylvania State University, University Park, PA 16802, USA

(Received December 7, 1988; accepted for publication January 28, 1989)

The longitudinal piezoelectric effect induced by a direct current bias field was investigated in PMN:PT family of relaxor ferroelectric ceramics in the frequency range from 0.1 Hz to 50 kHz. The piezoelectric d_{33} coefficient was studied by measuring the strain induced by the applied electric field. Under the 10 kHz driving field, the large piezoelectric strain coefficient, d_{33}, of 800 pC/N is obtained. The piezoelectric strain coefficient related dielectric and electrostrictive parameters were also studied under direct current bias and the d_{33} coefficient was calculated by the equation $d_{33}=2Q_{11}P_3\varepsilon_{33}$. The results are in good agreement with the directly measured ones. The dispersion of the piezoelectric effect is mainly due to the dielectric dispersion.

KEYWORDS: dc bias induced piezoelectric effect PMN:PT ceramics

§1. Introduction

Since the late 1960's, Lead Titanate: Lead Zirconate ceramics (PZT) near the tetragonal-rhombohedral morphotropic phase boundary have been the leading materials for piezoelectric applications.[1] The remanent polarization of these ceramics is very large, of the order of $40\mu C/cm^2$ and the piezoelectric strain coefficient is high, of the order of 400 pC/N for d_{33}.[2,3]

For these ceramic compositions, the tetragonal and rhombohedral phases have very similar free energies. The poling efficiency is greatly improved compared with the single phase ceramics because 14 ferroelectric axes are available for the reorientation of the spontaneous polarization. However, the piezoelectric strain coefficients depend not only on the remanent polarization but also on the dielectric permittivity. If the piezoelectric effect is regarded as a polarization biased electrostriction,[4] then for a ceramic poled in the direction of the 3 axis, the piezoelectric coefficient d_{33} is determined by the following equation:

$$d_{33}=2Q_{11}P_3\varepsilon_{33} \tag{1}$$

where Q_{11}($Q_{11}=Q_{22}=Q_{33}$ for an isotropic ceramic) is the average longitudinal electrostrictive coefficient of the prototypic phase, P_3 the polarization and ε_{33} the dielectric permittivity. Another obvious way to improve the piezoelectric strain coefficient is to increase the dielectric permittivity.

Relaxor ferroelectrics as compared to normal ferroelectrics[5] are known to have a much larger Curie Weiss constant C and less temperature dependence of dielectric permittivity near the dielectric maximum. Since the QC^2 value, the figure of merit of electrostriction, of the relaxor ferroelectrics is larger than that of the normal ferroelectrics, the relaxor ferroelectrics have found wide applications in transducers and actuators.[6] Though these ceramics, because of the absence of a remanent polarization, show no piezoelectric effects near the temperature of the dielectric maximum, a DC bias can induce the polarization and consequently the piezoelectric effects. A large piezoelectric d_{33} coefficient in the 0.9 PMN:0.1 PT multilayer actuator was demonstrated by Nakajima *et al.*[7] However, the frequency of the measurement was quasi-static (0.02 Hz) and the piezoelectric effect for a useful frequency range is still unknown. Although the piezoelectric resonance technique can be used to measure the DC bias field induced transverse piezoelectric d_{31} coefficient, it is difficult to be used for measuring the longitudinal piezoelectric coefficient d_{33} because the thickness resonance frequencies are high (thin sample in order to apply high DC bias) and tend to overlap with the overtones of other modes.

In this paper, we report on the large longitudinal piezoelectric effect induced by the DC bias field in the lead magnesium niobate: lead titanate family of relaxor ferroelectric ceramics over a wide frequency range and explore the possibility of this family of relaxor ferroelectrics for transducer applications.

§2. Experimental Procedure

2.1 *Ceramic samples and preparation*

The PMN:PT ceramic compositions selected for this study are listed below:

(1) $Pb(Mg_{1/3}Nb_{2/3})O_3$ (PMN)

(2) 0.9 $Pb(Mg_{1/3}Nb_{2/3})O_3$:0.1 $PbTiO_3$ (0.9 PMN:0.1 PT)

(3) 0.93 $Pb(Mg_{1/3}Nb_{2/3})O_3$:0.07 $PbTiO_3$ (0.93 PMN:0.07 PT)

(4) $La_{0.01}$(0.93 $Pb(Mg_{1/3}Nb_{2/3})O_3$:0.07 $PbTiO_3$)$_{0.99}$ ($La_{0.01}$(0.93 PMN:0.07 PT)$_{0.99}$).

The ceramic PMN:PT compositions were prepared using mixed oxides in the manner described by Swartz and Shrout.[8,9] In this processing, MgO and Nb_2O_5 are first reacted in a pre-calcine to form the columbite structure $MgNb_2O_6$ which is then reacted with PbO to form $Pb(Mg_{1/3}Nb_{2/3})O_3$:$PbTiO_3$ compositions. Among these ceramic compositions, 0.93 PMN:0.07 PT and $La_{0.01}$(0.93 PMN:0.07 PT)$_{0.99}$ were hot isostatically pressed to optical transparency. For both dielectric and strain

measurements, the ceramic samples were cut into rectangular plates, typically 0.6×0.4 cm^2, with a thickness of 0.04 cm.

2.2 *Measurement of piezoelectric coefficient d_{33} by field induced strain technique*

The piezoelectric strain coefficient d_{33} was measured using the converse piezoelectric effect, i.e. the strain induced by an electric field.

In the low frequency range (0.1–10 Hz), low frequency thermal and mechanical noises greatly affected the measurement when the induced displacement was small. To increase the signal to noise ratio, large electric fields (>10 kv/cm) were applied to induce large strains ($>10^{-4}$). Strain gauge technique was used to measure the induced strain. The piezoelectric strain coefficient d_{33} was derived from the strain vs the applied electric field by two methods. In the first method (0.1–1 Hz), the slope of the strain vs applied voltage (triangular wave form) was measured by inputting the strain signal to a differentiator which differentiated the strain with respect to time. The signal from the differentiator output is proportional to the piezoelectric d_{33} coefficient, since a triangular driving field (the field is proportional to time within 1/4 period) was applied. The differential signal and the applied field were displayed on the y-axis and the x-axis of a x-y oscilloscope respectively. The picture directly yields the DC bias field dependence of the piezoelectric d_{33} coefficient. This method will be referred to as the differentiator method. In the second method (0.1–10 Hz), the strain (y-axis) vs the applied field (x-axis) was directly displayed on a x-y oscilloscope. The pictures were digitized by a computer controlled digitizing eye and the d_{33} values were calculated by measuring the slopes at different electric field levels. This method will be referred to as the digitizing method. For the compositions such as 0.9 PMN:0.1 PT and 0.93 PMN:0.07 PT which display slim hysteresis loops, it was necessary to simulate the equilibrium strain by drawing a curve, in a way similar to that shown in Fig. 1, between the top curve (associated with the decrease of the electric field) and the bottom curve (associated with the increase of the electric field). The equilibrium path was digitized and then the slopes were calculated to yield the d_{33} coefficients.

A small induced strain technique was used to measure the d_{33} coefficient at frequencies higher than 100 Hz, since many experimental difficulties were encounted when a large electric field was applied to the ceramic samples to induce a large strain. A small induced strain technique is possible, since at high frequencies, the low frequency noises can be rejected easily. In this technique, a DC bias field was applied to the sample to induce the piezoelectric effect and a small AC voltage (~ 2 volts) was applied to induce an AC strain. The induced displacement was small, on the order of a few angstrons, was measured by the highly sensitivitive laser interferometer technique. The basic principles of this technique were published in an earlier paper.[10] The block diagram of the laser interferometer is shown in Fig. 2. In this set-up, the two major faces of the sample are facing the laser beams as shown in Fig. 3, bending effects are avoided. In addition, the measuring frequency of the double beam laser interferometer can be well above 1 kHz above which the single beam laser interferometer technique encounts "back motion" problem.[10] Since the dielectric constant of the relaxor ferroelectric ceramic is large, the contribution of the second mode (electrostriction) to the induced strain is not negligible especially under low bias field. The electronic signal from the photo detector was measured by a Lock-in amplifier set on 1f mode to reject the second mode and the random noises. The two major faces of the sample were polished to optical reflectance and then sputtered with gold to reflect light and conduct electricity. The sample was mounted on a wood made sample holder in a manner shown in Fig. 3. The block diagram of the

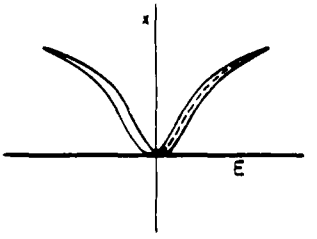

Fig. 1. Illustration of the digitizing method. For the strain vs applied electric field curve, a path (dashed curve) is drawn to simulate the equilibrium strain. The dashed curve is digitized for the piezoelectric coefficient calculation.

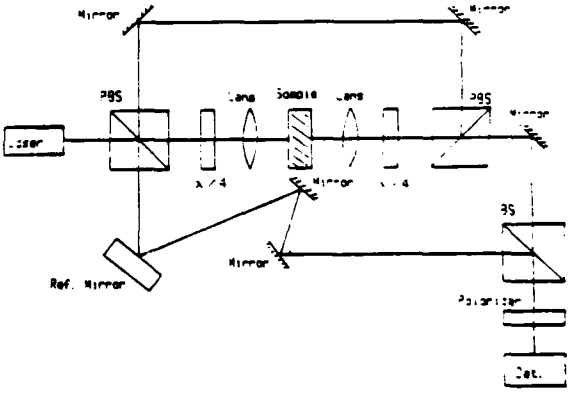

Fig. 2. Block diagram of the double beam laser interferometer system. PBS is the polarized beam splitter, BS is the beam splitter and $\lambda/4$ is the quarter wave plate.

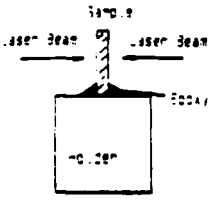

Fig. 3. Schematic diagram of the sample mounting for the double beam laser interferometer measurement.

circuit for the simultaneous application of AC and DC field is shown in Fig. 4.

2.3 *Measurement of piezoelectric d_{33} coefficient through dielectric and electrostrictive parameters*

As suggested in eq. (1), the piezoelectric coefficient d_{33} can be calculated by the relation $d_{33}=2Q_{33}P_3\varepsilon_{33}$, and hence the measurement of the dielectric and electrostrictive parameters can also yield the piezoelectric d_{33} coefficient.

Polarization as a function of bias field was measured using a modified Sawyer and Tower circuit. The Sawyer and Tower technique requires an AC driving field, so a quasi-static driving field (0.04 Hz) was applied to simulate the DC bias field. To decrease the low frequency impedance of the standard capacitance in series with the sample, a large capacitance (10 μF) was used.

The dielectric constant as a function of DC bias field was measured by the system shown in Fig. 5. Two large blocking capacitances were used to protect the capacitance bridge. A 20 MΩ resistor was put in series with the DC power supply so as not to bypass the AC current from the capacitance bridge.

The electrostrictive coefficients for PMN ceramics were measured using the strain gauge technique. The field induced strain and polarization were displayed on y and x axes of a x-y oscilloscope respectively. The pictures were then digitized by a computer controlled digitizing eye. The Q coefficients were calculated from the slopes of induced strain vs the square of polarization.

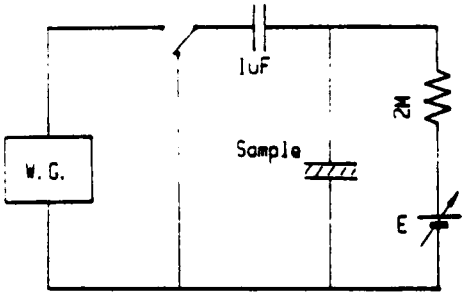

Fig. 4. Circuit for the simultaneous applications of DC and AC field. W. G stands for the waveform generator.

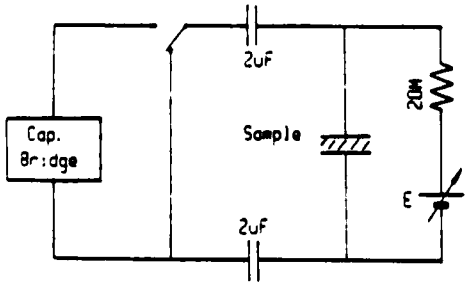

Fig. 5. Block diagram for capacitance measurement under DC bias field.

§3. Experimental Results

3.1 *Low frequency piezoelectric behavior*

The differentiator method directly gives the DC bias field dependence of the d_{33} coefficient. Figure 6 shows the original photographs which display the applied voltage on the horizontal axis and the time derivative of the strain signal on the vertical axis. When the applied voltage changes the swing direction, the time derivative of the strain changes sign. The two curves correspond to the increase and decrease of the applied voltage. Figure 7 shows d_{33} vs the DC bias field in the frequency range (0.1–10 Hz) measured by the digitizing method. Clearly, 0.93 PMN:0.07 PT and 0.9 PMN:0.1 PT ceramics show very large piezoelectric maxima, the peak d_{33} coefficient for 0.93 PMN:0.07 PT is 1260 pC/N at 0.1 Hz. For $La_{0.01}(0.93\ PMN{:}0.07\ PT)_{0.99}$ and PMN, the piezoelectric maxima shift toward the high field region. Another feature of the piezoelectric behavior is the dispersive nature. It is clear that the magnitude of d_{33} coefficient decreases with the increasing driving frequency. The field of the piezoelectric maximum increases with the increasing driving frequency, an effect similar to the dielectric relaxation of the relaxor ferroelectrics in which the dielectric maximum temperature increases with the applied AC field frequency. The shift of the piezoelectric maximum with the driving frequency may be clearly seen for 0.93

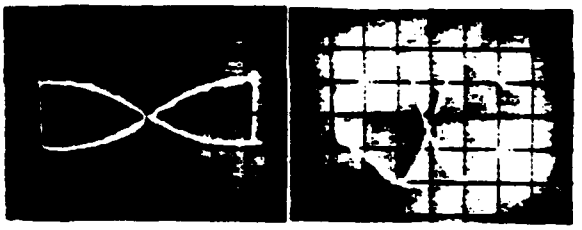

Fig. 6. The original photographs for the differentiator method measurement. The vertical axis displays the derivative of strain and the horizontal axis displays the applied voltage. (a) PMN at 0.1 Hz, (b) 0.93 PMN:0.07 PT at 0.1 Hz and (c) $La_{0.01}(0.93\ PMN{:}0.07\ PT)_{0.99}$ at 0.5 Hz.

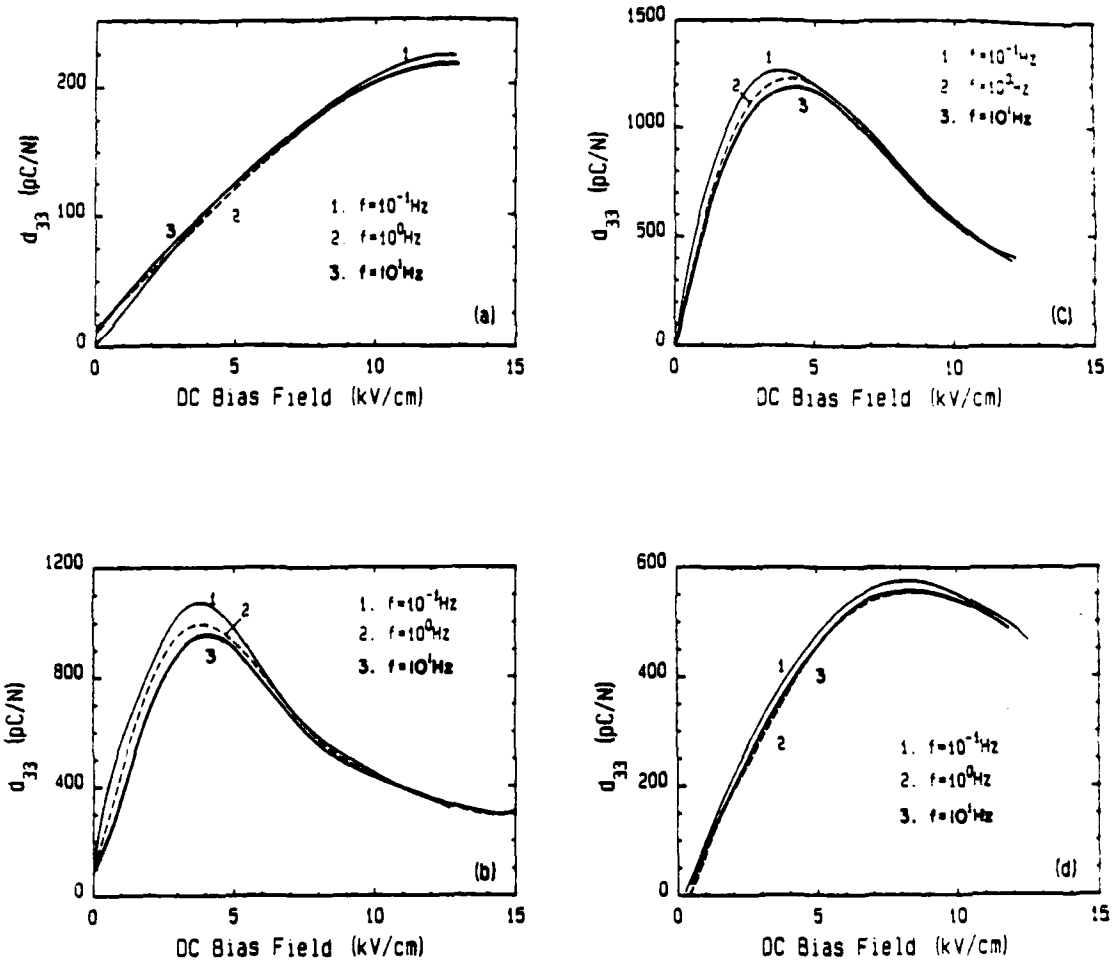

Fig. 7. d_{33} coefficient as a function of DC bias under different AC field frequencies for the digitizing method (a) PMN, (b) 0.9 PMN0.1 PT (c) 0.93 PMN:0.07 PT and (d) $La_{0.01}$(0.93 PMN:0.07 PT)$_{0.99}$.

PMN:0.07 PT and 0.9 PMN:0.1 PT ceramic compositions which have significant dielectric dispersion at room temperature.

3.2 *High frequency (100 Hz–50 kHz) piezoelectric behavior*

From 100 Hz to 50 kHz, the piezoelectric d_{33} coefficient is measured by the double beam laser interferometer. The piezoelectric strain coefficient d_{33} vs the applied DC bias field under different AC field frequencies is shown in Fig. 8. Clearly, the variation of the d_{33} coefficient with the applied DC bias field is similar to that of the low frequency measurement. Since the DC bias field was not continuously varied, the shift of the piezoelectric maximum with the measuring frequency is not as obvious as that for the low frequency measurements. Another feature of the curves is the variation of the dispersion of the d_{33} coefficient with the applied DC bias field. The initial dispersion depends on the compositions. PMN and $La_{0.01}$(0.93 PMN:0.07 PT)$_{0.99}$ have little dispersion while 0.9 PMN:0.1 PT and 0.93 PMN:0.07 PT have significant dispersion under low bias field. The dispersion is maximized at the fields of the piezoelectric maximum and markedly reduced well above the field of the piezoelectric maximum.

3.3 *Electrostrictive coefficients and DC bias dependence of polarization and dielectric constant*

To evaluate the d_{33} coefficient as a function of DC bias, the dielectric constant K_{33}, polarization P_3 and electrostrictive coefficient Q_{11} have to be evaluated as a function of DC bias. Since the electrostrictive coefficient Q_{11} is independent of polarization and was found to be true in ferroelectric relaxors up to a high polarization level,[11] the Q_{11} coefficient is assumed to be field and polarization independent.

The polarization vs the applied field with a quasi-static driving field (0.04 Hz) is shown in Fig. 9. Since slim hysteresis loops were observed for 0.93 PMN:0.07 PT and 0.9 PMN:0.1 PT ceramics, the average polarization values of the top curve and the bottom curve were taken to simulate the equilibrium polarization induced by a true DC bias field.

Dielectric constant vs applied DC bias for four ceramic

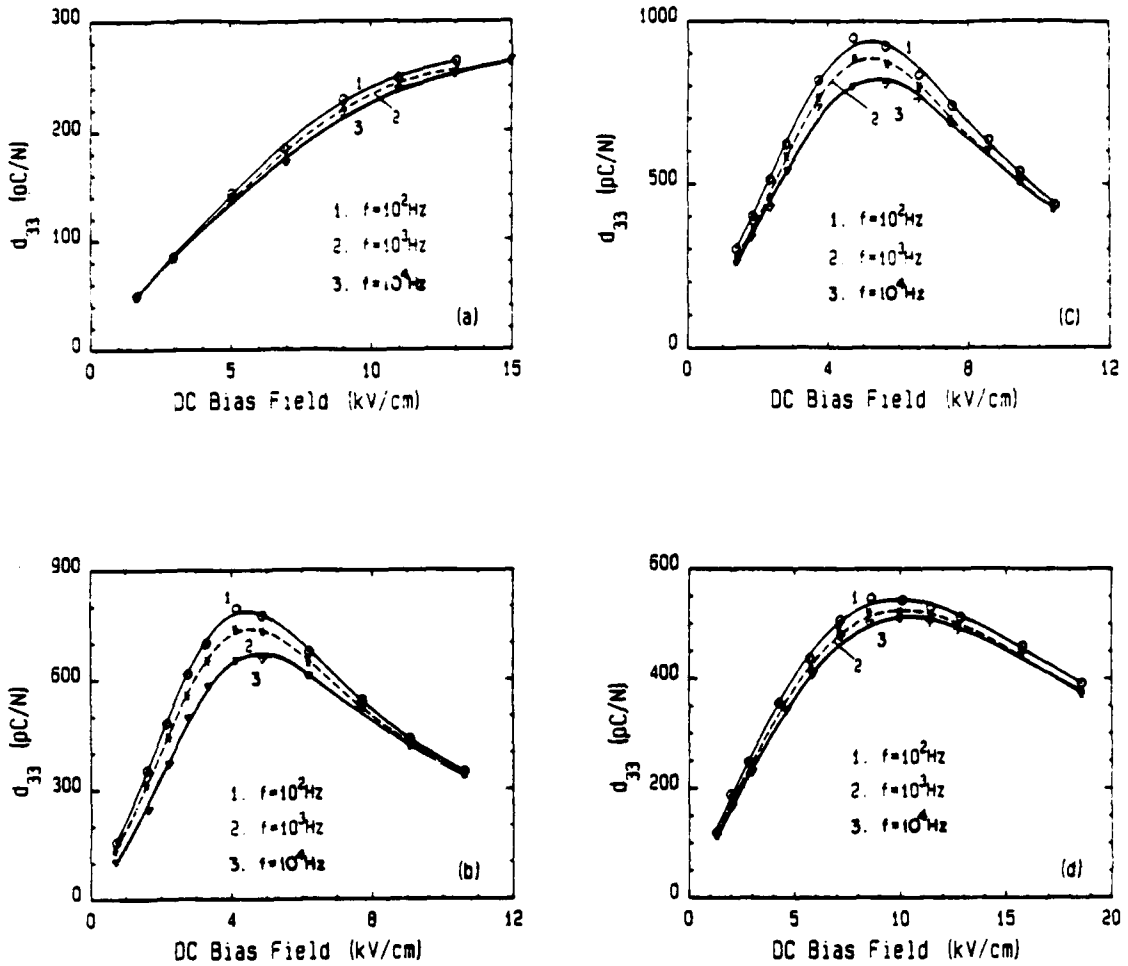

Fig. 3. d_{33} coefficient as a function of DC bias under different AC field frequencies for the high frequency measurement (a) PMN, (b) 0.9 PMN:0.1 PT (c) 0.93 PMN:0.07 PT and (d)$La_{0.01}$(0.93 PMN:0.07 PT)$_{0.98}$.

compositions is shown in Fig. 10. Clearly, the magnitude and dispersion of the dielectric constant decrease with increasing DC bias field. For PMN, no appreciable dispersion is observed.

The electrostrictive coefficients Q_{11} and Q_{12} were measured as a function of temperature under an AC field frequency of 0.1 Hz using the strain gauge technique. It is observed that the Q coefficients stay constant with respect to temperature. The average Q_{11} coefficient for PMN is 1.9×10^{-1} m^4/C^2 as shown in Fig. 11. The Q_{11} coefficient for the 0.9 PMN:0.1 PT ceramic was published in an earlier paper.[12] The room temperature Q_{11} value is 2.1×10^{-2} m^4/C^2.

The d_{33} coefficients for PMN and 0.9 PMN:0.1 PT ceramics were calculated according to eq. (1) using the above dielectric and electrostrictive parameters. The variation of the d_{33} coefficient with DC bias field under different AC field frequencies is shown in Fig. 12. It may be seen that the DC bias field dependence and frequency dispersion of the d_{33} coefficient are quite similar to those directly measured.

§4. Discussions

4.1 *DC bias field dependence of the piezoelectric d_{33} coefficient*

The variations of the 1kHz piezoelectric d_{33} coefficient with the applied DC bias field from both the directly measured result and that calculated from the dielectric and electrostrictive parameters are compared in Fig. 13 for PMN and 0.9 PMN:0.1 PT ceramics. Agreement is reasonably good, although there are differences in magnitude especially under the high bias field level. The agreement suggests that the DC bias field dependence of the d_{33} coefficient is determined by the DC bias field dependence of polarization and dielectric constant, while the electrostrictive Q_{11} coefficient could be assumed to be a field independent parameter within the applied field level of the experiment. Hence, in the relaxor ferroelectrics, the piezoelectric effect is basically a polarization biased electrostriction.

4.2 *Dispersion of the piezoelectric coefficient*

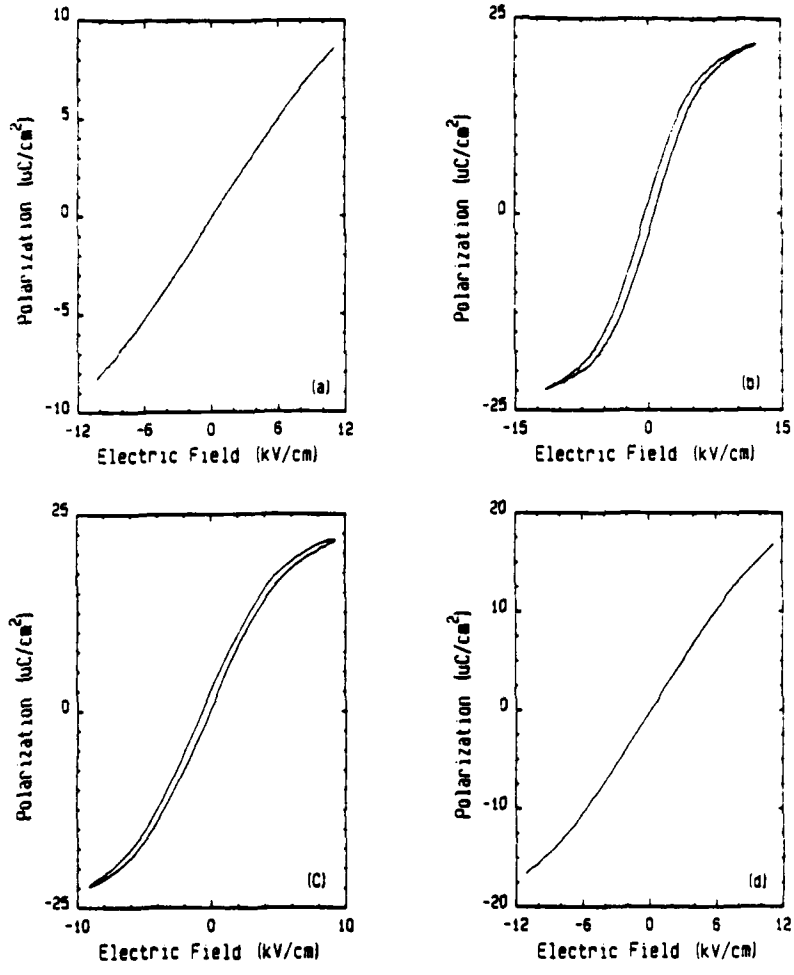

Fig. 9. Polarization-electric field relations: (a) PMN, (b) 0.9 PMN:0.1 PT, (c) 0.93 PMN:0.07 PT and (d) $La_{0.02}$(0.93 PMN:0.07 PT)$_{0.98}$.

Under low bias level, the piezoelectric dispersion is mainly dominated by the dielectric dispersion. It may be seen from Figs. 8 and 10 that the dispersion of the d_{33} coefficien under very low bias field level is very similar to that of the dielectric permittivity dispersion. At the field of the piezoelectric maximum, the dispersion in piezoelectric response is maximized. The same is true for the data calculated from the dielectric and electrostrictive parameters. This is because the piezoelectric dispersion caused by the dielectric dispersion at the field of the piezoelectric maximum is enhanced by the increased polarization level at the field of the piezoelectric maximum. For the fields much greater than the piezoelectric maximum fields, the dispersion of d_{33} coefficient is greatly reduced as shown in Figs. 8(b), (c) and (d). The correspondence in the dielectric dispersion may be found in the same field region as shown in Figs. 10(b), (c) and (d). Under high DC bias level, the induced polarization is saturated, and the reduction in dielectric dispersion will result in the reduction of piezoelectric dispersion.

Figure 14 shows the maximum piezoelectric d_{33} coefficient (directly measured) vs the measuring AC frequency for different compositions. It is obvious that above 20 kHz, most of the points are not expected. For the sizes of the samples we used, 20 kHz is well below the piezoelectric resonance frequency. The reason for these unexpected points is not very clear. It may be caused by some purely mechanical resonance modes which may be related to the acoustic properties of the epoxy and the sample holder. The real reason is still under investigation. However, below this frequency, the results reveal the dispersive nature of the piezoelectric behavior.

For the two ceramic compositions 0.93 PMN:0.07 PT and 0.9 PMN:0.1 PT, it can be seen that the piezoelectric dispersion is significant because the temperatures of the dielectric maxima are above room temperature, significant dielectric dispersion exists. On the other hand, for PMN ceramic, the dispersive nature is greatly reduced, since the temperature of the dielectric maximum is well below room temperature. However, the advantages of the reduced dispersion are penalized by the severely reduced magnitude of the piezoelectric coefficient.

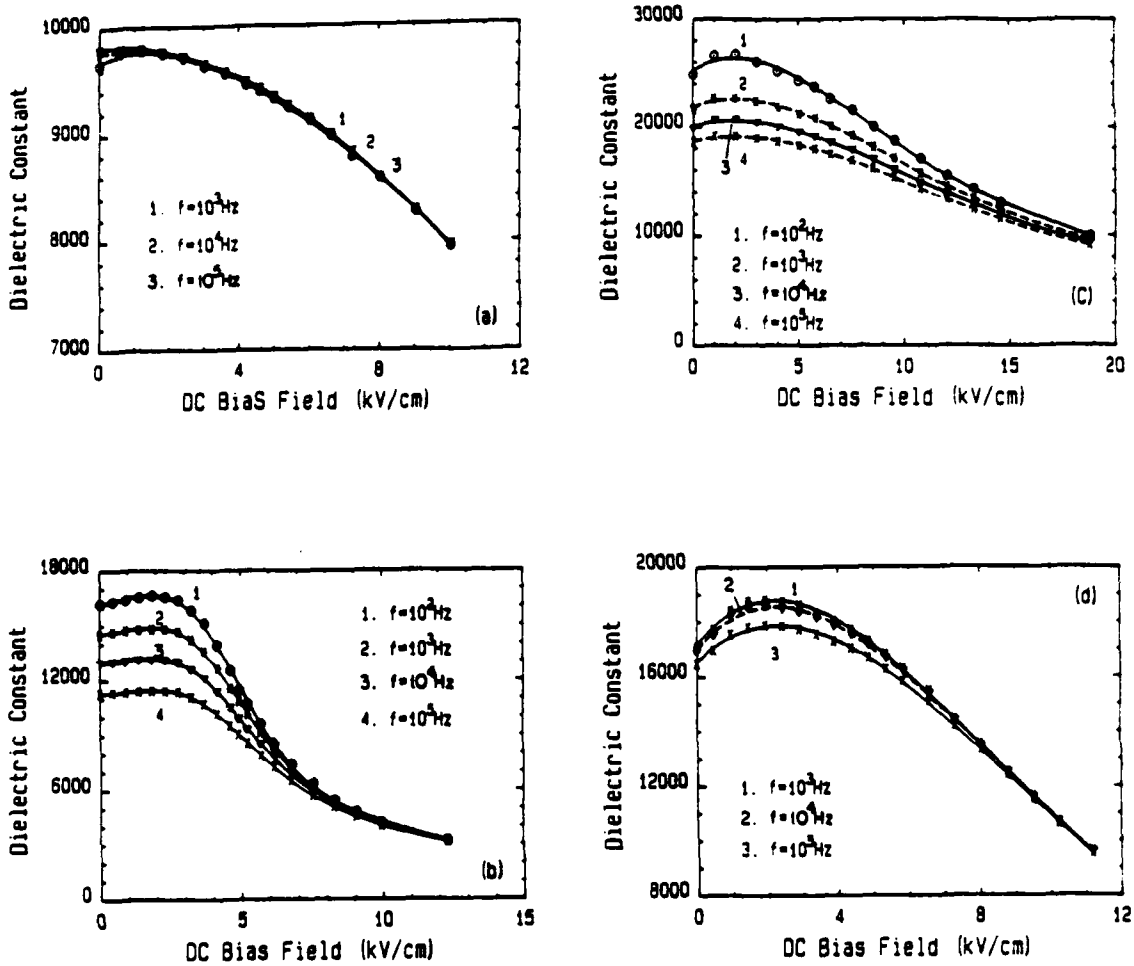

Fig. 10. Dielectric constant as a function of DC bias field under different frequencies: (a) PMN, (b) 0.9 PMN:0.1 PT, (c) 0.93 PMN:0.07 PT and (d) $La_{0.01}$(0.93 PMN:0.07 PT)$_{0.99}$.

It has to be pointed out that for 0.93 PMN:0.07 PT and 0.9 PMN:0.1 PT ceramics, steps appear between the data obtained by the low frequency measurement and that obtained by the high frequency measurement. The reason for this phenomenon is not very clear. It may be due to the experimental error or to the manners in which the AC field were applied. In the low frequency measurement, the DC bias field was simulated by a quasi-static driving AC field (0.1–10 Hz) and the AC field is essentially the same field. On the other hand, in the high frequency measurement, the DC bias field is a true static field, while the AC field is a small amplitude (~2 volts) with the frequency above 100 Hz. In the relaxor ferroelectrics, the energy barriers for the polarization process distribute over a range. When the amplitude of the applied AC field is fixed, frequency dispersion takes place because different times are required for the polarization processes with different energy barriers. When the frequency of the driving field is fixed, the amplitude of the driving field may also produce different dielectric and piezoelectric responses. Consider the dielectric response at the same electric field level, a small AC field oscillating on the top of a true DC bias field may exclude more contributions from the polarization processes with larger energy barriers than a large swing AC field. This may be the reason why a step decrease from 10 Hz to 100 Hz occurs for 0.93 PMN:0.07 PT and 0.9 PMN:0.1 PT ceramic compositions. For PMN and $La_{0.01}$(0.93 PMN:0.07 PT)$_{0.99}$ ceramic compositions, room temperature is on the right side of the dielectric maximum, intrinsic polarizability become more important for the polarization processes. The distribution of the "energy barriers" narrows down considerably; therefore, the step decrease from 10 Hz to 100 Hz is not obvious. An extreme case of this phenomenon may also be found in normal ferroelectrics. The large magnitude of the P-E slope at the coercive field of the dielectric hysteresis loop can not be obtained when the ferroelectric is biased at the coercive field and the dielectric permittivity is measured by a small excitation AC electric field.

4.3 *Potential piezoelectric applications*

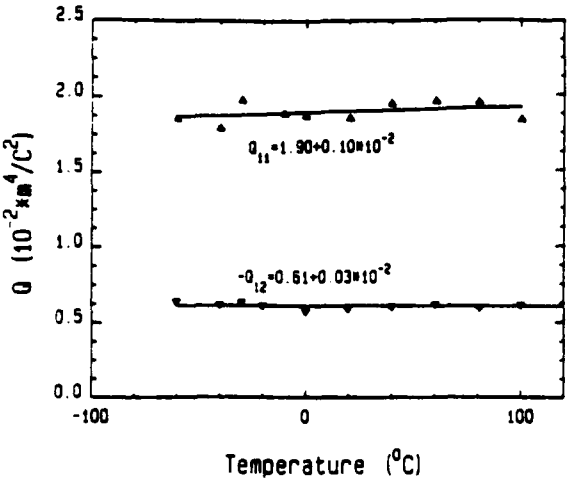

Fig. 11. Q_{11} and Q_{12} coefficients as a function of temperature for PMN ceramic measured by strain gauge technique under the driving frequency of 0.1 Hz

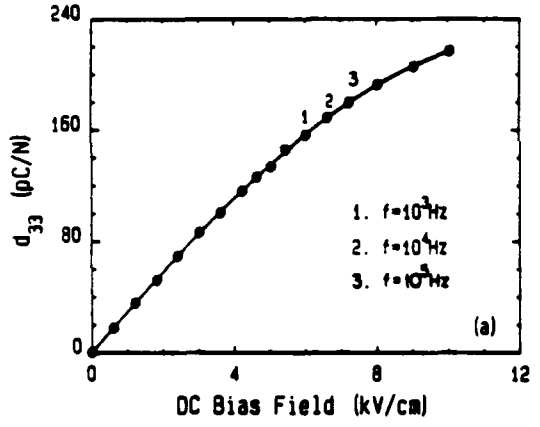

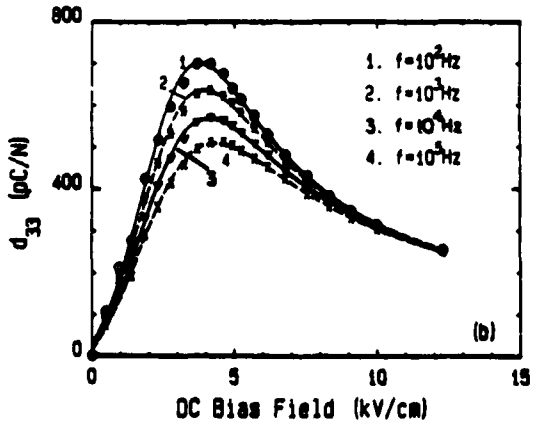

Fig. 12. d_{33} coefficient calculated from the dielectric and electrostrictive parameters. (a) PMN and (b)0.9 PMN:0.1 PT.

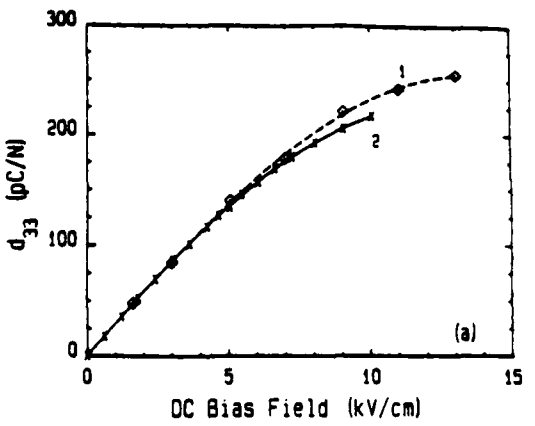

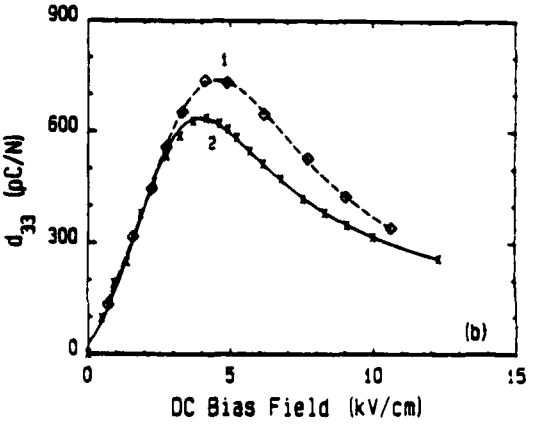

Fig. 13. Comparison of 1 kHz d_{33} coefficient vs the DC bias field for (a) PMN and (b) 0.9 PMN:0.1 PT. 1: directly measured result, 2: calculated from the dielectric and electrostrictive parameters.

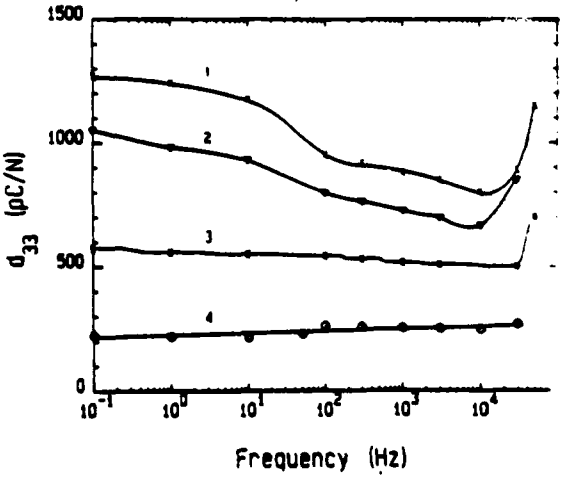

Fig. 14. d_{33} coefficient at the piezoelectric maximum vs the AC frequency. 1: 0.93 PMN:0.07 PT, 2: 0.9 PMN:0.1 PT, 3: La... PMN:0.07 PT)$_{0.99}$, 4: PMN.

It is observed that the maximum piezoelectric d_{33} coefficient at the 10 kHz range amounts to 800 pC/N, which is larger than that observed in PZT ceramics. Such a high frequency piezoelectric coefficient suggests the possibility of this family of ceramics for sonic and ultrasonic applications. Under a DC bias field, the materials are piezoelectrically active and therefore can sense the mechanical and acoustic perturbations in a passive fashion. If such a signal is fed back to control the field applied on the transducer, the transducer can also deform in an active fashion.

The sensitivity of the piezoelectric effect can be controlled and switched "on" and "off" by a DC bias field. Such a feat can not be accomplished in a permanently poled PZT ceramic. It is quite possible that switchable transducers of this type find useful applications in the field of sonics and ultrasonics.

Acknowledgements

The authors wish to thank Ms. S.Yoshikawa, Dr. T.R.Shrout and Dr. A. S. Bhalla for their help and discussions.

References

1) B. Jaffe, W. R. Cook and H. Jaffe: *Piezoelectric Ceramics* (Academic Press, London and New York, 1971).
2) D. Berlincourt, C. Cmolick, and H. Jaffe: Proc. IRE 48 (1960) 220.
3) B. Jaffe, R. S. Roth, and S. Marzullo: J. Res. Bur. Stds. 55 (1955) 239.
4) J. M. Herbert: *Ferroelectric Transducer and Sensor*, Electrocomponent Science Monographs, vol. 3 (Gordon Beach Publisher New York, London and Paris, 1982) Vol. 3.
5) K. Uchino, S. Nomura, L. E. Cross and R. E. Newnham: J. Phys. Soc. Jpn. 49 (1980) 45.
6) K. Uchino: Ceram. Bull. 65 (1986) 4.
7) Y. Nakajima, T. Hayashi, I. Hayashi and K. Uchino: Jpn. J. Appl. Phys. 24 (1983) 235.
8) S. L. Swartz and T. R. Shrout: Mater. Res. Bull. 17 (1982) 1245.
9) S. L. Swartz, T. R. Shrout, W. A. Schulze and L. E. Cross: J. Am. Ceram. Soc. 67 (1984) 311.
10) Q. M. Zhang, W. Y. Pan and L. E. Cross: J. Appl. Phys. 63 (1988) 2490.
11) S. J. Jang, K. Uchino, S. Nomura and L. E. Cross: Ferroelectrics 27 (1980) 31.
12) Q. M. Zhang, W. Y. Pan, A. S. Bhalla and L. E. Cross: J. Am. Ceram. Soc. (1989) April.

APPENDIX 13

Ferroelectrics Letters, 1990, Vol. 11, pp. 1-9
Reprints available directly from publisher
Photocopying permitted by license only

COMPLEX PIEZOELECTRIC, ELASTIC, AND DIELECTRIC COEFFICIENTS OF La-DOPED 0.93 $Pb(Mg_{1/3}Nb_{2/3})O_3$:0.07 $PbTiO_3$ UNDER DC BIAS†

D.J. Taylor, D. Damjanovic, A.S. Bhalla, and L.E. Cross
Materials Research Laboratory
The Pennsylvania State University
University Park, PA 16802

(Received for Publication October 27, 1989)

ABSTRACT: Complex material parameters (piezoelectric coefficient d_{31}, elastic s_{11}^E, and the dielectric constant K_{33}) of the relaxor ferroelectric ceramic (1-x) $Pb(Mg_{1/3}Nb_{2/3})O_3$-x$PbTiO_3$ (x = .07) with 1% La (lanthanum) were measured as a function of bias field using a bar resonator. The values of the dielectric and piezoelectric phase angles are found to be comparable (i.e., around 0.04 for a d.c. bias field of 2.5 kV/cm), while the elastic phase angle is an order of magnitude smaller (0.001 for the same d.c. bias). For comparison of complex material parameters found from bar resonators, a sample in the form of a small disk is used to measure Poisson's ratio as well as the real components of the piezoelectric and elastic coefficients as a function of bias field.

INTRODUCTION

In 1958, Smolenskii reported large dielectric and piezoelectric constants in a complex perovskite lead magnesium niobate, $Pb(Mg_{1/3}Nb_{2/3})O_3$ (PMN).[1] These properties of PMN (and PMN-based materials) have many device applications including multilayer capacitors and actuators, dielectric or pyroelectric bolometers and electro-optic shutters.

PMN is a relaxor ferroelectric[2] exhibiting a diffuse phase transition. Its dielectric constant and dissipation factor are strongly frequency dependent. With increasing frequency the dielectric constant decreases in magnitude and the maxima shifts to higher temperatures, while for the dielectric tanδ, maxima decrease with an increase in frequency. The relaxor dielectric maxima at 1 kHz occurs at -15°C. However, with the addition of $PbTiO_3$ (PT) (Curie temperature = 490°C), the relaxor T_c can be raised while the solid solution can maintain its favorable relaxor characteristics, large dielectric and piezoelectric constants.

In the past, several studies have been made on the piezoelectric, elastic, and dielectric constants of PMN ceramics, but very few studies have explored the piezoelectric, elastic, and dielectric properties as a function of d.c. bias or the relationship between the dielectric and piezoelectric phase angle. The intent of this paper is to present our initial findings on the field dependence of d_{31}, dielectric constant, elastic compliance and the imaginary parts of these complex parameters in 0.93 PMN:0.07 PT ceramics.

†Commissioned by Professor R. E. Newnham

In the present work the composition (1-x) PMN-xPT (x = 0.07) with 1% La doping has been selected. In accordance with the solid solution phase diagram,[3] the composition with x = 0.07 is a good candidate for a switchable piezoelectric material. With the 1% addition of La the Curie temperature of the composition is shifted down below room temperature, and with the applied electric bias field it is possible to switch the material from the passive (non-piezoelectric) to the active (piezoelectric) state. The addition of La also promotes densification of the sintered bodies. The ability to control grain growth could lead to a valuable study of the electromechanical properties of PMN-PT system as a function of grain size. The compositions near the PMN-PT solid solution morphotropic phase boundary (x = 0.30-0.35),[3] where larger values of the piezoelectric coefficients could be expected, have a transition into the paraelectric (cubic) phase around 100°C. Thus, these compositions are not suitable for room temperature switching applications as the material will remain poled (piezoelectric) even after the electric bias field is removed.

EXPERIMENTAL METHODS

(a) The Measurement Technique

The technique used to measure material parameters as a function of bias at room temperature is shown in Fig. 1. It uses an HP 4192 Impedance Analyzer, HP 9121 Computer, High Voltage Power Supply, two blocking circuits, and a sample holder adapted to the Impedance Analyzer. The details of this system will be furnished in another paper.[4]

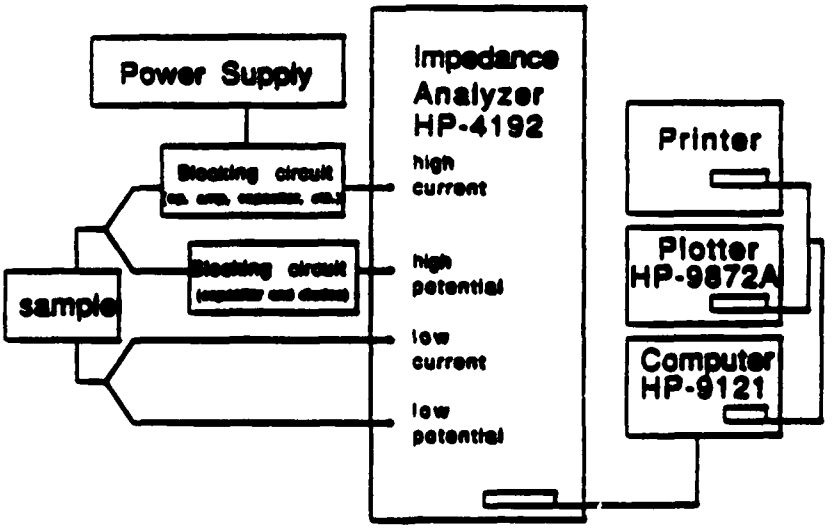

Figure 1. Schematic of the measurement system.

The samples (approx. > 95% of theoretical density) were cut and polished with 3 micron alumina and gold electrodes were sputtered on two opposite surfaces. Measurements of complex piezoelectric, dielectric, and elastic constants of PMN:PT as a function of bias were obtained for electric fields as high as 15 kV/cm. Beyond these fields the samples may have breakdown and thus the measurement system was designed with blocking circuits in order to protect the Impedance Analyzer.

The placement of the sample in the circuit was determined to minimize parasitic elements that would combine with the sample to give additional impedance. However, a correction factor was applied in the software in order to take into account the parasitic elements that are a consequence of the blocking circuits employed.[4]

The HP computer was interfaced with the Impedance Analyzer and using software[5] the impedance of the sample near resonance was determined as a function of frequency for an applied d.c. field.

(b) Calculation of the Complex d_{31}, s_{11}^E, K_3, and k_{31} for Bar Resonator

For a given bar resonator with its length (l) >> t (thickness), l > 3w (width), and for a d.c. field applied perpendicular to its length direction, the admittance, Y, of the bar can be described by:

$$Y = \frac{j\omega lw}{t}\left(\varepsilon_{33}^T - \frac{d_{31}^2}{s_{11}^E}\right) + \frac{j\,2wd_{31}^2}{\left(\rho s_{11}^E\right)^{\frac{1}{2}} s_{11}^E t}\tan\frac{1}{2}\omega l\left(\rho s_{11}^E\right)^{\frac{1}{2}} \qquad (1)$$

where s_{11}, d_{31}, and ε_{33} are assumed to be the complex quantities (i.e., $s_{11}^E = s_{11}^{E'} - js_{11}^{E''}$, $d_{31} = d_{31}' - jd_{31}''$, and $\varepsilon_{33}^T = \varepsilon_{33}^{T'} - j\varepsilon_{33}^{T''}$).

The calculation for the real and imaginary piezoelectric, elastic, dielectric, and coupling coefficients of a bar resonator are based on the method described by Smits.[6] The procedure involves three measurements of the admittance and an initial guess of the elastic constant. The values are determined in an iterative method for the complex admittance at three frequencies near the resonance.

The material coupling factor, k_{31}, is determined by using an expression:[7]

$$k_{31} = d_{31} / \left(\varepsilon_{33} s_{11}\right)^{\frac{1}{2}} \qquad (2)$$

(c) Calculation of the Real Part of s_{11}^E, d_{31}, and Poisson's Ratio for a Thin Disk

The calculation for real components of s_{11}, d_{31}, and Poisson's ratio, σ_{ab}, of a thin disk is based on a procedure developed by S.V. Bogdanov and A.M. Timonin[8,9] and involves measurements of the series (f_s) and parallel (f_p) frequency of the fundamental resonance and the series frequency of the first harmonic for the radial mode of the disk. The series frequency is taken at maximum conductance and the parallel frequency at maximum resistance for respective resonances. The equation that determines d_{31} is:

$$d_{31} = \sqrt{s_{11}^E \varepsilon_{33}^T} \sqrt{\frac{1-\sigma}{2}} \sqrt{\frac{\Delta f}{f_s}\left(K_1^2 + \sigma^2 - 1\right)(1+\sigma)} \qquad (3)$$

where $\Delta f = f_p - f_s$ and K_1 is the first root of the transcendental equation which defines the condition for the occurrance of mechanical resonance for radial vibrations of the thin piezoelectric disks. Further details of the calculations are described by Damjanovic.[9]

RESULTS

The results of the real component of d_{31} calculated for bar and disk resonators is shown in Fig. 2. The maximum d_{31}' for the bar and disk, both

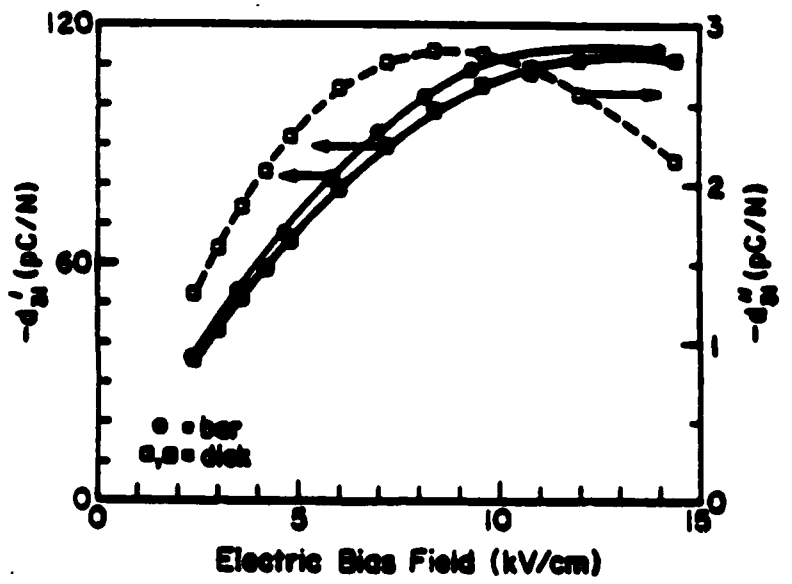

Figure 2. D.C. field dependence of the real (d_{31}') and imaginary (d_{31}'') part of d_{31} of 0.93 PMN:0.07 PT ceramics with 1% La.

measured at room temperature is between 110 pC/N and 115 pC/N and occurs at a bias field of 11-12 kV/cm. The maximum of the disk was slightly higher than the bar shaped sample. The two different sample geometries for measuring d_{31}' gave the same material coefficient and when the curves were extrapolated to zero field, d_{31}' values approach zero as expected. (The sample with no bias field is in the paraelectric state with no piezoelectric property.)

The imaginary part of d_{31} was determined only for a bar sample and is shown in Fig. 2 (with a dashed line). For various bias electric fields d_{31}'' has a maximum value ~ 3 pC/N at an electric field ~ 8 kV/cm. It is interesting to note that the imaginary d_{31}'' maximum occurs at lower field levels as compared to that of the real part of the d_{31} value. This behavior is similar in nature to the way the maximum dissipation factor occurs before the dielectric maximum in the dielectric constant versus temperature measurements (of a typical relaxor PMN).

The real and imaginary dielectric constant K_{33} ($K_{33} = \varepsilon_{33}^T/\varepsilon_o$, where ε_o is the permittivity of free space) for the bar samples as a function of d.c. bias is shown in Fig. 3. When extrapolated to zero field values, the dielectric constant value is 12,800. Confirmation of the real part of the dielectric permittivity of the bar samples was made with an independent measurement. The dielectric permittivity measured at 100 kHz, near the samples resonance, was 12,300 (in a weak a.c. field ~ 2 mV/cm) which compares well with the extrapolated value of K_{33}'.

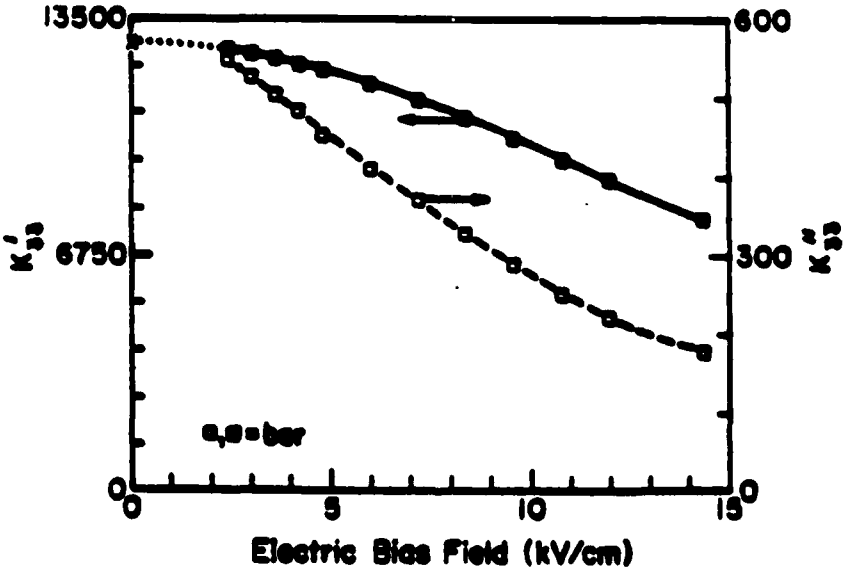

Figure 3. Plot of real (K_{33}') and imaginary (K_{33}'') part of dielectric constant as a function of d.c. bias at the samples resonance. Independent weak field measurement for K_{33}' is 12,300 near the samples resonance.

The imaginary part of the dielectric constant versus field for a bar is shown (with a dashed line) in Fig. 3. The trend of the imaginary dielectric constant is to decrease as one would expect for a relaxor ferroelectric.[2]

The real part of s_{11} for the bar and disk samples is shown in Fig. 4. The values show s_{11}' to be essentially constant with field. The slight difference in magnitude (~ 2%) between values for the disk and bar samples is probably due to the inaccuracy in determining the dimensions and density of the samples. The imaginary part of s_{11} is also shown in Fig. 4 with a dashed line and it varies slightly with field (~ 3%) in comparison to the substantial changes measured in the imaginary part of complex d_{31} and K_{33}.

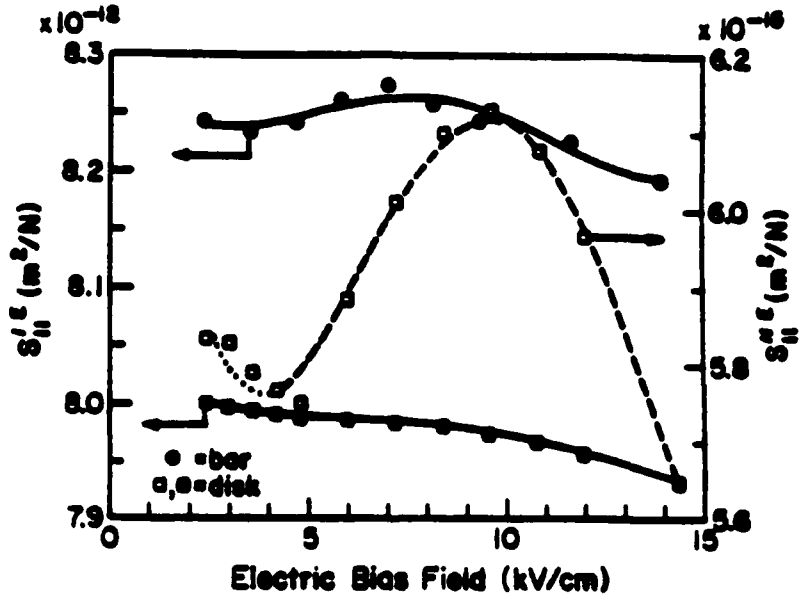

Figure 4. Plots of real (s_{11}') and imaginary (s_{11}'') part of elastic compliance versus d.c. bias.

In Fig. 5, the dielectric, piezoelectric, and elastic phase angle (K"/K', d"/d', and s"/s') are shown as a function of d.c. bias. The magnitude of the piezoelectric and dielectric phase angles are comparable leading us to believe that the dispersion of the piezoelectric coefficients is most likely due to the same type of effects that cause the dispersion in the relative dielectric permittivity.[2]

The mechanical coupling coefficient as calculated from the d_{31}, s_{11}, and ε_{33}^T data on a bar is shown in Fig. 6. The maximum k_{31} reaches 15% at field levels of 15 kV/cm. Also when extrapolated to zero field, k_{31} approaches zero as expected for a non-piezoelectric materials.

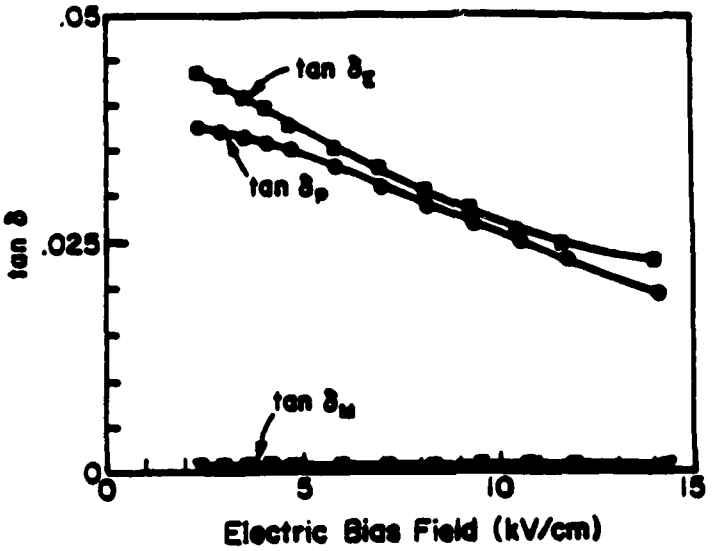

Figure 5. Dielectric, piezoelectric, and elastic phase angle as measured with various levels of d.c. bias.

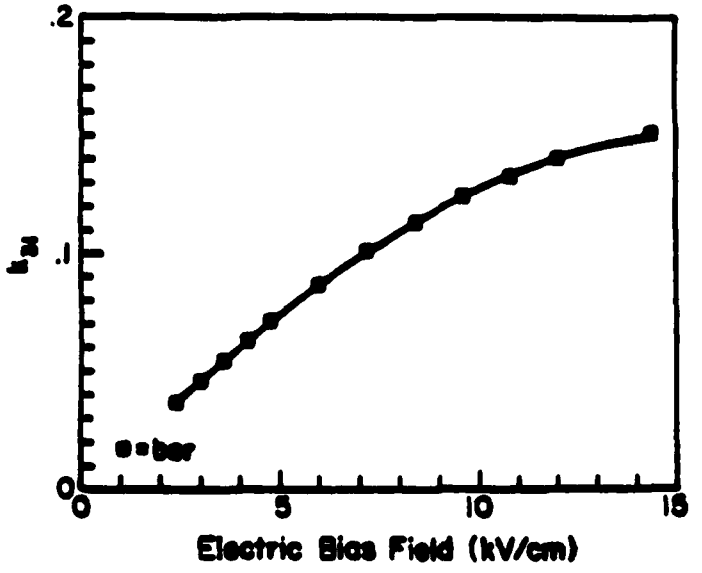

Figure 6. D.C. field dependence of electromechanical coupling coefficient (k_{31}) in 0.93 PMN:0.07 PT with 1% La disks.

Poisson's ratio calculated for a disk resonator sample is shown in Fig. 7. The values are comparable to those found in pure PMN.[10]

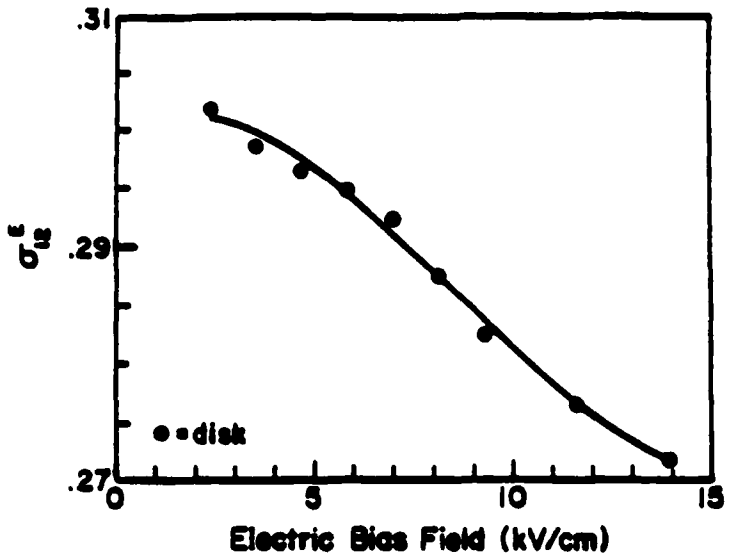

Figure 7. Poisson's ratio (σ_{12}) as calculated from the resonance measurements.

CONCLUSIONS

The real and imaginary values of d_{31}, s_{11}, and K_{33} along with k_{31} and σ_{12} are determined for the composition (1-x) PMN-(x)PT (x = 0.07) with 1% La. The maximum real part of d_{31} for this material is ~ 114 pC/N with a d.c. bias field of 12 kV/cm. While the size of the piezoelectric and dielectric phase angle are comparable, the elastic phase angle is an order of magnitude smaller and remains essentially constant with a d.c. bias. Also, the measured value of Poisson's ratio is comparable to that found in pure PMN.

The measurements on various compositions in the PMN:PT system and antiferroelectrics as a function of temperature, field, and the processing conditions of the sample is in progress and will be reported in the forthcoming publications.

ACKNOWLEDGEMENTS

The authors gratefully acknowledge the Office of Naval Research for financing this research work. Thanks are due to Paul Moses for his help and suggestions on the measuring apparatus, Namchul Kim for providing some of the samples used in this study, and Professor R.E. Newnham for valuable discussions during the preparation of this manuscript.

REFERENCES

1. G.A. Smolenskii and A.I. Agronovskaia. *Soviet Physics-Technical Physics*, 3, 1380 (1958).

2. L.E. Cross. "Relaxor Ferroelectrics," *Ferroelectrics*, 76, 241 (1987).

3. S.W. Choi, T.R. Shrout, S.J. Jang, and A.S. Bhalla. "Morphotropic Phase Boundary (MPB) in $Pb(Mg_{1/3}Nb_{2/3})O_3$-$PbTiO_3$ System" *Ferroelectrics* (to be published).

4. D.J. Taylor, P.J. Moses, D. Damjanovic, A. Bhalla, and L.E. Cross. (To be published).

5. P.J. Moses. "Circle" program (private communication).

6. J.G. Smits. *IEEE Trans. on Sonics and Ultrasonics*, SU-23, 393 (1976).

7. *IEEE Standards on Piezoelectricity*, ANSI/IEEE Standards, 176-1978, IEEE, New York (1978).

8. S.V. Bogdanov and A.M. Timonin. "A Method of Measuring Piezomodulus from Radial Vibrations of a Disk," *Izv. Akad Nauk USSR-Seriya Fazicheskaya*, 21, 397 (1957).

9. D. Damjanovic. "Highly Anisotropic Electromechanical Properties in Modified Lead Titanate Ceramics," Ph.D. Thesis, The Pennsylvania State University, University Park, PA 16802 (1987).

10. Y. Tsuchiya, K. Uchino, and S. Nomura. "Approximate Formulas for a Low-Q Electromechanical Resonator and their Applications to Electrostrictive PMN-Based Ceramics," *Jap. J. Appl. Phys.*, 20, 1841 (1981).

APPENDIX 14

Ferroelectrics, 1989, Vol. 89, pp. 47–59
Reprints available directly from the publisher
Photocopying permitted by license only

EFFECTS OF THERMAL TREATMENT AND DC BIAS ON DIELECTRIC AGING IN THE PLZT 9.5:65:35 RELAXOR FERROELECTRIC CERAMIC

W. Y. GU, W. Y. PAN and L. E. CROSS

Materials Research Laboratory, The Pennsylvania State University, University Park, PA 16802 USA

(Received July 12, 1988)

The dielectric aging effects after thermal treatments and under DC bias were studied and delineated for Lead Lanthanum Zirconate Titanate (PLZT 9.5:65:35) relaxor ceramic. Under room temperature aging, dielectric constant and loss tangent as a function of aging time obey a power law ($K = Kot^{-n}$) and the power index (n) follows the logarithmic law with measured frequency. The aging rate was enhanced by the quenching prior to the aging process. The DC bias reduced the aging rate especially under high measured frequencies. During aging, the Cole–Cole plot shrinks with aging time in such a way that the average relaxation time constant decreases and the distribution of relaxation time constant become narrow with aging time. All the effects are correlated and modeled with the characteristics of relaxor ferroelectrics. The aging process looks like that the polar microregions have a preferred orientation corresponding to the deepest minimum in energy and its contribution to the total permittivity will decrease.

1. INTRODUCTION

Dielectric aging is a well-known phenomenon observed in ferroelectric and antiferroelectric crystal and ceramics. It is generally accepted that aging is caused by the stabilization of the domain contribution due to the interaction between defects and spontaneous polarizations.[1,2,3] It has been observed that in $BaTiO_3$[4] and other[5] ferroelectrics that permittivity and dielectric loss reduction follow a logarithmic aging law under a constant temperature for many years. It was also shown[6] that both real and imaginary parts of the dielectric constant strongly deviate from the logarithmic aging law and tend to level out with time. In normal ferroelectric it was shown that K′ and K″ plots for isothermal aging are straight lines,[7] while in relaxor ferroelectric the plots are curved. Clearly, normal ferroelectrics and relaxor ferroelectrics have different aging behavior. The difference is obviously caused by different composition and phase homogeneities. The role compositional heterogeneity on the relaxor behavior was confirmed by Setter *et al.*[8] this heterogeneity must modify the dielectric aging as well.

For the investigated relaxor PLZT ceramic of the composition 9.5:65:35 there exists a volume fraction of ferroelectric polar region embedded within a non-polar matrix at room temperature.[9] Cross *et al.*[6,10] have suggested that the height of the energy barrier (Φ) between equivalent dipole directions is proportional to the volume of the polar region. These barriers become comparable to the thermal activation energy ($kT \sim \Phi$) and the polar vectors reorient thermally with a relaxation character, if the volume of the polar microregion is small enough. For compositionally heterogeneous crystals due to the compositional fluctuations the local

symmetry at a given polar region may not be the same as (lower than) the global crystal symmetry. Thus, the preferred vector directions for polarization may not be exactly energetically equivalent, and they may not necessarily conform exactly at the direction prescribed by the prototypic form. According to this model,[6,11] the polar microregions will have a preferred orientation corresponding to the deepest minimum in energy and its contribution to the total permittivity will decrease as the local anisotropy increases.

In this paper, we present a systematic measured data on dielectric aging in relaxor ferroelectric using PLZT 9.5:65:35 as a representative material and correlate the observed properties with the fundamental characteristics of relaxor ferroelectrics.

2. EXPERIMENT PROCEDURES

The permittivity and loss tangent were measured with a multi frequency LRC meter (HP4274A). The field level used in this measurement was 23 V/cm. The measurement was performed without DC bias for annealed samples. For the quenched samples the measurement was performed with and without DC bias. For the measurement under DC bias, a DC field of 2.34 kV/cm was applied to the sample during aging. The measurement was carried out at the frequency range from 100 Hz to 100 KHz. A micro computer (HP9816) was used for system control and data acquisition and also for calculating and fitting these measured results.

The Lanthanum modified Lead Zirconate-Titanate ceramic $Pb_{1-x}La_x(Zr_yTi_{1-y})_{1-x/4}O_3$, abbreviated PLZT X:Y:Z ($X = 100x$, $Y = 100y$ and $Z = 100 - Y$), of composition 9.5:65:35 is used in this study. The hot pressed and transparent samples were cut from a large block, and then polished with one micron diameter paste. The samples were then annealed 800°C for one hour. Gold were then sputtered on both sides as electrode. For quenching treatment, after heating to high temperature in a PbO atmosphere for one hour, the sample was then quenched in air. One or two minutes were required for cooling down from the elevated temperature (400°C) to room temperature. The aging process was carried out at room temperature (~23°C). The thermal deaging and depoling at more than 200°C one hour was performed before annealing.

3. EXPERIMENTAL RESULTS

Because of the sample was aged in furnace during the annealing prior to the measurement, we add 12 minutes room temperature aging time to take the aging during the annealing into account. If we plot the permittivity, loss tangent and loss factor (the imaginary part of dielectric constant) versus the aging time by double logarithmic scale, it was found that these measured points are almost linear (Figure 1). This indicates that the aging effect for this PLZT ceramic follows the power law. The Cole–Cole plot for different aging times are presented in Figure 2. As shown in the figure, the Cole–Cole plot shrinks with aging time.

For the sample quenched from 100°C, the aging process is shown in Figure 3.

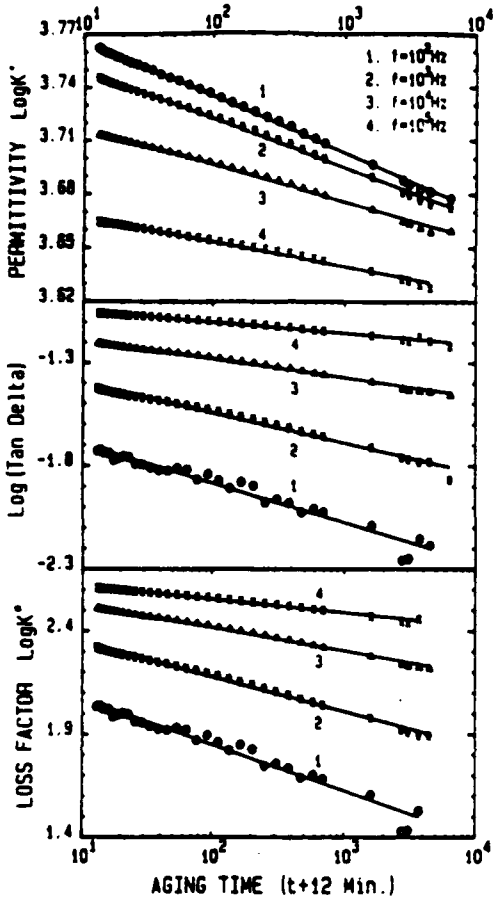

FIGURE 1 The permittivity and loss as a function of aging time by double logarithms scale and taken 12 minutes aging in furnace.

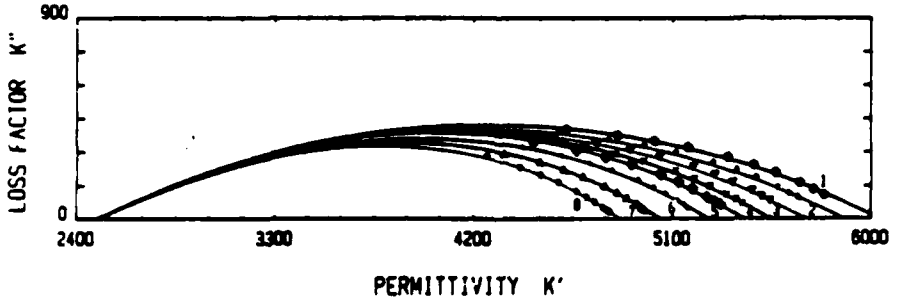

FIGURE 2 The Cole–Cole plot by the measured points and the mathematical fitting on different aging time for annealed sample. From 1 to 8, the aging time respectively are: 1.2, 11, 42, 100, 193, 460, 1580 and 3698 minutes.

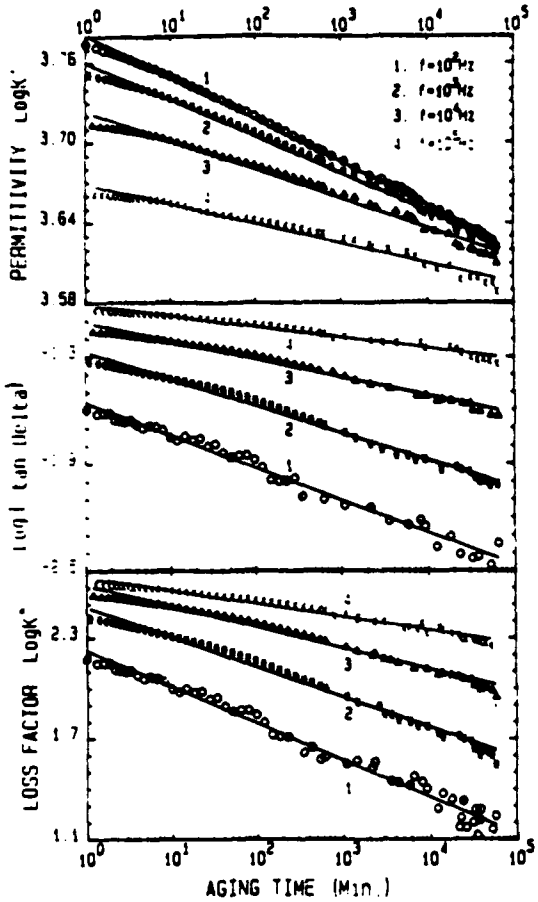

FIGURE 3 The permittivity, loss and loss factor dependent aging time for 100°C quenched sample.

The measured points are almost linear with a double logarithmic scale, indicating the aging process also follow power law. The quenching temperature is higher than the transition temperature (the peak of permittivity), therefore the quenching time is the start time for aging. The Cole–Cole plot for this quenched sample at 100°C (eleven different aging times) are shown in Figure 4.

Figure 5 shows the typical permittivity curves for the temperature dependence of a 400°C quenched sample at different aging time. Permittivity and loss are plotted as a function of the aging time for the 400°C quenched sample as shown in Figure 6. The measured points are almost linear with a double logarithm scale, indicating that aging also follows the power law. The Cole–Cole plot in a broad sense under different applied frequencies for 400°C quenched sample are presented in Figure 7. The shape of curves during aging looks similar to that in MnO doped PMNPT.[6] Figure 8 shows the Cole–Cole plot for different aging time in the quenched sample.

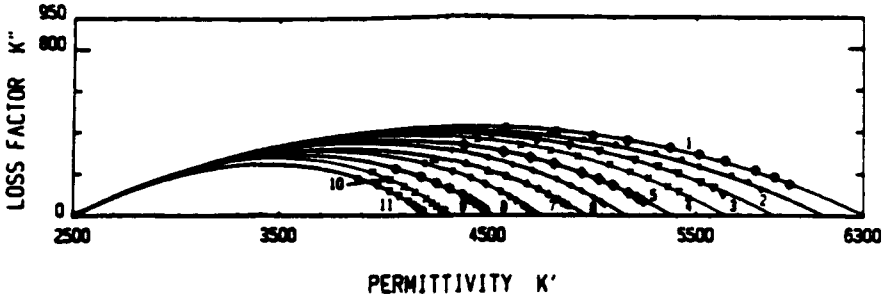

FIGURE 4 The measured and fitted Cole–Cole plot on different aging time for 100°C quenched sample. The aging time respectively are: 1.2, 3, 10, 27, 98, 290, 1100, 2980, 9270, 29890 and 63360 minutes (from 1 to 11).

The aging process for the sample quenched from 100°C with DC bias is presented in Figure 9. Permittivity and dielectric loss also follow power law with aging time. Figure 10 presents the Cole–Cole plot, and this plot shrinks during aging.

Figure 11 presents the permittivity and dielectric loss measured under DC bias versus aging time for 400°C quenched sample. For the aging process with DC bias,

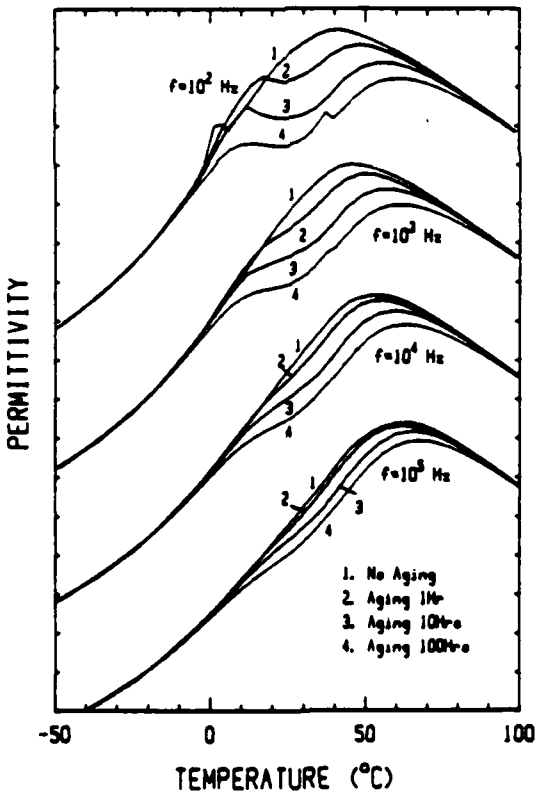

FIGURE 5 Typical curves of the temperature dependence of the permittivity for different aging time (400°C quenched sample).

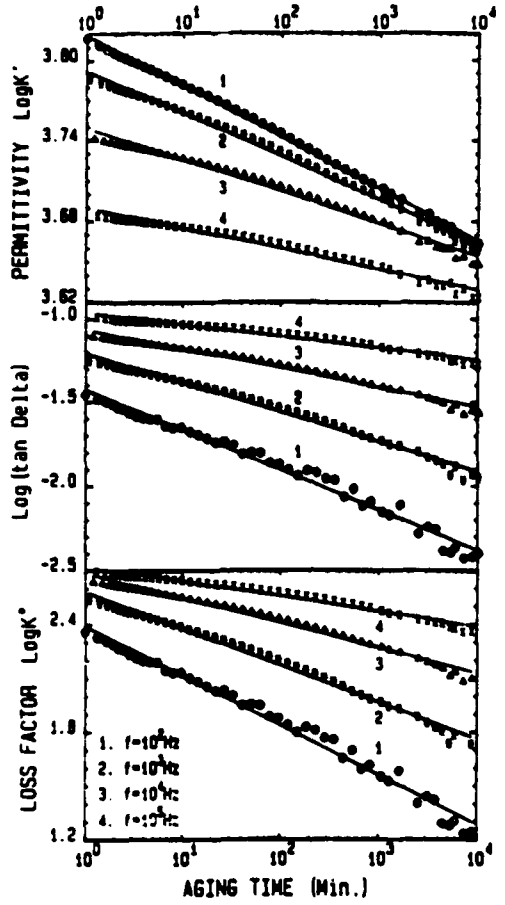

FIGURE 6 The permittivity, loss and loss factor as a function of aging time for quenched (400°C) sample.

permittivity and dielectric also follows the power law. The Cole–Cole plot shrinks with aging time (Figure 12).

4. DISCUSSION AND SUMMARY

The comparison of the coefficients obtained from the logarithmic law and power law for quenched and annealed samples during aging at room temperature are presented in Tables I and II. The n values of the loss factor for logarithmic law were obtained in two ways, the first coefficient was fitted from the measured data, and the second one was calculated from the logarithmic coefficients of permittivity and loss tangent. In the same way, the two power index for the loss factor were also compared. Clearly, the examined relaxor PLZT ceramics followed the power law closer than the logarithmic law in the aging process, for the permittivity (K'),

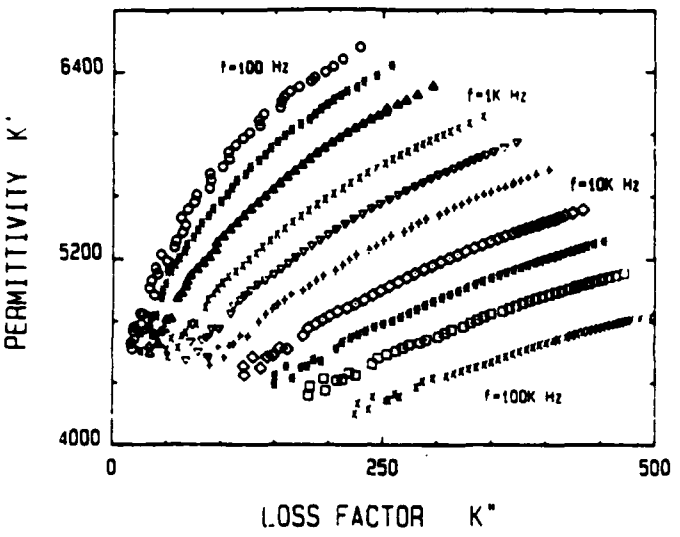

FIGURE 7 The Cole–Cole plot in a broad sense during aging by the ten different frequency for 400°C quenched sample.

dielectric loss (tanδ) and the loss factor (K"). The power aging law also fit the aging process for samples quenched at different temperatures with and without DC bias by the following equations:

$$K' = K_o t^{-n_K}; \qquad \tan\delta = D_o t^{-n_D}; \qquad K'' = K_o D_o t^{-(n_K + n_D)}$$

It was well accepted that a logarithmic law holds for a normal ferroelectric. However, a relaxor ferroelectric made up of the ferroelectric phase within the non polar matrix.[6,9] The power aging law may be the result of mixture of different phases and compositions, each of these phase and compositions may follow the logarithmic law.

The dipole flipping frequency f is given by[6]:

$$f = f_o^* \exp(-\Phi/kT) \qquad \text{or} \qquad \log f = A - B\Phi/kT$$

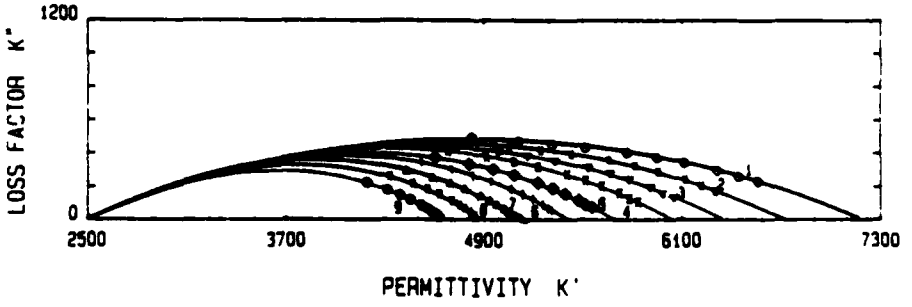

FIGURE 8 The measured and fitted Cole–Cole plot for 400°C quenched sample. From 1 to 9, the aging time respectively are: 1.2, 3, 10, 27, 97, 285, 1068, 3126 and 7286 minutes.

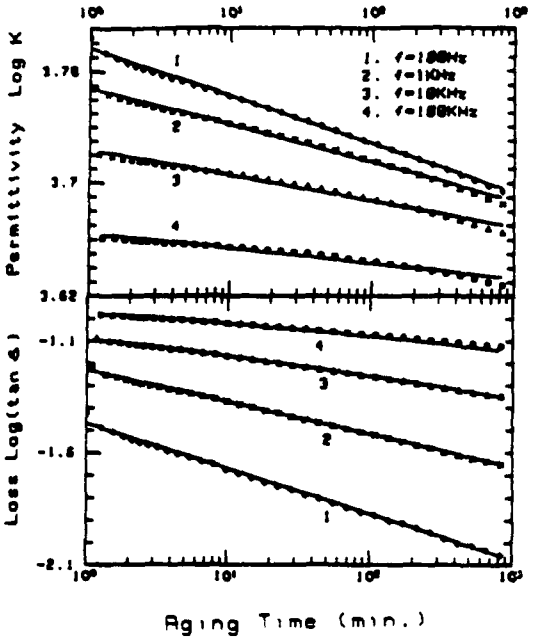

FIGURE 9 The permittivity, loss and loss factor dependent aging time with DC bias for 100°C quenched sample.

it was observed by Yao *et al.*[12] that under high enough temperature, a strong dielectric dispersion occurs even under an applied electric field bias, which means that these region are too actively flipping to be stabilized by DC bias. It may also be expected that these regions are also difficult to be stabilized by defect dipoles. Checking the power index with measured frequency, one finds that the power index follows the logarithmic law with the applied frequency (Figure 13). At low measured frequency, more large relaxation time constant components contribution to the dielectric constant. Under high frequency, these large relaxation time constant components make much less contribution to the dielectric constant due to the delay

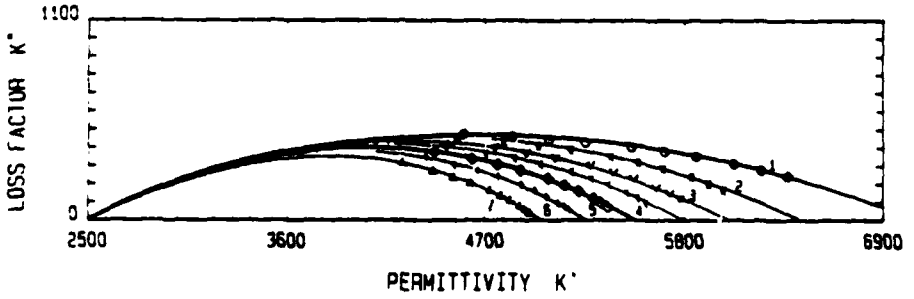

FIGURE 10 The measured and fitted Cole–Cole plot measured and fitted with DC bias for 100°C quenched sample. From 1 to 7, the aging time respectively are: 1.2, 3, 10, 29, 87, 268 and 830 minutes.

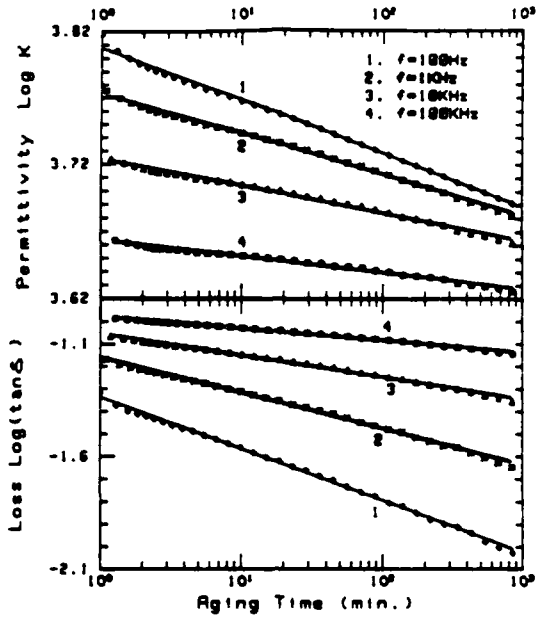

FIGURE 11 The permittivity, loss and loss factor as a function of aging time with DC bias for quenched (400°C) sample.

and dielectric dispersion, while the small relaxation time constant component still make significant contribution. The aging rate is higher in low measured frequencies which corresponds to the fact that the flipping of polar vectors in the large volume polar microregion is easy to stop, or the large relaxation time constant components age faster. During aging, the same larger polar microregions are age out and no longer contributes to the dielectric relaxation. The possible reason is that larger polar microregions are easily oriented and get the deepest minimum in energy.

Using the combination of both Cole–Cole and Cole–Davidson expressions, the measured points may be fitted in a Cole–Cole plot by the formula:

$$K(\omega) = K_\infty + (K_s - K_\infty)/\{[1 + (i\omega\tau)^{1-\alpha}]^{1-\beta}\}$$

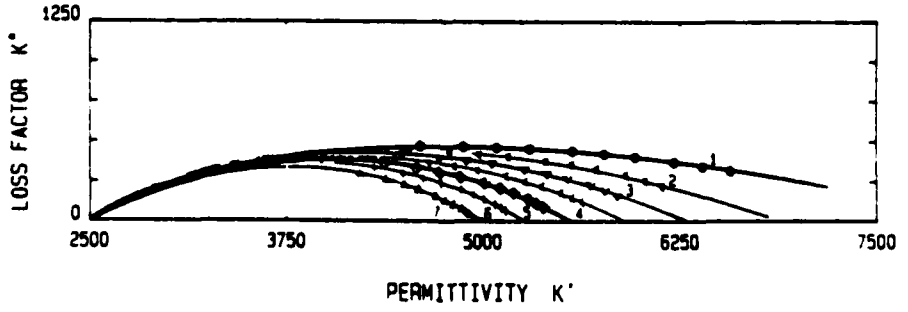

FIGURE 12 The measured and fitted Cole–Cole plot with DC bias for 400°C quenched sample. The aging time respectively are: 1.2, 3, 10, 29, 88, 272 and 845 minutes (from 1 to 7).

TABLE I

The Comparison Aging Process Using Logarithm Law

frequency (Hz)	n_1	n_2 (*.001)	n_1 (measured)	$n_1{}^*n_2$ (calculated)	error
100	487.249	7.3142	11.2742	3.56383	68.39%
200	463.552	8.4284	11.9717	3.90699	67.36%
400	435.896	9.7537	11.2175	4.25161	62.10%
1 K	395.981	11.397	9.67800	4.51300	53.37%
2 K	361.326	12.320	7.52749	4.45161	40.86%
4 K	324.959	12.929	4.99051	4.20124	15.82%
10 K	275.602	13.342	1.64416	3.67723	55.29%
20 K	238.984	13.262	−.816885	3.16932	125.8%
40 K	204.402	13.001	−2.90344	2.65745	191.5%
100 K	162.326	12.492	−5.16517	2.02777	139.3%

$K(f) = Ko - n_1 \log f$ $\quad \tan\delta(f) = D_o - n_2 \log f$

$K''(f) = K'\tan\delta = K_oD_o - (K_on_2 + D_on_1)\log f + n_1n_2(\log f)^2$

or $\quad K''(f) = K_o'' - n_4 \log f + n_3(\log f)^2$

The fitted results are shown in the Figures 2, 4, 8, 10 and 12. The fitting parameters are given in Table III. The fitted results are like the proposition of the system containing a distribution of relaxation time constant,[6] even though the PMNPT ferroelectric ceramics cannot be fitted as an arc of circle in this frequency range at room temperature. The fitting parameters show that the angle of tilt of the arc from the real axis α and the average time constant τ decrease during aging. The Cole–Cole plot become smaller in the process of aging. The change of permittivity is larger than that of loss factor especially at low frequency range, the centre of the circular in this plot was lifted toward the real axis.

The physical meaning of parameter α is the distribution of relaxation time constant. Since α decreases with aging time, this distribution become small as aging continues. This process will narrow down the distribution of the relaxation time constant. As these large relaxation time constant components age out, the dielectric response of the assemblage will be taken over by small relaxation time constant

TABLE II

The Comparison Aging Process Using Power Low

frequency (Hz)	n_K	n_D	$n_{K''}$ (measured)	$n_K + n_D$ (calculated)	Error
100	.0384721	.239094	.277566	.276243	.4767%
200	.0368394	.218192	.255032	.254119	.3308%
400	.0351604	.198975	.234136	.232454	.7182%
1 K	.0324016	.177284	.209686	.209411	.1310%
2 K	.0300289	158778	.188806	.188345	.2445%
4 K	.0275002	.138957	.166457	.165900	.3347%
10 K	.0240034	.116786	.140797	.140095	.4936%
20 K	.0213408	.100908	.122248	.121510	.6042%
40 K	.0187808	.086563	.105343	.104580	.7248%
100 K	.0155615	.070938	.086499	.085694	.9222%

The calculation by the formulas:

$K' = K_o f^{-n_K}$, $\quad \tan\delta = D_o f^{-n_D}$

$K'' = K_o'' f^{-n_K} = K_oD_o f^{-(n_K+n_D)}$

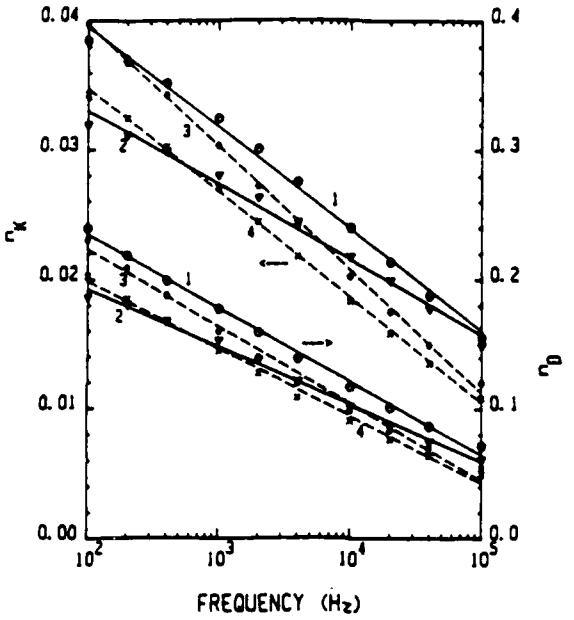

FIGURE 13 The relaxation between power index and measured frequency. 1, 3: 400°C quenched sample; 2, 4: 100°C quenched sample; 3, 4: Aging with DC bias (2.34 kV/cm).

components. The average time constant decreases with aging time. We attribute such effect of aging on the dielectric relaxation to the freeze-in of orientations of dipoles, especially those with large time constants and large volume, and thus no longer contribute to the dielectric relaxation.

Internal stress and strain energy are enhanced by the quenching in comparison with the annealed sample. The higher the temperature of quenching, the larger the created stresses. The internal stresses break the non-polar layer between the ferroelectric phase,[9] to augment the ferroelectric properties of the sample. The permittivity is higher for the quenched sample. For quenched and unaged sample, the permittivity with DC bias is higher than the result without DC bias (Figure 14), because the electric field with internal stresses may break some weaker non-polar layers to increase the ferroelectric properties of this sample.[9] The aging rate was increased by the liberation of internal stresses during aging, and by larger volume distributions of polar microregions. The increased aging rate was shown by the increased power index n_D and n_K (Figure 13).

With DC bias applied, polar vector flipping is already suppressed as demonstrated by Yao *et al.*[12] There are less flipping regions available for aging, and the aging rate is therefore reduced especially under high measured frequency. With DC bias, the ferroelectric phase was poled by the applied field. But the macropolarization is not the orientation preferred in polar microregion, and the macropolarization does not correspond to the deepest minimum in energy. Therefore the aging effect is smaller with DC bias in the measured frequency range.

When the applied DC bias voltage is removed, the thermal activation energy may move certain dipoles to depoling, and the weak measuring field may modulate

TABLE III

The Parameters of the Cole-Cole Plot

Treatment	time (min.)	K_s	K_∞	τ ($*10^{-7}$ sec.)	α	β
Annealing	1.2	6050	2500	4.66	.700	0.02
without	11	5890	2500	4.7	.688	0.08
bias	42	5710	2500	4.9	.678	0.13
	100	5560	2500	5.0	.658	0.18
	193	5460	2500	5.2	.645	0.21
	460	5275	2500	5.2	.640	0.26
	1580	5050	2500	5.0	.620	0.30
	3698	4870	2500	5.0	.600	0.35
Quenching	1.2	6325	2500	8.2	.722	0.0
(100°C)	3	6130	2500	8.5	.713	0.08
without	10	5880	2500	8.2	.695	0.13
bias	27	5650	2500	7.8	.680	0.17
	98	5390	2500	7.0	.665	0.20
	290	5170	2500	5.5	.648	0.23
	1100	4980	2500	4.2	.648	0.25
	2980	4760	2500	3.0	.620	0.28
	9270	4530	2500	2.8	.600	0.30
	29890	4330	2500	2.7	.570	0.34
	63360	4220	2500	2.5	.578	0.38
Quenching	1.2	7180	2500	15	.740	0.0
(400°C)	3	6740	2500	12	.720	0.08
without	10	6360	2500	10	.700	0.13
bias	27	6050	2500	8.0	.680	0.18
	97	5700	2500	6.0	.660	0.21
	285	5420	2500	4.5	.640	0.24
	1068	5130	2500	3.5	.622	0.27
	3126	4890	2500	2.8	.615	0.30
	7286	4655	2500	2.3	.610	0.33

The Cole-Cole plot are fitted by the combination of both Cole-Cole and Cole-Davidson expressions:

$$K(\omega) = K_\infty + \frac{K_s - K_\infty}{[1 + (i\omega\tau)^{1-\alpha}]^{1-\beta}}$$

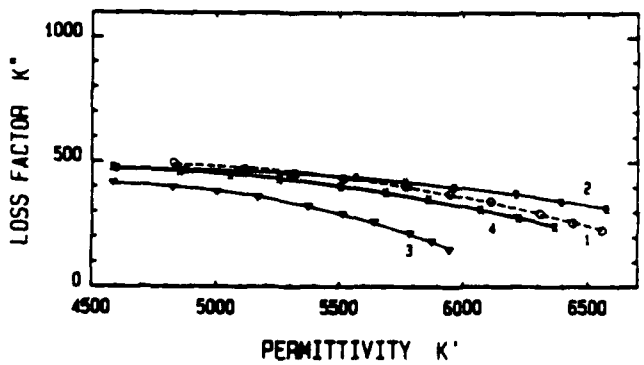

FIGURE 14 The DC bias effect for quenched and unaged samples. In the figure 1,3: 400°C quenched sample; 2,4: 100°C quenched sample and 3,4 measurement with DC bias (2.34 kV/cm).

the polar vectors to follow the electric field variation. So the permittivity has one sudden rise. For same reason, when a DC bias voltage is applied to an aged sample, the permittivity is increased suddenly because the polar vectors stabilized under random directions are pulled closer the field directions under these directions the polar vectors are in deaging states.

By extrapolating Cole–Cole plot and the examining elation between the power index and frequency, one observes that there is no aging effect at room temperature at the applied frequency higher than the 10^6 Hz. Under this higher measured frequency the large ferroelectric polar regions are delay and dielectric dispersion, therefore no longer contribution to permittivity. Only paraelectric phase, no polar matrix and some enough small microdomains which very difficult to stop will contribute to dielectric constant.

Aging of the dielectric properties in the relaxor PLZT ceramic is frequency dependent. In the frequency range of 100 Hz to 100 kHz, the decrease of these dielectric properties follows the power aging law and the power index with increasing frequency follows the logarithm law. Quenching could increase the ferroelectric properties and aging rate. The power index is reduced with DC bias during aging. During aging, the Cole–Cole plot shrinks with aging time in such a way that the average relaxation time constant decreases and the distribution of relaxation time constant become narrow with aging time. In this study, the dielectric aging could be considered the result of the orientation and the oriented polar microregion is stable and corresponds to the deepest minimum in energy. These oriented microregions will not contribute to the dielectric relaxation.

ACKNOWLEDGEMENTS

We would like to thank the Motorola Inc. for supplying the PLZT ceramics.

REFERENCES

1. G. Borchhardt, J. Von Cieminski and G. Schmidt, *Phys. Stat. Sol. (a)*, **59**, 749 (1980).
2. W. A. Schulze, J. V. Biggers and L. E. Cross, *Jour. Amer. Cera. Soci.*, **61**, 46 (1978).
3. M. Yokosuka and M. Marutake, *Japa. Jour. Appl. Phys.*, **25**, 981 (1986).
4. K. W. Plessner, *Proc. Phys. Soci. B*, **69**, 1261 (1956).
5. W. A. Schulze and J. V. Biggers, *Ferroelectrics*, **9**, 203 (1975).
6. W. Y. Pan, Q. Y. Jiang and L. E. Cross, *Ferroelectrics*, **77** (1988).
7. H. Dederichs and G. Arlt, *Ferroelectrics*, **68**, 281 (1986).
8. N. Setter and E. L. Cross, *J. Appl. Phys.*, **51**, 4356 (1980).
9. W. Y. Gu, E. Furman, A. Bhalla and E. L. Cross, *Amer. Cera. Soci. Meet. (Cincinnati)*, 1988.
10. E. L. Cross, A. Bhalla and F. Asadipour, *Amer. Cera. Soci. Meet. (Chicago)*, 1986.
11. D. N. Huang, Z. Yin and E. L. Cross, *IEEE Con. Int. Sysm. on App. of Ferr. Bethlehem, PA*, 1986.
12. X. Yao, Z. Chen and E. L. Cross, *J. Appl. Phys.*, **54**, 3399 (1983).

APPENDIX 15

Ferroelectrics, 1989, Vol. 93, pp. 361–372
Reprints available directly from the publisher
Photocopying permitted by license only

AGING MECHANISMS IN $Pb(Mg_{1/3}Nb_{2/3})O_3$-BASED RELAXOR FERROELECTRICS

T. R. SHROUT, W. HUEBNER, C. A. RANDALL and A. D. HILTON
The Materials Research Laboratory, Penn State University, University Park, PA 16802

(Received August 29, 1988)

I. INTRODUCTION

The complex perovskite $Pb(Mg_{1/3}Nb_{2/3})O_3$ [PMN] is just one of many relaxor ferroelectrics having the general formula $Pb(B_1B_2)O_3$. PMN, and solid solutions thereof with $PbTiO_3$ [PT] and $Pb(Zn_{1/3}Nb_{2/3})O_3$ [PZN], as well as other relaxor compositions, are excellent materials for use in a wide range of applications including electrostrictive actuators,[1] multilayer capacitors,[2] and pyroelectric bolometers.[3] For any of these applications it is imperative that dielectric aging be minimal. Past studies[4–13] on aging in relaxor ferroelectrics (primarily PLZT and PMN) have shown the aging rate depends on many variables including processing parameters, microstructure, dopant content, point defects, etc. Though great strides have been made with respect to modelling dielectric properties of relaxors, the lack of detailed information concerning defect structure, conduction, and ordering still hinders theoretical interpretation of aging results.

Significant differences between the aging characteristics of relaxor ferroelectrics (typified in Figures 1 and 2) and those of $BaTiO_3$-based dielectrics include:

(1) At T_{aging}, the dispersive character of ε' and ε'' is strongly damped; lower frequency components age much more rapidly than high frequency components.
(2) Aging occurs at $T > T_m$.
(3) Cooling to $T < T_{aging}$ "recovers" ε' and ε'' to unaged values.
(4) At T slightly $> T_{aging}$, the dispersion remains strongly damped.
(5) Aging is not log linear; over short time periods the aging rate (A.R.) is much higher.

Relaxor compositions can be prepared which exhibit low aging rates not achievable with "normal" ferroelectrics, though the requisite processing/dopant details suffer not only from empirical determination, but also are unattractive from a processing point of view (i.e., control of density, grain size, and second phase formation). For instance, excess PbO is commonly added in the fabrication of relaxor ceramics to: 1) suppress pyrochlore formation, 2) compensate for PbO volatility during heat treatment, 3) reduce the sintering temperature, and 4) promote grain growth. However, we have found excess PbO additions result in a large degree of aging. In addition to excess PbO, excess MgO is commonly added to

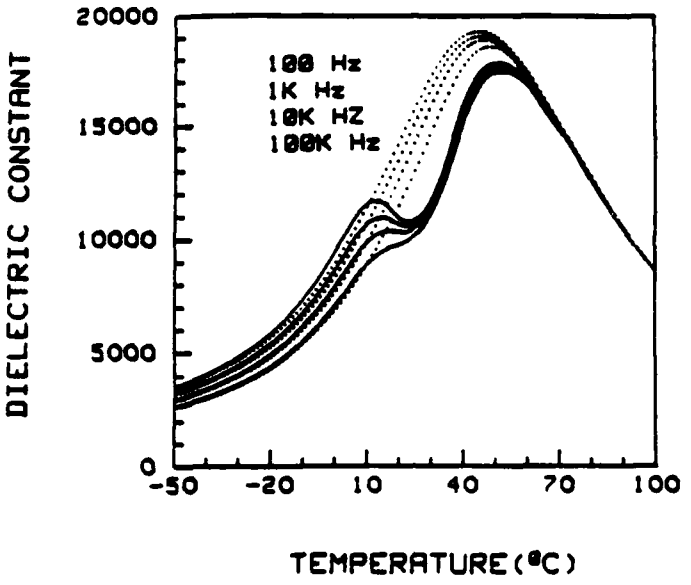

FIGURE 1 Aging Behavior of PMN:10% PT doped with 0.1 wt% MnO. Dielectric response vs. temperature after aging for different times at 20°C.

PMN to help prevent pyrochlore formation and to increase grain growth and subsequent dielectric properties. Also, many additives, not only from impurities, are added to modify T_c, ordering, etc.

The purpose of our ongoing studies is to correlate the effects of stoichiometry, dopant additions, and processing parameters with resultant dielectric properties.

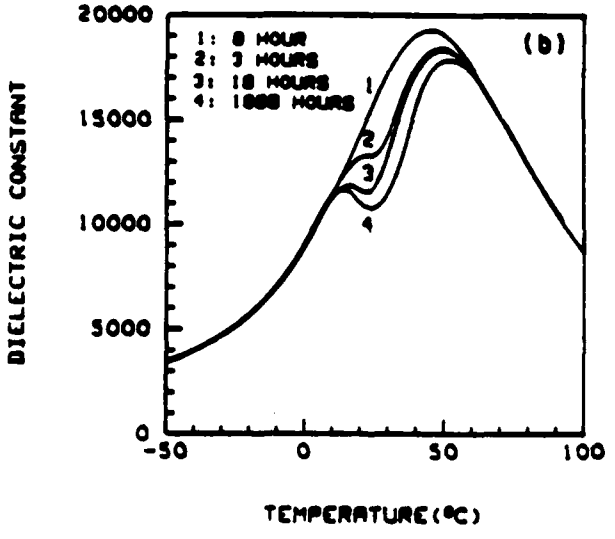

FIGURE 2 Aging behavior of PMN:10% PT doped with 0.1 wt% MnO showing preferential aging of the dispersive component of K'.

point defect formation, and nanostructure (i.e., ordering) of relaxor ferroelectrics. This paper focuses on the effects of stoichiometry, dopant additions, and sintering temperature on dielectric aging in PMN-based relaxors.

II. EXPERIMENTAL PROCEDURE

The compositions studied were based on solid solutions of PMN-PT and PMN-PZN modified such that their dielectric maximas were near that of room temperature. Powders were prepared using the Columbite precursor method.[14,15] In all cases, calcined powders were characterized for phase purity using x-ray diffraction analysis. Reagent grade raw materials were used throughout.

Compositional modifications included: 1) varying the A:B (ABO_3 perovskite) ratio through excess/deficient PbO and MgO additions, 2) acceptor doping with K^{1+}, and Ag^{1+}, 3) donor doping with La^{3+}, and 4) adding multivalent Fe and Mn. Nonstoichiometric compositions were batched as:

$Pb_x(Mg_{1/3}Nb_{2/3})O_3$; x = 0.98, 0.99, 0.995, 1.005, 1.01, and 1.02
$Pb(Mg_xNb_{2/3})O_3$; x = 0.30, 0.31, 0.32, 0.33, 0.34, 0.35, 0.36, 0.43, 0.53, 0.63

Dopants were evaluated by either adding them directly to the calcined PMN, or adding them to the precalcined components (stoichiometry maintained).

Disks were used throughout this study along with state-of-the-art multilayer capacitors containing high Ag:Pd electrodes. Sintering was performed over a temperature range of 850°C to 1250°C depending on composition. The sintering atmosphere with respect to partial pressure lead was varied by sintering in: 1) closed alumina crucibles containing $PbZrO_3$ source powder, 2) a coarse PMN sand of similar composition, and 3) a commercially used zirconate-based firing sand (for $T \leq 1100$°C).

Weight loss, geometric density, phase purity as determined by x-ray diffraction, and grain size were determined. The grain size was found from fractured surfaces using SEM analysis. Selected samples were also characterized using TEM analysis to investigate the influence of chemical modification on the nanostructure.

TABLE I
Effect of A:B Ratio on Aging Characteristics: Effect of Excess ↔ Deficient PbO

	Percent Aging			"Curie Temperature"	
	Multilayer		Disk	Multilayer	Disk
A:B Ratio	850°C	950°C	950°C	(°C)	(°C)
0.980	1.2	2.2	2.2	17–18	12–13
0.990	2.5	3	5	17–18	12–13
0.995	3.7	5	9	17	12–13
1.000	4.5	6.8	12	16	12–13
1.005	5.5	7.5	14	14	12–13
1.010	6.5	7.5	15	13	12–13

Samples were surface ground and electroded using sputtered gold or a fritless fire-on silver. Dielectric properties evaluated included capacitance and dissipation factor measured for applied frequencies ranging from 0.1 to 100 KHz, over a temperature range of −55°C to 125°C.

Dielectric aging studies typically extend to over 1000 hrs; to facilitate evaluation of a large number of parameters, *relative* percent aging values were determined from capacitance readings taken at 24 hrs and on a deaged specimen. We confirmed these short aging rates directly correlate with those gathered during extended aging runs. It is important to note, however, that aging rates determined in this study as well as conventionally determined aging rates performed out to 1000 hrs, neglect information on the level and degree of any non-log linear behavior observed within the first 1000 minutes.[13]

III. RESULTS

Aging in stoichiometric PMN is generally low/negligible, but can vary widely depending upon processing conditions including sintering temperature, time, and atmosphere, as well as the purity of starting powders. We have found high purity PMN (starting components ≥99.99% purity) has a negligible aging rate. The following sections present our results concerning the effects of nonstoichiometry and doping on the aging behavior.

A. Effect of A/B ratio: excess ↔ deficient PbO

The effect of nonstoichiometry due to excess ↔ deficient PbO on the percent aging is tabulated in Table I, and graphically represented in Figures 3 and 4. Two effects

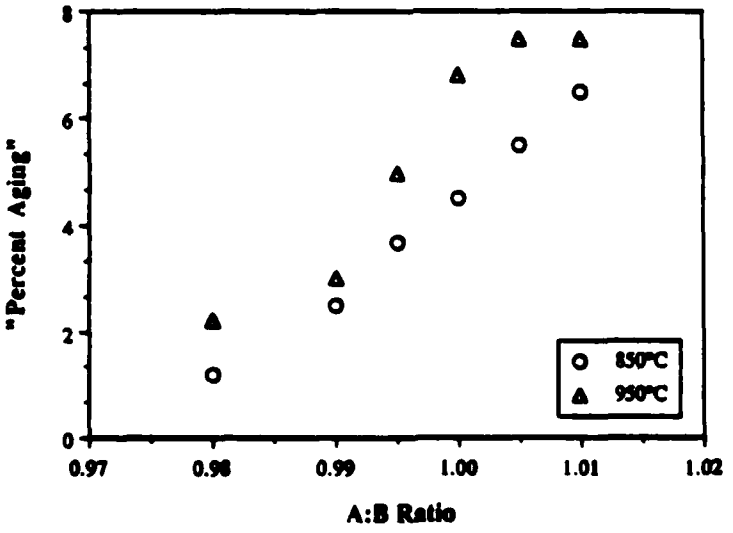

FIGURE 3 "Percent Aging" vs. A:B ratio and sintering temperature.

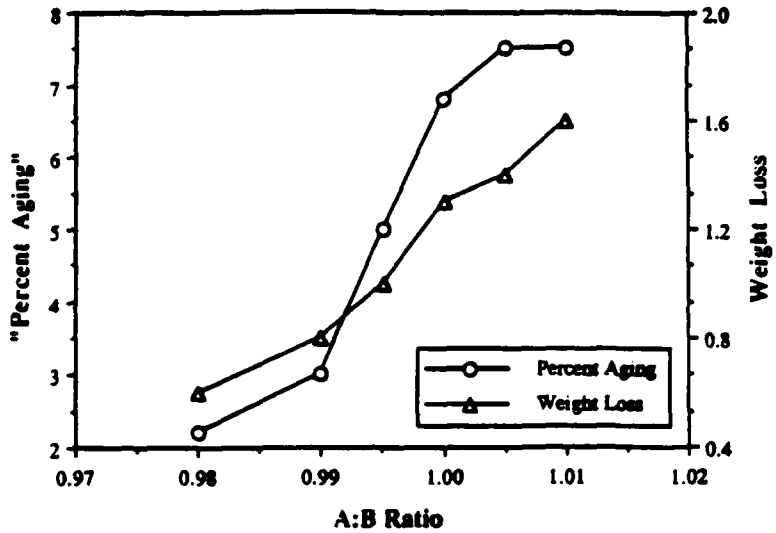

FIGURE 4 "Percent Aging" and weight loss vs. A:B ratio.

are immediately apparent: increasing either the A:B ratio or sintering temperature increases the percent aging. Clearly excess PbO additions dramatically increase the aging rate. In addition, as shown in Figure 5 the aging rate for disks is much higher than for the multilayer configuration. As discussed below, this is most likely attributable to the electrode material. Though not graphically shown, maintaining a lead rich atmosphere by sintering in a closed container also increases the aging rate.

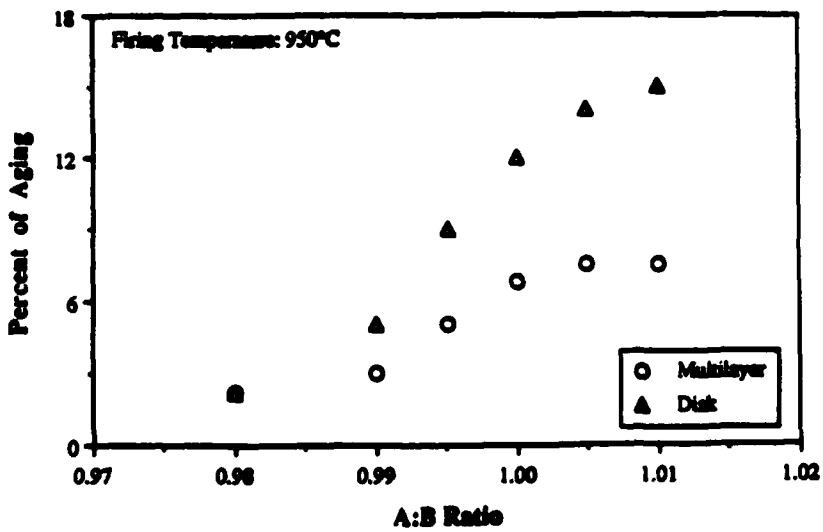

FIGURE 5 Comparison of aging for disk and multilayer configurations vs. A:B ratio.

Although decreasing the stoichiometry to ≤ 1.000 significantly reduces the aging rate, problems exist with these compositions with respect to processing, i.e., pyrochlore formation and densification.

B. Effect of A:B ratio: excess ↔ deficient MgO

The effect of nonstoichiometry due to excess ↔ deficient MgO is tabulated in Table II, and graphically represented in Figure 6. Deficient MgO compositions exhibit very low aging rates, while excess MgO additions continuously increase the aging rate.

As contained in Table II, larger MgO additions up to 30% dramatically increase the aging rate to ≈30%. Microstructurally, at this dopant level free MgO is found locally isolated at not only triple points, but also dispersed within the PMN grains.[16] For 10% MgO additions, doping with 0.5 wt% Cr_2O_3, or MnO_2 dramatically decreased the percent aging, while Fe_2O_3 left it virtually unchanged.

C. Effect of dopants

Table III contains a summary of our results on the influence of donor and acceptor doping on the aging behavior. They can be summarized quite simply: *for PMN compositions which exhibit aging, acceptor dopants dramatically increase the aging rate, while donor dopants decrease it.* In order to interpret this effect, clearly we need to understand the influence of dopants on the concentration of electronic or ionic point defects. In the following discussion section we propose a simple model for the defect chemistry of PMN. Within this scenario, acceptor dopants can be electronically compensated by the creation of holes, i.e., $p = [A']$, or ionically

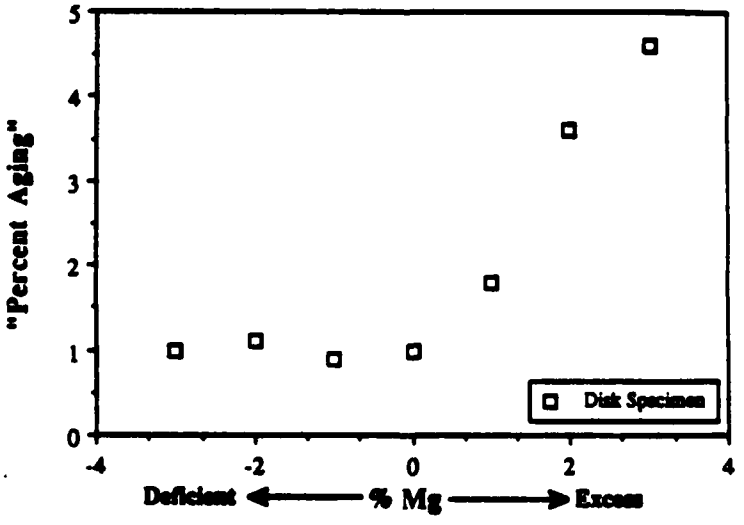

FIGURE 6 "Percent Aging" vs. magnesium content.

TABLE II

Effect of A:B Ratio on Aging Characteristics: Effect of Excess ↔ Deficient MgO

Mole % Magnesium	Percent Aging		% Pyrochlore (calcined powder)	Grain Size (μm)		Curie Temperature
	Multilayer	Disk		Multilayer	Disk	
3	2.7	4.6	1	2–3	3–4	18
2	2.6	3.6	3	2–3	4	19
1	3.3	1.8	3	2–3	2–3	19
0	1.9	1.0	4	2–3	1–4	20
1	1.7	0.9	3	1	1–2	21
2	1.7	1.1	7	1	1–2	22
3	—	1.0	13	—	1–2	—

Composition	Additives	"Percent Aging"	Percent Weight Loss
PMN-PT	—	4.0	0.3–0.4
PMN-PT via Mixed Oxide	10% MgO	25	2
PMN-PT via Columbite	10% MgO	30	2
"	20% MgO	25–30	1.7
"	30% MgO	30	2.5
PMN-PT via Columbite	10% MgO & 0.5 wt% Cr_2O_3	4.7	0
"	10% MgO & 0.5wt% MnO_2	5.6	0.2
	10% MgO & 0.5wt% Fe_2O_3	15	0

compensated by the creation of oxygen vacancies, i.e., $[A'] = 2[V_O^x]$. Similarly, donor dopants can be electronically compensated by the creation of electrons, i.e., $n = [D^\circ]$, or ionically compensated by the creation of lead vacancies, i.e. $[D^\circ] = 2[V''_{Pb}]$.

IV. DISCUSSION

Understanding the active mechanisms responsible for the observed aging effects is clouded by a lack of basic knowledge concerning polarization mechanisms, nanostructure, defect structure, conduction, and ordering in relaxors. Clearly we need

TABLE III

Effect of Donor and Acceptor Dopants on Aging Characteristics

Dopant	Effect	Comment
La^{3+}	↓ ↓ A.R.	—
K^{1+}	↑ ↑ A.R.	—
Na^{1+}	↑ ↑ A.R.	—
Mn	↑ or ↓ A.R.	↑ if added prior to calcination of PMN ↓ if added to perovskite PMN

a grasp on these concepts. Recent experimental evidence supports the compositional heterogeneity model of a relaxor ferroelectric first proposed by Smolenski.[17] The currently "accepted" model suggests:

- Fluctuations in the B_1B_2 cations on the B-site of $Pb(B_1B_2)O_3$ relaxor perovskites are necessary for the relaxor behavior.
- The polar orientation of micropolar regions is dynamically disordered at higher temperatures due to thermal motion.

The latter suggests the activation energy between the energetically degenerate [111] polar directions is small, and on the order of several kT (Figure 7). It is likely compositional fluctuations/gradients will give rise to differences in local ↔ global symmetry, which in turn will perturb the energy minima associated with the polarization direction (Figure 8). The main consequence of such lowering is that: statistically the polar vector will spend a longer time along the crystallographic direction giving rise to the deepest minima.

Aging phenomena becomes explicable then if the micropolar P_s orientation is stabilized due to the presence of a defect dipole. Addressing several of the significant features of aging in relaxors listed earlier:

- Polar microregions with the longer relaxation times will stabilize first; these are not too large to prevent reorientation nor too small to be thermally activated. ∴ the lower frequency permittivity will age at a faster rate.
- Cooling to $T < T_{aging}$ creates new unstabilized micropolar regions, recovering the dispersive component of ε' and ε''.
- Heating to T slightly $> T_{aging}$ does not create new micropolar regions, therefore the dispersive character of ε' and ε'' is not recovered.

We propose the aging effects exhibited by the doped and nonstoichiometric PMN compositions can be ascribed to variations in the oxygen vacancy, V_O^x, and lead vacancy, V''_{Pb} concentrations. In the following section we present a possible defect scheme to support this hypothesis.

V. PROPOSED DEFECT CHEMISTRY OF PMN

Elucidating the identity and concentration of point and electronic defects in PMN is certainly a difficult task. In order to thermodynamically define PMN (a quarternary system) in its environment, we need to control not only the temperature and partial pressure of oxygen, but also the activity of lead (a_{Pb}) due to its volatility. The latter can be approached by firing in closed crucibles with volatile lead species, but lacks precise determination. Although this limits obtaining quantitative data, one can make qualitative analyses with respect to effects of processing and compositional parameters on the relative concentration of defects.

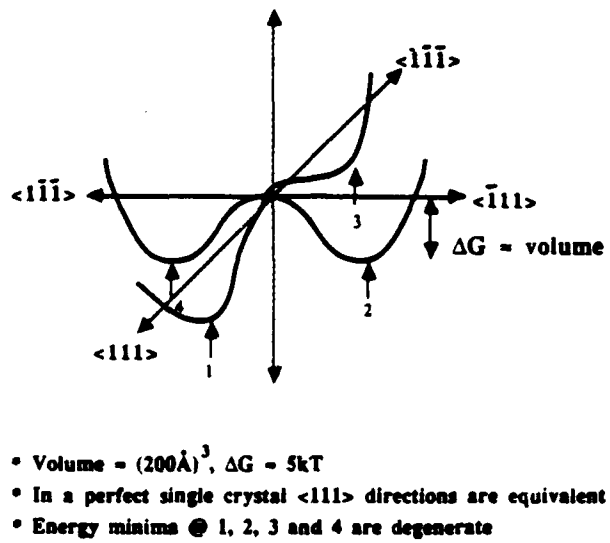

FIGURE 7 Schematic of the elastics Gibbs free energy, ΔG_1 vs. polarization for four of the eight equivalent (111) directions in a perovskite ferroelectric in the rhombohedral phase.

The defects one can reasonably hypothesize exist in doped PMN include lead vacancies (V''_{Pb}), oxygen vacancies (V^{x}_{o}), electrons (n), and holes (p), and donors (D°), and acceptors (A′) if doped. The existence of B-site vacancies will not be addressed here, although B-site vacancies have been hypothesized to form in PLZT

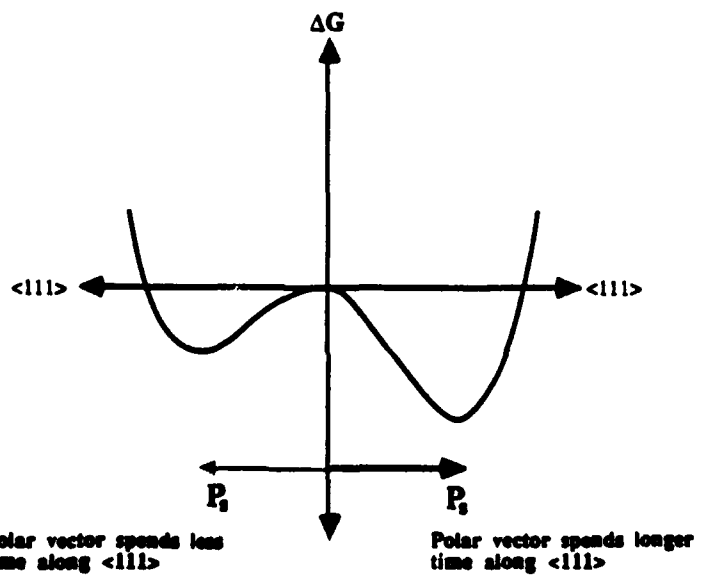

FIGURE 8 Two dimensional representation of the perturbation of the Elastic Gibbs free energy vs. polarization direction due to local ↔ global symmetry differences.

to compensate high donor concentrations. The relationship between the relative concentration of these defects is referred to as the electrical neutrality condition, and is expressed by:

$$n + [A'] + 2[V''_{Pb}] = p + [D^{\circ}] + 2[V^{x}_{o}] \quad (1)$$

Several reactions are needed to describe the defect chemistry in order that the relative concentrations of the above defects can be determined as a function of temperature and partial pressure oxygen and lead. Direct thermal ionization of electrons across the band gap, referred to as the intrinsic reaction, is expressed as:

$$\text{nil} \leftrightarrow e' + h^{\circ} \quad (2)$$

$$K_i = np = A \exp[-\Phi/kT] \quad (3)$$

where Φ is the band gap energy, and K_i is the equilibrium mass action constant.

For a constant lead activity, the formation of V^{x}_{o} can be expressed as:

$$O^{x}_{o} \leftrightarrow 1/2O_2 + V^{x}_{o} + 2e' \quad (4)$$

$$K_{V_o} = n^2[V^{x}_{o}]PO_2^{1/2} \quad (5)$$

where PO_2 is the oxygen partial pressure. If the PO_2 is constant, then the formation of V^{x}_{o} can be expressed as:

$$Pb(g) \leftrightarrow Pb^{x}_{Pb} + V^{x}_{o} + 2e' \quad (6)$$

$$K_{V_o} = n^2[V^{x}_{o}]a^{-1}_{Pb} \quad (7)$$

where a_{Pb} is the lead activity.

For a constant lead activity, the formation of V''_{Pb} can be expressed as:

$$1/2\ O_2 \leftrightarrow O^{x}_{o} + V''_{Pb} + 2h^{\circ} \quad (8)$$

$$K_{V''_{Pb}} = p^2[V''_{Pb}]PO_2^{-1/2} \quad (9)$$

If the PO_2 is constant, then the formation of V''_{Pb} can be expressed as:

$$Pb^{x}_{Pb} \leftrightarrow Pb(g)\uparrow + V''_{Pb} + 2h^{\circ} \quad (10)$$

$$K_{V''_{Pb}} = p^2[V''_{Pb}]a_{Pb} \quad (11)$$

a_{Pb} will be directly related to the lead partial pressure, P_{Pb}, assuming the volatile species is Pb ions.

The relative concentrations of these defects will be a function of T, PO_2, and P_{Pb}, although the predominate defect at any specific T, PO_2, and P_{Pb} is not clear. Recent TEM studies have clearly shown regions of PMN exhibit 1:1 ordering of the B-site cations, see Figure 9. The "sea" surrounding these ordered regions must necessarily be rich in Nb. In order to maintain charge neutrality in these regions, we propose that the lattice must contain compensating charged point defects. Within ordered regions V^{x}_{o} would be the favored defect, while in the "sea" V^{x}_{Pb} would form.

Regardless, we can use the proposed defect equilibria to analyze the effect of nonstoichiometry and doping on the point defect concentration. Reiterating, excess

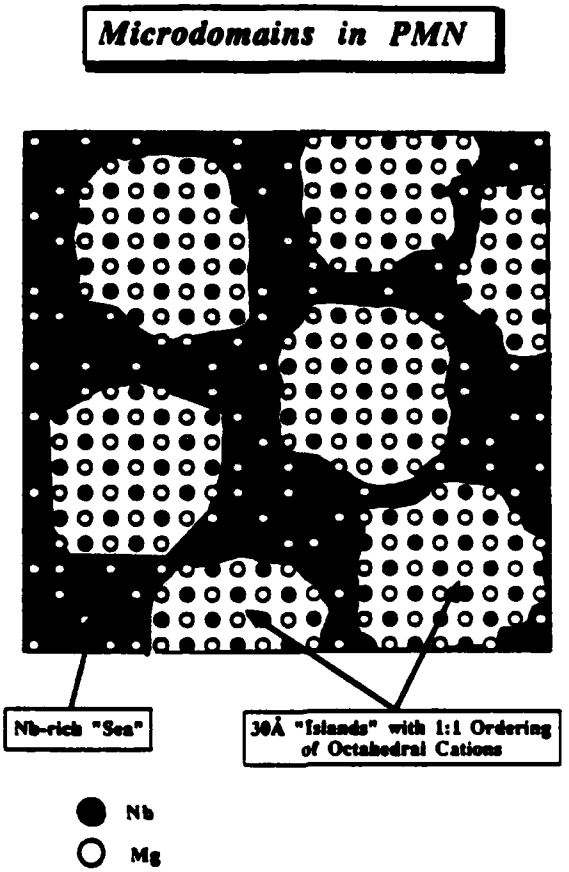

FIGURE 9 Schematic representation of the nanostructure of PMN showing regions with 1:1 ordering of the B-site.

PbO additions cause aging. If one of the major effects of PbO present during sintering is increasing the local a_{Pb}, then as described by Equations (7) and (11) *the* $[V_o^x]$ *would increase*, and $[V''_{Pb}]$ would decrease. Acceptor doping also dramatically increases the aging rate. As acceptor doping with Na^{1+} and K^{1+} does not have an appreciable effect on the resistivity, it is reasonable to assume ionic compensation occurs, i.e. $[A'] = 2[V_o^x]$. Donor doping virtually eliminates aging if present. If we assume ionic compensation, as is exhibited by PLZT, then $[D^\circ] = 2[V''_{Pb}]$. Fixing the $[V''_{Pb}]$ at a given PO_2 and P_{Pb} suppresses the $[V_o^x]$ at a level lower than if the donors were not present.

Preliminary studies comparing MLC with high Ag:Pd internal electrodes to disks of the same composition showed the MLC's always had a lower aging rate. From purposeful additions of Ag salts we suspect that at low temperatures Ag^{1+} remains in the grain boundary and decreases the aging rate. Increasing the sintering temperature results in interdiffusion and incorporation of Ag^{1+} onto the lattice. This increased the aging rate, which correlates well with other results which show the ionic compensation of acceptors by V_o^x results in aging.

We propose that changes in the lead activity and dopant levels effect the equilibration of the charge-compensating defects in the Nb-rich "sea" and ordered

nonstoichiometric regions, resulting in an internal field within and across these regions. We believe it is these local fields associated with the defects which give rise to aging of the polar microregions in the PMN-PT compositions.

VI. SUMMARY

The results of our aging studies to date can be summarized as:

(1) Aging in PMN-based relaxor ferroelectrics is strongly dependent on stoichiometry. Excess PbO or MgO increases the aging rate.
(2) Acceptor doping with Ag^{1+}, K^{1+}, or Na^{1+} increases the aging rate.
(3) Donor doping with La^{3+} decreases the aging rate.

By assuming a simple model for the defect chemistry, these results can be consistently explained by the concentration of oxygen and lead vacancies.

Other effects observed (see Table II) but not fully addressed include the effects of Cr_2O_3, MnO_2, and Fe_2O_3 dopants. We have also found the hydrostatic stresses associated with encapsulating a MLC increases the aging rate. We are also currently evaluating the effects of varying the PO_2 while maintaining the a_{Pb} constant. Our ultimate goal is to understand the aging phenomena exhibited by relaxor ferroelectrics, and in this manner control it.

REFERENCES

1. K. Uchino, S. Nomura, L. E. Cross and S. J. Jang, *J. Appl. Phys.*, **51**, 1142, (1980).
2. J. W. Smith, Ph.D. Thesis, The Pennsylvania State University, University Park, PA 16802.
3. W. A. Bonner *et al.*, *Appl. Phys. Lett.*, **10(5)**, 163 (1967).
4. R. Herbert, H. Tenbrock and G. Arlt, "The Aging Behavior of the Complex Material Parameters ε, d, and s in Ferroelectric PZT Ceramics," *Ferroelectrics*, **76**, 319 (1987).
5. K. Carl and K. H. Hardtl, "Electrical After-Effects in Pb(Ti,Zr)O_3 Ceramics," *Ferroelectrics*, **17**, 473 (1978).
6. W. A. Schulze, J. V. Biggers and L. E. Cross, "Aging of Dielectric Dispersion in PLZT Relaxor Ferroelectrics," *J. Am. Ceram. Soc.*, **61(1)**, 46 (1978).
7. W. A. Schulze and J. V. Biggers, "Dielectric Aging in the PLZT System," *Ferroelectrics*, **9**, 203 (1975).
8. S. Takahashi, "Effects of Impurity Doping in Lead Zirconate-Titanate Ceramics," *Ferroelectrics*, **41**, 143 (1982).
9. L. Eyraud, P. Eyraud, J. C. Mathieu and B. Claudel, "Effect of Simultaneous Heterovalent Substitutions on Both Cationic Sites on the Electrical Conductivity and Ageing of PZT Type Ceramics," *Ferroelectrics*, **50**, 103 (1983).
10. W. Wersing, "On the Stabilizing Field of Lead-Titanate-Zirconate Ceramics Doped with Transition Metal Ions," *Ferroelectrics*, **12**, 143 (1976).
11. H. Thomann, "Stabilization Effects in Piezoelectric Lead Titanate Zirconate Ceramics," *Ferroelectrics*, **4**, 141 (1972).
12. G. Borchhardt, J. von Cieminski and G. Schmidt, "Aging of Strontium Barium Niobate and PLZT Ceramic," *Phys. Stat. Sol.*, (a) **59**, 749 (1980).
13. W. Y. Pan, T. R. Shrout and L. E. Cross, "Modeling the Aging Phenomena in 0.9 PMN-0.1 PT Relaxor Ferroelectric Ceramics," submitted for publication.
14. S. L. Swartz and T. R. Shrout, *Mat. Res. Bull.*, **17**, 1245 (1982).
15. S. L. Swartz and T. R. Shrout, *Mat. Res. Bull.*, **18**, 663 (1983).
16. E. Goo and G. Thomas, "Microstructure of Lead-Magnesium-Niobate Ceramics," *J. Am. Ceram Soc.*, **69(8)**, C188 (1986).
17. G. A. Smolenski and A. I. Agronovskaia, *Soviet Physics-Technical Phys.*, **3**, 1380 (1958).

APPENDIX 16

JOURNAL OF MATERIALS SCIENCE LETTERS 8 (1989) 771-776

Modelling the ageing phenomena in 0.9PMN–0.1PT relaxor ferroelectric ceramics

W. Y. PAN, T. R. SHROUT, L. E. CROSS
Materials Research Laboratory, The Pennsylvania State University, University Park, Pennsylvania 16802, USA

Dielectric ageing effects have been well investigated in normal ferroelectrics. The deterioration of various properties with time has been found to be related to one common feature: the gradual stabilization of the ferroelectric domain structure via the fixation of domain walls. The stabilization of various domain configurations is considered to be due to the presence of defects. Several mechanisms responsible for the stabilization of polar regions (domains) as a result of interaction with defects are summarized by Carl and Hardtl [1] and more recently by Schulze [2]. As modelled by Plessner [3], a distribution of activation energies reflecting the random nature of obstacles (defects) to domain wall motion mathematically results in the observed logarithmic ageing behaviour found in normal ferroelectrics. Experimentally it has been shown that the logarithmic decay in the dielectric and piezoelectric properties holds for many years.

Ageing in ferroelectrics infers that the dielectric response includes intrinsic as well as extrinsic phenomena, e.g. domain wall motion with the later ages with time. Recent studies on isothermal ageing in PZT ceramics doped with iron by Diederich and Arlt [4] demonstrate that plots of dielectric constant (K') against dielectric loss (K''), for various frequencies, result in a linear relationship which when extrapolated to a common intercept at the K' axis yields the bulk dielectric constant value. Thus the intrinsic dielectric properties could be obtained.

Ageing effects in "non-normal" ferroelectrics have also been observed in relaxor ferroelectrics including PLZT by Schulze *et al.* [5], in the tungsten bronze $Sr_xBa_{1-x}Nb_2O_6$ (SBN) by Borchhart *et al.* [6], and perovskite $Pb(Mg_{1/3}Nb_{2/3})O_3$ (PMN) doped with MnO by Pan *et al.* [7]. It must be remembered that in normal ferroelectrics the phase and composition are homogeneous throughout the ceramic and/or crystals, whereas in relaxor ferroelectrics these conditions no longer exist. A relaxor ferroelectric may be considered an intimate mixture of different paraelectric and ferroelectric regions due to micro-inhomogeneity as a result of lattice and/or cation disorder. Different regions thus have a different degree of ferroelectricity and Curie temperature depending on the composition and the size of the chemical microregions [8]. The overall effect is a ferroelectric with a broad Curie maximum and associated frequency dispersion in the dielectric properties [9]. It may be expected, then, that when a relaxor undergoes ageing, the behaviour of the ageing is modified by the characteristic composition and phase inhomogeneity.

Hence, the purpose of this paper was to propose a model to explain the ageing phenomena previously observed in relaxor ferroelectrics, in particular MnO-doped 0.9PMN–0.1PT ceramics. The relaxor composition used throughout this study was 0.1 wt % MnO-doped 0.9PMN–0.1PT, having been previously found to exhibit significant ageing. The addition of 0.1 mol of $PbTiO_3$ was used to shift the Curie maximum to slightly above room temperature.

The ceramic processing technique developed by Swartz and Shrout [10] was adopted for the preparation of the PMN–PT ceramics. The process basically involves the pre-reaction of MgO and Nb_2O_5 to form the precursor $MgNb_2O_6$ prior to reaction with PbO and TiO_2. This process has been highly successful in the limitation of undesirable phases, in particular the PbO–Nb_2O_5 pyrochlore(s). The PMN–PT was doped with the addition of 0.1 wt % MnO using a diluted solution of $Mn(NO_3)_2$ [7]. Discs were prepared from the calcined powder followed by sintering. The densified discs were cut and ground and sputtered with gold electrodes. Further details of the sample preparation have been previously reported [7].

The dielectric behaviour as a function of time in the MnO-doped PMN–PT ceramics was investigated isothermally and (pseudo-)dynamically as well. Isothermal ageing studies involved monitoring the change in dielectric properties as a function of time at a given temperature, whereas dynamic ageing looked at the influence of a well-aged sample on the dielectric-temperature behaviour, particularly near the Curie maximum. Prior to dielectric-temperature runs, samples were de-aged by heating to 150° C and held for about a half hour and then brought down to a fixed temperature to allow ageing. The "time equals zero" on the measuring clock was given at this point. Samples aged at room temperature were placed in a dessicator in an air-conditioned laboratory space (23 to 26° C). Ageing at temperatures higher than room temperature was carried out in a Plexol oil bath heated by a powerstat with temperature fluctuation ± 3° C. Ageing at temperatures lower than room temperature was carried out in a commercial freezer with a measured temperature variation of ± 2° C.

The relative permittivity (dielectric constant K) against temperature measurement was carried out in a computer-controlled environment chamber (Delta design Model 2300). The dielectric properties were measured using a Hewlett-Packard LCR meter (Model 4274A) under computer control covering a frequency range from 100 Hz to 100 kHz. The field

0261–8028/89 $03.00 + .12

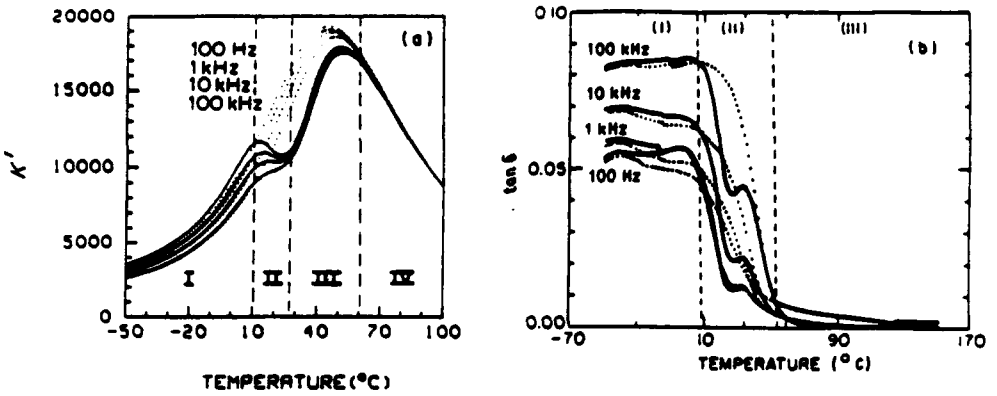

Figure 1 (a) Dielectric constant and (b) loss against temperature for 0.1 wt % MnO-doped 0.9PMN–0.1PT ceramic samples after ageing for 1000 h at room temperature. Solid curves are for heating run and dotted curves are for cooling run.

strength of the measuring field was less than 10 V cm^{-1}, low enough not to cause de-ageing effects. The temperature was determined with a Fluke 8520A digital multimeter via a platinum resistance thermometer mounted directly on the ground electrode of the sample fixture. A Model HP 985A desk-top computer was used for on-line control of the measurements through an HP 6904B multi-programmer interface. The samples were put into the chamber at a temperature far below the ageing temperature to avoid de-ageing before the measurement. The temperature was then lowered to $-70°C$ and the dielectric properties were measured using a heating rate of $4°C\,min^{-1}$. For de-ageing study the sample was kept at 150° C for half an hour, then the temperature was cooled down at the same rate and the dielectric properties were measured.

Isothermal ageing studies were carried out in an insulating chamber comprised of Styrofoam. A multi-sample holder was used so as to be able to monitor the dielectric properties of many samples simultaneously. A constant temperature was achieved by the circulation of controlled temperature water through copper tubing. Above room temperature, the temperature of the water was maintained by a temperature-controlled water bath. The temperature was controlled to within $\pm 0.1°C$ for a period of 1000 min. Below 22° C, control was made by using a mixture of hot and cold water and was better than $\pm 0.3°C$ for a period of 1000 min. Dielectric properties were again measured using a Hewlett-Packard Packard LCR meter (Model 4272A). Both the real K' and imaginary part (K'') of the dielectric constant were determined. K'' was calculated using the expression $K'' = K' \tan \delta$ where $\tan \delta$ is the dielectric loss. The data were taken about 20 times per decade of time to ensure a uniform distribution of the data points in dielectric constant against log(time) curves. The r.m.s. amplitude of the measuring field was again under 10 V cm^{-1} and the frequencies were from 1 to 100 kHz.

Fig. 1 shows the dielectric constant (Fig. 1a) and loss (Fig. 1b) at various frequencies (0.1, 1, 10, and 100 kHz) against temperature for 0.1 wt % MnO-doped 0.9PMN–0.1PT ceramics. The solid curves represent the dielectric data for a sample aged at room temperature for 1000 h and then measured upon heating. The dashed curves represent the data for samples thermally de-aged at 150° C and then measuring during cooling. Several interesting features are apparent in the figures, including saddle-shaped depressions in the dielectric constant and loss at the temperature of ageing and the reduction of frequency dispersion, with the latter being recovered at a point below the ageing temperature.

The characteristic "saddle" in the dielectric temperature curves reflects the reduction of the dielectric constant and corresponding loss as a result of ageing. The position of the saddle point was found to occur at the temperature at which ageing took place, as seen in Fig. 2 showing dielectric against temperature curves for samples aged at 40° C, room temperature (R.T.) and $-15°C$. Though the point at which the saddle occurs is dependent on the temperature at which ageing took place, the depth and overall shape of the saddle are not. As observed, the saddles for the 40° C and R.T. dielectric ageing curves were much sharper and deeper than that for the $-15°C$ curve.

In order to explain both the depth and shape of the

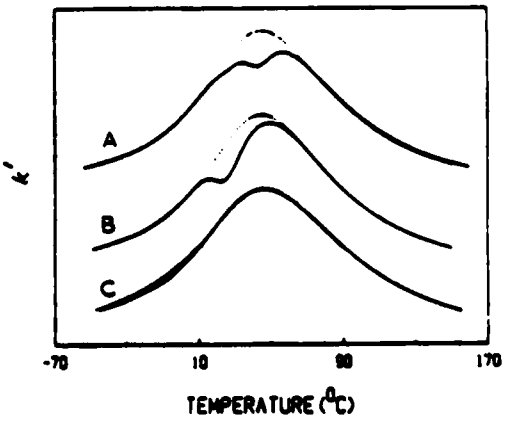

Figure 2 Effect of ageing temperature on 100 Hz dielectric constant against temperature in 0.1 wt % MnO-doped 0.9PMN–0.1PT ceramic samples. Solid curves are for aged samples: curve A is for the sample aged 70 h at 40° C, curve B is for the sample aged 10 h at room temperature and curve C is for the sample aged 100 h at $-15°C$; dashed curves are for freshly de-aged samples.

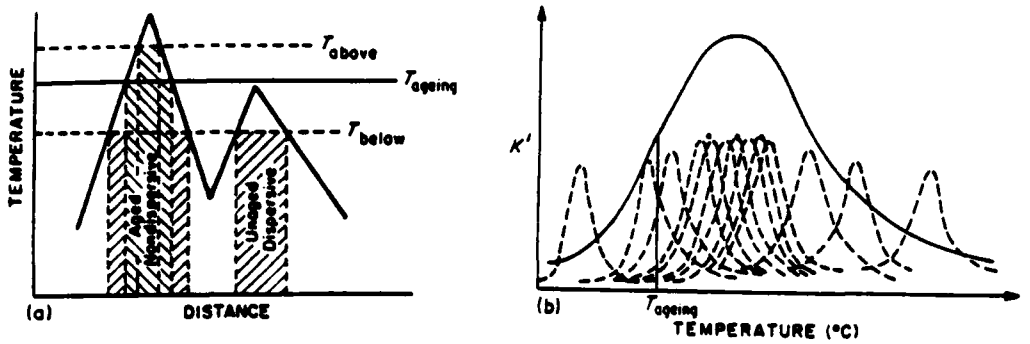

Figure 3 (a) Schematic diagram of Curie temperature against one-dimensional distance for a relaxor. (b) Scheme of dielectric constants against temperature for (- - -) individual homogeneous regions in a relaxor ferroelectric and (——) the relaxor system as a whole.

saddle point occurring at the ageing temperatures, clearly we must first postulate a model to explain the dielectric constant against temperature behaviour for a ferroelectric relaxor system and its overall relationship to the individual micro-regions. In a relaxor ferroelectric, the size of the polar regions is much smaller than the domain size in a normal ferroelectric. Thus the energy required for the reorientation of the spontaneous polarization vectors is comparable to the thermal energy. Therefore, the reorientation of the spontaneous polarization vectors under a weak field contributes to a major part of the weak-field permittivity. The observed permittivity–temperature response through the radio frequency range is a result of a statistical spread of Curie temperatures and a statistical distribution of "flipping" frequencies. Recently, a phenomenological model combining these two contributions has been attempted by Yokosuka and Marutake [11]. However, this model is still incomplete as the observed dielectric behaviour should also depend on the kinetics and interaction between neighbouring polar microregions which weights any statistical distribution. Nevertheless, with a qualitative understanding of the superparaelectric behaviour, the observed ageing behaviour can be explained.

According to this model, various physical constants vary continuously from place to place due to the compositional inhomogeneity. The crystal can be divided into small regions and within each one, the physical constants are assumed to be uniform. Fig. 3 shows a scheme for the weak-field dielectric constant–temperature response and its relation to those of the individual regions. As depicted, each region has its own dielectric peak situated at a different temperature as a result of micro-chemical inhomogeneity associated with relaxor ferroelectrics. It must be mentioned that the dielectric maximum temperature for a region should be lower than the Curie temperature of the region, and the peak must be much broader than the intrinsic dielectric peak due to the "flipping" contribution of the spontaneous polarization vectors. The overall dielectric maximum of the relaxor ferroelectric thus situates at the temperature where the small peaks are the most densely populated, which infers statistically that most of the regions transform into ferroelectrics at the dielectric maximum temperature upon cooling.

Fig. 3a is a schematic diagram showing the Curie temperature against one-dimensional distance for the relaxor. When ageing is carried out at a temperature marked by T_{ageing}, the ferroelectric region indicated by "Aged Non-Dispersive" undergoes ageing. After ageing, when the temperature decreases below T_{ageing} the region is aged and non-dispersive, while the region indicated by "Unaged Dispersive" is a fresh ferroelectric region which is unaged and dispersive. It is these "unaged", "dispersive", and "fresh" ferroelectric regions which raise the dielectric constant and dispersion below the ageing temperature. If the small dielectric peaks shown in Fig. 3b are sharp, it is not difficult to visualize the quick recovery of the dielectric constant below the ageing temperature and then the dielectric constant, as well as the dispersion, recovers as was shown in Fig. 1a. Apparently, how soon the dielectric behaviour shown recovers below the ageing temperature depends on how much paraelectric ferroelectric phase conversion takes place upon cooling past the ageing temperature. Naturally, since most of the regions transform into ferroelectrics near the temperature of the dielectric maximum, the recovery of the dielectric constant is very fast and the saddle points are sharp (deep) for ageing at 40° C and at room temperature as shown in Fig. 2. At −15° C, most of the assemblage has transformed into ferroelectrics, and therefore little phase transformation takes place below this temperature and thus the saddle point is not sharp.

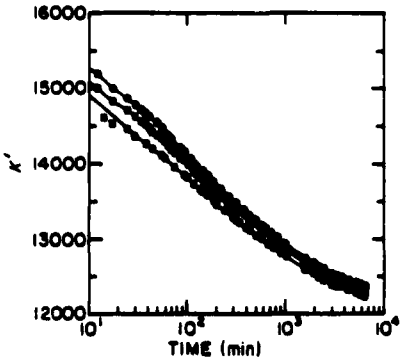

Figure 4 Dielectric constant against log(time) for undoped 0.9PMN–0.1PT ceramic samples at 37° C: (●) 1 kHz, (□) 10 kHz, (■) 100 kHz.

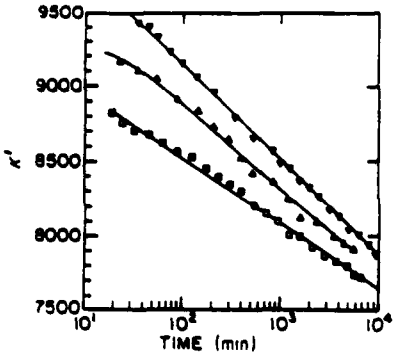

Figure 5 Dielectric constant against log(time) for undoped 0.9PMN–0.1PT ceramic samples at 15°C. (▽) 1 kHz, (△) 10 kHz, (□) 100 kHz.

For isothermal ageing, the dielectric constant against log(time) for doped PMN–PT aged at 37° C is shown in Fig. 4. The anticipated log-linear relationship, which holds for several years in normal ferroelectrics, was not found. As shown, in the early stages, ageing took place at a relatively fast rate (~ 10% per decade) before levelling out just beyond 1000 min (~ 3% per decade) to what appears to be a linear region. Since most ageing experiments use time periods ranging between 10 and 100 h, in order to avoid problems in short-term thermal equilibrium and associated "zero-point determination," much of the vital ageing information in relaxors has been overlooked. To explain both the level of ageing as well as the non-linear behaviour, one must again propose a model explaining the dielectric behaviour and its overall relationship to the micro-regions.

For normal ferroelectrics, as the unit cell distortion becomes less, the ageing rate increases because less strain is involved in domain wall movement [10]. For relaxor ferroelectrics, however, the fact that the polar vectors are easily moved/flipped by room-temperature thermal energy indicates little lattice distortion, yet for undoped or stoichiometric PMN–PT relaxors, little ageing is observed. The role in which the manganese addition results in ageing is probably related to an internal bias, as shown in "hard PZT ceramics," yet as demonstrated by Yao *et al.* [13] above certain temperatures, even a large electric d.c. bias (up to about several kV cm $^{-1}$) cannot stabilize the thermally fluctuating polarization vectors. Therefore, we may assume that as the dynamic nature of the fluctuating polar (P_r) vectors increases, the interaction with the defects becomes less efficient and thus ageing becomes slower. From here on, we will refer to the regions with relatively stable P_r vectors as the *fast* ageing regions and the regions with flipping dynamic P_r vectors as the *slow* ageing regions. If the fast-ageing ferroelectric regions age preferentially, leaving the paraelectric and slow-ageing ferroelectric regions behind, the ageing rate will decrease and level out with time as observed in Fig. 4. At a temperature highly populated with ferroelectric regions with relatively stable P_r vectors, the levelling-off effect caused by the paraelectric and slow-ageing ferroelectric regions would thus take a longer time to be observed. As shown in Fig. 5, the "levelling-off" effect for ageing at 15°C is not obviously visible within 10^4 min. In addition, a more pronounced dependence of ageing on frequency was observed. This was expected, being located in the more dispersive component region of the Curie transition.

The effect of temperature on the ageing behaviour is further illustrated in Fig. 6. For the sake of comparison, the curves have been normalized to that of their respective values of the de-aged state (value at "zero time" or close proximity). For higher ageing temperatures, the normalized values of the dielectric constants were found to be lower initially, approaching the values for lower ageing temperatures at about 10^3 min. The lower initial values are caused by the fast ageing under higher temperature, since ageing is a thermally activated process. Apparently, there are fewer ferroelectric polar regions available to maintain the initial ageing rate under higher temperatures than under lower temperatures. When the ageing time is extended to 10^3 min, the amount of the remaining unaged ferroelectric polar regions is not enough to maintain the earlier ageing rate and consequently a "levelling-off" effect occurs faster earlier.

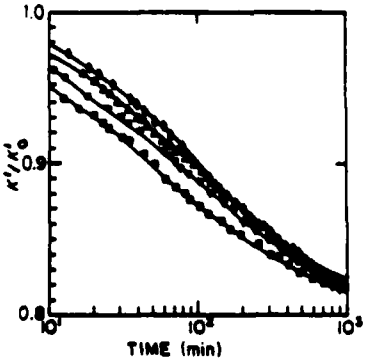

Figure 6 1000 Hz dielectric constant (normalized to the initial de-aged values) against log(time) for 0.1 wt % MnO-doped 0.9PMN–0.1PT ceramic samples at different temperatures: (◆) 15°C, (△) 26°C, (▽) 37°C, (□) 46°C.

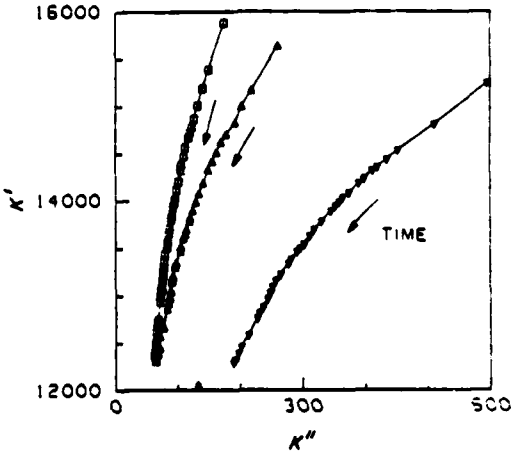

Figure 7 K' against K'' plots of isothermal ageing for 0.1 wt % MnO-doped 0.9PMN–0.1PT ceramic samples at 37°C (□) 1 kHz, (△) 10 kHz, (▽) 100 kHz.

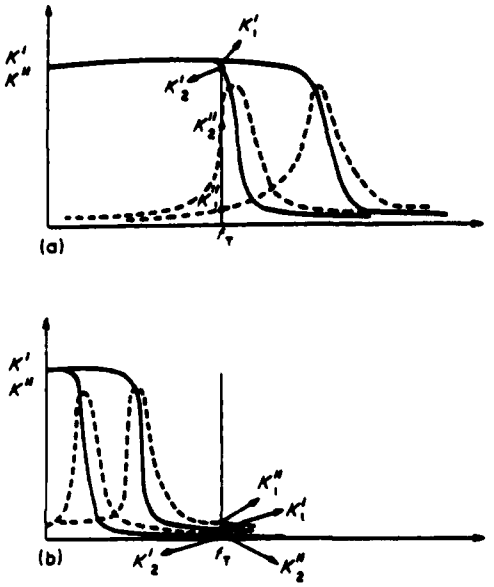

Figure 8 Dielectric dispersion curves for two micropolar regions in a relaxor ferroelectric with different cut-off frequencies: (a) before ageing and (b) after ageing.

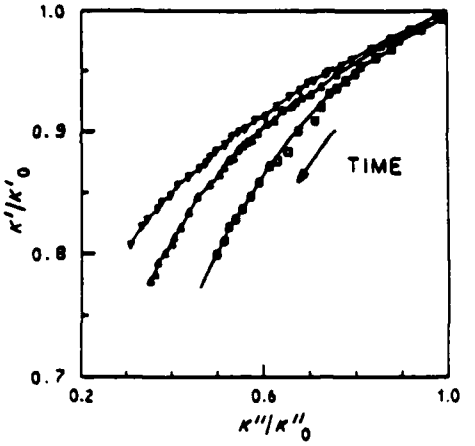

Figure 9 K' against K'' plots of isothermal ageing of 1000 Hz dielectric constant (normalized to the initial values) at different temperatures for 0.1 wt % MnO-doped 0.9PMN–0.1PT ceramic samples (▼) 26°C, (▲) 37°C, (■) 46°C.

Complex ageing curves of K' against K'' at different frequencies for PMN–PT aged at 37°C are shown in Fig. 7. As shown, these curves are obviously not straight lines as found for normal ferroelectrics. Further, it is not possible to extrapolate these curves to the K' axis to obtain the bulk value of the real part of the dielectric constant. This is to be expected since a major contribution to the weak-field permittivity of a relaxor ferroelectric comes from the extrinsic P_r vector reorientation under the measuring E-field. Another feature to note is that the curves keep bending downward as ageing continues. This implies that as the ageing increases, the ageing rate of the real part (K') increases relative to the imaginary part of the dielectric constant (K''). To understand this phenomenon clearly, a "distribution" of relaxation time constants for the polar vector reorientation in different polar regions needs to be considered as done for the dielectric constant in Fig. 3. Given that regions of relatively stable P_r vectors possess longer relaxation times than these of regions of dynamically flipping polarization vectors, the "cut-off frequency," as defined in Fig. 8, for various regions is distributed over a wide range accordingly. For simplicity, Fig. 8a shows dispersion curves for only two regions with different corresponding cut-off frequencies. Naturally, the dielectric dispersion curve for the whole system is a weighted average of those for all individual regions. If the ageing of a single region is a pure "timing" process, i.e. the cut-off frequency for the region moves continuously lower, then after a sufficiently long time the cut-off frequencies for both regions may have moved below the frequency of the measuring field. Dispersion curves for the two regions for an aged sample are depicted in Fig. 8b, where it may be seen that the longer relaxation time-constant region shows more reduction in loss tangent after ageing than the shorter relaxation time-constant region. Over a relatively long ageing period, after the long relaxation time-constant components have aged out, the dielectric response is taken over by the short relaxation time-constant regions and the reduction in loss tangent is less with time. As a result, the curves keep bending downward with time as shown in Fig. 7.

The observed "bending" effect also depends on the temperature at which ageing takes place. The normalized real dielectric constant K' against imaginary dielectric constant K'' is shown in Fig. 9. Clearly, the curves for higher ageing temperatures are always below those for lower ageing temperatures. This suggests that for the same ageing time, high-temperature ageing eliminates a greater fraction of the real dielectric constant than low-temperature ageing for the same fraction of the imaginary dielectric constant eliminated. Apparently, as temperature increases, the polar vectors become more dynamic and the relaxation time constants for the polarizabilities of these vectors become less and less. As demonstrated in Fig. 8, the stabilization of these vectors involves more reduction in the real dielectric constant and less reduction in the imaginary dielectric constant; this is the reason why the curves for higher ageing temperatures are always under those for lower ageing temperatures.

To summarize, the dielectric ageing effects in MnO-doped 0.9PMN–0.1PT relaxor ferroelectrics were found to be correlated with the micro-compositional inhomogeneity nature of the relaxor ferroelectric. The recovery of the magnitude and dispersive component of the weak-field permittivity below the ageing temperature was correlated with the diffused phase transition of the relaxor. The paraelectric matrix at the ageing temperature is being transformed into ferroelectric polar regions which reorient under the weak field, re-establishing the magnitude and dispersive component of the permittivity.

The observed non-linear behaviour of dielectric constant against log(time) at a constant temperature was also a manifestation of the micro-compositional

inhomogeneity. At a constant temperature, regions with different relaxation time constants and ageing rates coexist. Larger relaxation time-constant components (fast ageing components) age first, leaving the small relaxation time-constant components (slow ageing components) behind. This "distribution change" thus gave rise to the "levelling-out" of the dielectric constant against log(time) curves.

The non-linear K' against K'' plots of isothermal ageing correlated with the associated dispersive behaviour of the different regions with long and short relaxation time constants. Long relaxation time-constant components were accompanied by larger loss tangents than short relaxation time-constant components. Larger relaxation time-constant components age preferentially, giving rise to a large initial rate of decrease in K''. As the "distribution" changes, the shorter relaxation time-constant components dominate the later part of the ageing, giving rise to the reduced rate of K''. The K' against K'' plots are therefore not straight lines.

Acknowledgement

The authors wish to thank Dr C. A. Randall for valuable discussions.

References

1. K. CARL and K. H. HARDTL, *Ferroelectrics* **17** (1978) 473.
2. W. A. SCHULZE, submitted to *Ferroelectrics*.
3. K. W. PLESSNER, *Proc. Phys. Soc. B* **69** (1965) 1261.
4. H. DEDERICHS and G. ARLT, *Ferroelectrics* **68** (1986) 281.
5. W. A. SCHULZE, J. V. BIGGERS and L. E. CROSS, *J. Amer. Ceram. Soc.* **61** (1978) 46.
6. G. BORCHHARDT, J. Von GIEMINSKI and G. SCHMIDT, *Phys. Status Solidi (a)* **59** (1980) 747.
7. W. Y. PAN, E. FURMAN, G. O. DAYTON and L. E. CROSS, *Mater. Lett.* **5** (1986) 647.
8. N. SETTER and L. E. CROSS, *J. Appl. Phys.* **51** (1980) 4356.
9. G. A. SMOLENSKII and V. A. ISOPOV, *Sov. Phys. Dokl.* **9** (1964) 653.
10. S. L. SWARTZ and T. R. SHROUT, *Mater. Res. Bull.* **17** (1982) 1245.
11. M. YOKOSUKA and M. MARUTAKE, *J. Appl. Phys.* **25** (1986) 981.
12. M. C. McQUARRIE and W. R. BUESSEM, *Amer. Ceram. Soc. Bull.* **34** (1955) 402.
13. XI YAO, Z. CHEN and L. E. CROSS, *J. Appl. Phys.* **54** (1983) 3399.

Received 5 October
and accepted 7 November 1988

APPENDIX 17

EFFECTS OF THE LAPPED SURFACE LAYER AND SURFACE STRESS ON THE DIELECTRIC PROPERTIES OF PLZT CERAMICS

Q.Y.Jiang, S.B.Krupanidhi, and L.E.Cross
Materials Research Laboratory
The Pennsylvania State University
University Park, PA. 16802

ABSTRACT

The effects of surface layer and surface stress on the dielectric properties of PLZT ferroelectric ceramics were studied. The specimens with surfaces prepared by grinding and polishing showed anomalous dielectric properties, i.e. smaller dielectric constant, lower dielectric loss below Curie temperature and smaller polarization than those of the specimens whose lapped surface layers were removed by chemical etching. After annealing at 650 ^{o}C for 1hr, the dielectric properties showed improved values; the behavior may be attributed to the existence of surface layers produced during grinding and polishing which seem to be nonferroelectric in nature while under 2-D tensile stress, and having large capacitance of the order of 0.1—1.0 $\mu F/cm^2$.

I. INTRODUCTION

The surface layers of ferroelectrics have been widely studied by many investigators,[1-3] in early 1960's. Most experimental studies on surface layers of ferroelectrics have been performed on single crystals of $BaTiO_3$[4], TGS[5] and $Pb_5Ge_3O_{11}$[6], with very few studies being related to the ferroelectric ceramics. Jyomura et al.[7] investigated the effects of surface layer on barium and strontium doped PZT ceramics and concluded that the lapped surface layer was a 0.1—2 μm thick nonferroelectric layer with 2-D stress of 5—15 kbars. But their experiments were confined only to unannealed specimens. If the two dimensional tensile stress generated during lapping does influence the dielectric properties, annealing could greatly reduce such surface stress, with a possible improvement in the dielectric properties. In this paper, the effects of the lapped surface layer on dielectric properties are studied on both unannealed and annealed PLZT ceramic specimens, and the possible mechanisms of the surface layer discussed.

II. EXPERIMENTS

The material used was hot pressed lanthanum doped PZT with the composition of 7/68/32

$[Pb_{0.93}\ La_{0.07})(Zr_{0.68}Ti_{0.32})_{0.9825}\ O_3]$.The samples were subjected to different surface preparations: (a) After slicing, the specimen were annealed at 650 °C for 1hr, then ground to the desired thickness of about 200 μm, some of the ground samples were further polished or chemically etched. (b) After slicing, the specimens were ground to about 200 μm thick; some of them were further polished or chemically etched, then the ground and polished samples were annealed at 650 °C for 1hr. Electrodes were either sputtered gold or evaporated gold for different measurements.

The temperature dependence of dielectric constant and dielectric loss were measured by Hewlett Packard LRC meter (model 4274A). The pyroelectric currents were measured with the HP 4140B picoampere meter. Temperature was measured with a Fluke 8502A digital multimeter. Ferroelectric hysteresis loops were measured by using a modified Sawyer-Tower circuit at room temperature.

III. RESULTS AND DISCUSSION

A. Lapped Surface Layer

Temperature dependences of dielectric constant (K) and loss tangent (tan δ) at 1 kHz with ground, polished and chemically etched surfaces are given in Fig.1; and similar results were obtained at the other two freqencies of 10 kHz and 100 kHz. There are differences in the behavior of the dielectric constant with temperature near the Curie temperature (T_C). The specimen with ground surface which is the roughest had the lowest K, the one with etched surface had the largest K and the one with polished surface had a K value between the two. It may also be noted that loss tangent below Tc is different for different surfaces. Etched surface had the highest value of tan δ, the ground surface had the lowest value of tan δ, and the polished surface had an intermediate value.

These anomalies in dielectric properties are caused by ground and polished layers on the surfaces of ceramic bodies. If we consider the homogeneous surface layer on the two faces of the specimen in contact with the electrode and assume the resistance of the sample and of the surface to be very large, then the lapped surface layers could be thought of as capacitors connected in series with the bulk; the total measured capacitance, C_T, can be represented by:

$$1/C_T = 1/C_B + 2/C_S \qquad (1)$$

where C_B, C_S are bulk capacitance and surface layer capacitance respectively.

If we take the capacitance measured from ground sample as C_T, the one measured from etched sample as C_B, the C_S calculated from eqn. (1) is 0.2 to 1 μF/cm^2 in the temperature range of -40 °C to 160 °C, it only increases slightly with increase in temperature with no T_C

peaks, and hence lapped surface layer is non ferroelectric. In Fig. 1, at low temperature, the K value for the 3 surfaces are very close, C_B is very small compared to C_S at low temperature. From eqn. (1), it may be seen that $C_T = C_B$, and the lapped surface layers do not influence C_T to a notable scale. But near T_C , C_B becomes much larger, comparable to the value of C_S. Therefore, the measured C_T deviates from C_B, C_T being lower than C_B.

It is well known that high dielectric loss below T_C in ferroelectrics is generally due to the hysteretic ferroelectric domains. Since the lapped surface layers are non ferroelectric, they have lower loss than the bulk. The total measured loss $(\tan \delta)_T$ can be represented by:

$$(\tan \delta)_T - (\tan \delta)_B = (\tan \delta)_S - (\tan \delta)_B/(1+C_S/2C_B) \qquad (2)$$

where $(\tan \delta)_B$, $(\tan \delta)_S$ are loss tangents of the bulk and the surface layer, respectively.

Below T_C, $(\tan \delta)_S$ is smaller than $(\tan \delta)_B$, $[(\tan \delta)_S - (\tan \delta)_B]$ is negative, and so is $[(\tan \delta)_T - (\tan \delta)_B]$. Therefore, $(\tan \delta)_T$ is smaller than $(\tan \delta)_B$, as can be seen from Fig. 1. tan δ of the etched sample is higher than those of the lapped ones. The hysteresis loops for lapped and etched samples at 0.1 Hz are shown in Fig. 2. The loop of the etched sample is squarer than those of the lapped samples,and the remnant polarization is higher for the etched specimen. From experiments, it is known that the lapped surface layers which may be considered amorphous and mechanically disturbed, influence the dielectric properties but the surface tensile stress induced by polishing and grinding may also be responsible for the anomalies of the dielectric properties, which will be discussed in sec. III (B).

B. Two-Dimensional Tensile Stress on Lapped Surfaces.

In section III (A), the measurements were done on specimens which were ground and polished after annealing. In order to get a better understanding of the surface layers, the dielectric measurements were carried out on specimens which were annealed after grinding and polishing. Fig. 3 shows the temperature dependence of dielectric constant and loss tan δ for the two thermal treatments. In Fig. 3(a) and Fig. 3(b), near T_C, the dielectric constant of the specimens annealed after lapping are higher than those of the specimens annealed before lapping. The loss tan δ below T_C also behaves similarly. In Fig. 3(c), the etched samples were made by chemically etching specimens that were polished after annealing and by chemically etching specimens that were polished before annealing. They showed an almost identical behavior which means that the bulk properties are same under the two thermal treatments. The different K and tan δ of the two thermally treated lapped samples may be attributed to the nature of surface layers.

There are two possibilities that may be responsible for this anomalous dielectric behavior caused by the two thermal treatments. One is that annealing after lapping may change surface

composition, surface structure or domain structure; the other is that two-dimensional tensile stresses may exist on the surfaces. In the first, since the annealing temperature is low (650 ^{o}C), such changes are unlikely to happen; to examine this, measurements were performed on specimens which were annealed after etching. The results, shown in Fig. 4, indicate no change after annealing. So it is the surface stress that is responsible for the anomalous behavior which is in good agreement with the studies of Jyomura et al. [7] who found that the surface stress generated during lapping was about 5 to 15 kbars.

The tensile stresses on lapped surface are sensitive to the thermal treatment. Annealing could reduce these stresses and improve the dielectric properties as seen in Fig.3. It was found that the electrode sputtering process could also be considered as a kind of thermal treatment. During the sputtering process, due to the high energetic bombardment of the surface of the sample, the surface temperature could be rather high during a short time, and the surface stresses could be partially reduced by sputtering. However in the process of evaporating the electrode, such high energetic bombardment is absent. The tensile stress on the surface with evaporated gold was expected to be higher than those on the surface with sputtered gold.

The dielectric measurements were performed on the specimens with evaporated gold electrodes. Fig. 5 shows the result of the dielectric constant and tan δ versus temperature for samples annealed both before polishing and annealed after polishing. Comparing Fig.5. with Fig. 3(b), one can clearly notice that the deviations of K and tan δ between the specimens annealed brfore polishing and the ones annealed after polishing in Fig.5. are more profound than those in Fig. 3(b), as was expected.The hysteresis loops in Fig. 6. were measured at room temperature at 0.1 Hz; the remanent polarization is larger for samples annealed after polishing. The temperature dependence of spontaneous polarization and pyroelectric coefficient were also measured, which are not show here. The spontaneous polarization and pyroelectric coefficient was larger in the case of samples annealed after polishing. The surface stresses could decrease the remanent and spontaneous polarization and the pyroelectric coefficient.These results suggest that the lapped surface layer with tensile stresses considerably alters the dielectric properties. It is necessary to anneal the specimens after lapping in order to get adequate properties, especially when the samples are thin. The properties of the bulk could be measured by chemical etching since it relieves the surface stress and eliminates the amorphous lapped layer.

IV. CONCLUSIONS:

Surface layers on PLZT ceramics, produced by grinding and polishing seem to be non ferroelectric and have apparent capacitance to be of the order of 0.1 to 1 $\mu F/cm^2$.The surface

capacitance lowers the total measured capacitance, C_T, especially near T_C. Surface stresses, which appear to be in the nature of 2-D tensile stresses, are also found on ground and polished surface of PLZT. The surface stresses are partially responsible for the anomalous dielectric behavior, and annealing could greatly reduce the surface stresses.The nature of electroding seems to affect the dielectric and polarization behavior as well. Deposition of electrodes by sputtering causes bombardment of surfaces with energetic species and can affect the intrinsic surface stress conditions. Such surface bombardment is absent in the case of evaporation.The chemical etching of samples with lapped surface can offer better dielectric behavior, the dielectric properties of the bulk ferroelectrics may be measured by this way. More detailed experiment to complement these observations in other compositions are already in progress.

REFERENCES:

1. W.Kanzig, "Space Charge Layer Near the Surface of a Ferroelectric", Phys. Rev., 98, 549-50 (1955).
2. D.R. Callaby, "Surface Layer of $BaTiO_3$", J. Appl. Phys., 37, 2295-98 (1966).
3. H. Schlosser, M.E. Drougard, "Surface Layers in Barium Titanate Single Crystals Above the Curie Point", J. Appl. Phys., 32, 1227-31 (1961).
4. A.G. Chynoweth, "Surface Space-Charge Layers in Barium Titanate", Phys. Rev., 102, 705-14 (19 5).
5. V.S. Chincholkar, H.G. Unreh, "Surface Layers of TGS Single Crystals", Phys. Stat. Sol., 229, 669-73 (1968).
6. A. Mansingh, K.N.Srivastava, Bachchan Singh, "Effect of Surface Capacitance on the Dielectric Behavior of Ferroelectric Lead Germanate", J. Appl. Phys., 50, 4319-23 (1979).
7. S. Jyomura, I. Matsuyama, G. Toda, "Effects of the Lapped Surface Layers on the Dielectric P operties of Ferroelectric Ceramics", J. Appl. Phys., 51, 5838-44 (1980).

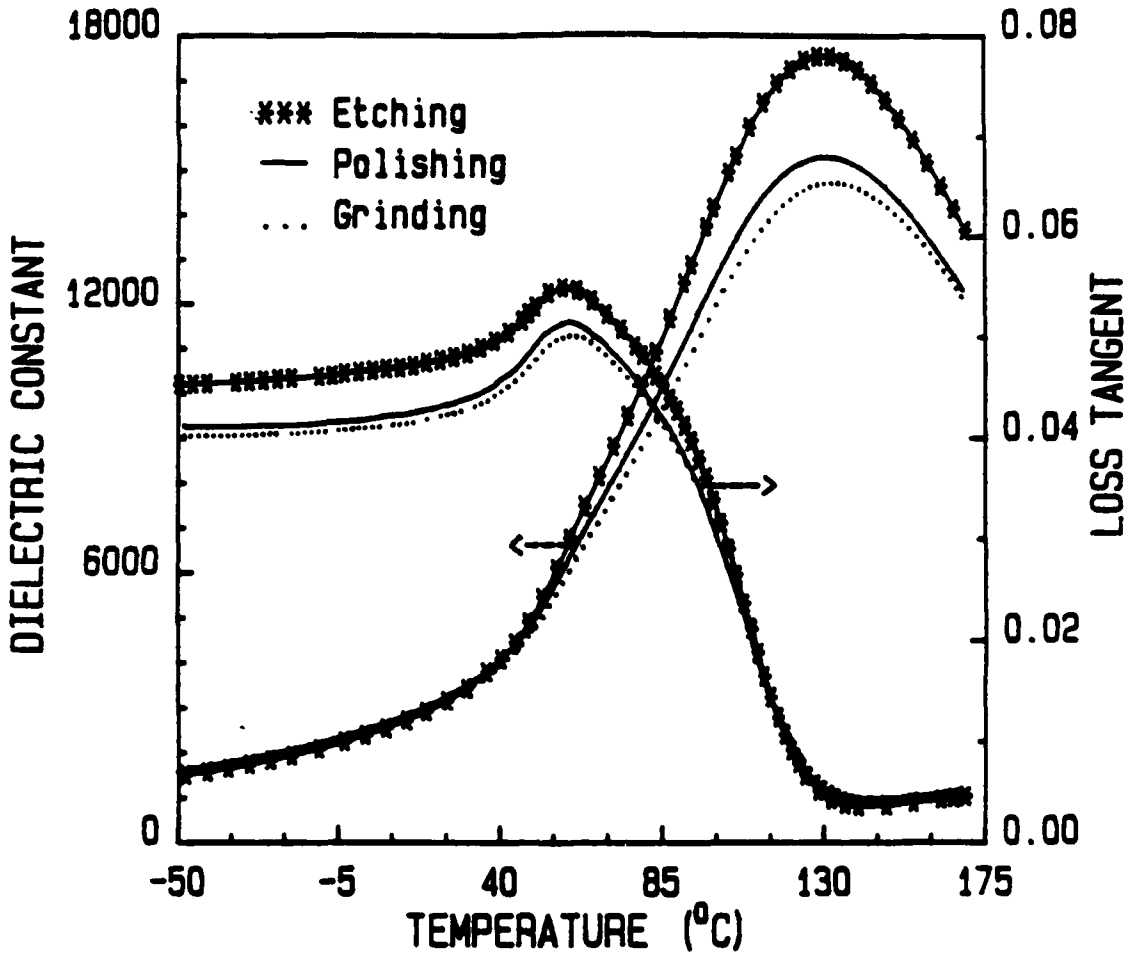

Fig.1. Dielectric constant and loss tangent vs. temperature at 1 kHz with various surface treatments (specimens were annealed before grinding and polishing).

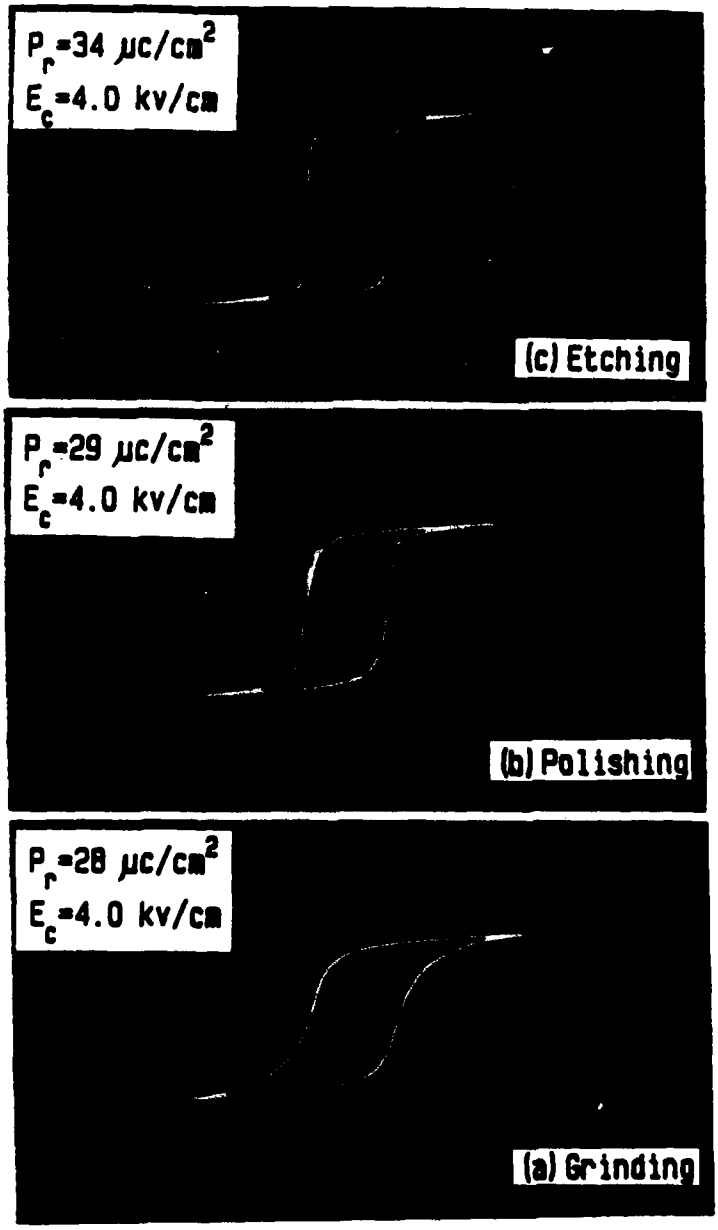

Fig.2. P-E hysteresis loops with various surface treatments. Specimens were annealed before grinding and polishing.

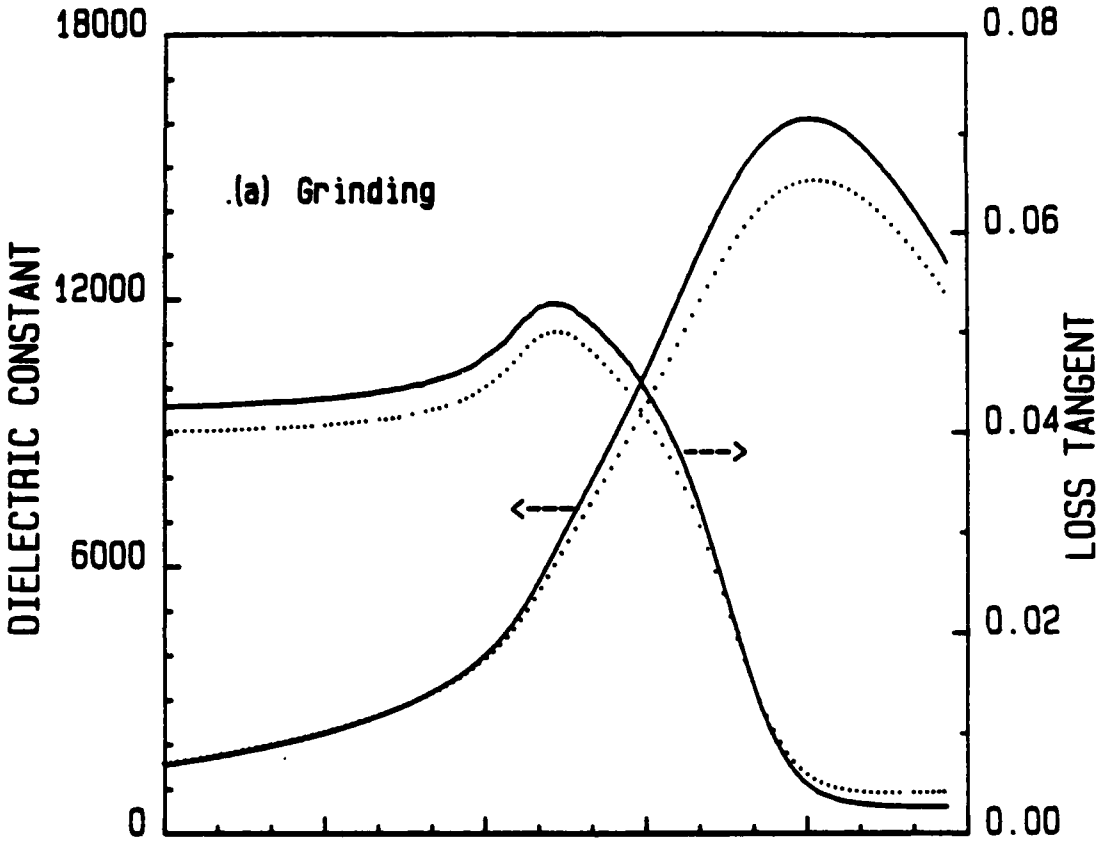
18000
12000
6000
0
0.08
0.06
0.04
0.02
0.00
(a) Grinding
DIELECTRIC CONSTANT
LOSS TANGENT

Fig 3(a)

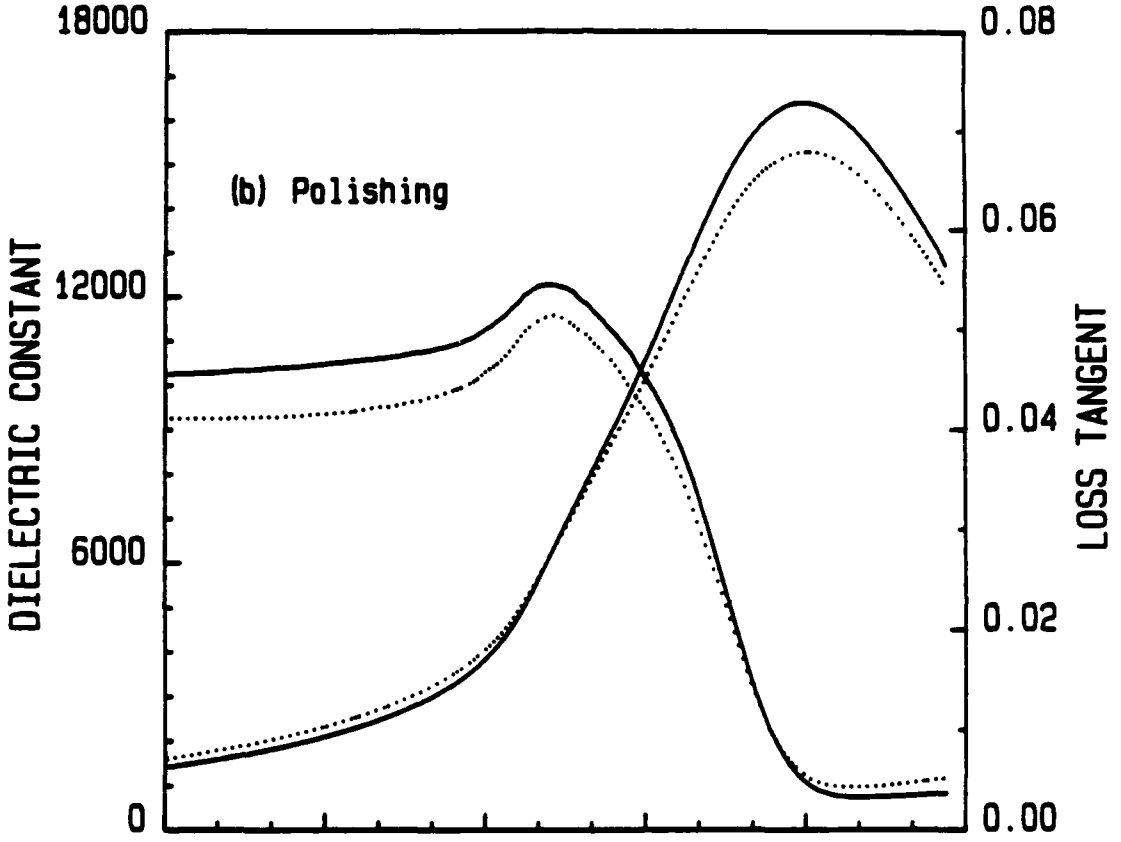
18000
12000
6000
0
DIELECTRIC CONSTANT
(b) Polishing
0.08
0.06
0.04
0.02
0.00
LOSS TANGENT

Fig 3(b)

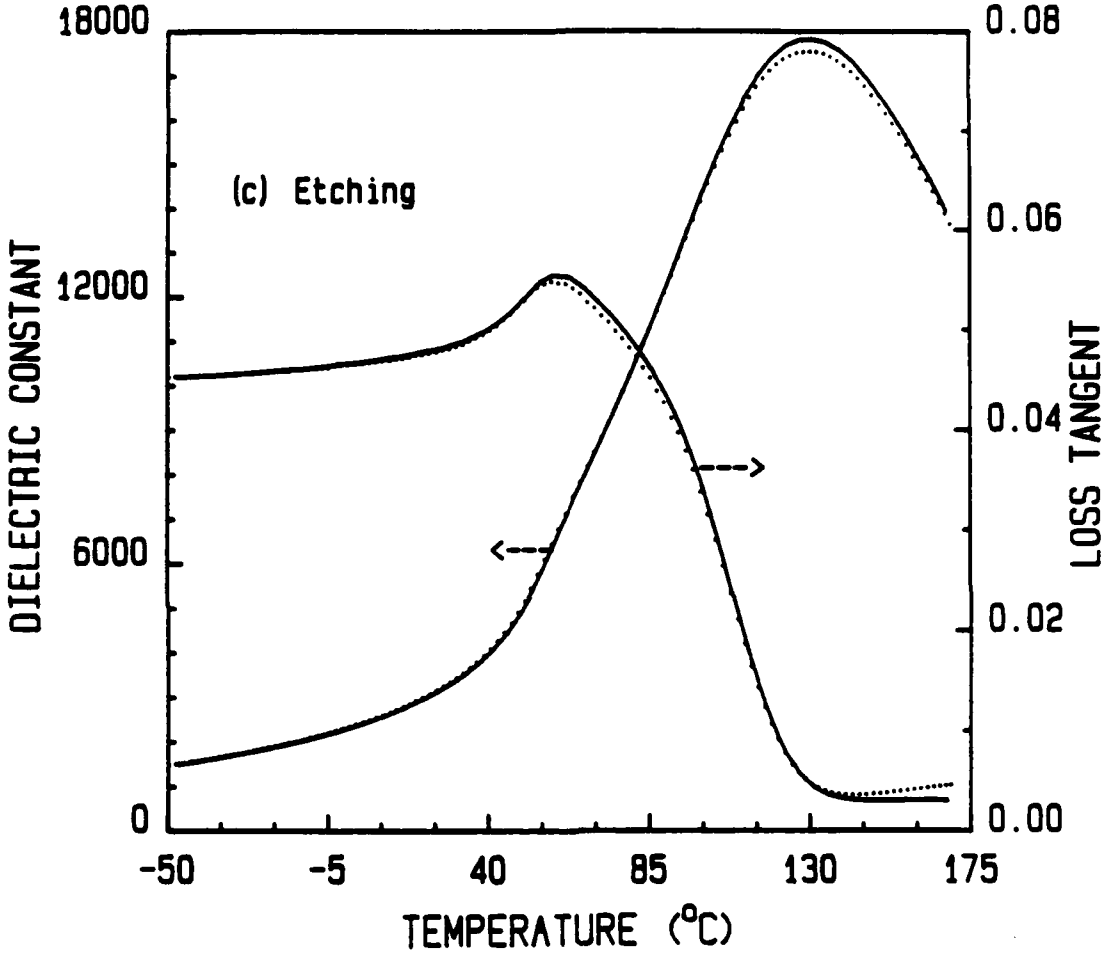

Fig. 3. Dielectric constant and loss tangent vs. temperature. The solid lines are for specimens annealed after grinding or polishing, the dotted lines are for specimens annealed before grinding and polishing.

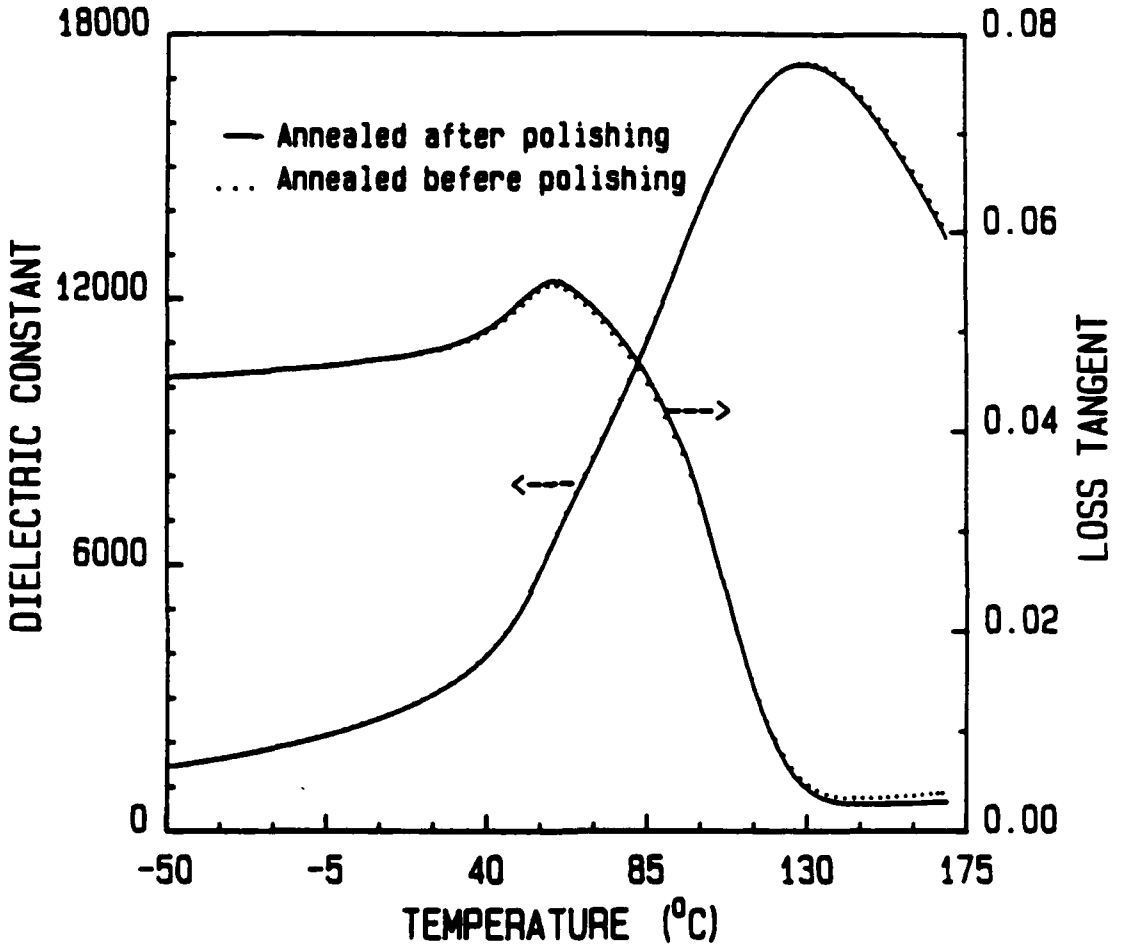

Fig.4. Dielectric constant and loss tangent vs. temperature at 1 kHz for chemically etched samples.

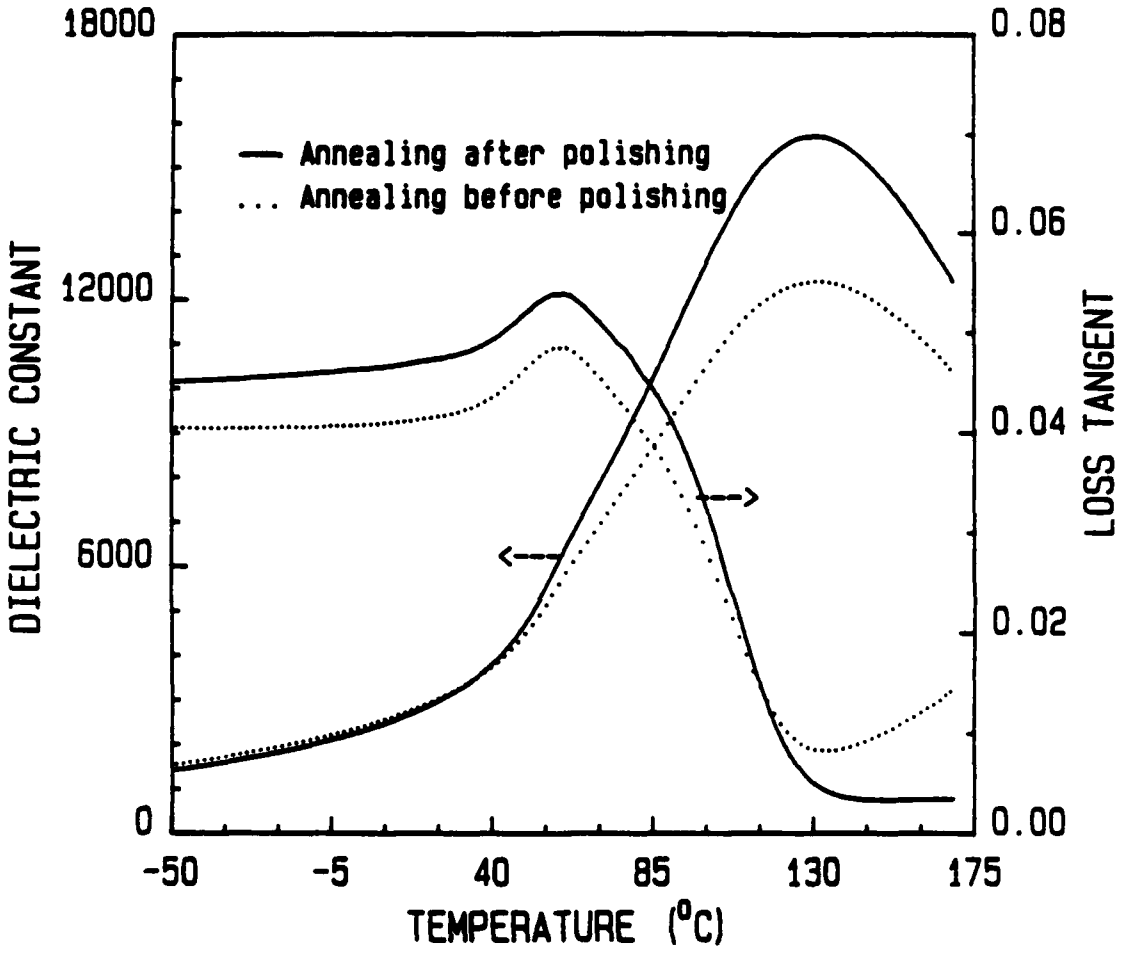

Fig.5. Dielectric constant and loss tangent vs. temperature at 1 kHz with evaporated gold electrodes.

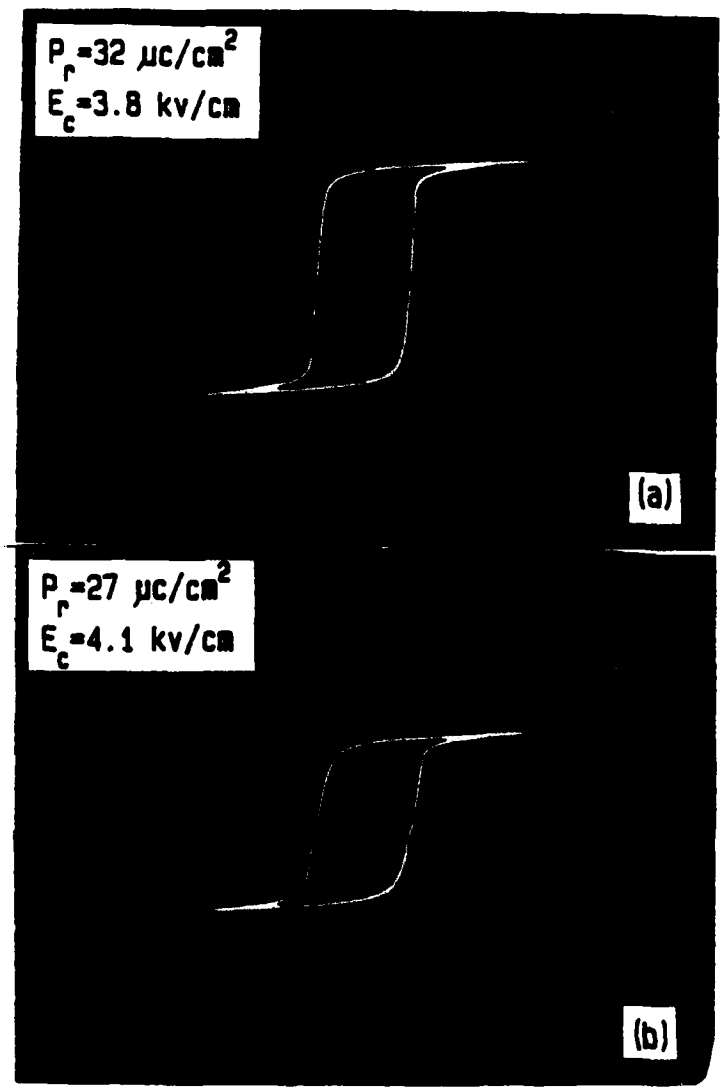

Fig. 6. P-E hysteresis loops with evaporated gold electrodes. (a) Annealed after polishing and (b) annealed before polishing.

APPENDIX 18

MORPHOTROPIC PHASE BOUNDARY IN $Pb(Mg_{1/3}Nb_{2/3})O_3$–$PbTiO_3$ SYSTEM

S.W. CHOI [1], T.R. SHROUT, S.J. JANG and A.S. BHALLA
Materials Research Laboratory, The Pennsylvania State University, University Park, PA 16802, USA

Received 3 May 1989

Dielectric and pyroelectric properties in the solid solution $(1-x)Pb(Mg_{1/3}Nb_{2/3})O_3 : xPbTiO_3$ across the morphotropic phase boundary compositions, $x = 0.275$–0.4, are studied as a function of temperature. The studies revealed that the true morphotropic boundary is in the vicinity of $x \approx 0.3$ and it has a small curvature.

Relaxor ferroelectric lead magnesium niobate, $Pb(Mg_{1/3}Nb_{2/3})O_3$ (PMN) has an anomalously large dielectric constant and a broad diffuse phase transition near −15°C [1,2]. Though the Curie temperature or better yet Curie range, of PMN is well below room temperature it can be shifted upward with $PbTiO_3$ (PT) additions, a normal ordered ferroelectric compound which has a transition at 490°C. It has been reported that a morphotropic phase boundary (MPB) exists in the solid solution system $(1-x)$PMN–xPT near $x = 0.4$ separating pseudocubic (on the PMN-rich side) and tetragonal phases (on the PT-rich side) [3]. As observed in other systems such as $PbZrO_3$–$PbTiO_3$, anomalously large dielectric and piezoelectric properties are observed for compositions lying near the morphotropic phase boundary [4]. This note reports the dielectric and pyroelectric properties for PMN–PT compositions in the vicinity of the MPB and the nature of the boundary.

Ceramic samples (from the reagent grade powders) across the PMN–PT morphotropic phase boundary were prepared by using the columbite precursor method as described by Swartz and Shrout [5]. Upon milling the various powder mixtures of $PbMgNb_2O_6$, PbO, and TiO_2 were cold pressed is disk shapes and then sintered at 1250°C for 1–2 h in closed alumina crucibles. $PbZrO_3$ powder was added to help control Pb stoichiometry in the samples.

Sintered disks were polished and coated with sputtered gold electrodes on both sides. The dielectric constant and loss and pyroelectric coefficients were measured over a temperature range encompassing the transition temperature for each composition. The dielectric properties were measured as a function of frequency using an automated system.

The pyroelectric coefficients were measured by the Byer–Roundy method as the samples were heated at a rate of 4°C/min through the phase transition. Prior to the pyroelectric measurements each sample was poled by applying a dc bias of 15 kV/cm while cooling from well above the transition to a temperature well below.

Fig. 1 shows the typical plot of the dielectric constant at various frequencies (100 Hz–100 kHz) and

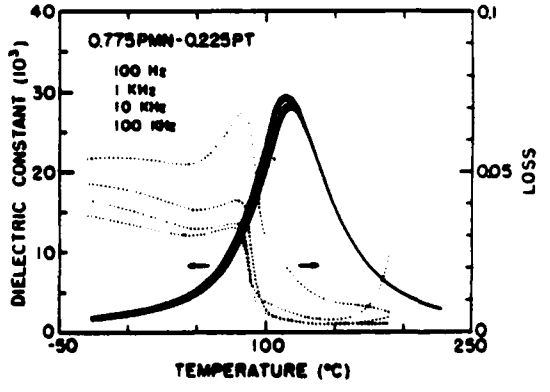

Fig. 1. K versus T at various frequencies for composition 0.775 PMN : 0.225 PT.

[1] Visiting Scientist from the Physics Department, Dankook University, Chon-An, Korea.

0167-577x/89/$ 03.50 © Elsevier Science Publishers B.V.
(North-Holland Physics Publishing Division)

as a function of temperature for a composition 0.775 PMN : 0.225 PT.

The dielectric constant versus temperature data depict the typical relaxor behavior of this composition. When the samples were poled and x varied from 0.25 to 0.4, the dielectric behavior on various samples showed a slight increase in the T_c and the systematic increasing trend in the magnitude of the dielectric peak in various composition ceramics (fig. 2).

On poling the compositions $x = 0.275$, 0.3, 0.325 show two maxima (not observed for the unpoled samples) in the dielectric constant versus temperature measurements on these samples. Such anomalies could represent a second phase transition and

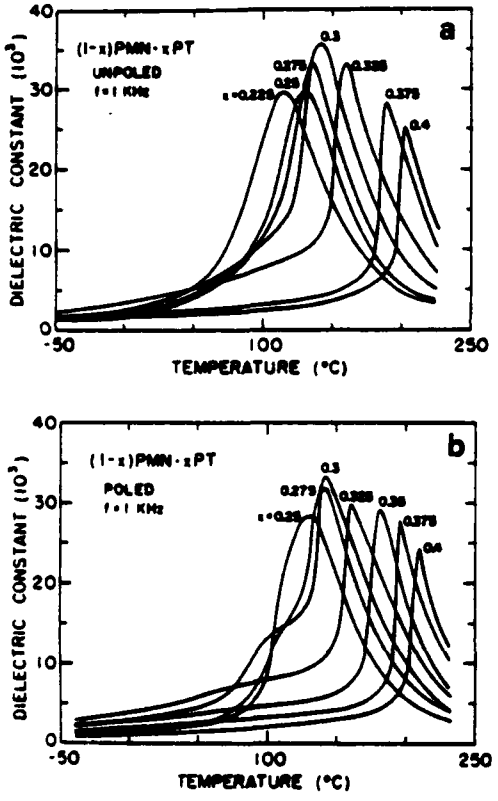

Fig. 2. (a) Dielectric behavior of $(1-x)$PMN–xPT ceramics at 1 kHz measuring frequency and as a function of temperature. (b) Dielectric behavior of poled $(1-x)$PMN–xPT ceramics at 1 kHz measuring frequency as a function of temperature. Samples were poled by applying 15 kV/cm field while cooling down through the phase transition.

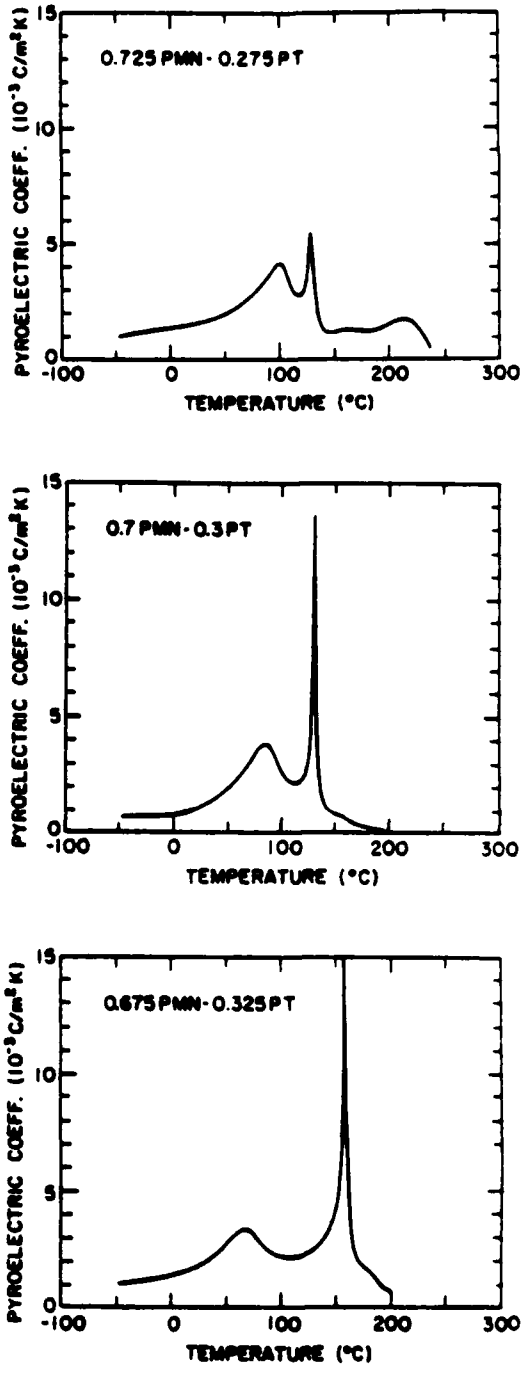

Fig. 3. Pyroelectric coefficient versus temperature measurements for the composition near the MPB.

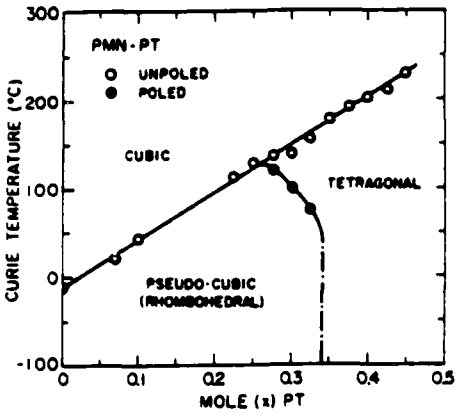

Fig. 4. Phase diagram of $Pb(Mg_{1/3}Nb_{2/3})O_3$–$PbTiO_3$ system.

therefore pyroelectric measurements were done on these samples. The pyroelectric coefficient versus temperature measurements showed anomalies in the same temperature range as observed in the K versus T plots. Thus both the dielectric and pyroelectric data (fig. 3) indicated the presence of a second phase transition in the compositions in the morphotropic phase boundary. The possible transition can be explained by the presence of a small curvature closer to the morphotropic boundary as shown in fig. 4. It is clear that the morphotropic boundary has some curvature at composition around 0.7 PMN : 0.3 PT. It is evident that the two transitions represent cubic→tetragonal→rhombohedral (pseudo-cubic) respectively near the MPB compositions. The compositions with $x > 0.35$ show the characteristics of a normal single-phase ferroelectric material.

Since the nature of K versus T and p versus T measurements are also dependent on the quality of the ceramics, dopants, grain size, and other processing parameters, further studies of these factors in relation to the nature of MPB are in progress.

Thus the studies revealed that the morphotropic phase boundary in the $(1-x)$PMN : xPT system is in the vicinity of $x \approx 0.3$ and it has a small curvature and as a result the compositions near the MPB show two phase transitions, rhombohedral→tetragonal →cubic, when the samples are heated up to the higher temperature.

References

[1] G.A. Smolenskii and A.I. Agranovskaya, Soviet Phys. Tech. Phys. 3 (1958) 1380.
[2] G.A. Smolenskii, V.A. Isupov, A.I. Agranovskaya and S.N. Popov, Soviet Phys. Solid State 2 (1961) 2584.
[3] W. Wersing, Ferroelectrics 7 (1974) 163.
[4] B. Jaffe, W.R. Cook and H. Jaffe, Piezoelectric ceramics (Academic Press, New York, 1971).
[5] S.L. Swartz and T.R. Shrout, Mater. Res. Bull. 17 (1982) 1245.

APPENDIX 19

Ferroelectrics, 1989, Vol. 93, pp. 341–349
Reprints available directly from the publisher
Photocopying permitted by license only

DIELECTRIC AND PIEZOELECTRIC PROPERTIES OF LANTHANUM-MODIFIED LEAD MAGNESIUM NIOBIUM-LEAD TITANATE CERAMICS

N. KIM, W. HUEBNER, S.-J. JANG and T. R. SHROUT
Materials Research Laboratory, The Pennsylvania State University, University Park, PA. 16802

(Received August 29, 1988)

Dielectric and piezoelectric properties of relaxor ferroelectrics in the solid solution, formulated $(1-x)(Pb_{1-x}La_x)(Mg_{1/3}Nb_{2/3})_{1-x/4}O_3 - x\ PbTiO_3$, have been investigated.

The dielectric properties show typical first order ferroelectric behavior for PT ≥ 35% and relaxor type below being indicative of the morphotropic phase boundary. Lanthanum doping resulted in reduction of grain size and shifting of the T_c (Curie Temperature) −25 °C/mole% downward in PMN-PT polycrystalline ceramics. The optimum value of piezoelectric constant, d_{33}, obtained was 560 pC N for compositions near the morphotropic phase boundary.

Based on this investigation, La doped PMN-PT compositions appear to be promising candidates, for fine grain size piezoelectrics, pyroelectric bolometers, and through hot pressing or hot isostatic pressing, for electro-optic applications.

INTRODUCTION

Perovskite lead magnesium niobate {$Pb(Mg_{1/3}Nb_{2/3})O_3$, hereafter designated PMN} was first synthesized by soviet workers in the late 1950's.[1] The dielectric properties of PMN have been widely investigated in both the single crystal[2,3] and polycrystalline ceramic forms.[1,4,5] The main feature of the dielectric properties of PMN is a broad maximum of the dielectric constant at the transition temperature. The magnitude of this maximum decreases and the temperature of this maximum increases with increasing frequency. A corresponding frequency dispersion of the dissipation factor was also observed, but at a temperature range lower than that of the dielectric constant maxima. This behavior is typical of what are now commonly referred to as relaxor ferroelectrics.[1-9] PMN's disordered diffuse phase transition, from a cubic paraelectric to a rhombohedral ferroelectric phase, occurs near −15°C.[8] Perovskite $PbTiO_3$ (hereafter designated PT) is a normal ferroelectric material having a transition from a cubic paraelectric to tetragonal ferroelectric phase near 490°C. Compositions in the PMN-PT solid solution exhibit a morphotropic phase boundary, MPB, between a rhombohedral phase and tetragonal phase about 30–35 mole % PT.[11] The dielectric and piezoelectric constants for materials near MPB, as expected, are anomalously high, making the PMN and PMN-based materials ideal candidates for electrostrictive strain applications,[4-15] electro-optic application[3,10] and dielectric/pyroelectric bolometers.[10]

In the present work, polycrystalline ceramics in the PMN-PT system were prepared by doping with lanthanum. As found in lead zironate titanate (PZT) ceramics,[22] La addition to PMN has been shown to promote densification and through

hot uniaxial pressing, optically transparent materials have been achieved, allowing the determination of various optic and electro optic properties.[16] Our work in progress has also shown that similar densities to that of hot uniaxial pressing can be achieved by hot isostatic pressing.[17] Lanthanum additions to PMN have also been found to inhibit grain growth and thus compositions near the morphotropic phase boundary should result in fine grain materials with properties only achievable in conventional piezoelectric materials. In addition to the above, La additions further allow the flexibility in adjusting the Curie temperature without significantly effecting the order/disorder phenomenon or dielectric temperature behavior, thus making them promising candidates for dielectric/pyroelectric bolometers.

It is the purpose of this work to report the dielectric and piezoelectric properties of a wide range of lanthanum doped PMN-PT solid solutions.

EXPERIMENTAL PROCEDURE

Polycrystalline ceramic samples along the $(1\text{-}x)Pb(1\text{-}3/2y)\ (Mg_{1/3}Nb_{2/3})\text{-}xPbTiO_3\text{-}yLa$, as shown in Table I, were prepared by solid state reaction using the appropriate amount of reagent grade raw materials of lead carbonate $PbCO_3$,† magnesium carbonate $MgCO_3$,‡ titanium dioxide TiO_2,§ niobium pentoxide Nb_2O_5,‖ and lanthanum oxide La_2O_3.¶

Since it is well known that the formation of perovskite PMN is difficult to fabricate without the appearance of a parasitic pyrochlore phase ($Pb_3Nb_4O_{13}$), the columbite precursor method by Swartz and Shrout was used.[18,19] In the first stage a precursor columbite phase, $MgNb_2O_6$, was prepared by mixing MgO and Nb_2O_5 in stoichiometric ratio and calcining. In the second stage, the precursor was mixed in stoichiometric ratios with PbO, TiO_2 and La_2O_3. An excess of 0.5 weight percent PbO was added to compensate for PbO volatility during calcining and sintering. In processing the columbite precursor, the poor dispersion characteristics of MgO power can lead to insufficient mixing intimacy and thus incompletely reacted calcined power. To insure proper mixing, both steric hinderance (polyelectrolyte dispersant) an electrostatic repulsion (pH adjustment by ammonia) dispersion mechanisms were required to prepare a 25 vol. % slurry with deionized H_2O.[13] The slurry was vibratory milled, followed by drying and calcination at 1100°C for 4 hours. The calcined slug was pulverized using a hammermill and the appropriate amounts of PbO, TiO_2, La_2O_3 were added. A 30 vol. % slurry was prepared and vibratory milled followed by drying and calcination at 700°C for 4 hours. Both the columbite and subsequent PMN-PT-La calcined powders were examined by X-ray diffraction to insure phase purity. Less than 1% pyrochlore phase (compared to perovskite phase) was observed. To obtain yet a more uniform and reactive powder, the calcined PMN-PT-La powder was milled again as above.

†Hammond Lead Products, Inc., White Lead Grade HLPA (99%)
‡Fisher Scientific Co., Magnesium Carbonate Purified Grade
§Fansteel Metals, Nb_2O_5 Tech. Grade (99.5%)
‖Whittker, Clark and Daniels, TiO_2 Grade (99%)
¶Alfa Products Co., Lanthanum Oxide Grade (99.9%)

Discs were prepared using Polyvinyl alcohol (PVA) binder followed by burnout prior to sintering. Pellets of 16 mm in diameter and 2–3 mm thick were pressed at 10 Mpa. The binder was burned out by a slow heating process at 300°C for 90 minutes and at 500°C for 90 minutes consequently.

Compositions with $x = 0, 0.07, 0.20, 0.25, 0.30, 0.35, 0.40$ and $y = 0.01$ were sintered at 1100°C for 4 hours and 1200°C for 4 hours. Pellets were placed on platinum foil in an enclosed alumina crucible. To further reduce PbO volatility, sintering was performed in a lead rich atmosphere by placing a small amount of an equimolar mixture powder of PbO and ZrO_2 in a crucible. A heating rate of 900°C per hour was used to further help prevent PbO loss.

Weight loss, geometrical density and grain size were determined for all the various compositions and firings. Powder X-ray diffraction patterns of calcined and sintered powders were analyzed to determine the lattice parameters, appropriate structure, theoretical density and the presence of pyrochlore. The grain size was determined on fracture surfaces monitored by SEM.

In preparation for dielectric and piezoelectric measurements, sample discs were polished flat and parallel and electroded using sputtered on gold. An air drying silver paste was also applied to insure good electrical contact. The dielectric measurements were carried out on an automated system in which a temperature control box (Model 2300, Delta Design, Inc.) and LCR meter, (Model 4274A and Model 4275A LCR meter, Hewlett-Packard, Inc.). Both the dielectric constant and dissipation factor of unpoled samples were measured pseudo-continuously at various frequencies (0.1, 1, 10, and 100 kHz) as the samples were heated from −50°C to 220°C at a rate 2 to 4 degrees per minute. The dielectric measurements of poled samples were also carried out to see if any rhombohedral to tetragonal phase transition occurs near the MPB as observed in the undoped PMN-PT system. For ferroelectrics with diffused phase transitions, the law, $1/K - (T - T_c)^2$, is found instead of the normal Curie-Weiss Law,[5,20] from which the level of diffuseness (δ) of the phase transition was obtained.

TABLE I

Physical and dielectric properties of PMN-PT-La ceramics

Composition	Firing	ρ (g/cc)	Grain (μm)*	K_{max} (@ 100 Hz)	T_c (°C)	δ (°C)
PMN-01LA	1100°C 4 hrs.	7.81	2.0	8500	−33	62
	1200°C 4 hrs.	7.82	3.2	9700	−36	57
PMN-07PT-01LA	1100°C 4 hrs.	7.79	1.2	12000	−3	51
	1200°C 4 hrs.	7.80	2.4	16300	−6	43
PMN-20PT-01LA	1100°C 4 hrs.	7.80	0.7	15000	96	37
	1200°C 4 hrs.	7.81	1.6	25500	92	29
PMN-25PT-01LA	1100°C 4 hrs.	7.82	0.7	14800	119	37
	1200°C 4 hrs.	7.84	1.5	26600	115	28
PMN-30PT-01LA	1100°C 4 hrs.	7.77	0.7	10800	145	40
	1200°C 4 hrs.	7.80	1.7	23600	139	28
PMN-35PT-01LA	1100°C 4 hrs.	7.70	0.7	9300	162	—
	1200°C 4 hrs.	7.81	1.8	23200	153	—
PMN-40PT-01LA	1100°C 4 hrs.	7.82	0.6	9100	215	—
	1200°C 4 hrs.	7.85	1.6	12800	195	—

*intergranular fracture surface

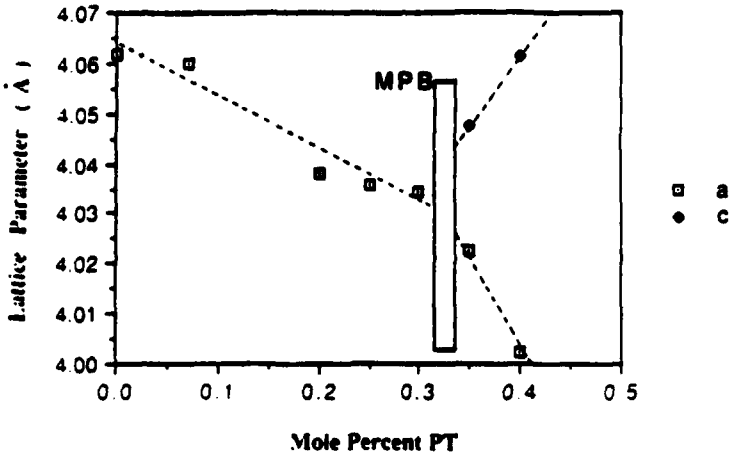

FIGURE 1 Lattice parameters as a function of composition.

In the case of piezoelectric measurements, poling was performed on selected samples by cooling from above the transition temperature in a stirred oil bath to room temperature in air with an applied field of 25 kv/cm. The piezoelectric coefficent, d_{33}, was measured on a Berlincourt d_{33}-meter (Model CPDT 3000, Channel Products, Inc.)

RESULTS AND DISSCUSION

Lattice parameter, density and grain size

As determined by XRD, less than 1% pyrochlore phase was detected for the various compositions. Also observed by slow scan XRD, splitting of the pseudo-cubic

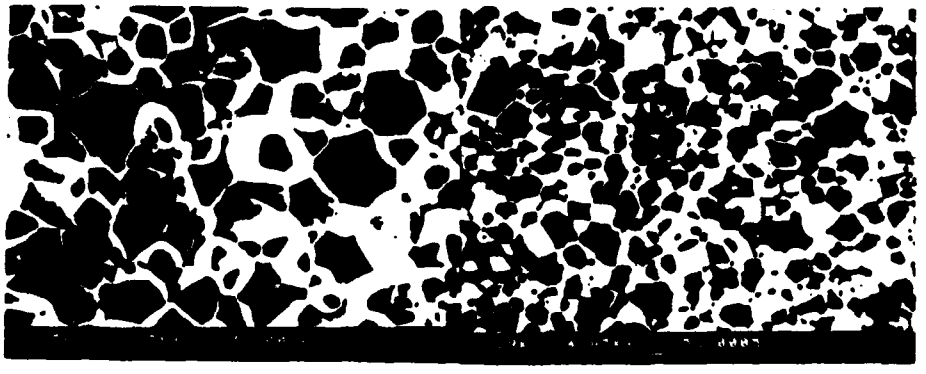

FIGURE 2 SEM photomicrographs of fractured surfaces of PMN-based samples fired 1100°C 4 hrs (left-PMN.; right-La doped PMN).

(rhombohedral) phase peak occurred in the 35 and 40 mole % PT compositions, as indicated in Figure 1; the plot of lattice parameters versus composition. This is evidence that the MPB between the rhombohedral and tetragonal phases lies between 30% and 35% PT, being similar to that observed by Choi *et al.* in the undoped PMN-PT system.[11]

Physical and dielectric properties for selected PMN-PT-La samples are reported in Table I. As tabulated, the resulted densities were greater than 95% theoretical, being 8.15 g/cc for PMN-01La. Also reported in Table I, La inhibited grain growth as expected. A narrow range in grain sizes (~ .5 μm to 3 μm) was found for all the various composition and firings. It is clearly evident that La-doped polycrystalline ceramics have smaller grain sizes than undoped polycrystalline ceramics.[13] Typical SEM photomicrographs of fractured surfaces are shown in Figure 2. As observed, grain sizes were reduced 5 μm to 2.4 μm for PMN and PMN-La, respectively.

Dielectric and piezoelectric properties

As shown in Figure 3, plots of the dielectric constant and loss as a function of temperature and frequency for compositions less than 35 mole % were characteristic of relaxor ferroelectrics with broad dielectric maximas. Also characteristic of relaxors, the dielectric maxima decreased and the peak transition temperature shifted upward with increasing frequency. The maximum of dielectric constant was also found to increase with increasing PT until 30 mole % PT at which above decreased, with the behavior becoming sharp and more normal or "ordered" ferroelectric like. No evidence of a rhombohedral to tetragonal phase transition in the K vs. T

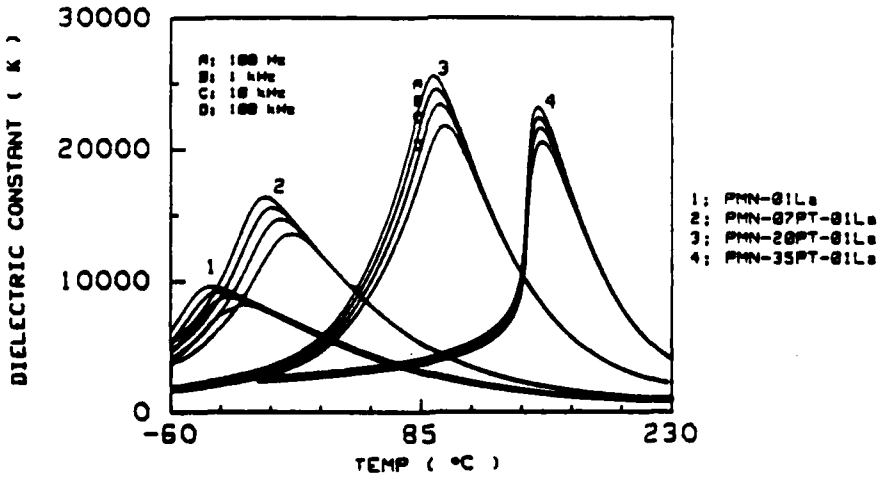

FIGURE 3 Dielectric constant K at various frequencies vs. temperature for PMN-PT-La compositions sintered at 1200°C/4 hours.

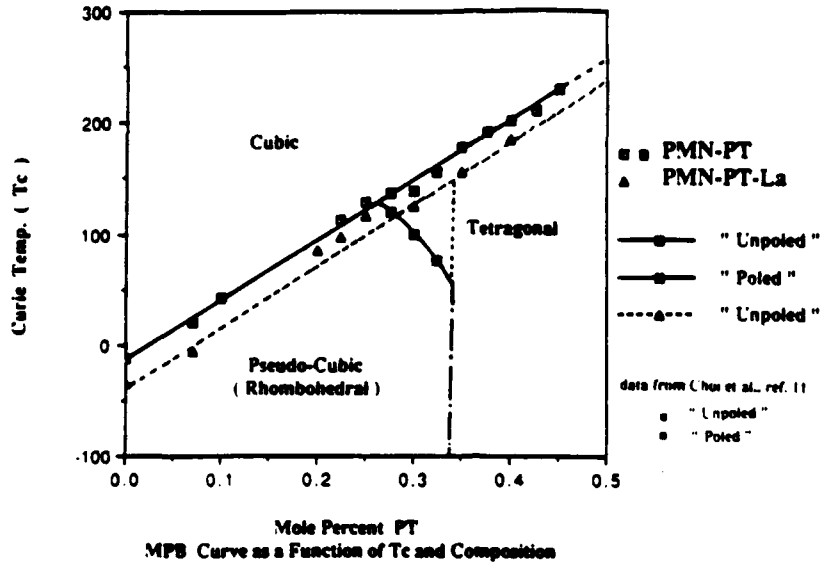

FIGURE 4 Phase diagram for PMN-PT (Choi *et al.*, Reference 11) and PMN-PT-La systems showing morphotropic phase boundaries (MPB).

plots of poled compositions near the MPB was observed as was found in the undoped PMN-PT system by Choi,[11] inferring a less curved morphotrophic boundary, as shown in Figure 4.

Presented in Table I and shown in Figure 3, the level of K_{max} was not only dependent on the amount of PT, but on the firing condition as well. With increased firing temperature and subsequent grain growth, K_{max} was found to be significantly increased. The grain size dependence of K is believed to be similar to that observed in undoped PMN-PT[13] and PLZT,[22] being the result of compositional gradients near the grain boundary resulting in regions highly stressed and disordered affecting the thermal orientation of polar micro-regions and thus a reduction in dielectric constant. Evidence of this model is depicted in Figure 5a, where near the grain boundary a large concentration of non-stoichiometric ordering of Mg:Nb cations (white regions) is observed. The *F*-spot superlattice, shown on Figure 5b, indicates the 1:1 Mg:Nb ordering.[21]

Variations in the level of K and shape of K vs. T curves, can also be directly related to the diffuseness coefficient, δ in Table I, which for relaxors reflects the level of disorder in terms of the broadness of the Curie maxima. Obviously no diffuseness coefficients were reported the 35 and 40 mole % PT compositions, since their K vs. T behavior reflected nearly "normal" ferroelectric behavior. As reported for many relaxors, the δ coefficient correlates well with the level of K_{max}, yet for given values of undoped PMN-PT, the values for La-doped PMN-PT are much smaller for equivalent K_{max}'s, inferring that La additions result in a reduction in K, while increasing the degree of ordering. It has been found in PMN-PT, that

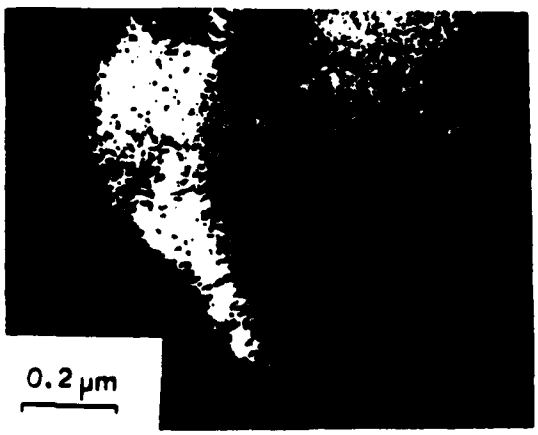

FIGURE 5a TEM analysis of PMN:La with white regions indicating non-stoichiometric ordering of Mg:Nb cations. Larger white region is near the grain boundary.

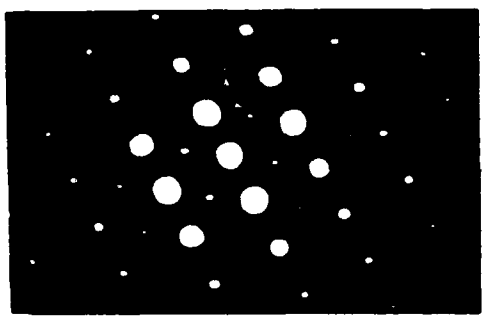

FIGURE 5b F-spot superlattice indicating 1:1 Mg:Nb ordering.

the degree of dielectric ordering can be varied through thermal annealing resulting in virtually no grain size dependency. Annealing studies have yet to be performed to determine whether or not the very fine grain samples can exhibit equivalent Ks. to that of large grain size samples.

Another effect of La doping was to shift the T_c downward, approximately 25°C/mole %, being reported in Table I and shown in Figure 6, where 1, 3 and 5 mole % additions of La was made to PMN-35% PT composition. Though the T_c shifts continuously downward, the general shape of the "normal" type ferroelectric behavior and level of K_{max} is nearly maintained. It is felt that such materials will be promising candidates for dielectric/pyroelectric bolometers, providing the needed high dielectric constants and large field induced pyroelectric coefficients required for thermal IR detectors, as discussed in Reference.[10]

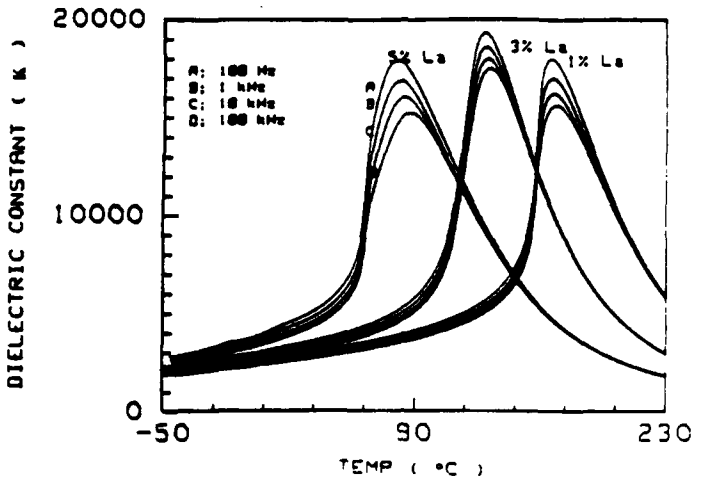

FIGURE 6 Dielectric constant K at various frequencies vs. temperature with increasing La in the PMN-35PT system sintered 1200°C 4 hours.

The values of the piezoelectric coefficient (d_{33}) for selected samples are reported in Table II. Compositions near the MPB showed maximas in the piezoelectric properties, with $d_{33} > 500$ pC/N, being slightly improved with annealing. Work is still ongoing to optimize firing and annealing conditions to further improve the piezoelectric properties.

SUMMARY

1. The addition of La_2O_3 to the PMN-PT relaxor ferroelectric system was found to promote densification and inhibit grain growth.
2. The effect of La-doping on the dielectric properties was to shift the T_c downward about 25°C/mole %. In addition the dielectric properties were strongly dependent on grain size. In contrast, La-doping resulted in slightly reduced K and more dielectric ordering.

TABLE II

Piezoelectric constant of PMN-PT-La ceramic

Composition	Piezoelectric Constant, d_{33} ($\times 10^{-12}$ C/N)		
	1100°C 4 hrs	1200°C 4 hrs	Annealed*
PMN-20PT-01LA	200 ~ 210	300 ~ 384	380 ~ 420
PMN-25PT-01LA	225 ~ 260	450 ~ 502	430 ~ 510
PMN-30PT-01LA	270 ~ 310	450 ~ 510	490 ~ 560
PMN-35PT-01LA	210 ~ 240	310 ~ 320	370 ~ 400
PMN-40PT-01LA	200 ~ 220	210 ~ 240	200 ~ 300

*Annealed 900°C 4 hours following sintering at 1200°C 4 hours.

3. The position of the morphotropic phase boundary in PMN-PT appeared not to be effected by the addition of La_2O_3. No evidence of a rhombohedral to tetragonal phase transition was observed near MPB.

4. Further additions of La_2O_3 could be used to dramatically shift the *Tc* downward without significantly changing the dielectric behavior.

5. Piezoelectric d_{33} coefficients > 560 pc/N for compositions near MPB were obtained. Current annealing studies have demonstrated the potential of fine grain materials possessing large piezoelectric activity.

All in all, La-doped PMN-PT type materials appear to be promising candidates for high K dielectrics, fine grain piezoelectrics, dielectric/pyroelectric bolometers and with hot uniaxial pressing suitable for electro-optic applications.

FUTURE AND ONGOING WORK

1. Preliminary work has demonstrated that transparent materials suitable for optical evaluation can be achieved by hot isostatic pressing without the restrictions of a pressure vessel (raws, die, sands etc.) required in hot uniaxial pressing.

2. Compositional tuning near the MPB to achieve optimal fine grain piezoelectric material.

3. Pyroelectric property measurements of selected compositions for potential pyroelectric/bolometers.

REFERENCES

1. G. A. Smolenskii and A. I. Agronovskaia, *Soviet Physics—Technical Physics*, **3**, 1380–82 (1958).
2. J. W. Smith Ph. D. Thesis, The Pennsylvania State University, University Park, PA. (1967).
3. W. A. Bonner, E. F. Dearborn, J. E. Geusic, H. M. Marcos and L. G. Van Uitert, *Appl. Phys. Lett.*, **10** [5], 163–65 (1967).
4. S. J. Jang, "Electrostrictive Ceramics for Electrostrictive Applications," Ph.D. Thesis, The Pennsylvania State University, University Park, PA (1979).
5. K. Uchino, S. Nomura, L. E. Cross and S. J. Jang, *Ceramics, J. Appl. Phys.*, **51**,[2] 1142–45 (1980).
6. L. E. Cross, S. J. Jang, R. E. Newnham, S. Nomura and K. Uchino, *Ferroelectrics*, **232**, 187–92 (1980).
7. S. J. Jang, K. Uchino, S. Nomura and L. E. Cross, *Ferroelectrics*, **27**, 31–34 (1980).
8. S. L. Swartz, T. R. Shrout, W. A. Schulze, and L. E. Cross, *J. Am. Cer. Soc.*, **67**, 311–15 (1984).
9. T. R. Shrout, A. Halliyal, *Am. Cer. Soc. Bull.*, **66**,[4] 704–11 (1987).
10. R. W. Whatmore, P. C. Osbond and N. M. Shorrocks, *Ferroelectics*, **76**, 351–67 (1987).
11. S. W. Choi, T. R. Shrout, S. J. Jang and A. S. Bhalla, to be published in *Ferroelectrics*.
12. J. KuWata, K. Uchino and S. Nomura, *Jpn. J. Appl. Phys.*, **21**,[9] 1298–02 (1982).
13. T. R. Shrout, U. Kumar, M. Megherhi, N. Yang and S. J. Jang, *Ferroelectrics*, **76**, 479–87 (1987).
14. S. Takahashi, A. Ochi, M. Yonezawa, T. Yano, T. Hamatsuki and I. Fukui, *Ferroelectrics*, **50**, 181–90 (1983).
15. K. Uchino, *Am. Cer. Soc. Bull.*, **65**,[4] 647–52 (1986).
16. D. McHenry, J. Giniewicz, S. J. Jang, A. Bhalla and T. R. Shrout, to be published in *Ferroelectrics*.
17. J. Giniewicz, D. McHenry, S. J. Jang and T. R. Shrout, to be published in *Ferroelectrics*.
18. S. L. Swartz and T. R. Shrout, *Mat. Res. Bull.*, **17**, 1245–1250 (1982).
19. S. L. Swartz and T. R. Shrout, *Mat. Res. Bull.*, **18**, 663–667 (1983).
20. T. Yamada, *J. Appl. Phys.*, **43**, 328 (1972).
21. A. D. Hilton, C. A. Randall, D. J. Barber and T.R. Shrout, to be published.
22. B. Jaffe, W. R. Cook, Jr. and H. Jaffe, "Piezoelectric Ceramics," Academic Press, London and New York (1971).

APPENDIX 20

journal

J. Am. Ceram. Soc., 72 [3] 481-83 (1989)

Dielectric Behavior of the Relaxor $Pb(Mg_{1/3}Nb_{2/3})O_3$–$PbTiO_3$ Solid-Solution System in the Microwave Region

Michael T. Lanagan,*,* Ning Yang, Dinesh C. Dube,† and Sei-Joo Jang*

Materials Research Laboratory, The Pennsylvania State University, University Park, Pennsylvania 16802

Dielectric behavior of the relaxor ferroelectric $Pb(Mg_{1/3}Nb_{2/3})O_3$–$PbTiO_3$ solid-solution system was studied from −50° to 200°C in the 100 to 12×10^9 Hz frequency region, and a broad dielectric relaxation was measured for compositions throughout the system. The relative microwave permittivity of the composition $0.9Pb(Mg_{1/3}Nb_{2/3})O_3\cdot0.1PbTiO_3$ decreased by 1 order of magnitude from the 1-MHz value of 11 800, and similar decreases were observed for other compositions in the system. Dielectric loss (tan δ) values ranged from 0.5 to 1.0 at microwave frequency. The temperature of the broad dielectric constant maximum shifts toward higher values with increased frequency. [Key words: titanates, lead, dielectric properties, microwaves, temperature.]

HIGH-DIELECTRIC-CONSTANT materials in the radio frequency and microwave frequency regimes are required for the growing needs of advanced microwave integrated circuits and high-speed computational systems. Microwave measurements of high-dielectric-constant materials will assist in materials selection for decoupling capacitors and electromagnetic interference filters that have operational frequencies approaching 1 GHz.[1-3] Perovskite ferroelectric relaxors have attracted a considerable amount of attention because of their large dielectric constants and electrostrictive strains. These materials have an advantage of relatively low processing temperatures, which are compatible with the sintering requirements of other materials in packaging devices.[4] One of the best-known materials in the lead-based relaxor family is $Pb(Mg_{1/3}Nb_{2/3})O_3$.[5,6] The lead magnesium niobate–lead titanate solid solution (herein designated PMN–PT) has several interesting compositional modifications,[7] and the low-frequency dielectric properties have been studied previously.[8]

Experimental Methods

Perovskite solid solutions of PMN–PT were prepared by a mixed-oxide route from reagent-grade $PbCO_3$, MgO, Nb_2O_5, and TiO_2. Precalcination of MgO and Nb_2O_5 was required to avoid pyrochlore formation in the final product.[9] The absence of pyrochlore phase formation was confirmed by powder X-ray diffraction (XRD). Ceramic specimens were sintered at about 1100°C to more than 95% of theoretical density.

Dielectric properties were measured through a broad frequency range from 100 Hz to 10 GHz. An automated bridge[‡] with a temperature controller[§] was used to measure the dielectric constant from 100 Hz to 1 MHz. Dielectric measurements in the microwave region were measured previously for lead zirconate and rutile, which have relatively low dielectric constants and losses.[10] These materials have dielectric constants that are over an order of magnitude lower than in the PMN–PT system. The measurement procedure for high-dielectric-constant materials is similar, although the equations for determining the permittivity from microwave transmission parameters are different.

Microwave dielectric measurements were conducted by a transmission technique. The specimens were machined to completely fill the cross section of an X-band rectangular waveguide. Scattering parameters in reflection and transmission, S_{11} and S_{21}, respectively, from the dielectric loaded waveguide were measured by a network analyzer.[¶] Experimental details have been discussed elsewhere,[10] and the following expression has been given for the complex permittivity, ε_r, in terms of S_{11} and S_{21}:[11]

$$\left(\frac{\gamma}{\gamma_0}\right)^2=\frac{(1-S_{11})^2-S_{21}^2}{(1+S_{11})^2-S_{21}^2} \qquad (1)$$

where $\gamma_0=(K_c^2-K_0^2)^{1/2}$ and $\gamma=(K_c^2-\varepsilon_r\cdot(K_0)^2)^{1/2}$. In Eq. (1), γ_0 and γ are the propagation constants of an air-filled and dielectric-filled waveguide, respectively; K_c is the cutoff wave number; and K_0 is the free-space wave number. Equation (1) has an eigenvalue solution, and a prior estimate of dielectric constant was conducted using a frequency difference technique.[12] The maximum standard deviation for dielectric constant and loss (201 measurements) at room temperature was 16% for all of the samples measured in the X-band.

The analytical procedure mentioned previously could not be extended to dielectric measurment as a function of temperature because of the large scatter in permittivity data which was exhibited by this technique. The temperature change caused a geometrical variation in the waveguide, which severely limited the accuracy of the S_{11} measurement. Dielectric measurement as a function of temperature was conducted using adjoining quarterwave matching plates of Teflon** on both sides of the sample in the waveguide. A similar procedure was utilized in the system $Ba_xSr_{1-x}TiO_3$,[13] and it had the advantage of requiring only the S_{21} measurement to obtain the dielectric constant. The use of quarterwave plates negated the swept frequency advantage of the transmission method discussed previously.

The network analyzer was first calibrated using a standard X-band calibration kit.†† The entire assembly was placed in a temperature chamber (controlled to ±1°C). Phase and attenuation of S_{21} were recorded at 10 GHz for each temperature, and the dielectric parameters were calculated for a sample of thickness l.

$$S_{21}=\exp(\gamma l) \qquad (2)$$

Equation (2) is solved for γ, from which the dielectric properties are calculated.[14] The measurement error between S_{21} measurements at separate temperatures was determined from uncertainty in the phase and magnitude of the network analyzer and was calculated for dielectric constant and loss to be 2% and 11%, respectively. Air gaps between the quarterwave plate and sample have a deleterious effect on the measurement accuracy, because of the unaccounted reflection at the Teflon–PMN interface.

Contributing Editor — D. J. Shanefield

Manuscript No. 199274. Received March 1, 1988; approved August 25, 1988.

Presented at the 90th Annual Meeting of the American Ceramic Society, Cincinnati, OH, May 5, 1988 (Electronics Division, Paper No. 119-E-88).

*Member, American Ceramic Society.

*Current address: Argonne National Laboratory, Argonne, IL.

†On leave from the Indian Institute of Technology, New Delhi, India.

‡Model 4274A and 4275A LCR meters, Hewlett-Packard Co., Palo Alto, CA.

§MK 2300 environmental control chamber, Delta.

¶Model 8510T, Hewlett-Packard Co.

**E.I. du Pont de Nemours and Co., Inc., Wilmington, DE.

††Model X7005B, Maury Microwave Corp., Cucamonga, CA.

Table I. X-Band Dielectric Properties Determined for Various Compositions at Room Temperature

Material	Dielectric constant	Dielectric loss
0.9 PMN-0.1 PT	1190	1.0
0.8 PMN-0.2 PT	620	0.7
0.7 PMN-0.3 PT	530	0.8
0.6 PMN-0.4 PT	620	0.7

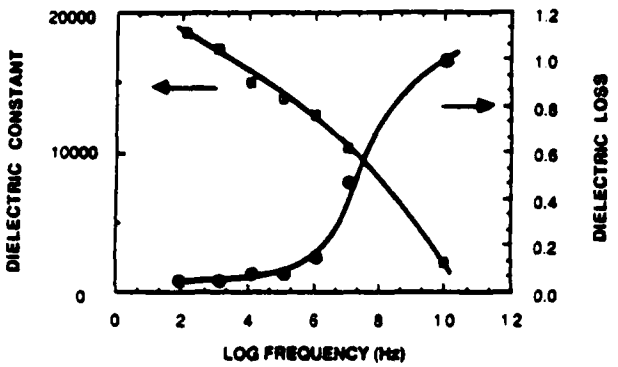

Fig. 1. Dielectric properties of 0.9PMN-0.1PT as a function of frequency.

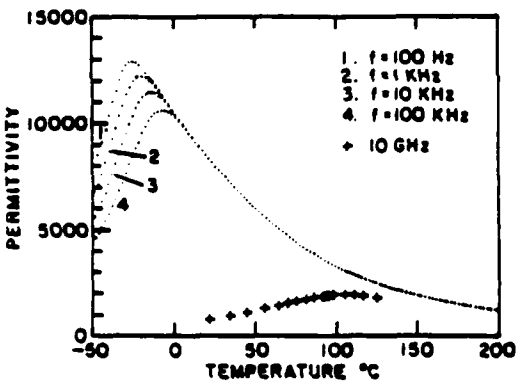

Fig. 2. Dielectric constant of PMN as a function of temperature for selected frequencies.

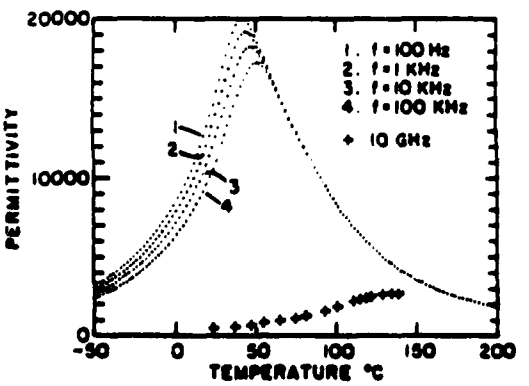

Fig. 3. Dielectric constant of 0.9PMN-0.1PT as a function of temperature for selected frequencies.

Results and Discussion

In the present study, five compositions were selected in the xPMN–$(1-x)$PT system, in which $x = 0.0$, 0.9, 0.8, 0.7, and 0.6. Dielectric constant and loss were calculated from measured S parameters using Eq. (1). A flat dielectric response in the 8- to 12-GHz region was observed at room temperature for all compositions, and the average dielectric constant and loss values are shown in Table I.

The dielectric properties of 0.9PMN-0.1PT calculated from Eq. (1) are shown in Fig. 1. A large relaxation was observed at low frequency and continued into the microwave range. The dielectric constant decreased by over 1 order of magnitude and the loss increased by a factor of 6 as frequency was increased from 1 MHz to 10 GHz. Similar relaxations were observed for other compositions in the PMN–PT solid-solution system.

Permittivity as a function of temperature and frequency for various compositions is shown in Figs. 2–6. The microwave dielectric constant was calculated from Eq. (2). A rapid decrease in the dielectric constant as a function of frequency and a corresponding increase in the dielectric loss were observed. The decrease in dielectric constant became more dramatic as the maximum temperature was approached. These experimental observations agree qualitatively with Khuchua's work on PMN.[15] As is characteristic with all ferroelectric relaxor materials, the temperature of dielectric constant maximum shifts toward higher temperatures with increasing frequency. The shifts in the microwave permittivity maxima for pure PMN and 0.9PMN-0.1PT are 113° and 87°C, respectively, from the 100-kHz value. It is believed that this transition occurs at temperatures greater than for 150°C for compositions with larger amounts of lead titanate and is greater than the temperature capability of our equipment.

The 0.7PMN-0.3PT composition exhibits a more complicated response at microwave frequency (10 GHz) as a function of temperature (Fig. 5). Measure-

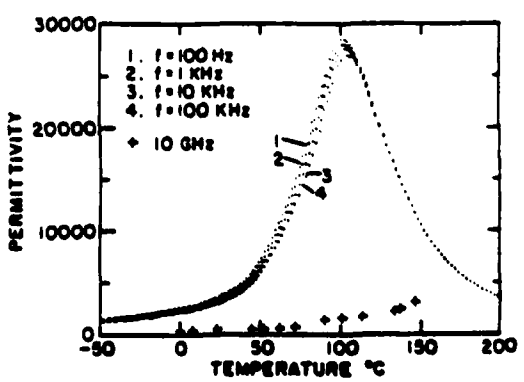

Fig. 4. Dielectric constant of 0.8PMN-0.2PT as a function of temperature for selected frequencies.

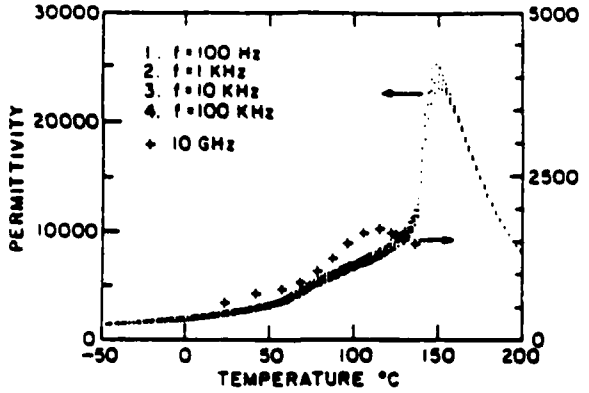

Fig. 5 Dielectric constant of 0.7PMN·0.3PT as a function of temperature for selected frequencies; 10-GHz data are plotted on an expanded scale for clarity.

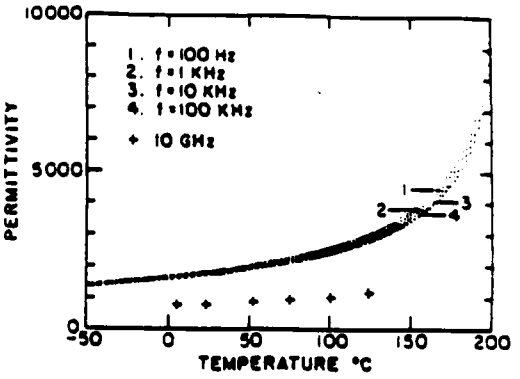

Fig. 6. Dielectric constant of 0.6PMN·0.4PT as a function of temperature for selected frequencies.

ments of other properties, such as X-ray and pyroelectric coefficients, suggest that the morphotropic boundary exists in the PMN–PT solid-solution system at about 0.32 mol% of PT content.[16] As temperature decreases, the 0.7PMN·0.3PT composition may experience the phase transition from cubic to tetragonal and subsequently to the rhombohedral structure. Verification of this phenomenon in samples close to the 0.7PMN·0.3PT composition is a subject of further research.

Conclusions

The relative dielectric permittivities for the PMN–PT solid-solution system show a response that is independent of frequency from 8 to 12 GHz, although a large dielectric relaxation was observed from 100 Hz to 10 GHz. The dielectric constants of all compositions decrease significantly at microwave frequency, and a corresponding increase in the dielectric loss was also observed. The broad temperature region of maximum permittivity for all compositions shifts toward higher temperatures as the measurement frequency increases, which implies that thermally activated processes are contributing strongly to the dielectric polarizability. Results on the 0.7PMN·0.3PT composition indicate that the morphotropic boundary may exist near this composition, which is in agreement with earlier studies.

Acknowledgments

The authors thank Drs. A. Bhalla and L. E. Cross for their helpful discussions and D. Laubacher for her low-frequency dielectric measurements.

References

[1]D. A. Chance, C.W. Ho, C. H. Bajorek, and M. Sampogna, "A Ceramic Capacitor Substrate for High Speed Switching VSLI Chips," *IEEE Compon., Hybrids, Manuf. Technol.*, 5, 368 (1982).

[2]T. C. Reiley, J. V. Badding, D. A. Payne, and D. A. Cance, "A Low-Temperature Firing Thick-Film Capacitor Material Based on Lead Iron Niobate/Tungstate," *Mater. Res. Bull.*, 19, 1543 (1984).

[3]I. G. Sarda and B. H. Payne, "Ceramic EMI Filters—A Review," *Am. Ceram. Soc. Bull.*, 67 [4] 737–46 (1988).

[4]M. Yonezawa, "Low Firing Multilayer Materials," *Am. Ceram. Soc. Bull.*, 62 [12] 1375–83 (1983).

[5]G. A. Smolenskii and A. I. Agronovuska, "Dielectric Polarization of a Number of Complex Compounds," *Sov. Phys. Solid State*, 1, 1429–37 (1959).

[6]T. R. Shrout and A. Halliyal, "Preparation of Lead-Based Ferroelectric Relaxors for Capacitors," *Am. Ceram. Soc. Bull.*, 66 [4] 704–11 (1987).

[7]S. J. Jang, "Electrostrictive Ceramics for Electrostrictive Applications", Ph.D. Thesis, Pennsylvania State University, University Park, PA, 1979.

[8]S. J. Jang, K. Uchino, S. Nomura, and L. E. Cross, "Electrostrictive Behavior of Lead Magnesium Niobate-Based Ceramic Dielectrics," *Ferroelectrics*, 27, 31–34 (1980).

[9]S. L. Swartz and T. R. Shrout, "Fabrication of Perovskite Lead Magnesium Niobate," *Mater. Res. Bull.*, 17, 1245–50 (1982).

[10]M. T. Lanagan, J. H. Kim, S. J. Jang, and R. E. Newnham, "Microwave Dielectric Properties of Antiferroelectric Lead Zirconate," *J. Am. Ceram. Soc.*, 71 [4] 311–16 (1988).

[11]L. P. Ligthart, "A Fast Computational Technique for Accurate Permittivity Determination Using Transmission Line Methods," *IEEE Trans. Microwave Theory Tech.*, MTT-31 [3] 249–54 (1983).

[12]M. T. Lanagan, J. H. Kim, D. C. Dube, S. J. Jang, and R. E. Newnham, "A Microwave Dielectric Measurement Technique for High Permittivity Materials," *Ferroelectrics*, 82, 91–97 (1988).

[13]J. G. Powles, "Measurement of High Permittivity Values at Centimeter Wavelengths," *Nature (London)*, 161, 25 (1948).

[14]A. R. von Hippel, Dielectric Materials and Applications; Chs. 2 and 5. MIT Press, Cambridge, MA, 1966.

[15]N. P. Khuchs, "Microwave Investigation of Some Ferro- and Antiferroelectrics of Perovskite Type", pp. 161–70 in Proceedings of International Meeting on Ferroelectricity, Prague, Yugoslavia, 1966.

[16]S. W. Choi, T. R. Shrout, S. J. Jang, and A. S. Bhalla, "Dielectric and Pyroelectric Properties of PMN–PT Solid Solution", unpublished work. □

APPENDIX 21

Ferroelectrics, 1988, Vol. 87, pp. 303–308
Reprints available directly from the publisher
Photocopying permitted by license only

STUDYING A FERROELECTRIC AT MICROWAVE FREQUENCIES

D. C. DUBE
Physics Department, Indian Institute of Technology, New Delhi 110016 (India)

S. J. JANG and AMAR BHALLA
Materials Research Laboratory, The Pennsylvania State University, University Park, PA 16802 USA

(Received 18 April 1988)

Microwave investigations of ferroelectric materials pose special problems because of their dielectric parameters. Special techniques are therefore required. A few techniques suitable for ferroelectric materials have been described. Typical results obtained from them are presented and discussed.

INTRODUCTION

Dielectric studies of ferroelectrics in the microwave region are important in view of possible applications of these materials in microwave circuits and devices. High frequency investigations not only support low frequency measurements but give additional information in many cases regarding polarization processes and associated loss mechanisms. The importance of high frequency measurements is further enhanced by the fact that a lot of experimental data is needed before a theory is developed to correctly explain and predict the microwave behavior of the ferroelectrics.

The high frequency dispersion of the dielectric constant in displacement type and ordered and disordered type ferroelectrics has been discussed by Smolenskii *et al.*[1] They have discussed the behavior of Barium Titanate and Triglycine Sulphate as protypes of the two types of ferroelectrics. The dielectric behavior of diffused phase ferroelectrics at microwave frequencies show some interesting features.[2–4] The dielectric constant at microwave fields decreases by an order of magnitude while the loss tangent increases by more than one order as compared to their low frequency values. In relaxor ferroelectrics like PMN–PT (lead magnetium niobate-lead titanate), the frequency response in 8–12 gigahertz (GHz) range is flat and the peak in ϵ' versus temperature shifts towards higher temperature as the frequency increases. These findings call for more work at microwave frequencies.

High frequency experimental studies pose some problems.[3–5] They may be due to the requirement of precise sample geometry in some cases and in others these may be the result of the often encountered typical combinations of dielectric parameters. Thus the use of special techniques becomes necessary. The purpose of this paper is to discuss some of the promising experimental methods and report the results by using them.

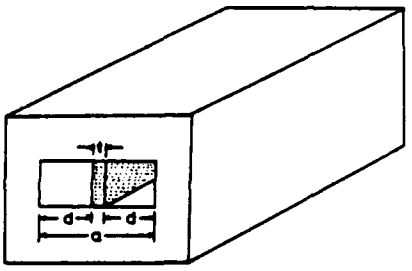

FIGURE 1 Sectional view of the specimen in position in the waveguide.

MEASUREMENT TECHNIQUES

The choice of measurement technique for the study of ferroelectrics in the microwave region is often decided by the magnitude of the dielectric parameters of the specimen. This is contrary to the practice at low frequencies wherein a single technique proves sufficient for a wide range of parameters.

Ferroelectrics having a low dielectric constant and moderate losses such as TGS and polymer like PVDF can be conveniently measured at microwave frequencies using inhomogeneously filled waveguide technique.[6,7] This measurement method is also suitable for studying ferroelectric films.

In this technique the specimen in the form of a thin sheet/wafer or film deposites on a substrate[8,9] is placed longitudinally at the centre of rectangular waveguide (Figure 1). The complex dielectric constant is calculated from the measured phase and attenuation introduced by the specimen. These quantities can be measured by adopting one of the experimental arrangements[6,7] depending on the availability of microwave equipment. A simple convenient design for sample holder wave guide is also available.[7]

Based on the geometry shown in Figure 1 the expressions for the dielectric constant (ϵ') and loss factor (ϵ'') are

$$\epsilon' = \frac{1}{k_0^2}\left(\beta^2 - \alpha^2 + \frac{a_1a_2 + a_2a_4}{a_3^2 + a_4^2} \cdot \frac{2}{td}\right)$$

$$\epsilon'' = \frac{1}{k_0^2}\left(2\beta\alpha - \frac{a_2a_3 - a_1a_4}{a_3^2 + a_4^2} \cdot \frac{2}{td}\right)$$

and the loss tangent,

$$\tan\delta = \frac{\epsilon''}{\epsilon'}$$

where $k_0 = \omega(\mu_0\epsilon_0)^{1/2}$ is the free space wave number (ω being the angular frequency of measurement), and

$$a_1 = d\ \mathrm{Re}\,(k_0^2 - r^2)^{1/2}$$

$$a_2 = d\ \mathrm{Im}\,(k_0^2 - r^2)^{1/2}$$

$$a_3 = \frac{2\sin 2a_1}{\exp(2a_2) + \exp(-2a_2) + 2\cos 2a_1}$$

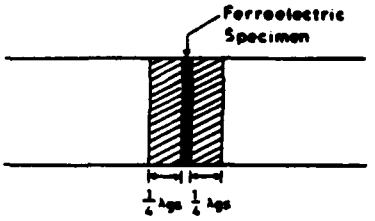

FIGURE 2 Specimen placed between Teflon quarter wave plates in rectangular waveguide.

$$a_4 = \frac{\exp(2a_2) - \exp(-2a_2)}{\exp(2a_2) + \exp(-2a_2) + 2\cos 2a_1}$$

and

$$\beta = \beta_p + \beta_0 \quad (\text{radians m}^{-1})$$

where

β_p = phase shift produced by the unit length of the specimen,

$\beta_0 = \dfrac{2\pi}{\lambda g}$ where λg is the guide wavelength in the empty guide,

$$\alpha = \frac{\text{attenuation (in db)}}{\text{length of specimen} \times 8.686} \quad (\text{nepers m}^{-1})$$

t = thickness of specimen, and

$d = (1/2) * (a - t)$, 'a' being the width of the waveguide (Figure 1)

In the above expressions, $r(=\alpha + j\beta)$ is complex propagation constant.

Diffused phase ferroelectrics exhibit dielectric constant of several hundred and varied losses in the microwave region. Such high permittivity materials when placed in a waveguide for measurement transmit insufficient microwave signal for generating accurate reproducible data. The transmission in such cases can be enhanced by the uses of quarter wave plates on either side of the specimen in the waveguide as shown in Figure 2.

Recently different compositions of PMN–PT were investigated using this technique.[4] A small waveguide section containing thin slabs of PMN–PT (thickness 0.2–2 mm) sandwiched between quarter wave plates of teflon was attached to a network analyser† for measurement. With the quarter wave plates alone in the guide, the network analyser was first calibrated for reflection and transmission using standard X-band calibration kit.‡

Dielectric constant ϵ' and loss tangent $\tan\delta$ were calculated using the following expressions.

$$\epsilon' = \lambda_0^2\left(\frac{1}{\lambda_c^2} + \frac{\beta^2 - \alpha^2}{4\pi^2}\right)$$

$$\tan\delta = \left(\frac{2\alpha\beta}{\beta^2 - \alpha^2 + 4\pi^2/\lambda_c^2}\right)$$

† Hewlett-Packard 8510T Network Analyser
‡ Model X7005E, Maury Microwave Corporation, California.

where λ_0 denotes the free space wavelength,

λ_c is the cutoff wavelength,

$$\beta = \frac{\text{measured phase (in degrees)} + 2\pi N}{\text{sample thickness}}, \text{ and}$$

$$\alpha = \frac{\text{measured loss (in db)}}{\text{sample thickness} \times 8.686}$$

Prior knowledge of the dielectric constant is required to choose the appropriate value of the integer N in Equation for β above. Therefore, dielectric constant was first estimated using a frequency method of measurement.[10]

It may be noted that the quarter wave plate is useful only at one frequency and negates the swept frequency advantage of transmission methods.

RESULTS AND DISCUSSION

Four different compositions of xPMN-$(1-x)$PT (where $x = 0.9, 0.8, 0.7, 0.6$) were selected for the present microwave studies. Figure 3 shows the room temperature permittivity and dielectric loss in 0.6PMN–0.4PT and 0.7PMN–0.3PT in the 8–12 GHz frequency region. These results were obtained from the frequency difference technique.[10] Other compositions of PMN–PT showed similar behavior. The flat frequency response of PMN–PT is in tune with the true nature of ferroelectric relaxors.

Figure 4 illustrates the permittivity of 0.9PMN–0.1PT at 10 GHz as a function of temperature. A broad dielectric maximum at 140°C is observed. For comparison, Figure 4 also contains low frequency data which exhibits less broad maxima in the vicinity of 50°C. These results are significant and suggestive of dominance of thermally activated processes in these ferroelectrics.

Dielectric maxima were not observed for PMN–PT compositions containing higher than 10 mole percent of PT because these maxima perhaps lie beyond our upper temperature limit for measurement, which is 150°C.

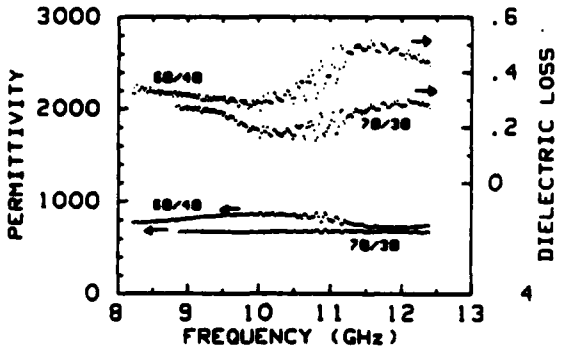

FIGURE 3 Dielectric properties of 60/40 and 70/30 PMN–PT ceramics in the microwave region at room temperature.

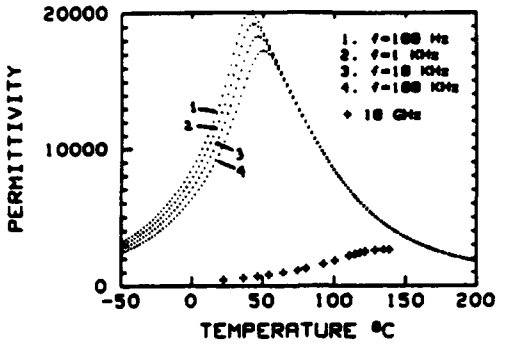

FIGURE 4 Temperature dependance of the dielectric permittivity of 0.9 PMN–0.1 PT ceramic at microwave (10 GHz) and low frequencies 100 Hz, 1 KHz, 10 KHz and 100 KHz.

The dielectric response of 0.7PMN–0.3PT as a function of temperature is more complex and reveals some interesting features. At 10 GHz, a dielectric peak is observed around 110°C (Figure 5). This is attributed to the presence of morphotropic boundary in 0.7PMN–0.3PT system. X-Ray and pyroelectric studies[11] also indicate the existence of such a phase boundary. As the temperature goes down from well above the Curie point 70/30 composition may experience the phase transition from Cubic to tetragonal and to rhombohedral structures. Low frequency dielectric studies of this composition also reflect the possible transition from cubic to tetragonal and tetragonal to rhombohedral phase changes around 150° and 70°C respectively. In this respect the well formed peak at 110°C in the microwave permittivity of 0.7PMN–0.3PT (Figure 5) is unique and demonstrates the vestality of the technique.

Plots shown in Figure 1 were obtained as mentioned earlier by frequency difference technique. Scatter in experimental data is seen which increased at higher temperatures. Therefore temperature studies were conducted with quarter

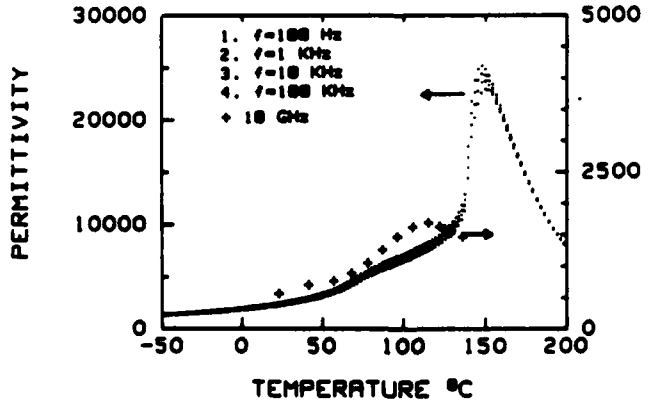

FIGURE 5 Dielectric permittivity of 0.7PMN–0.3PT at microwave (10 GHz) and low frequencies. (note the different scale for microwave data).

wave plates but then the investigations were restricted to a single frequency for obvious reasons.

A perturbation technique was recently developed for the study of low permittivity materials.[12] Work is in progress to develop a modified perturbation technique suitable for wide range of materials including high permittivity ferroelectrics. This work will be reported separately.

The authors wish to dedicate this paper to Prof. L. E. Cross who has inspired not only us but scientists all over the world in their endeavour to investigate ferroelectric materials. One of the authors (DCD) wants to make a special mention of the support he received from Prof. Cross while working at MRL. His (DCD) contribution to this paper reflects his indebtedness to Prof. Cross.

ACKNOWLEDGEMENTS

The authors thank Prof. S. C. Mathur (IIT Delhi) for helpful discussions.

REFERENCES

1. G. A. Smolenskii, V. A. Bokov, V. A. Isupov, N. N. Krainik, R. E. Pasynkov and A. I. Sokolov, "Ferroelectricity and Related Materials" Editor-in-Chief: G. A. Smolenskii, Vol 3, Gordon and Breach Science Publishers (1986).
2. N. P. Khuchua in Proceedings of the International Meeting on Ferroelectricity, Institute of Physics of the Czechoslovak Academy of Sciences, Prague p. 161 (1966).
3. Yu. M. Poplavko, ibid p 171 (1966).
4. M. T. Lanagan, N. Yang, D. C. Cube and S. J. Jang, *Am. Ceram. Soc. Bull.* (1988). To appear.
5. J. G. Powles and W. Jackson, *Proc. IEEE* **96**, 383 (1949).
6. D. C. Dube and R. Natrajan, *J. Appl. Phys.* **44**, 4927 (1973).
7. D. C. Dube, M. T. Lanagan and S. J. Jang, *J. Am. Ceram. Soc.* **70**, C-278 (1987).
8. D. C. Dube, R. Natrajan and V. K. Tripathi, *Indian J. Phys.* **52A**, 405 (1978).
9. R. Natarajan, D. C. Dube and V. K. Tripathi, *Indian J. Phys.* **52**, 567 (1978).
10. M. T. Lanagan, J. H. Kim, D. C. Dube, S. J. Jung and R. E. Newnham, *Ferroelectrics* (1988). To appear.
11. S. W. Choi, T. R. Shrout, S. J. Jang and A. S. Bhalla. To be published.
12. D. C. Dube, M. T. Lanagan, J. H. Kim and S. J. Jang, *J. Appl. Phys.* **63**, 2466 (1988).

APPENDIX 22

"LEAD BASED $Pb(B_1B_2)O_3$ RELAXORS VS $BaTiO_3$ DIELECTRICS FOR MULTILAYER CAPACITORS"

Thomas R. Shrout and Joseph P. Dougherty
Materials Research Laboratory
The Pennsylvania State University
University Park, PA 16802

ABSTRACT

Historically, $BaTiO_3$-based dielectrics have been the material of choice for multilayer capacitors (MLCs). Recently, compositions in the perovskite family having the general formula $Pb(B_1B_2)O_3$, known as relaxor ferroelectrics, have generated considerable interest. Their high dielectric constants, broad maxima, low E-field dependency, and low firing temperatures, as compared to conventional $BaTiO_3$-based dielectrics, make them attractive materials for MLCs. However, the complexities involved in the fabrication of MLCs makes it difficult to accurately compare the two families of dielectrics. In order to help in this comparison, the results from a questionnaire addressing the various issues of MLC manufacturing was prepared. The compiled results represent the collective opinion of more than 40 manufacturers and researchers throughout the world, including Japan, Korea, China, Europe, and the U.S. The status of relaxors and how they "stack up" against the well established $BaTiO_3$ dielectrics are discussed.

INTRODUCTION

Historically, the primary materials utilized for Class II multilayer capacitors (MLCs) have been modified $BaTiO_3$ and other various titanates.[1] Great strides in the capacitor industry in the overall reliability,* cost and compactness (F/cm^3) of MLCs have been made as a result of the demands put on them by the continuing miniaturization and rapidly growing integrated circuit technology. The increased reliability of MLCs has been the result of an enormous amount of research on understanding the various microstructural-property relationships as correlated to the overall MLC manufacturing process, including powder processing, thin sheet formation, metallurgical interactions, electrical testing and screening, etc. In addition, novel fabrication techniques and automation have led to vastly increased yields and cost reductions. Further reduction in costs have come from ways to eliminate the necessity for precious metal internal electrodes.[2]

Decreases in electrode cost have been accomplished by (1) addition of fluxes to reduce the sintering temperature, thereby allowing the use of less expensive Ag:Pd alloys; (2) use of non-noble metals, such as Ni and Cu, which require a reducing atmosphere during firing;[3,4] and (3) lead injection, in which molten lead is impregnated into porous layers to act as the electrode, also known as the fugitive phase process.[5] Though (2) and (3) may result in substantial metal cost reductions, their inherently more sophisticated processes may result in reduced yields and poorer reliability. In addition, ~ 25 μm is the minimum layer thickness achievable in the fugitive phase, lead-injected process being limited by the overall mechanical integrity.

*Reliability is defined as the probability of which a capacitor will perform its specified function, under a set of external conditions for a specified period of time.

To increase the capacitance volumetric efficiency (~ K/t^2) for a given Electronics Industry Association's (E.I.A.) specification, e.g., Y5V, Z5U, X7R, etc., efforts to maximize the dielectric constant K and manufacturing processes to reduce the thickness (t) of the active dielectric layer to significantly less than 25 μm have been made. Thin layers of $BaTiO_3$-based materials have been prepared by wet stacking methods with fine powders. However, intrinsic electrical characteristics of $BaTiO_3$ (a.c. and d.c. electric field effects on loss and K) usually preclude thin layer capacitors of these materials from meeting present day E.I.A. standards.

Limitations on achieving high dielectric constant and thin layers, simultaneously, in $BaTiO_3$-based capacitors, has led researchers to focus on other types of families of dielectric materials. Perovskite ferroelectric relaxors* is one such family.(6)

A chemical class of particular interest for MLCs are the lead based (PbO) relaxors having the general formula $Pb(B_1B_2)O_3$ where B_1 is typically a low valence cation, e.g., Mg^{+2}, Zn^{+2}, Fe^{+3}, Ni^{+2}, and Sc^{+3} and B_2 a high valence cation, e.g., Ti^{+4}, Nb^{+5}, Ta^{+5}, W^{+6}.(7) Characteristics of relaxor ferroelectrics that make them attractive candidates for MLCs include: 1) anomalously large dielectric constants (K > 20,000; 2) broad dielectric maximas or diffuse phase transition, and relatively low firing temperatures that allow the use of low cost Ag:Pd electrodes. The dielectric behavior for a $Pb(Mg_{1/3}Nb_{2/3})O_3$ [PMN] based relaxor is shown in contrast to a normal ferroelectric $BaTiO_3$ and a representative high K modified $BaTiO_3$ composition [Fig. 1]. Obvious disadvantages of relaxors, however, for use in MLCs include their strong dependence of dielectric properties on frequency and high dielectric loss below the Curie range or T_C. Also, having only a single transition does not allow for the possibility of dielectric stability over a wide temperature range necessary for a X7R type capacitor. Not shown is the E-field dependency. Relaxors have the advantage over $BaTiO_3$-based dielectrics in their E-field/capacitance percent change ($\Delta C/C/E$) being significantly lower.

To date numerous relaxor compositions being proposed for capacitor use are based on a wide variety of solid solutions comprised of relaxor and normal type ferroelectric perovskite end members as well as a variety of modifiers. Additional compositions are referred to in references 7 and 8 (see Table I). Representative examples and their associated E.I.A. designation are presented in Table II.

Table I. Commonly Employed Perovskite End Members for Relaxor-Based MLCs.

Complex Perovskites	*T_c (°C)	**Behavior	Simple Perovskites	T_c(°C)	Behavior
[PMN]	-10	Relaxor-FE	$PbTiO_3$	490	FE
[PZN]	140	Relaxor-FE	$PbZrO_3$	230	AF
[PNN]	-120	Relaxor-FE	$BaTiO_3$	130	FE
[PFN]	110	Normal-FE	$SrTiO_3$	---	Para
[PFW]	-95	Relaxor-FE			
[PMW]	38	AF			
[PNW]	17	AF			

*Transition temperatures for relaxors are averages or at 1 kHz.
**FE-Ferroelectric, AF-Antiferroelectric, Para-Paraelectric.

[PMN]:	$Pb(Mg_{1/3}Nb_{2/3})O_3$	[PFW]:	$Pb(Fe_{2/3}W_{1/3})O_3$
[PZN]:	$Pb(Zn_{1/3}Nb_{2/3})O_3$	[PMW]:	$Pb(Mg_{1/2}W_{1/2})O_3$
[PNN]:	$Pb(Ni_{1/3}Nb_{2/3})O_3$	[PNW]:	$Pb(Ni_{1/2}W_{1/2})O_3$
[PFN]:	$Pb(Fe_{1/2}Nb_{1/2})O_3$		

*The term "relaxor" is used herein to designate all PbO-based complex perovskites though many may not exhibit the strong dielectric frequency dispersion characteristic of relaxor ferroelectrics. As such, these materials, e.g., $Pb(Fe_{1/2}Nb_{1/2})O_3$, show dielectric and related behavior more similar to $BaTiO_3$-based dielectrics.

Table II. Compositional Families for Relaxor-Based MLCs

Composition	EIA Temp Specification	Manufacturer (Assignee)	Patents and Refs.
PLZT-Ag	X7R	Sprague	U.S. Pat. 4,027,209 (1973) Ref. 9
PMW-PT-ST	X7R	DuPont	U.S. Pat. 4,048,546 (1973)
PFN-PFW	Y5V	NEC	U.S. Pat. 4,078,938 (1978)
PFN-PFW-PZN	Y5V	NEC	U.S. Pat. 4,236,928 (1980)
PFN-PMT	—	TDK	U.S. Pat. 4,216,103 (1980)
PMN-PT	Y5V	TDK	U.S. Pat. 4,265,668 (1981)
PMN-PFN	Y5V	TDK	U.S. Pat. 4,216,102 (1980)
PMN-PFN-PMW	Y5V	TDK	U.S. Pat. 4,287,075 (1981)
PFW-PZ	Z5U	TDK	U.S. Pat. 4,235,635 (1980)
PFW-PT-MN	Z5U	Hitachi	U.S. Pat. 4,308,571 (1981)
PMN-PZN-PT	Z5U	Murata	U.S. Pat. 4,339,544 (1982)
PFN-PFW-PbGe (MSC)	X7R		Ref. 10
PFN-PFM-PNN	Z5U, Y5V	Ferro	U.S. Pat. 4,379,319 (1983)
PMW-PT-PNN	Z5U	NEC	U.S. Pat. 4,450,240 (1984) Ref 11
PFN-Ba Ca(CuW)-PFW	Y5V	Toshiba	U.S. Pat. 4,544,644 (1985) Ref 12
PMN-PZN	Z5U	STL	U.K. Pat. 2,127,187A (1984)
PMN-PFN-PT	Z5U	STL	U.K. Pat. 2,126,575 (1984)
PMN-PZN-PFN	Z5U	Matshshita	Japan Pat. 59-107959 (1984)
PMN-PFW-PT	—	Matsushita	Japan Pat. 59-203759 (1984)
PNN-PFN-PFW	Y5V	Matsushita	Japan Pat. 59-111201 (1984)
PZN-PT-ST	—	Toshiba	Ref. 13
PMN-PFN-PbGe	Z5U	Union Carbide	U.S. Pat. 4,550,088 (1985)
PFN-PNN	Y5V		Ref. 14
PFW-PFN (MSC)		NTT	Refs. 15-17
PMN-PT-PNW	Z5U	Matsushita	Ref. 18
PMW-PT-PZ	X7R	NEC	Ref. 19
PZN-PMN-PT-BT-ST	Z5U	Toshiba	Japan Pat. 61-155245 (1986)
PZN-PT-BT-ST	X7R	Toshiba	Japan Pat. 61-250904 (1986)
PZN-PMN-BT	Y5U, Y5S	Toshiba	Ref. 20
PMN-PLZT	Z5U	MMC	U.S. Pat. 4,716,134 (1987)
PMN-CT, ST, BT	Z5U	Matsushita	Japan Pat. 62-115817 (1986)
PFW-PFN-PT	Y5V		Ref. 21
BT-PMN-PZN (MSC)	X7R, X7S	Toshiba	U.S. Pat. 4,767,732 (1988)
PMN-PS-PNW-Ca (Base Metal)	Z5U	Matsushita	Refs. 22-23

It was the purpose of this paper to review the status of lead-based relaxors in the world of multilayer capacitors and how they "stack up" against the well established $BaTiO_3$-based dielectrics. To assist in the evaluation, a questionnaire addressing the various issues associated with MLC manufacturing from powder processing through electrical testing and product usage, was prepared and sent to various capacitor manufacturers and university researchers in the field of dielectrics. Geographically, respondents included the U.S. (23), Europe (8), and the Far East (Japan (7), Korea (3), and China (2)) many of which are included in the acknowledgements. Based upon the responses to our survey we found a tendency to praise the attributes of relaxors even though their companies may not be making this product. The results reported are ones of a general concensus and not of an individual nature.

MULTILAYER CAPACITOR FABRICATION

Details of the processing and fabrication of multilayer capacitors is reviewed in references 3 and 24. A generalized flow chart for the manufacturing of MLCs is presented in Fig. 2. As shown, the process was broken down into various sections as follows: 1) powder processing; 2) multilayer fabrication; 3) densification/characterization; 4) finishing; 5) electrical testing; 6) end product analysis; and 7) applications. In each section, $BaTiO_3$ dielectrics will be compared to relaxor type materials used in multilayer capacitors. In addition, some results were grouped geographically.

Powder Processing

Raw Materials/Cost

The overall cost of dielectric powders is only ~ 5% of the total cost of an MLC, however, it is still deemed important in this highly competitive industry. First of all, in comparing $BaTiO_3$ with relaxor-based dielectrics, the lower density of $BaTiO_3$-based materials (~ 6 g/cc), or approximately 75% of relaxor's density (~ 8 g/cc) results in more MLCs per unit weight of powder. Secondly, the cost of powders depends on the purity and process by which it is produced, for example, conventional oxide processing vs. chemical preparation techniques. Cost also varies from individual components to a packaged dielectric formulation. In the U.S. and Europe, the average cost of $BaTiO_3$ based materials is ~ 6$/kg using conventional powder technology. Relaxor formulations are typically somewhat more expensive, mainly due to the cost of Nb_2O_5, one of the primary components. To date, only a few powder manufacturing houses offer relaxor-based dielectrics, with their costs being substantially higher (~ 20 - 30$/kg). In China, the availability of Nb_2O_5 as a natural resource makes relaxor based capacitors very inexpensive and is one of the driving forces by which relaxor based MLCs have been in place for more than 20 years.[25] In contrast, Japanese MLC manufacturers' powder costs are upwards of 10 to 40$/kg, being slightly higher for relaxors. The higher costs are the result of high purity and chemically prepared powders which are typically used. It is widely believed that the use of such powders ultimately improves the overall reproducibility and yields.

Powder Handling/Toxicity

PbO-containing materials are usually regarded as highly toxic and a major environmental issue. This is particularly true in Europe and the U.S. The well-established piezoelectric industry, which is primarily based on PZT, has already dealt with the concerns of PbO toxicity and its environmental issues. Most manufacturers and device users already handle toxic materials that abound in the manufacturing process, and as such, precautions for the use of heavy metals have already been addressed.

The toxicity of PbO in relaxors, however, remains a major concern and their use in existing MLC manufacturing facilities requires substantial capital investment to meet air quality and waste requirements. With proper precautions, no problems in the handling and manufacturing of relaxor based MLCs dielectrics have been found.

Calcination/Reactivity

Many relaxor based ferroelectrics, $Pb(Mg_{1/3}Nb_{2/3})O_3$ [PMN] for example, are difficult to prepare in the perovskite form without the appearance of pyrochlore phase(s). The appearance of pyrochlore has been found to be strongly related to the refractory nature of the B-site cation oxides [MgO in PMN] in relation to the other phases in the PbO-Nb_2O_5 binary system. Ceramic processes that improve the reactivity of the refractory oxide(s) such as better mixing/milling and dispersability, enhance the formation of the perovskite phase.[7,26]

$BaTiO_3$-based materials generally require higher calcination temperatures (> 1100°C) although calcining temperatures equivalent to that of relaxors (~ 700-900°C) can be achieved for chemically and conventionally (with additives) prepared $BaTiO_3$ dielectrics. However, PbO stoichiometric problems as a result of volatility and reaction with saggers is of great importance for relaxors. In some cases, to help minimize PbO loss, more costly

specialized saggers, e.g., MgO are used. In addition, to help eliminate the possibility of second phases such as pyrochlore, the well known columbite precursor method[27] is often used, resulting in an overall increase in reproducibility but with some additional costs.

To obtain the desired particle size/distribution for multilayer fabrication, wet milling of the calcined powders requires knowledge of the powder characteristics. The inherently softer relaxor based powers mill to a given particle size more efficiently than the high temperature calcined $BaTiO_3$ powders. In fact, it has been reported that submicron Pb-based perovskite powders can be produced using only conventional raw materials without milling.[28] This is an important consequence if one wishes to obtain submicron powders necessary for ultra-thin MLCs.

Multilayer Fabrication

Thin Sheet Formation and Binder Burnout

In the fabrication of MLCs, several techniques to fabricate thin sheets are used, including tape casting and various wet lay down processes.[24] The latter is more suited for the ultra-thin layers down to ~ 10 μ. Whichever technique is used, different intrinsic problems for each dielectric chemistry exist, with no significant advantages or disadvantages found for either system.

Subsequent to thin sheet formation virtually no differences in terms of lamination and dicing or binder burnout between the two dielectric systems are found.

Densification/Characterization

Sintering/Atmosphere Control

The firing conditions for various $BaTiO_3$ and relaxor-based systems are outlined in Table III. As presented, $BaTiO_3$ dielectrics can be subdivided into three groups: (1) high fire (HF) > 1250°C; (2) medium fire (MF) ~ 1100-1250°C; and (3) low fire (LF) < 1100°C, with relaxors subdivided into two groups (1) HF > 1000°C and (2) LF < 1000°C. Naturally, these

Table III. Firing conditions for various types of $BaTiO_3$ and relaxor-based MLCs.

Dielectric	Firing Condition		Electrode	
HF-BT	>1250°C	(air) (reducing)	Pd Ni*	(100%)
MF-BT	1100-1250°C	(air) (reducing)	Ag:Pd Cu, Ni	(70/30 to 30/70)
LF-BT (R&D only)	<1100°C	(air)	Ag:Pd	(70/30)
HF-Relaxor	>1000°C	(air) (reducing)	Ag:Pd Cu,	(70/30)
LF-Relaxor	<1000°C	(air) (reducing)	Ag:Pd (85/15), Ag (100%) Cu,	

*The partial pressure pO_2 at which Ni ---> NiO occurs is such that PbO ---> Pb_{metal} results, hence Ni-based electrodes are thermodynamically not feasible for relaxors.

latter systems using base metal electrodes must be fired in reducing well-controlled atmospheres, using sophisticated and costly furnaces. In general, HF $BaTiO_3$ capacitors can readily be fired in air whereas systems fluxed with Bi or Pb require atmosphere control usually accomplished with seasoned ZrO_2-based firing sands. Firing sands of similar composition to that being sintered work well for controlling the PbO atmosphere of relaxors, but are not practical in production.

Though certain relaxor-based formulas can be sintered at temperatures less than ~ 900°C in open air, overall most relaxors require some kind of PbO atmosphere control. The PbO stoichiometry, whether deficient or excess is probably one of the most important factors in relation to the ultimate physical and electrical characteristics of relaxors. The control of the PbO atmosphere is one of the biggest concerns of manufacturers. To compensate for PbO volatility, excessive amounts of PbO are sometimes added which aids in sintering and allows the samples to be fired in open air. However, poor overall uniformity in the distribution of PbO throughout the samples, along with problems of PbO deposits in the kilns and environment, typically occurs. As in the calcination step, the use of modern furnaces, specialized setters and saggers (MgO) allow better control of PbO atmosphere and ultimately product reproducibility.

Microstructure

The importance of microstructural features on the ultimate properties of $BaTiO_3$-based materials has long been an issue. Problems such as exaggerated grain growth as found for Ba:Ti ratios < 1, have been solved. Grain size variations do exist, but generally in a controlled manner to help meet specific capacitor designations. Typically, high K (K > 10,000) Y5V capacitors have grain sizes in the range of ~ 5-10 μ, medium K (6,000-10,000) Z5U's having grain sizes ~ 5 μ and low K (2000-4000) X7R bodies with grain sizes in the range of 1-3 μ. Naturally, control of the grain size and distribution of such will be of utmost importance in the manufacturing of MLCs with ≤ 10 μ layers.

As in $BaTiO_3$-based materials, the microstructure of relaxor dielectrics is strongly related to the compositional stoichiometry and, in particular, to the PbO stoichiometry. Compositions deficient in PbO tend not to fully densify and form pyrochlore. Compositions with excess PbO often result in a wide range of grain sizes (1-20 μ) with varying amounts of free PbO in the grain boundaries and triple points.[29-32] Such variations in microstructure correspondingly result in variations in the dielectric properties. If care is taken throughout the processing of relaxors, however, resulting microstructures can be quite uniform with grain sizes in the range of 1-2 μ.[33] Further additives such as La, have been shown to inhibit grain growth in PMN-based relaxors to less than 1 μ, while maintaining a high dielectric constant K > 10,000.[34] The fact that fine grain (≤ 1 μ) relaxor dielectrics can maintain very high dielectric constants is a distinct advantage to that of $BaTiO_3$-based ceramics and of considerable consequence for ultra-thin MLCs.

Mechanical Strength[*]

Probably the one most critical factor concerning the development and implementation of relaxor based MLCs is the fact that they are, in general, approximately 50-80% weaker than their $BaTiO_3$ (BT) counterparts. The mechanical strengths of various $BaTiO_3$ and relaxor type dielectrics can be generally ranked as follows:

> HF-BT (X7R) > MF-BT (X7R) > HF-BT (Z5U) > MF-BT (Z5U) ~ HF Relaxor (Y5U or Z5U) > LF Relaxor (Y5V or Z5U)

As evidenced by intergranular fracture the poor mechanical strength of relaxors is believed to be associated with the relatively weak amorphous grain boundary phase found in these

---

*Mechanical strength comparisons are based on 3-point bending fracture tests. Reported values are in the range of 30-70 MPa. A more relevant means of comparison is made through the toughness of materials, being proportional to the strength for a given flaw size. The toughness of PMN-based materials are reportedly in the range of ~ 0.6-1.0 MPa $m^{1/2}$ as compared to $BaTiO_3$ (~ 0.8-1.5 MPa $m^{1/2}$).[35,36]

materials. Recent work in Japan has suggested that the mechanical strength can be markedly improved by the substitution of the Pb^{+2} cation with Ba, Sr, Ca, or La.

It is important to remember that the mechanical strength of an MLC is not only related to the dielectric itself but to the integrity of the entire structure including the bonding strength between the metal electrode and dielectric, tendency for delaminations, MLC design and defects induced during other processing steps such as electrode termination and final finishing. At present, though mechanically inferior to $BaTiO_3$, the strength of relaxor based MLCs is adequate for many applications. However, their weaker mechanical integrity makes it difficult to successfully use them in surface mount technology (SMT) with current generation assembly machines.

Electrode Interactions

As stated, electrode problems associated with $BaTiO_3$-based MLCs, e.g., Pd --> PdO, Pd-Bi reactions, have been addressed. In high Ag:Pd (70:30) electrodes used in all systems, the problem of Ag migration and Ag volatility, is a concern. In relaxor-based MLCs, some of which use pure Ag electrodes the problem of Ag migration (or dissolution), volatility and possible reactivity with Pb needs to be investigated.

Finishing

Electrode Termination and Packaging

Prior to electrode termination, MLCs are corner rounded to help insure good electrical contact and for cosmetic reasons as well. Corner rounding of $BaTiO_3$ based MLCs usually requires somewhat longer times than for relaxors due to barium titanate's inherently higher mechanical strengths.

The termination electrode inks developed for $BaTiO_3$ MLCs are usually incompatible with relaxor-based materials. Their high firing temperatures (> 800°C) tend to result in undesirable chemical reactions between Pb and the glass frits used in the inks. Termination electrodes compatible with Pb-based materials are required and work in this area is presently underway. Problems associated with lead attachments in relaxor based MLCs may also be related to termination electrode incompatibility and the poor mechanical strength of these materials. For the most part, plating techniques for electrode termination can be made to work adequately for both types of dielectrics, although PbO-based systems require more stringent requirements as was found in the PZT industry.

Electrical Testing

The MLC is a major cause of circuit failures in modern electronic systems and devices. Thus, the testing of MLCs is one of the most important parts of the manufacturing process.

Capacitance/Loss

Determination of the room temperature capacitance value and loss at 1 KHz is performed automatically on every MLC manufactured; a few manufacturers 100% test for insulation resistance (IR). The temperature coefficient of capacitance (TCC) and appropriate EIA designation (Z5U, X7R, etc.) is done on a sampling basis. To compare and contrast relaxor and $BaTiO_3$ dielectrics in terms of capacitance, one actually needs to compare their capacitance volumetric efficiency. For simplicity, the dielectric constants available in these materials will be used for comparison assuming similar active layer thicknesses can be achieved. Further, comparison of the two dielectrics will be based on specific EIA designations as given in Table IV. Except for X7Rs, relaxor-based dielectrics have higher dielectric constants for a given TCC designation. Data for Y5□ systems is shown in Fig. 3. To meet X7R specifications for a dielectric having only a single, yet broad, dielectric transition is expectedly difficult and as such, relatively few X7R relaxor-based compositions have been developed. Examples given in Table II are generally based on antiferroelectrics, e.g., PLZT and $Pb(Mg_{1/2}W_{1/2})O_3$ [PMW]. In addition, relaxor dielectrics comprised of incompletely reacted phases or mixed sintered ceramics (MSC) have been developed. Such processes are somewhat related to the

chemically inhomogeneous "grain core shell structures" associated with many $BaTiO_3$ dielectrics developed to meet X7R temperature requirements.[37]

The dielectric loss (dissipation factor) of relaxors below T_C are found to be generally higher than that in normal ferroelectrics (see Fig. 1). However, most relaxor-based dielectrics are compositionally adjusted such that the T_C is well below room temperature, hence resulting in very low room temperature loss values. For example, loss values < 0.5% for high K -Y5V materials can be achieved. This is of considerable consequence for dielectric layers less than 10 μ. At this thickness and at the measurement standard of 1 Vrms @ 1 KHz, the loss of $BaTiO_3$-based MLCs may become unacceptably high.

Aging

The degree of aging in relaxors varies depending on composition and associated T_C. As with dielectric loss, room temperature aging can be reduced by shifting the T_C downward so as to be more in the paraelectric region. Typical aging rates for various $BaTiO_3$ and relaxor-based dielectrics are reported in Table IV. As presented, the determined aging rates are quite similar, however, dielectric aging in relaxors is strongly dependent on the composition and stoichiometry, particularly with excess PbO, acceptor dopants and the overall defect structure.[38] In other words the aging rate is very process dependent, and aging rates > 10%/dec have been observed.

Table IV. Electrical Characteristics of $BaTiO_3$ and Relaxor-Based Dielectrics for Multilayer Capacitors

*EIA Designation	Material	K (25°C, 1 Vrms @ 1 kHz)	Loss	RC @ 125°C (ΩF)	BDV v/μ	Aging (%/Decade)
Y5V	$BaTiO_3$	8,000-15,000	<4%	~ 1,000	~ 20-30	<5
	Relaxor	> 20,000	0.5-2%	~ 5,000	~ 15-30	1-3
Z5U	$BaTiO_3$	5,000-10,000	<3%	~ 1,000	~ 25-35	2.0-5.0
Y5U	Relaxor	10,000-20,000	0.5-2%	~ 5,000	~ 20-35	0.5-2.0
X7R	$BaTiO_3$	2,000-3,500	<1.5%	---	~ 30-40	0.5-2.5
	Relaxor	2,000-4,000	<1.5%	---	~ 25-35	1-3
Y5 □, R, S, T	Relaxor	3,000-7,000				

*EIA Characteristics:

Temperature:	Low:	Z, Y, X (+10, -30, -55°C)
	High:	5, 7, (+85, 125°C)
Max. Cap. %: Change		R, S, T, U, V, (±15%, ±22%, (+22, -33%), (+22, -56%), (+22, -82%)

The aging behavior of relaxors is also of particular concern. In relaxors, the anticipated log-linear relationship, observed for normal $BaTiO_3$ type ferroelectrics may not hold.[39,40] It has been reported that in the early stages, aging can occur at an anomalously fast rate (~ 10%/dec) before leveling out to ~ 3%/dec after the initial 1000 minutes to what appears to be a linear region. Since most capacitor manufacturers, determine aging rates between 10 to 1000 hrs, much of the vital aging information in relaxors could be overlooked. Examples of this can be found in relaxor compositions reported to have their TCCs improved by the addition of various dopants, e.g., MnO_2, which give rise to a large depression or saddle in the capacitance temperature behavior due to competing aging and TCC effects.

E-Field Dependency

For a given K, relaxors have significantly smaller E-field (a.c. or d.c.) dependency as compared to $BaTiO_3$-based dielectrics,[9,12,19,21,41] as shown in Fig. 4. This lower sensitivity to E-field in relaxor ferroelectrics is related to the level of bias required to overcome the energy (kT)

of thermally fluctuating microdomains which contribute to the dielectric polarizability.[6] Naturally, improved E-field dependency is desirable for MLCs comprised of ultra-thin layers.

Breakdown Strength (BDS)

In general, the breakdown strength of polycrystalline dielectrics is approximately inversely proportional to the level of K. As expected, and reported in Table IV, the (BDS) of relaxors is somewhat lower than that for $BaTiO_3$-based capacitors, however, the values are within acceptable limits. It is important to remember that the BDS is strongly related to various defects, and overall uniformity of the MLC.

Insulation Resistance (RC product)

The broad spectrum of compositional types of dielectrics for both relaxor and $BaTiO_3$ MLCs makes it difficult to contrast their respective RC products. For the most part, RC products for relaxors are greater than that for $BaTiO_3$ dielectrics, and less sensitive to temperature as shown in Fig. 5. However, relaxor-based dielectrics comprised of cations with multiple valence states such as in $Pb(Fe_{1/2}Nb_{1/2})O_3$ and $Pb(Fe_{2/3}W_{1/3})O_3$ tend to have lower values. As with many of the dielectric properties, values of RC are also related to processing, e.g., low values are observed when excessive amounts of PbO are present.

Degradation/Life Testing

Overall, it is difficult to state whether relaxors show less degradation than $BaTiO_3$ dielectrics, since the reliability of an MLC may depend on many variables including impurities, porosity, internal electrode material, MLC design, structural defects, etc. Poor degradation and/or life test failures tends to correlate well in relaxor based MLCs that exhibit low RC values, as stated above. However, relaxor MLCs that exhibit satisfactory degradation and life testing in dry atmosphere may not in wet/humid conditions. This behavior is believed to be the result of electrolytic Ag migration along microcracks, a problem related to relaxors inherent mechanical weaknesses.[42] For the most part, research in the basic origin and understanding of degradation in relaxors has yet to be performed.

End Product

Yields

The overall yield for any MLC is related to many variables, including the technical level, experience, and process controls in manufacturing, As such, $BaTiO_3$-based dielectrics have a distinct advantage. Present yields for $BaTiO_3$ MLCs are in the range of 80 to 95% whereas relaxors are ≤ 80%.

Costs

As with yields, there are many factors that affect the overall cost of an MLC. One of the biggest driving forces to use relaxor based materials are their large K, low firing temperatures and compatibility with less expensive Ag:Pd electrodes. Based on the same manufacturing, our respondents stated that the overall cost of a relaxor capacitor is somewhere between 20 to 50% lower than that of high firing $BaTiO_3$, of similar capacitance. $BaTiO_3$ MLCs with base metal electrodes, however, are reported to be less expensive than relaxor MLCs. The possibility that base metals may be used with relaxors also exists, as stated earlier.

Figure of Merit

In order to better accurately contrast MLCs, a "figure or merit," which relates the amount of coulombs/cm^3 and/or coulombs/$ for capacitors is needed.

A qualitative figure of merit which encompasses many of the important parameters of an MLC and associated fabrication processes was formulated by Yamashita[8] given as:

$$\text{Figure of Merit} = \frac{K \times BDS \times RC @ 125°C}{TCC \times G.S. \times \text{Sintering Temperature}}$$

From this expression, the desirable qualities of an MLC are clearly expressed. MLCs with high K, BDS and RC product at 125°C infer high capacitance volumetric efficiency, low loss and less susceptibilty to degradation. In addition, it has been reported that there is a good correlation between BDS and mechanical strength.[43] A low TCC not only implies temperature stability of capacitance, but connotes stability against E-field and frequency. Possessing a small grain size (G.S.) implies good mechanical strength and uniformity as well as the possibility of utilization in ultra-thin layers. A low sintering temperature obviously implies overall lower costs. This figure of merit was a first attempt and can be further improved based on the specific needs and requirements of various device applications, whereby certain parameters in the expression may be weighted in terms of their importance.

Based on this expression and the results presented thus far, relaxor based MLCs (Y5V and Z5U) possess the higher figure of merit with normalized values* in the range of 200-1000 being nearly an order of magnitude more than $BaTiO_3$ counterparts. This result is contrary to the fact that only a few companies now manufacture relaxor based MLCs and may suggest that a different figure of merit is used in the market place.

Applications

Military/Commercial

Applications for MLCs are usually classed into two groups 1) military and 2) commercial, with the former having much more stringent voltage ratings, temperature stability, and reliability requirements. MLCs most commonly used in military applications are the highly reliable $BaTiO_3$-based X7Rs, a class present-day relaxors have yet to invade. Commercially, most capacitors are used in computer and telecommunications type applications, where cost and capacitance volume efficiency are the most important issues and as such relaxor-based MLCs may have an advantage, although problems still exist for use in SMT. In addition, for unconventional applications, such as in multicomponent packaging, the low firing temperature, and chemical compatibility of relaxors with existing substrate materials allows them to be co-fired and thus incorporated into these hybrid structures.[44-46] Relaxor ferroelectric materials are also being widely investigated and used for a variety of piezoelectric sensors and electrostrictive actuators.[47]

Operational Parameters

Important operational parameters for MLCs are their voltage capabilities and frequency of operation. Below 1 MHz, both $BaTiO_3$ and relaxor-based MLCs show similar performance and for dielectrics with Ks above 2000, they both have problems in high loss at higher frequencies. Frequency limitations are not an issue in applications such as bypass and bulk decoupling. The voltage capability of an MLC is strongly related to the K, loss and BDS of the material. As such the voltage rating for relaxor MLCs is generally somewhat lower than $BaTiO_3$-based MLCs.

Based on overall performance, relaxors may never replace the high reliable, $BaTiO_3$-based X7R MLCs. Applications utilizing the low fire X7R bodies, may be replaced by relaxor Y7S bodies (K ~ 3000-6500) which have considerable advantages in terms of cost and capacitance volume efficiency. The main target of relaxors in today's market are the low cost, Z5U and Y5V type markets. In Japan, it is believed that much of this market will be substituted by relaxors within the next 10 years although this time frame will probably be longer in the U.S. and Europe.

*The figure of merit expression was normalized in terms of K/1000, BDS (v/μm), RC @ 125°C (1000/ΩF), TCC (max % ΔC/°C), G.S. (μm), and sintering temperature (T/1000).

SUMMARY

The complexities involved in the fabrication of MLCs makes it difficult to accurately compare families of dielectrics. Given this, to the best of our knowledge, the comparison between relaxor and $BaTiO_3$-based dielectric materials, as reported by our respondents can be summarized as follows:

1) In general, relaxors exhibit a higher K, lower loss, less E-field dependency and higher RC @ 125°C as compared to their $BaTiO_3$-based counterparts.

2) In terms of manufacturing, the cost of the raw materials used for relaxors is somewhat more than that for $BaTiO_3$ dielectrics, but low cost electrodes, can result in overall reduced costs. $BaTiO_3$-based MLCs which utilize low cost base metal electrodes, however, are reported to be less costly to manufacture.

3) The many disadvantages associated with the manufacturing of relaxor MLCs, including PbO toxicity/handling, atmosphere control, reactivity (pyrochlore formation), electrode interaction, etc., are historical in nature, and may be overcome with time, many have already been addressed.

4) Probably the biggest disadvantage of relaxor-based dielectrics are their mechanical strength and toughness being ~ 50 to 80% of that for $BaTiO_3$, which may limit their usage in SMT and military applications.

5) Certain capacitor type designations, e.g., X7R, are difficult to achieve with relaxor formulations, thus, requiring manufacturers to process contrasting materials. Also, the most adequate TCC designations for relaxors are Y7 □ and Y5 □ (□ = RSTUV), whereas the two most commonly accepted today are X7R and Z5U.

6) In the ultimate fabrication of MLCs with dielectric layers < 10 μ, relaxors look most promising. Their relative ease of powder reduction to submicron size without utilizing nonconventional powder processing, small G.S., high K, low E-field dependency of K and loss, make them very attractive. In fact, relaxor-based MLCs with an active dielectric thickness of only 6 μ with twice the volume efficiency of tantalum electrolytic capacitors has been reported.[44]

7) Ultimately, the lowest cost for a reliable component will be the figure of merit that decides whether relaxors will be substituted for $BaTiO_3$ in any application.

ACKNOWLEDGEMENTS

The authors wish to thank all those who took time out from their busy schedules to answer the questionnaire. The following is a partial list of industries and universities from which the responses came from; USA: Radio Materials, Corning, North American Philips, TAM, AVX, E.I. DuPont de Nemours, Sprague Electric, San Fernando Electronic Manufacturing, Spectrum Control, Rogers, Ferro, Erie-Murata, Centre Engineering, Transelco, Kemet, Centralab, Vitramon, ALCOA, Alfred University, and North Carolina State University; Europe: A.F. Ioffe Physia-Technical Institute, Philips Gmbh Furslungsloboutorium, Cookson Group, Plessey, Institute des Sciences de la Matiere, ENS Ceramique Industrielle, Ecole Polytechnique, Centre National D'Etudes, and Rhone-Poulenc Chimie de Base; Japan: Nippondenso, Murata, TDK Electronics, Marcon Electronics, Toshiba, Matsushita Electric Industrial, and Mitsubishi Mining and Cement; China: Huazhong University of Science and Technology and Xian Jiaotong University; and Korea: Seoul National University and Samhwa Condenser.

A special thanks goes to Joyce Baney for her help in putting together the questionnaire and this manuscript.

REFERENCES

1. J.M. Herbert. "Ceramic Dielectrics and Capacitors," Electrocomponent Science Monographs, Vol. 6, Gordon and Breach, NY (1985).
2. W.R. Buessem and T.I. Prokopowicz. "Electrode and Materials Problems in Ceramic Capacitors," Ferroelectrics, 10, 225-30 (1981).
3. J.M. Herbert. "Method of Making Ceramic Dielectric Material," U.S. Pat. 2, 934, 442 (1959).
4. I. Burn and G.H. Maher. "High Resistivity $BaTiO_3$ Ceramics Sintered in CO-CO_2 Atmospheres," J. Mater. Sci., 10, 633-640 (1975).
5. T.L. Rutt and J.A. Syne. "Fabrication of Multilayer Ceramic Capacitor by Metal Impregnation," IEEE Trans. Parts, Hybrids, Packaging, PHP-9 (1973).
6. L.E. Cross. "Relaxor Ferroelectrics," Ferroelectrics, 76, 241-267 (1987).
7. T.R. Shrout and Arvind Halliyal. "Preparation of Lead-Based Ferroelectric Relaxor for Capacitors," Amer. Cer. Soc. Bull., 66:704-711 (1987).
8. Y. Yamashita. "Lead Based Dielectrics for Multilayer Capacitors," New Ceramic Series, No. 3, pp. 94-99 (Gakukenshu, publisher) (in Japanese) (1988).
9. G. Maher. "Effect of Silver Doping on the Physical and Electrical Properties of PLZT Ceramics," J. of Amer. Cer. Soc., 66, 408-413 (1983).
10. S.J. Jang, W.A. Schulze, and J.V. Biggers. "Low Firing Capacitor Dielectrics in the System $Pb(Fe_{2/3}W_{1/3})O_3$-$Pb(Fe_{1/2}Nb_{1/2})O_3$-$Pb_5Ge_3O_{11}$," Cer. Bull., 62, 216-218 (1983).
11. K. Utsumi, A. Ochi, and M. Yonezawa. "Small Y5V Chip-Capacitors with Very Large Capacitance," Proc. 4th US-Japan Seminar on Dielectric and Piezoelectric Ceramics," Washington, DC (1988).
12. Y. Yamashita, S. Mukaeda, K. Inagaki, N. Ohba, and K. Handa. "Medium Voltage Large Capacitance Multilayer Ceramic Capacitors Employing Lead Perovskite Ferroelectric Material," Jpn. J. Appl. Phys., 26, Suppl. 26-2, 87-89 (1987).
13. Y. Yamashita, O. Furukawa, M. Harata, T. Takahashi, and K. Inagaki. "A New Lead Perovskite Y5S Dielectric for Multilayer Ceramic Capacitor," Jpn. J. Appl. Phys., 24, 1027-29 (1985).
14. T.R. Shrout, S.L. Swartz, and M.J. Haun. "Dielectric Properties in the $Pb(Fe_{1/2}Nb_{1/2})O_1$-$Pb(Ni_{1/3}Nb_{2/3})O_3$ Solid Solution System," Am. Ceram. Soc. Bull., 63[6], 808-810, 820 (1984).
15. H. Takahara and K. Kiuchi. "Dielectric Properties of Mixed-Sintering Ceramics in the System $Pb(Fe_{2/3}W_{1/3})O_3$-$Pb(Fe_{1/2}Nb_{1/2})O_3$," Advanced Cer. Mat., 1, 346-349 (1986).
16. H. Takahara. "Preparation and Dielectric Properties of Mixed-Sintering Ceramics (MSC)," Jpn. J. Appl. Phys., 24, Suppl. 24-2, 427-429 (1985).
17. K. Sakata and H. Takahara. "Liquid Phase Sintering of Mixed Sintering Ceramics Using $Pb(Li_{1/4}Fe_{1/4}W_{1/2})O_3$," Jpn. J. Appl. Phys., 26, Suppl. 26-2, 83-86 (1987).
18. J. Kato, Y. Yokotani, M. Nishida, S. Kawashima, and H. Ouchi. "Dielectric Properties of $Pb(Mg_{1/3}Nb_{2/3})Ti(Ni_{1/2}W_{1/2})O_3$ Ceramic," Jpn. J. Appl. Phys., 24, Suppl. 24-3, 90-92 (1975).
19. M. Yonezawa, M. Miyauchi, K. Utsumi, and S. Saito. "A New Low Firing X7R Multilayer Ceramic Capacitors," High Tech Ceramics, ed., P. Vincenzini, Elsevier Science Publishers, Amsterdam (1987).
20. O. Furukawa, M. Harata, Y. Yamashita, K. Inagaki, and S. Mukaeda. "A Lead Perovskite Y5U Dielectric for Multilayer Ceramic Capacitor," Jpn. J. Appl. Phys., 26, Suppl. 26-2, 34-37 (1987).
21. G.-F. Chen and S.-L. Fu. "Low Firing Y5V Relaxor Multilayer Ceramic Capacitors," IEEE Trans. Comp., HYB., and Manu. Tech., 12, 91-95 (1989).
22. J. Kato, Y. Yokotani, and H. Kagata. "Resistance to Reduction of a Lead-Based Perovskite and its Application to Multilayer Capacitor with Copper Electrode," Ferroelectrics (to be published).
23. J. Kato, Y. Yokotani, H. Kagata, and H. Niwa. "Multilayer Ceramic Capacitor with Copper Electrode," Jpn. J. Appl. Phys., 26, 90-92 (1987).

24. J.H. Adair, D.A. Anderson, G.O. Dayton, and T.R. Shrout. "A Review of the Processing of Electronic Ceramics with an Emphasis on Multilayer Capacitor Fabrication," J. of Mat. Ed., 9:71-118 (1987).
25. Y. Xi. "Ceramic Capacitor in China, Past Record and Perspective," Proc. 6th IEEE Int. Symp. Appl. Ferroelectrics," Lehigh, PA, 352 (1986).
26. T.R. Shrout, B. Jones, J.V. Biggers, and J.H. Adair. "Enhanced Processing of Perovskite $Pb(Mg_{1/3}Nb_{2/3})O_3$ Relaxors Through Understanding the Surface Chemistry of the Component Powders," Ceramic Powder Science, II, A, eds. G. Messing, E. Fuller, Jr., and H. Hausmer, 519-527 (1988).
27. S.L. Swartz and T.R. Shrout. "Fabrication of Perovskite Lead Magnesium Niobate," Mater. Res. Bull., 17, 1245-50 (1982).
28. T. Takagi, K. Anetami, and K. Shimiza. "Lead-Containing Oxide Powder," U.S. Pat. 4,812,426 (1989).
29. E. Goo and G. Thomas. "Microstructure of Lead-Magnesium Niobate Ceramics," J. Am. Ceram. Soc., 69[8], C-188-C-190 (1986).
30. H.C. Wang, W.A. Schulze, and P.F. Johnson. "SEMS Characterization of the Role of Excess PbO and MgO in Lead Magnesium Niobate," presented at 87th Annual Meeting, The American Ceramic Society, Chicago, IL (1986).
31. K.Z. Babi-Kishi and D.J. Barber. "Application of Transmission Electron Microscopy to Studies of Pb-Rich Second Phase Particles in Perovskite $Pb(Sc_{1/2}Ta_{1/2})O_3$ Ferroelectric Ceramics," presented at the International Symposium on the Applications of Ferroelectrics, Zurich, Switzerland (1988), Ferroelectrics (to be published).
32. A. Hilton. "Transmission Microscopic Characterization of Ferroelectric Relaxors," Ph.D. Thesis, Essex University, United Kingdom (1989).
33. T.R. Shrout, U. Kumar, M. Megherhi, N. Yang, and S.J. Jang. "Grain Size Dependence of Dielectric and Electrostriction of $Pb(Mg_{1/3}Nb_{2/3})O_3$-Based Ceramics," Ferroelectrics, Vol. 76, 479-487 (1987).
34. N. Kim, W. Huebner, S.J. Jang, and T.R. Shrout. "Dielectric and Piezoelectric properties of Lanthanum-Modified Lead Magnesium Niobium-Lead Titanate Ceramics," presented at the International Symposium on the Applications of Ferroelectrics, Aug. 29-Sept. 1, 1988, Zurich, Switzerland, accepted for publication in Ferroelectrics.
35. M.H. Megherhi. "The Effect of Additives, Microstructure, and Macrostructure on the Fracture Behavior of Lead Magnesium Niobate-Based Ceramic Actuators," M.S. Thesis, The Pennsylvania State University (1988).
36. S.W. Freiman and R.C. Pohanka. "A Review of Mechanically Related Failures of Ceramic Capacitors and Capacitor Materials," Proceedings of the Center for Dielectric Studies Symposium on Improvement of Multilayer Capacitor Reliability, 199-218 (1989).
37. D. Hennings and G. Rosenstein. "Temperature-Stable Dielectrics Based on Chemically Inhomogeneous $BaTiO_3$," J. Am. Ceram. Soc., 67, 244-54 (1987).
38. T.R. Shrout, W. Huebner, C.A. Randall, and A.D. Hilton. "Aging Mechanisms in $Pb(Mg_{1/3}Nb_{2/3})O_3$-Based Ferroelectrics," presented at the International Symposium on the Applications of Ferroelectrics, Zurich, Switzerland (1988), Ferroelectrics (to be published).
39. W. Pan, T.R. Shrout, and L.E. Cross. "Modeling the Aging Phenomena in 0.9 PMN:0.1 PT Relaxor Ferroelectric Ceramics," J. of Mat. Sci. Lett. (in press).
40. W.A. Schulze and K. Ogiro. "Review of Literature on Aging of Dielectrics, Ferroelectrics, 87, 361-377 (1988).
41. W.A. Schulze. "Dielectric Properties of $PbZrO_3$-$PbTiO_3$-La_2O_3," Ph.D. Thesis, The Pennsylvania State University (1973).
42. H.C. Ling and A.M. Jackson. "Correlation of Silver Migration with Temperature-Humidity-Bias (THB) Failures of Multilayer Ceramic Capacitors," IEEE Trans. Comp, Hybrids, and Manuf. Tech., 12, 130-133 (1989).
43. A. Kishimoto, K. Koumoto, and H. Yanoyida. "Comparison of Mechanical and Dielectric Strength Distributions for TiO_2 Ceramics," Cer. Soc. of Japan, 96[9], 954-957 (1988).

44. T. Yasumoto, N. Iwase, and M. Harata. "High Dielectric Constant Y5U Thick Film Capacitors Based on Relaxor," Proc. 4th U.S.-Japan Seminar on Dielectric and Piezoelectric Ceramics, Oct. 30-Nov. 2, Gaithersburg, MD (1988).
45. Y. Shimada, K. Utsumi, T. Ikeda, and S. Nagasako. "Monolithic Multicomponents Ceramic (MMC) Substrate," Int. J. Hybrid Microelec., 7(4), p. 29 (1984).
46. Y. Shimada, K. Utsumi, M. Suzuki, H. Takamizawa, M. Nitta, and T. Watari. "Low Firing Temperature Multilayer Glass-Ceramic Substrate," IEEE Trans. Comp. Hyb. Manuf. Tech., CHMT-6(4), 382 (1983).
47. K. Uchino. "Electrostrictive Actuators: Materials and Applications," Ceram. Bull., 65, 4, (1986).

LIST OF FIGURES

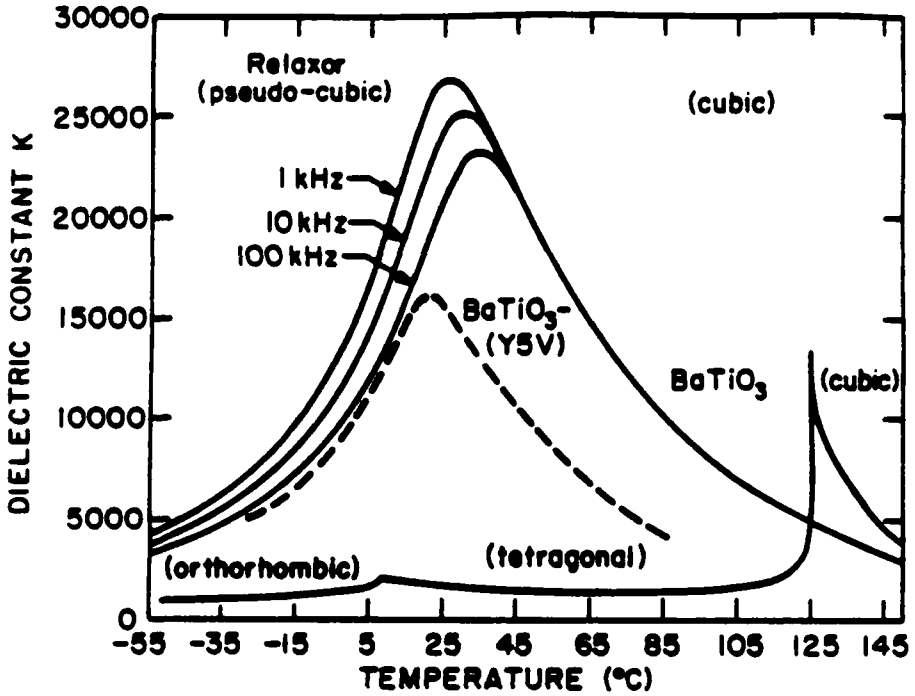
30000
25000
20000
15000
10000
5000
0
DIELECTRIC CONSTANT K
Relaxor
(pseudo-cubic)
(cubic)
1 kHz
10 kHz
100 kHz
BaTiO3-
(Y5V)
BaTiO3
(cubic)
(orthorhombic)
(tetragonal)
-55 -35 -15 5 25 45 65 85 105 125 145
TEMPERATURE (°C)

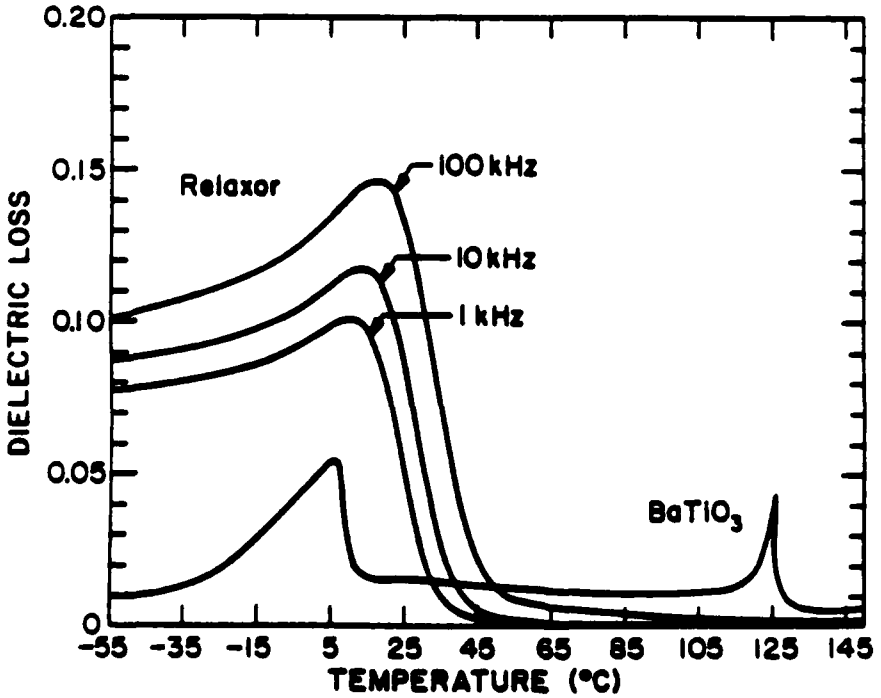
0.20
0.15
0.10
0.05
0
DIELECTRIC LOSS
Relaxor
100 kHz
10 kHz
1 kHz
BaTiO3
-55 -35 -15 5 25 45 65 85 105 125 145
TEMPERATURE (°C)

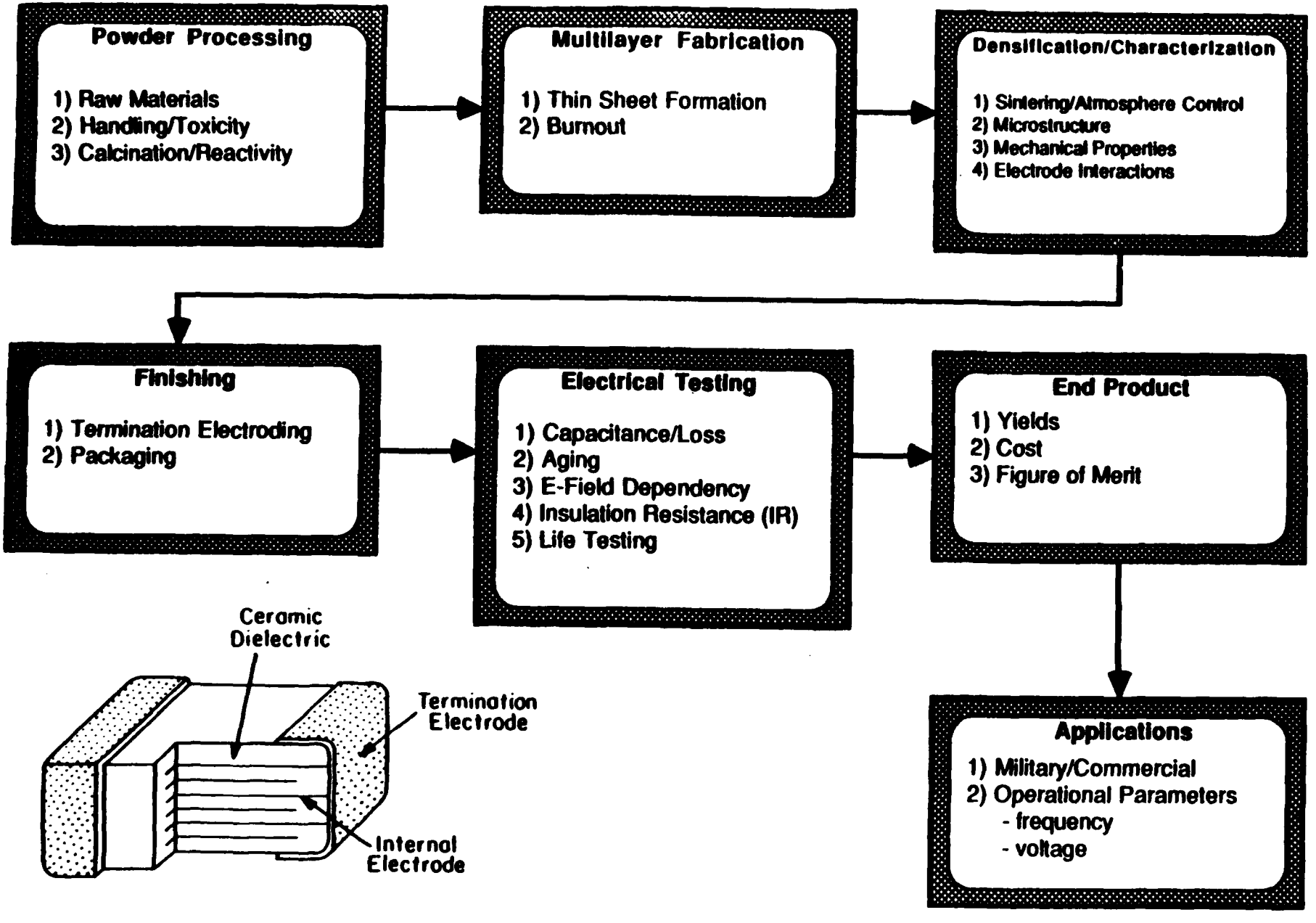

Figure 2. Flow Chart for the Production of Multilayer Capacitors.

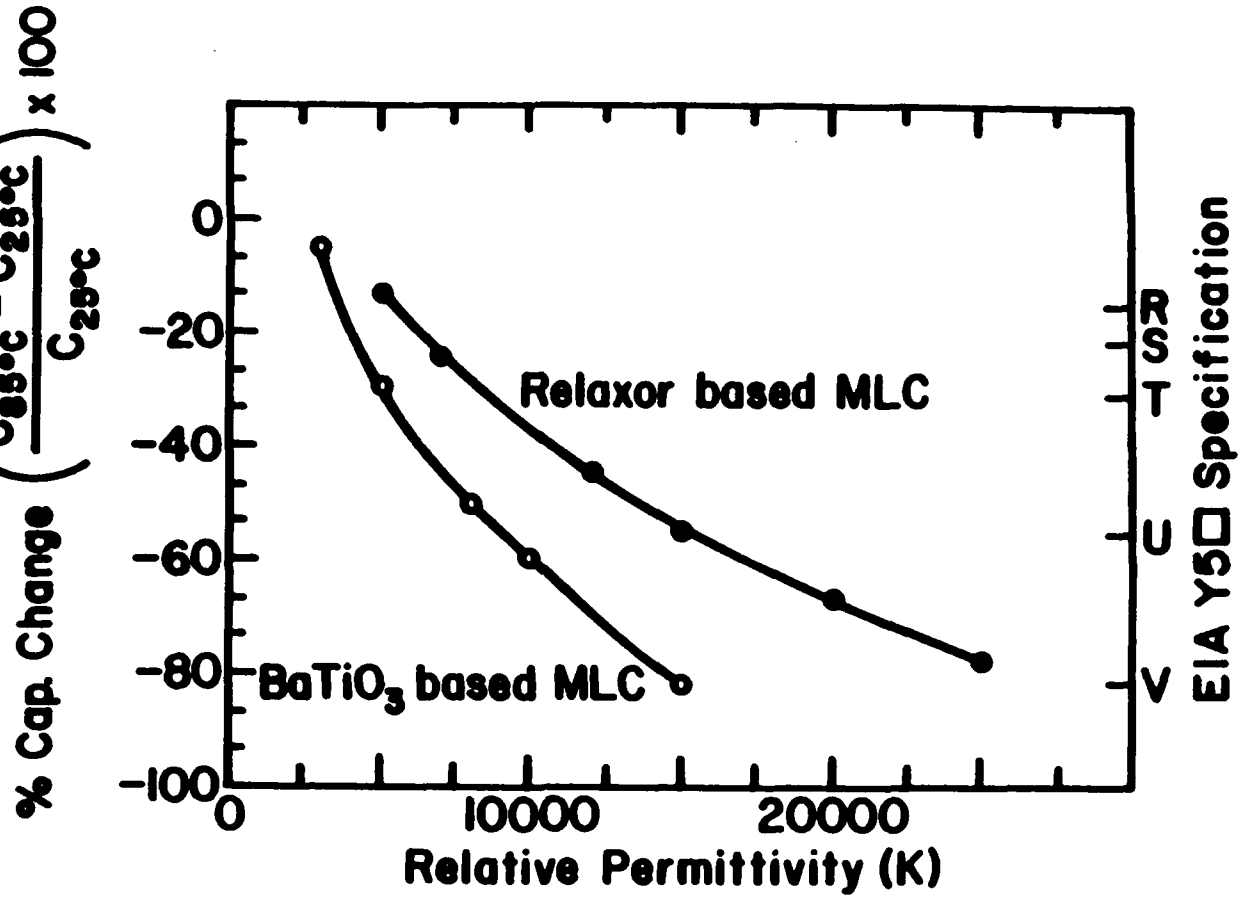
% Cap. Change $\left(\frac{C_{85°C} - C_{25°C}}{C_{25°C}}\right) \times 100$
0
-20
-40
-60
-80
-100
0
10000
20000
Relative Permittivity (K)
Relaxor based MLC
$BaTiO_3$ based MLC
R
T
C
V
EIA Y5□ Specification

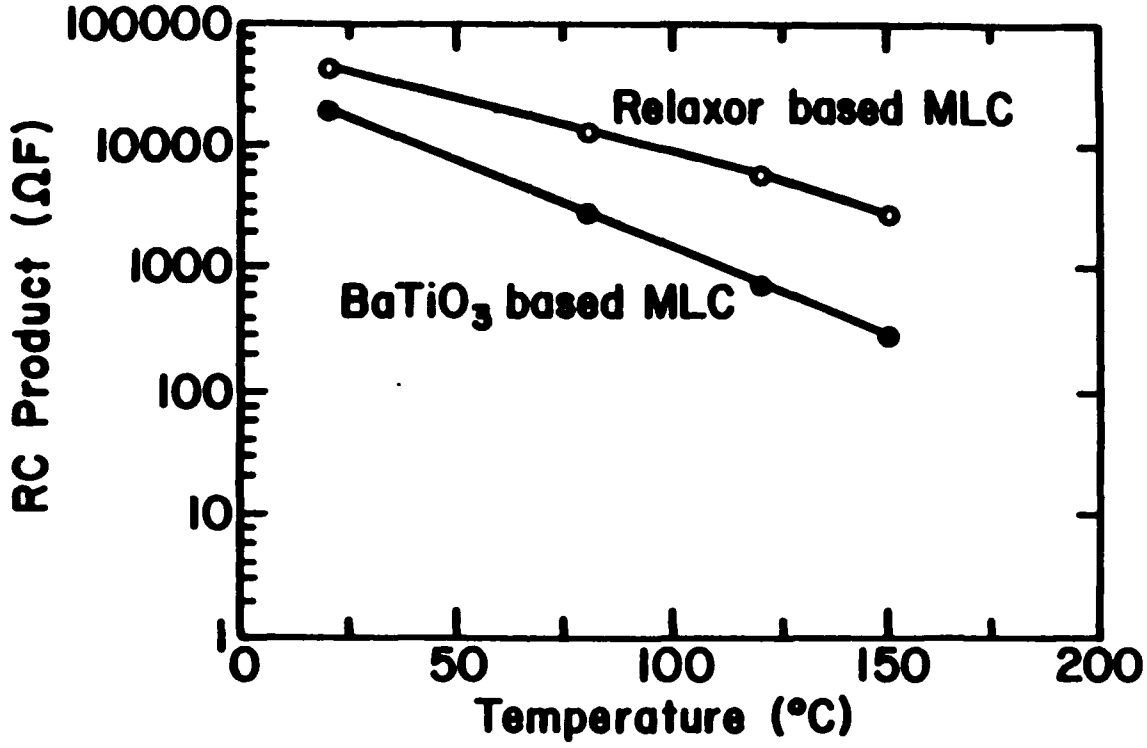
100000
10000
1000
100
10
1
RC Product (ΩF)
Relaxor based MLC
BaTiO3 based MLC
0
50
100
150
200
Temperature (°C)

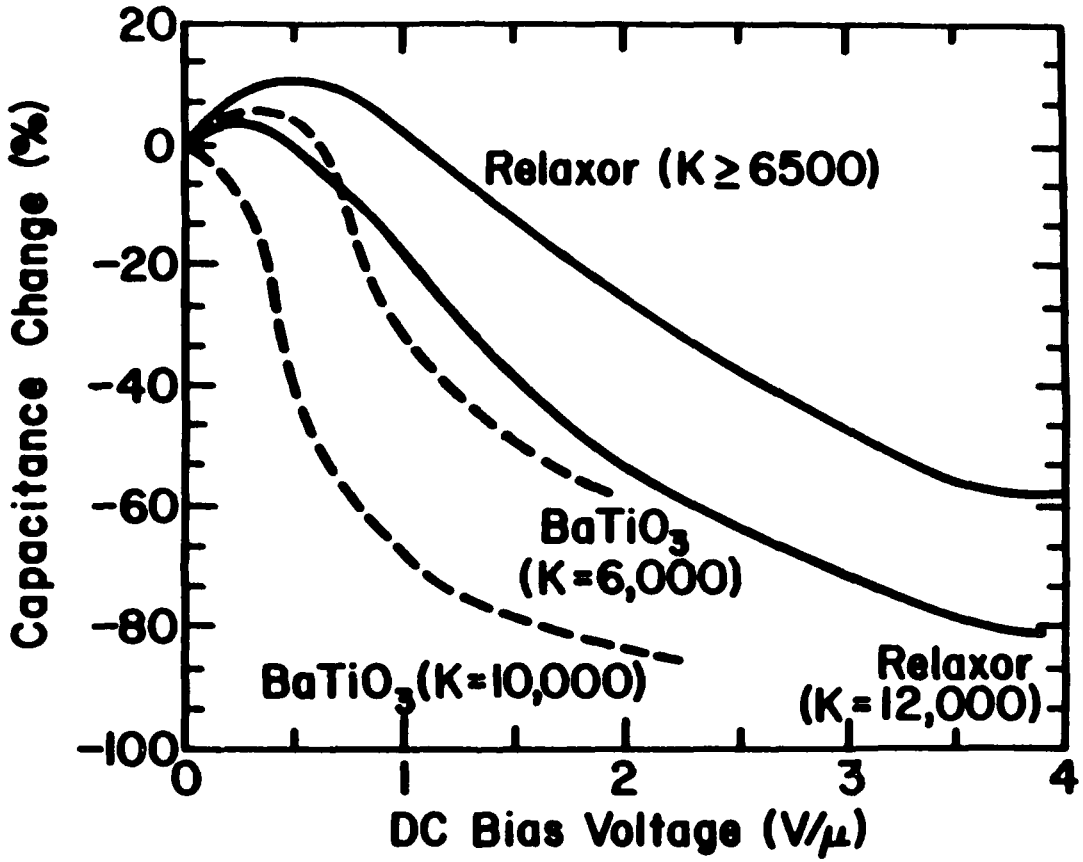
20
0
-20
-40
-60
-80
-100
Capacitance Change (%)
0
1
2
3
4
DC Bias Voltage (V/μ)
Relaxor (K≥6500)
BaTiO3
(K=6,000)
BaTiO3 (K=10,000)
Relaxor
(K=12,000)